Simulation of Integrated Energy Systems with a Focus on Gas Grids and Heating Technologies

Vom Promotionsausschuss der
Technischen Universität Hamburg
zur Erlangung des akademischen Grades

Doktor-Ingenieur (Dr.-Ing.)

genehmigte Dissertation

von

Carsten Bode

aus München

2022

1. Gutachter:	Prof. Dr.-Ing. Gerhard Schmitz
2. Gutachter:	Prof. Dr.-Ing. Klaus Görner
Prüfungsvorsitzender:	Prof. Dr.-Ing. Wolfgang Kersten

Tag der mündlichen Prüfung: 11. 02. 2022

Author  : https://orcid.org/0000-0002-0497-8888
DOI: https://doi.org/10.15480/882.4192
Handle: http://hdl.handle.net/11420/11769
URN: urn:nbn:de:gbv:830-882.0173350

Acknowledgments

First of all, I would like to thank Prof. Dr.-Ing. Gerhard Schmitz for the opportunity to conduct this research under his supervision at the Hamburg University of Technology. I highly appreciate the fruitful discussions, granted scientific freedom, and, in general, the great working conditions at the Institute of Engineering Thermodynamics. Also, I would like to thank Prof. Dr.-Ing. Klaus Görner from the University of Duisburg-Essen for being my second reviewer and Prof. Dr.-Ing. Wolfgang Kersten for taking over the chairmanship of the examination board.

This thesis is based on the research done in the project ResiliEntEE, financed by the German Federal Ministry of Economic Affairs and Energy. My special thanks are expressed to my colleagues within this research project, Anne Senkel, Oliver Schülting, and Jan-Peter Heckel. It was a pleasure to work with them in this research team. Furthermore, I would like to thank the team at XRG Simulation GmbH, especially Robert Flesch, for the great programming support and also the advisory board of the project for the valuable feedback. Special thanks go to Lisa Andresen for leading me into the area of energy system analysis as my Master thesis supervisor and later on as my colleague. I would also thank more than 15 students who conducted their theses under my supervision and strongly contributed to both the project and my thesis. Many thanks also go to all colleagues at the Institute of Engineering Thermodynamics for the great working atmosphere but also the very delightful leisure time.

Furthermore, I would like to thank my family and friends for their love and support during my studies and research years. I am especially grateful to my parents, who enabled me to pursue my dreams. Finally, my deepest gratitude goes to my wife Aurélie for the continuous support, wonderful moments, and simply being the love of my life. Last but not least, I am grateful for our daughter Lena who has enriched our lives in the best way possible.

Hamburg, March 2022

Abstract

The German government has set the goal for Germany to reach near carbon neutrality by 2050. This entails a significant change in the whole German energy system, including installing different kinds of new technical plants, for example, renewable power generators, energy storage plants, and energy conversion plants. Also, the power and the gas grid infrastructure have to follow this development. This leads to a very complex and dynamic system that has to be investigated beforehand using simulations.

In this thesis, two main questions are answered: First, how do different renewable gases in the gas grid, namely hydrogen and synthetic natural gas, influence the energy system and mainly the gas grid directly? Second, what is the effect of different heating technologies on the system? The latter focuses primarily on hybrid heating systems, combining electric and gas-fired heating technologies. To answer these questions, different models are developed and assessed. The geographical scope of those models is Germany, with a focus on Northern Germany. The sectors power, heat, and gas are considered, excluding the transportation sector.

The first model is a quasi-stationary model with which cost-efficient configurations for the future German energy system are found using optimization. The second model represents the Northern German gas grid for which a quasi-stationary grid computation is implemented. Based on the results, an aggregation algorithm simplifies the gas grid to build a dynamic gas grid model. This model can then be integrated into a dynamic integrated energy system model of Germany, including all energy producers and consumers as well as energy storage and conversion technologies and an aggregated power grid. The results of the optimization are used to parametrize the model.

The optimization results show extensive use of renewable power generators, Power-to-Gas plants, gas power plants, and lithium-ion batteries, but the latter only for scenarios using synthetic natural gas. The most economical heating technology is the hybrid heating system consisting of a gas boiler and an electric heat pump.

Using those results in quasi-stationary and dynamic grid computations enables a comparison of the two methods. It shows that the results are similar, but, in the dynamic simulations, the peaks in pressure are dampened due to the dynamic effects.

After that, the influence of the aggregation of the gas grid model can be examined. The complexity of the model and its computation time can be reduced drastically, but errors occur. However, they are only significant for highly aggregated gas grids.

Using the dynamic integrated energy system model, the questions mentioned above can be answered. First, the use of hydrogen drastically increases the required gas grid extension compared to the systems with synthetic natural gas. Second, using the hybrid heating system reduces the required grid extension for both gas and electricity in most cases.

Contents

List of Figures

List of Tables

Nomenclature

Latin Symbols

$\mathbf{A}$	Nodal incidence matrix of a graph
$\mathbf{A}_1$	Nodal incidence matrix of the load nodes of a graph
$\mathbf{A}_2$	Nodal incidence matrix of the reference nodes of a graph
a_{ij}	Entry of $\mathbf{A}$
$\mathbf{B}$	Branch-loop incidence matrix of a graph
b_{ij}	Entry of $\mathbf{B}$
C	Mass flow rate capacity of a pipeline in kg/s
c	Number of loops and chords in a graph
D	Diameter in m
d	Relative density
E	Energy in J
$e_{\mathrm{m},p}$	Mean error in pressure in bar
F	Vector in matrix-based pressure calculation in $\mathrm{kg}^2/\mathrm{s}^2$
f	Factor for modification of pressure loss equation
f_{stor}	Factor for calculation of nominal storage set pressure
G	Aggregation grade
$H_{\mathrm{i,n}}$	Net calorific value in J/kg or $\mathrm{J/m^3_N}$
$H_{\mathrm{s,n}}$	Gross calorific value in J/kg or $\mathrm{J/m^3_N}$
$\dot{H}$	Enthalpy flow rate in W
h	Specific enthalpy in J/kg
I	Current in A
i	Continuous index
j	Continuous index

$j_{\mathrm{comp,dep}}$	Indices of dependent components in fluid
$j_{\mathrm{comp,free}}$	Indices of free components in fluid
K	Compressibility factor
k	Surface roughness in m
L	Node load in m^3/s
l	Length in m
M	Molar mass in kg/mol
m	Number of branches in a graph
m_{CV}	Mass in the control volume in kg
$\dot{m}$	Mass flow rate in kg/s
N	1-norm of the average change in mass flow rate in kg/s
n_{comp}	Number of components in a fluid
n_{CV}	Number of control volumes
n_{G}	Number of nodes in a graph
n_{G1}	Number of load nodes in a graph
n_{G2}	Number of reference nodes in a graph
n_{P}	Number of pipes
n_{P1}	Number of pipes in first path of a loop
n_{P2}	Number of pipes in second path of a loop
n_{step}	Number of time steps
n_{tl}	Number of transmission lines
P	Quadratic pressure in Pa^2
P_{el}	Electric power in W
p	Pressure in Pa
Q	Volume flow rate in m^3/s
$\dot{Q}$	Heat flow rate in W
R	Specific gas constant in $\mathrm{J}/(\mathrm{kg\,K})$
Re	Reynolds number

$\mathbf{R}$	Jacobi matrix in $\mathrm{Pa^2\,s/m^3}$
r_{ij}	Entry of $\mathbf{R}$
SOC	State of charge
T	Temperature in K
t	Time in s
U	Voltage in V
u	Utilized capacity
V	Volume in $\mathrm{m^3}$
v	Exponent
$W_{\mathrm{i,n}}$	Wobbe Index related to the net calorific value in J/kg or $\mathrm{J/m^3_N}$
$W_{\mathrm{s,n}}$	Wobbe Index related to the gross calorific value in J/kg or $\mathrm{J/m^3_N}$
w	Velocity in m/s
$\mathbf{X}$	Pressure matrix in $\mathrm{Pa^2\,s^2/kg^2}$
x_{ij}	Entry of $\mathbf{X}$ in $\mathrm{Pa^2\,s^2/kg^2}$
y	Variable
z	Continuous index

Greek Symbols

α	Correlation coefficient
Γ	Capacity in W m
Δ	Difference
η	Dynamic viscosity in Pa s
λ	Friction factor
$\dot{\Xi}$	Mass flow rate of component of the fluid in kg/s
ξ	Mass fraction in kg/kg
ρ	Density in $\mathrm{kg/m^3}$
σ_p	Standard deviation of pressure in bar
τ	Time delay in s

Φ	Function
φ	Volume fraction in m^3/m^3
ψ	Molar fraction in mol/mol

Indices

air	Air
arithm	Arithmetic
base	Base
bw	Bandwidth
c	Chord
def	Default
e	Relative
eq	Equivalent
ext	Extension
gas	Gas
grid	Grid
ground	Ground
H_2	Hydrogen
id	Ideal
in	Entering
inlet	Inlet
MOP	Maximum operating pressure
m	Mean
max	Maximum
N	Node
NG	Natural gas
n	Norm
nom	Nominal

nonagg	Non-aggregated
origin	Origin
out	Leaving
outlet	Outlet
P	Pipe
Pk_i	Pipes to be combined into the ith pipe in loop aggregation
power	Power
region	Region
rem	Remaining
res	Residual
set	Set value
stor	Storage
t	Tree branch
tl	Transmission line

Abbreviations

A-CAES	Adiabatic compressed air energy storage
AC	Air conditioning
CCGT	Combined cycle gas turbine
CCS	Carbon capture and storage
CHP	Combined heat and power
CPU	Central processor unit
DAC	Direct air capture
DVGW	Deutscher Verein des Gas- und Wasserfaches (German Technical and Scientific Association for Gas and Water)
EHP	Electric heat pump
EHPEHR	Electric heat pump coupled with an electric heating rod
EHPGB	Electric heat pump coupled with a gas boiler

GB	Gas boiler
GCV	Gross calorific value
GHP	Gas heat pump
GPS	Global positioning system
GT	Gas turbine
H2	Hydrogen
HP	Heat pump
HT	High temperature
ICT	Information and communication technology
IES	Integrated energy system
LAU	Local administrative unit
Li	Lithium
LNG	Liquefied natural gas
LSCHP	Large-scale combined heat and power
LT	Low temperature
MOP	Maximum operating pressure
MT	Medium temperature
NCV	Net calorific value
NG	Natural gas
NUTS	Nomenclature des unités territoriales statistiques (Nomenclature of Territorial Units for Statistics)
O&M	Operation and maintenance
PHS	Pumped hydro storage
PtG	Power-to-Gas
PtGtP	Power-to-Gas-to-Power
PtH	Power-to-Heat
PV	Photovoltaics
RE	Renewable energy

SNG	Synthetic natural gas
SOC	State of charge
SSCHP	Small-scale combined heat and power

1 Introduction

1.1 Motivation and Background

To contribute to the limitation of the effects of climate change, the German government has decided to reduce greenhouse gas emissions by 80-95 % compared to 1990 by 2050 (BMWi, 2018). The United Nations have even agreed on achieving carbon neutrality until 2050 (United Nations, 2015), and the European Union has adopted this goal (European Commission, 2018).

A significant change of the whole energy system is necessary to reach those goals, defined by BMWi (2018) using two core factors: First, a vast extension of renewable energy generators is needed to provide the system with carbon-neutral energy. Second, the system itself has to become more energy efficient to reduce the necessary energy input. Furthermore, the necessity of storage and coupling technologies to connect the different energy sectors is mentioned: Since most renewable power generators depend on wind and sunlight, generally, generation and demand do not match. Storage plants can help to shift the energy on a time scale. Coupling technologies shift the energy as well, but from one sector to the other: Most of the renewable energy producers generate electricity, but 25 % of the final energy consumed in Germany in 2019 was provided by a gaseous energy carrier, primarily natural gas (BMWi, 2020). That is why sector coupling will gain more importance, especially the Power-to-Gas technology since it can produce renewable gases using renewable electricity.

However, some processes might be convertible from gas to electricity, for example, space heating for households, but there are some limitations, especially for industrial processes. Also, it is questionable if a space heat supply entirely by electricity is possible since it would lead to remarkably high peak loads during cold spells. This would necessitate a significant power plant reserve and power grid extension merely for this purpose.

Furthermore, the power grid is not only a bottleneck of the system in those cases but also in times of high renewable power generation. In 2019, 6.5 $\mathrm{TWh_{el}}$ of electricity, which resembles 1.2 % of the produced electricity, were curtailed because the power grid was not designed to transport that amount of power (Bundesnetzagentur, 2020). With increasing renewable power generation, this issue is expected to grow.

Also, there will be many changes in the gas sector that will need closer investigation: First, the gas production will change from natural gas extraction to, for example, Power-to-Gas with a high timely variability since it depends on renewable power generation. Second, there might be a switch from natural gas in the gas grid to hydrogen, which has significantly different gas properties. Third, the gas demand will change primarily due to the increased use of gas in power plants to provide power at times of low renewable power generation, leading to more dynamics in the gas grid.

In general, this shows that the whole energy system, from energy production over storage and conversion to demand, including the energy grids, has to be examined to

answer the essential questions about the future energy system. Due to the fluctuating nature of energy generation, conversion, storage, and transport in the future, dynamic simulations are a suitable tool for those investigations.

1.2 Thesis Overview and Outline

This thesis investigates the influence of different heating technologies and different renewable gases on the entire integrated energy system consisting of the sectors power, heat, and gas, excluding the transportation sector. First, optimal configurations of the future German integrated energy system for 60 %, 80 %, and 100 % renewables are searched using optimization of a quasi-stationary model from an economic perspective. The results are used to parametrize a dynamic model of an integrated energy system representing Germany with a focus on Northern Germany. The model includes all necessary dynamic effects of the system components. To examine the energy grids and especially the required grid extension, the model also contains a power and a gas grid. The heat sector is provided with the desired energy from the other two sectors.

Due to the complexity, both grids have to be aggregated to be used in the dynamic integrated energy system model. Hence, an algorithm is developed for the gas grid and, for the power grid, an algorithm from Heckel et al. (2020) is employed. Since the gas grid aggregation needs detailed information about the grid, including pressures at the nodes and mass flow rates in the pipes, a quasi-stationary gas grid computation is implemented. This enables, first, the comparison of a quasi-stationary and a dynamic gas grid computation and, second, the evaluation of the errors resulting from the aggregation.

The thesis starts in Chapter 2 with a description of the state of the art, including an overview of the system's components, recent studies in the field, and the theory of gas and power grids, including available aggregation methods. Afterward, in Chapter 3, all developed and employed models are described as well as details about the considered scenarios and the data used. In Chapter 4, the results of the models are presented. This includes results from the optimization, the comparison of the quasi-stationary and dynamic gas grid computation, the aggregation, and the dynamic integrated energy system model. The latter focuses on the differences in required gas and power grid extension depending on the renewable gases and heating technologies used in the system. The thesis is closed by a summary of all findings and an outlook of possible future developments in Chapter 5.

2 State of the Art

In this chapter, the state of the art is described: First, general information about integrated energy systems is given in Section 2.1, and in Section 2.2, different studies are presented which model those systems. Second, a general description of gas grids and ways to compute them are shown in Section 2.3, followed by the aggregation techniques for fluid networks in Section 2.4. The chapter closes with a brief description of power grids in Section 2.5.

2.1 Integrated Energy Systems

An integrated energy system (IES) is an energy system in which several sectors are coupled with each other through endogenous energy conversion, so conversion inside the system. Figure 2.1 shows an integrated energy system schematic, including the sectors power, heat, and gas. Another sector, which is not shown here, is the transportation sector which can be integrated as well. Figure 2.1 shows the different exogenous inputs for each sector that come from outside the system. Examples are power from renewable power generators and coal power plants for the power sector or biogas and fossil gases for the gas sector. The exogenous energy inputs are covered in Section 2.1.1. Those inputs are used to satisfy the different demands. To meet the demand at every time instance, each sector can use storage units, described in Section 2.1.2. Also, energy can be converted endogenously, see Section 2.1.3, that is, within the system, from one form of energy to the other, so from one sector to the other. There are classic coupling technologies which have been used for decades, for example, gas boilers or gas power plants, and others which are gaining or will gain more importance in an integrated energy system with high shares of renewables: Since most of the renewable energy (RE) converters produce electricity directly, but the power sector has only small storage capacities (Sterner and Stadler, 2019), it is beneficial to use the storage technologies of the other sectors. That is why the coupling technologies Power-to-Heat (PtH) and Power-to-Gas (PtG) are expected to play a significant role in a future integrated energy system.

2.1.1 Exogenous Energy Input

Exogenous energy input is an input that enters the defined system consisting of the power, heat, and gas sector from outside. In the following, the most relevant inputs for each sector are described.

Power Sector

Conventional power production occurs in power plants in which fossil fuel is combusted, most commonly nowadays coal or natural gas but also oil. The combustion of fossil fuels

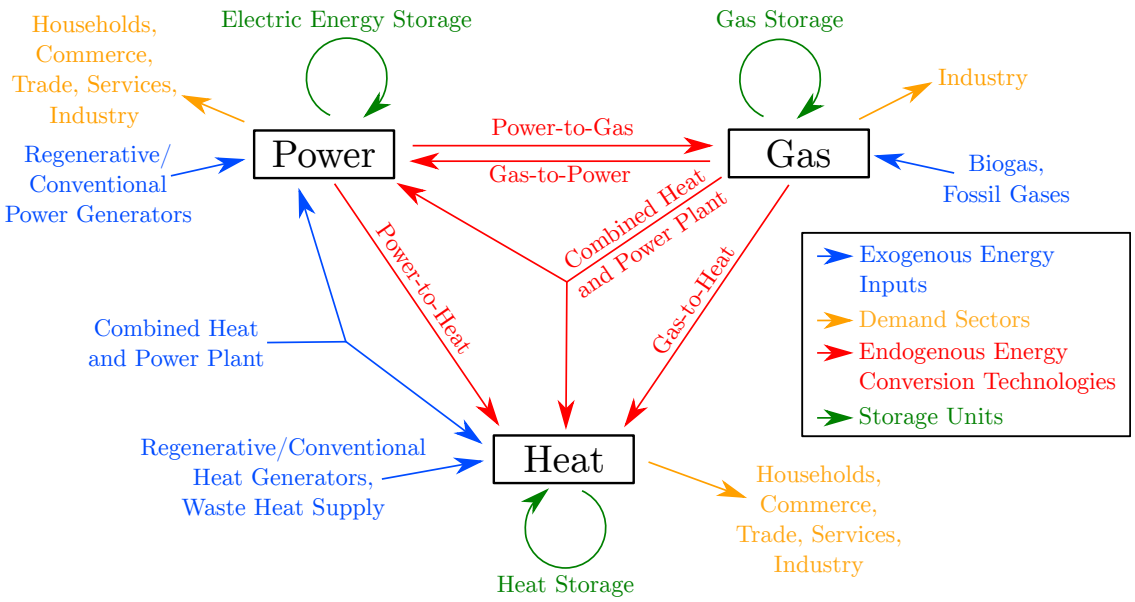

Figure 2.1: General schematic of an integrated energy system including the sectors power, heat, and gas.

always generates CO_2, which is nowadays emitted into the atmosphere. Alternatively, it can be separated from the flue gas and stored underground, so-called Carbon Capture and Storage (CCS). This reduces the greenhouse gas effect of the power plants but requires additional separation plants, available CO_2 storage, and possibly pipelines for transport as well as the acceptance of the population. A review of all relevant technologies of conventional power plants and CCS can be found in Packer et al. (2018).

Alternative CO_2-free power production is possible by using nuclear power plants. Due to the risks and the problematic waste, Germany has decided to phase out nuclear power plants by 2022 (Bundesrepublik Deutschland, 2020).

The most promising CO_2-neutral power generators are renewable energy converters since their operation avoids CO_2 generation. Renewable energy is provided by the moon's movement, stored inside the earth, or delivered as solar radiation (Sørensen, 2017). This way, the energy is almost available unlimited in the time span of humans. The most important renewable energy converters for power generation in Germany are photovoltaic plants, wind turbines, and run-of-river power plants. A thorough review of all technologies can be found in Sørensen (2017).

Heat Sector

Exogenous heat generation in a future energy system will mostly be done using solar thermal collectors or geothermal plants as well as combustion of biomass, described in Sørensen (2017). Also, waste heat integration, for example, from industrial processes, into district heating networks is possible.

Gas Sector

The exogenous gas inputs nowadays are almost exclusively natural gas and biogas whereat natural gas provides by far the larger share with 23.5 % of the primary energy consumption

compared to 2.6 % for biogas in Germany in 2019 (BMWi, 2020).

The process of natural gas reservoir exploitation is explained in Cerbe et al. (2017) and is not described here since natural gas extraction in Germany is strongly declining. It is forecasted that the German production will reduce by 40 % from 2019 to 2030 (FNB Gas, 2020) and has to be zero at least by 2050 to meet the climate goals without CCS.

With an increasing demand for CO_2-neutral energy carriers, the importance of biogas will rise. Biogas is most commonly produced by fermentation of organic material in an anaerobic reactor, as described by Homann, Hüwener, et al. (2017). Different substrates can be used, ranging from renewable raw materials, for example, corn or wheat, over manure to other agricultural or communal waste. Raw biogas contains a high share of CO_2, which can be separated in a biogas cleaning plant. This process is called biogas-upgrading, and the resulting biomethane can be fed directly into the natural gas grid.

Alternatively, hydrogen can be produced by gasifying biomass. Different technologies were evaluated by Zech et al. (2014).

2.1.2 Energy Storage

A comprehensive review of all kinds of energy storage technologies can be found in Sterner and Stadler (2019). Figure 2.2 illustrates the different storage technologies, showing typical capacities and discharge durations. Typical short-term storage technologies are found in the bottom left of the diagram, whereas long-term storage options lie in the top right. In the following, the essential technologies for each sector are shortly described.

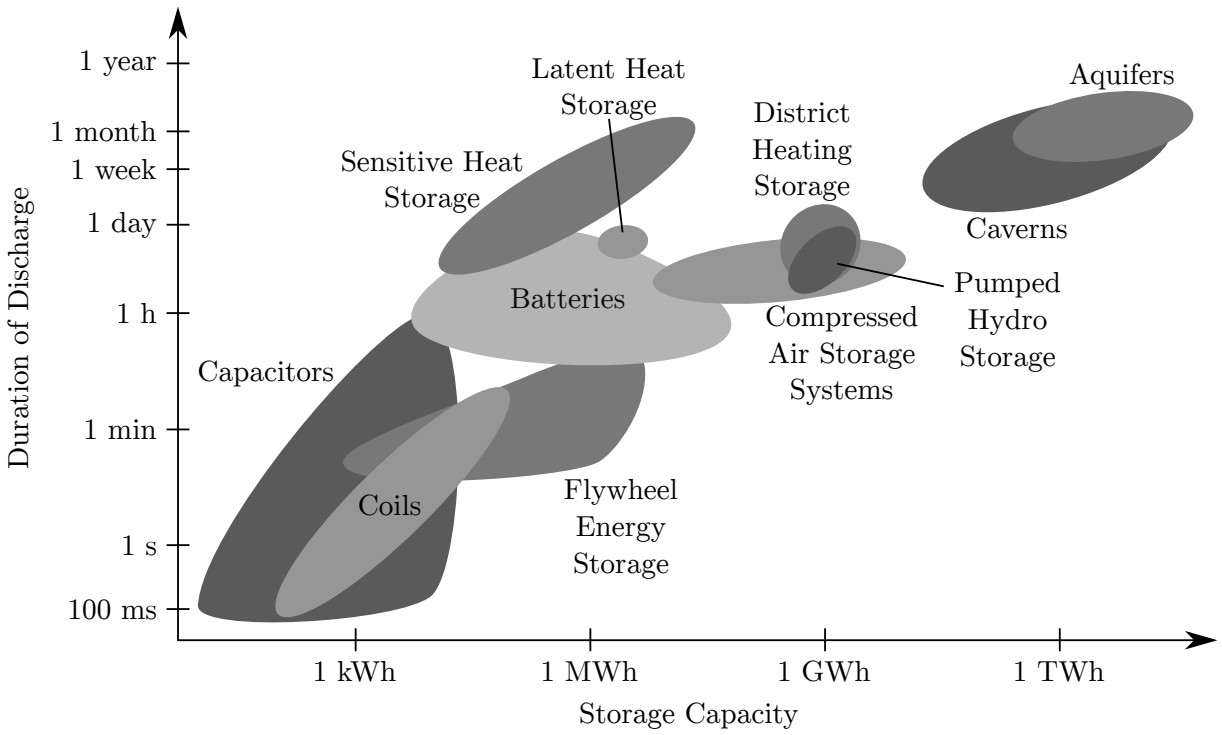

Figure 2.2: Ragone plot showing the duration of discharge in relation to the capacity of different storage technologies, own representation based on Sterner and Stadler (2019).

Power Sector

The most established or promising energy storage technologies in the power sector are batteries, pumped hydro storage plants (PHS), and adiabatic compressed air energy storage plants (A-CAES). Other storage technologies are included in the other sectors, for example, gas storage technologies which can be charged with electricity using PtG and possibly discharged, generating electricity again in gas power plants.

A battery is an electrochemical energy storage that uses different materials that are reduced and oxidized to enable a flow of electrons. The most promising technology is the lithium-ion battery which has high efficiency and good charging and discharging characteristics. Recent developments have led to a substantial decrease in cost, which will continue (Elsner and Sauer, 2015).

Pumped hydro storage plants are based on the use of the potential energy of water. It is pumped into an elevated basin using electricity and generates power later by flowing through a turbine and powering a generator. It relies on height differences and uses much space, which limits the potential strongly. In Germany, the potential is almost entirely exploited (Benndorf et al., 2014).

Adiabatic compressed air energy storage plants use a storage volume into which air is pressed. The air heats up when compressed and is cooled down before entering the storage while the heat is stored in suitable heat storage. When the air is released from the storage, it is subsequently heated up with the stored heat and drives a turbine with a generator which produces electricity. This functionality makes it independent from height differences but dependent on large storage volumes, which are most commonly salt caverns to provide large storage capacities.

Heat Sector

Hot water storage tanks are the most commonly used heat storage in all kinds of applications with temperatures below the boiling point of water. This technology is well-established and will still be used in a future energy system. There is ongoing research about other heat storage technologies, such as phase change materials and thermochemical storage. However, those technologies have not reached broad larger-scale applications yet, and future use is difficult to project.

Gas Sector

The most crucial gas storage technology is large-scale storage in salt caverns, depleted natural gas reservoirs, or aquifers. Those storage technologies are well-established for natural gas and can at least partly store hydrogen: Some salt caverns are already used for hydrogen storage, and town gas with more than 50 vol% hydrogen has already been stored in depleted natural gas reservoirs. Also, recent research suggests that pure hydrogen is possible (Amid et al., 2016; Heinemann et al., 2018).

2.1.3 Endogenous Energy Conversion

In this section, the endogenous energy conversion is shortly presented, which is the energy conversion within the defined system, so from one of the sectors power, heat, and gas to one or two of the other sectors and thus the core of the coupling between the sectors.

Power-to-Gas

Power-to-Gas is the central energy conversion technology to allow the utilization of the gas storage volumes for the power sector: In electrolyzers, electricity is used to split water into hydrogen and oxygen. Different electrolysis technologies with different advantages exist; an overview is given by Homann, Hüwener, et al. (2017).

The hydrogen can then be stored or further transformed into other energy carriers. The most interesting transformation for the gas sector is the methanation in which hydrogen reacts with CO_2 in a reactor with the help of a catalyst or bacteria to react to methane. More details about the process can be found in Homann, Hüwener, et al. (2017). The resulting gas is called Synthetic Natural Gas (SNG) since it has the same characteristics as natural gas and thus can be fed into the natural gas infrastructure without any adjustments. Also, if the CO_2 is separated from ambient air or, for example, separated from the flue gas of a biomass combustion plant, the SNG can be defined as carbon-neutral.

To have access to the necessary amount of CO_2 for large-scale methanation, direct air capture (DAC) seems promising since it is independent of sources of high content CO_2 streams like biomass combustion plants. This way, the DAC plant can be directly placed next to the methanation plant to avoid CO_2 pipelines. The process is based on the absorption of CO_2 from ambient air and regeneration using electricity and heat, if available. More details can be found in Keith et al. (2018).

Gas-to-Power

Gas-fired power plants are gas turbines and combined-cycle gas turbines, as described by Packer et al. (2018). With those plants, the electric energy stored as gas via PtG can be re-electrified and closes the cycle of the Power-to-Gas-to-Power (PtGtP) plant. A possibility to avoid CO_2 generation is to switch the power plants to renewable gases, that is, gases that are CO_2-neutral. Examples are hydrogen, biogas, or even SNG, as long as the used CO_2 originates from the atmosphere.

Power-to-Heat

There are different technologies to convert electricity to heat. The simplest is an electric boiler, often realized as a flow-type heater for tap water (Recknagel et al., 2017). Alternatively, an electric heating rod can be used, which can either be integrated directly into a hot water storage tank or other heating devices.

Compared to an electric boiler's efficiency, an electric heat pump has a higher coefficient of performance, defined as delivered heat related to the consumed electricity. It uses a thermodynamic process that enables the utilization of ambient energy via a heat exchanger, which results in coefficients of performance greater than one. However, it decreases with increasing supply temperature. A more thorough description is given by Sørensen (2017).

To reduce the investment cost, an electric heat pump is often combined with an electric heating rod that supports the electric heat pump at low ambient temperatures, for example, below $-5\,°C$, as advised by Recknagel et al. (2017).

Gas-to-Heat

The most common heating technology in Germany is the gas boiler, currently installed in approximately 50 % of all households (Klocke et al., 2020). It relies on the combustion of natural gas and heat transfer to the heating water. The technology is divided into low-temperature and condensing boilers with the difference that the latter cool down the flue gas so much that water condensation occurs. This leads to an increase in efficiency since the enthalpy of condensation is used as well.

Another way to generate heat using gas is a gas heat pump with higher efficiency than a condensing boiler but still lower than an electric heat pump (Klocke et al., 2020). There are different types: A gas-powered heat pump works similar to an electric heat pump but uses a gas-fired engine to drive the compressor instead of an electric motor. Absorption or adsorption heat pumps use a thermal condenser instead of a mechanical compressor exploiting absorptive or adsorptive properties of a coolant (absorption) or a material (adsorption). More details can be found in Klocke et al. (2020).

Gas-to-Power-and-Heat

To increase the overall efficiency of power and heat generation, they can be combined in a combined heat and power (CHP) plant, described by Packer et al. (2018). Large-scale CHP plants, typically CCGT power plants, also produce heat, most commonly fed into a heating network. Another possibility is a small-scale combustion engine that drives a generator to generate power, and the coolant collects the waste heat, which can be used for space heating, for example.

Combined Systems

To increase flexibility for the consumer and the entire system as well as efficiency, different heating technologies can be combined (Sterner and Stadler, 2019): Electric heat pumps and gas boilers can jointly decrease the electric load on cold winter days compared to a purely power-driven heat provision. Such a hybrid heating system is, for example, offered by Viessmann (2020). Analogously, any combination of a Gas-to-Heat technology with a Power-to-Heat technology is possible.

2.2 Modeling of Integrated Energy Systems

In the last years, many studies about the future German integrated energy systems have been published, which cover different sectors and use different methodologies and modeling techniques. In the following, a short description of a selection of studies will be given to give an overview of the field.

First, studies can be distinguished depending on the sectors which were considered. Sterner, Thema, et al. (2014) and Elsner, Fischedick, et al. (2015) focus on the power sector, but the other sectors are partly included in the model as boundary conditions. Robinius, Otto, et al. (2017) focus on combining the power and transport sector, whereas Bürger et al. (2016) analyze how the building sector can be greenhouse gas-neutral in 2050.

The majority of recently published studies consider the whole energy system since integrating the different sectors has gained more attention. There are different kinds of studies: The first kind describes the future either by extrapolating trends or assuming certain developments, those studies are called scenario studies, for example, Nitsch et al. (2012), Benndorf et al. (2014), Schlesinger et al. (2014), Repenning et al. (2015), and Bründlinger et al. (2018). The other kind conducts an economic optimization to obtain the most cost-effective solution. Political guidelines or technical limitations can be included as boundaries. Those studies are called optimization studies, for example, Breyer et al. (2013), Palzer (2016), Bernath et al. (2017), Purr et al. (2019), Sterchele et al. (2020a), and Robinius, Markewitz, et al. (2020). However, even if the most economical configuration is found, there might be another one that is just slightly less cost-effective but might contain completely different technologies, as is mentioned by Palzer (2016) and Breyer et al. (2013).

Second, another difference is the modeling technique. The vast majority of studies employ quasi-stationary models due to their numerical efficiency. Only a few studies exist which use dynamic models, for example, Senkel et al. (2021), Andresen (2019), Schülting (2021), and Benthin et al. (2020), but they are often limited by their geographical scope due to the complexity of the models. The advantage is that dynamic effects are included, which leads to more realistic results. Especially as soon as resilience, that is, the ability to withstand disturbances, is considered, dynamic simulation is inevitable, as used by Senkel et al. (2021).

Third, even though most of these studies consider all sectors (power, heat, gas, and transportation), there are still some differences in the considered aspects: First, most of the studies focus on CO_2 as the only greenhouse gas, but some studies also look at other emissions, for example, nitrous oxide or methane which mainly occur in the agricultural sector and also cause a greenhouse effect (Benndorf et al., 2014; Repenning et al., 2015; Purr et al., 2019). Second, the non-energetic fuel demand, for example, natural gas or mineral oil, is often neglected since the consumption is by definition not part of the energy sector because the fuels are not used energetically. However, some studies include it in their models since the demand can have a significant impact on the results, for example, Nitsch et al. (2012), Benndorf et al. (2014), Schlesinger et al. (2014), Purr et al. (2019), Robinius, Markewitz, et al. (2020), and Fette et al. (2020). One study even quantified the consumption of all kinds of resources as part of a sustainable system (Purr et al., 2019).

Furthermore, the energy grids are not always considered. Some studies include a power grid (Nitsch et al., 2012; Breyer et al., 2013; Bründlinger et al., 2018; Robinius, Markewitz, et al., 2020; Fette et al., 2020), and only a few consider a gas grid (Fette et al., 2020) because the capacities are commonly assumed to be sufficient.

Due to the limited potential of renewable energies, the German energy demand might not be satisfiable without importing, for example, hydrogen or synthetic energy carriers. That is why in recent studies (Purr et al., 2019; Bründlinger et al., 2018; Sterchele et al., 2020a; Robinius, Markewitz, et al., 2020) also the import of different energy carriers was considered.

In general, most of the studies agree that renewable gases like hydrogen or SNG will play an essential role in the future energy system due to their beneficial storage capabilities. Only a few studies neglect those gases, mainly for economic reasons (Schlesinger et al., 2014; Bernath et al., 2017).

2.3 Gas Grids

In this section, an overview of the fundamentals of gas grids is given, including general gas properties, specific information about natural gas and hydrogen, as well as the German gas grid and its components. Afterward, the basics of the mathematical description of gas grids are presented.

2.3.1 Gas Properties

Certain gas properties are used to describe gases. First, the composition can be given in percentages of mole, volume, or mass. The molar fraction of component i in a gas mixture ψ_i can be converted to its mass fraction ξ_i by using the molar mass of the component M_i and the gas mixture M (Schmitz, 2020).

$$\xi_i = \frac{M_i}{M}\psi_i \quad \text{with} \quad M = \sum_i \psi_i M_i \tag{2.1}$$

For an ideal gas, volume fraction φ_i and molar fraction ψ_i are identical (Schmitz, 2020).

Second, the net calorific value (NCV) indicates the energy released when combusting the gas. The gas, the combustion air, and the flue gas enter and leave the system at an arbitrary reference temperature, and the water vapor in the flue gas does not condensate (Schmitz, 2020). The gross calorific value (GCV) is defined the same way, except that it is assumed that the water vapor condensates completely. That is why the GCV is always higher than the NCV as soon as the combustible contains hydrogen atoms.

Third, the Wobbe Index defines the heat load of a gas (DVGW Arbeitsblatt G 260, Mar. 2013), which means that two gases with the same Wobbe Index can be exchanged without changing the burner valve. It is calculated by dividing the GCV $H_{\mathrm{s,n}}$ or NCV $H_{\mathrm{i,n}}$ by the square root of the relative norm density d_{n} of the gas $\rho_{\mathrm{n,gas}}$ in relation to air $\rho_{\mathrm{n,air}}$.

$$W_{\mathrm{s,n}} = \frac{H_{\mathrm{s,n}}}{\sqrt{d_{\mathrm{n}}}} \quad \text{or} \quad W_{\mathrm{i,n}} = \frac{H_{\mathrm{i,n}}}{\sqrt{d_{\mathrm{n}}}} \quad \text{with} \quad d_{\mathrm{n}} = \frac{\rho_{\mathrm{n,gas}}}{\rho_{\mathrm{n,air}}} \tag{2.2}$$

2.3.2 Natural Gas and Hydrogen

The classification of gases for the public gas supply in Germany is regulated by the German Technical and Scientific Association for Gas and Water (Deutscher Verein des Gas- und Wasserfaches, DVGW). According to DVGW Arbeitsblatt G 260 (Mar. 2013), those gases are divided into three gas families, which have different properties:

1. Gases high in hydrogen, which originated from coal gasification (not distributed anymore),

2. gases high in methane, such as natural gas, and

3. liquefied gases, such as Liquefied Petroleum Gas which is a mixture of propane and butane.

Table 2.1: Limitations and properties of natural gas and hydrogen according to DVGW Arbeitsblatt G 260 (Mar. 2013) and Cerbe et al. (2017).

Property	Unit	Natural Gas		Hydrogen
		L-gas	H-gas	
Gross Calorific Value	MJ/m^3	30.2-47.2		12.7
Relative Density	-	0.55-0.75		0.07
Wobbe Index Related to GCV	MJ/m^3	39.6-46.8	49.0-56.5	13.4

For those gas families, different limits for concomitant substances or connection pressure apply; see DVGW Arbeitsblatt G 260 (Mar. 2013). Since natural gas is widely used, the second family is the most relevant. To account for different gas properties depending on the origin of the gas, natural gases are split into two groups: high calorific gas (H-gas) and low calorific gas (L-gas), with the limitations listed in Table 2.1. H-gases have higher limits for the Wobbe Index than L-gases, and both types are transported and distributed in separate gas grids. Since L-gases primarily come from the Netherlands, where the production is continuously decreased, L-gas grids are subsequently transformed to H-gas grids. Hence, H-gases will gain more importance in the short term until the gas consumption decreases due to the energy transition. Currently, H-gas is mainly imported to Germany from Russia and Norway (Klocke et al., 2020).

Due to the different densities, calorific values, and Wobbe Indices of natural gas and hydrogen, see Table 2.1, hydrogen admixture changes the gas mixture's relevant properties. Additionally, DVGW Arbeitsblatt G 262 (Sep. 2011) limits hydrogen admixture to 2 vol%, if the mixture is used as a fuel in cars due to the risk of embrittlement of the tank material, and to 5 vol%, if the gas is stored in depleted gas reservoirs or aquifers due to the risk of hydrogen sulfide production by bacteria (DVGW Arbeitsblatt G 260, Mar. 2013). Also, gas turbine manufacturers suggest limits due to the change of combustion behavior with increasing hydrogen content. To enable the use of the gas grid as energy storage for hydrogen, the aim is to increase the limit for the whole gas grid to 20 vol% or switch to pure hydrogen (DVGW, 2019). However, energetically, 20 vol% of hydrogen merely resembles 7.38 %, assuming Russian H-gas and gross calorific values from Cerbe et al. (2017):

$$\frac{E_{\mathrm{H_2}}}{E_{\mathrm{H_2}} + E_{\mathrm{NG}}} = \frac{\varphi_{\mathrm{H_2}} H_{\mathrm{s,n,H_2}}}{\varphi_{\mathrm{H_2}} H_{\mathrm{s,n,H_2}} + \varphi_{\mathrm{NG}} H_{\mathrm{s,n,NG}}} \tag{2.3}$$

$$= \frac{20\,\mathrm{vol\%} \cdot 12.745\,\mathrm{MJ/m^3}}{20\,\mathrm{vol\%} \cdot 12.745\,\mathrm{MJ/m^3} + 80\,\mathrm{vol\%} \cdot 39.96\,\mathrm{MJ/m^3}} \tag{2.4}$$

$$= 7.38\,\% \tag{2.5}$$

That is why the rededication of natural gas pipelines to hydrogen pipelines is planned to enable the transport of pure hydrogen while avoiding building a new infrastructure (DVGW, 2019; FNB Gas, 2020). Alternatively, installing a separate hydrogen grid is considered, for example, by Reuß (2019). In general, the transmission of pure hydrogen pays off as soon as high quantities are reached, as Andresen et al. (2018) investigated.

Assuming that hydrogen and natural gas can be stored in gas storage volumes at the

same pressure and temperature, the energy capacity will be different for both gases due to unequal densities and calorific values. For example, for storage between 58 bar and 175 bar at 44 °C (Tietze et al., 2015), the energetic storage capacity of hydrogen storage is less than a quarter of the capacity of natural gas storage using values for hydrogen and Russian H-gas from Cerbe et al. (2017) and NIST (2018):

$$\frac{E_{\mathrm{H_2,NCV}}}{E_{\mathrm{NG,NCV}}} = \frac{\left(\rho_{\mathrm{H_2}}(175\,\mathrm{bar}, 44\,^\circ\mathrm{C}) - \rho_{\mathrm{H_2}}(58\,\mathrm{bar}, 44\,^\circ\mathrm{C})\right) H_{\mathrm{i,n,H_2}}}{\left(\rho_{\mathrm{NG}}(175\,\mathrm{bar}, 44\,^\circ\mathrm{C}) - \rho_{\mathrm{NG}}(58\,\mathrm{bar}, 44\,^\circ\mathrm{C})\right) H_{\mathrm{i,n,NG}}} \tag{2.6}$$

$$= \frac{(12.14\,\mathrm{kg/m^3} - 4.29\,\mathrm{kg/m^3}) \cdot 119.95\,\mathrm{MJ/kg}}{(126.22\,\mathrm{kg/m^3} - 38.81\,\mathrm{kg/m^3}) \cdot 49.13\,\mathrm{MJ/kg}} \tag{2.7}$$

$$= 21.93\,\% \tag{2.8}$$

2.3.3 The German Natural Gas Grid

In Germany, the natural gas grid is divided into different levels according to the relative pressure p_e (relative to the ambient pressure) (Cerbe et al., 2017):

- low pressure: $p_\mathrm{e} < 100\,\mathrm{mbar}$
- medium pressure: $100\,\mathrm{mbar} < p_\mathrm{e} < 1000\,\mathrm{mbar}$
- high pressure: $p_\mathrm{e} > 1000\,\mathrm{mbar}$

The gas transmission grid is the backbone of the German gas grid because it enables the transnational natural gas transport. That part of the gas grid consists of more than 40 000 km of pipelines and is operated by the 16 transmission system operators for gas (FNB Gas, 2020). It is part of the high-pressure grid and has maximum operating pressures (MOP) of up to 100 bar. A map representation of the natural gas transmission grid can be found in ENTSOG (2014).

2.3.4 Gas Grid Components

The essential part of a gas grid is the pipelines since they transport the gas from the production site to the consumer. An overview of the planning and building process for pipeline projects is given in Homann, Hüwener, et al. (2017).

Besides the passive component pipeline, there are also active components essential for the operation of a gas grid: compressor stations and pressure regulating stations. A quick summary for both technologies is given below; more details can be found in Homann, Reimert, et al. (2013).

Compressor stations are exclusively used on the transmission level to compensate for the pressure losses in the pipes. Otherwise, the pressure sinks too low, and the nominal transmission capacity cannot be reached. A compressor station consists of different parts, such as filters and valves, but the compressor is the main component. Different compressor types can be used, depending on the technical requirements, for example, pressure increase and volume flow rate. They can either be powered by a gas turbine, which consumes gas directly out of the pipeline, or by an electric motor.

Since large amounts of gas are well transported with high pressure, but the consumption usually occurs at a few mbar above ambient pressure, several steps of expansions have

to occur on the way of the gas. Those expansions are most commonly done in pressure regulating stations which often separate gas grids with different MOPs. The main component is the pressure regulating valve, which controls the pressure depending on upstream and downstream pressure as well as the mass flow rate. Since natural gas has a positive Joule-Thomson coefficient, the gas is cooled down by 0.4-0.7 K/bar when expanded. If the temperature falls below 5-8 °C, there is a risk of hydrate formation where hydrocarbons form a solid with water which can cause damage to the gas grid's components. To avoid hydrate formation, the gas is preheated using natural gas out of the pipeline.

2.3.5 Pressure Loss Calculation

In this section, the pressure loss equations will be derived. The derivation is based on Cerbe et al. (2017).

The general equation to calculate the infinitesimal pressure loss $\mathrm{d}p$ of a fluid with density ρ and velocity w through a pipe with infinitesimal length $\mathrm{d}l$ and diameter D is

$$\mathrm{d}p = -\lambda \frac{1}{D} \frac{\rho}{2} w^2 \mathrm{d}l. \tag{2.9}$$

Using the continuity equation for a pipe

$$\dot{m} = \frac{\pi}{4} D^2 w \rho, \tag{2.10}$$

Equation (2.9) becomes

$$\mathrm{d}p = -\frac{8}{\pi^2} \lambda \frac{1}{D^5} \frac{1}{\rho} \dot{m}^2 \mathrm{d}l. \tag{2.11}$$

λ represents the friction factor calculated using different correlations, which can depend on the Reynolds number Re, defined with the dynamic viscosity η as follows.

$$Re = \frac{wD\rho}{\eta} \tag{2.12}$$

The Reynolds number defines if a flow is laminar or turbulent. For laminar flow ($Re < 2320$), the friction factor does not depend on the pipe wall's roughness. It is calculated with the following formula.

$$\lambda = \frac{64}{Re} \tag{2.13}$$

For turbulent flow ($Re > 2320$), the surface roughness k of the pipe wall must be taken into account. The formula from Zanke is valid for the whole turbulent regime.

$$\lambda = \left[-2 \log \left(2.7 \frac{(\log Re)^{1.2}}{Re} + \frac{k}{3.71 D} \right) \right]^{-2} \tag{2.14}$$

Equation (2.11) can be directly integrated for incompressible flow since the density, and

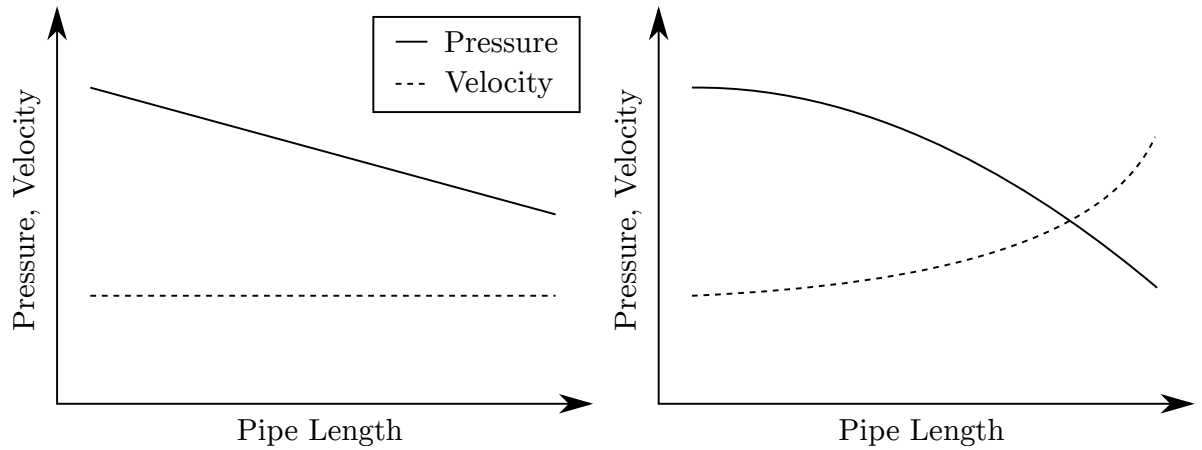

(a) Incompressible flow **(b)** Compressible flow

Figure 2.3: Comparison of velocity and pressure of incompressible and compressible flow, own representation based on Cerbe et al. (2017).

thus also the velocity, are constant. This leads to

$$p_1 - p_2 = \frac{8}{\pi^2}\lambda\frac{l}{D^5}\frac{1}{\rho}\dot{m}^2 \tag{2.15}$$

with the inlet and outlet pressures p_1 and p_2, respectively.

For compressible flow, the density varies significantly, influencing the fluid velocity and thus the pressure loss, as shown in Figure 2.3. So, Equation (2.11) cannot be integrated directly. Also, the density's dependence on the pressure is not easily described for real gases, so the following approach is chosen.

First, the real gas density is transformed into the ideal gas density ρ_{id} using the compressibility factor K which describes the deviation of the real gas from the ideal gas.

$$\rho = \frac{\rho_{\mathrm{id}}}{K} \tag{2.16}$$

Boyle's law can be applied since an isothermal flow is assumed and the density of the ideal gas is used.

$$\frac{p_1}{\rho_{\mathrm{id},1}} = \frac{p}{\rho_{\mathrm{id}}} = \text{const.} \tag{2.17}$$

Combining Equations (2.11), (2.16), and (2.17) leads to

$$\mathrm{d}p = -\frac{8}{\pi^2}\lambda\frac{1}{D^5}\frac{1}{\rho_{\mathrm{id},1}}\frac{p_1}{p}\dot{m}^2 K\mathrm{d}l \tag{2.18}$$

which is sorted to enable integration.

$$\frac{1}{p_1}\int_{p_1}^{p_2} p\mathrm{d}p = -\frac{8}{\pi^2}\lambda\frac{1}{D^5}\frac{1}{\rho_{\mathrm{id},1}}\dot{m}^2\int_0^l K\mathrm{d}l \tag{2.19}$$

Since K varies over the pipe length depending on the pressure, the integral mean value K_m is used. It is calculated using the integral mean pressure which equals to

$$p_\mathrm{m} = \frac{2}{3}\frac{p_1^3 - p_2^3}{p_1^2 - p_2^2} \tag{2.20}$$

due to the pressure's parabolic course. Solving the integrals and using K_m, equation (2.19) becomes

$$p_1^2 - p_2^2 = \frac{16}{\pi^2}\lambda\frac{l}{D^5}\frac{p_1}{\rho_{\mathrm{id},1}}\dot{m}^2 K_\mathrm{m}. \tag{2.21}$$

The ideal gas law can be used to eliminate the density and use the specific gas constant R and constant temperature T instead.

$$p_1^2 - p_2^2 = \frac{16}{\pi^2}\lambda\frac{l}{D^5}RT\dot{m}^2 K_\mathrm{m} \tag{2.22}$$

Applying the third binomial formula to the left side and using the arithmetic mean pressure $p_{\mathrm{m,arithm}}$ leads to

$$p_1 - p_2 = \frac{8}{\pi^2}\lambda\frac{l}{D^5}\frac{p_1}{p_{\mathrm{m,arithm}}}\frac{1}{\rho_{\mathrm{id},1}}\dot{m}^2 K_\mathrm{m}. \tag{2.23}$$

Depending on the given values, any of the Equations (2.21), (2.22), or (2.23) can be used to calculate the pressure loss.

2.3.6 Quasi-Stationary Gas Grid Computation

The flow situation within a gas grid is described by mass flow rates in the pipes and pressures at the nodes. To determine those values numerically, the gas grid has to be transformed into a mathematical structure. Such a structure can be represented as an undirected graph where the pipes are the branches, and the junctions are the nodes. Osiadacz (1987) gives an introduction to graph theory with the application to gas grid computation. Figure 2.4a illustrates the basic elements of a graph, which will be described below.

A graph consists of nodes and branches. Let the graph have n_G nodes that can be separated into n_{G1} load nodes, that is, nodes with a given load, and n_{G2} reference nodes that supply or consume an unknown mass flow to keep the pressure at a given value.

$$n_\mathrm{G} = n_{\mathrm{G1}} + n_{\mathrm{G2}} \tag{2.24}$$

Also, loops are an essential structure of a gas grid since Kirchhoff's second law states that the sum of pressure losses over one loop must be zero. If all reference nodes have the same pressure, this condition also has to be valid for a connection between two reference nodes. That is why, in the following, those connections will be counted as loops.

If the graph has m branches, the number of loops c in the graph can be calculated as follows. It also includes the minimum number of connections between reference nodes $n_{\mathrm{G2}} - 1$.

$$c = m - n_{\mathrm{G}} + n_{\mathrm{G2}} = m - n_{\mathrm{G1}} \tag{2.25}$$

A graph can be split into subgraphs, that is, a part of the graph, where the most important types are the dendrite and the co-tree. A dendrite is a subgraph of the graph with no loops and includes all nodes of the graph. However, if several reference nodes exist in the same graph, all dendrites together include all nodes, and each dendrite contains precisely one reference node. The branches of a dendrite are called tree branches. All other branches are called chords, and together they form the co-tree, so dendrite and co-tree combined yield the entire graph again. There are as many chords as loops, so c chords and $m-c$ tree branches which build n_{G2} dendrites. The choice of loops and chords is not unique; different arrangements are possible depending on the graph's complexity, see Figure 2.4b.

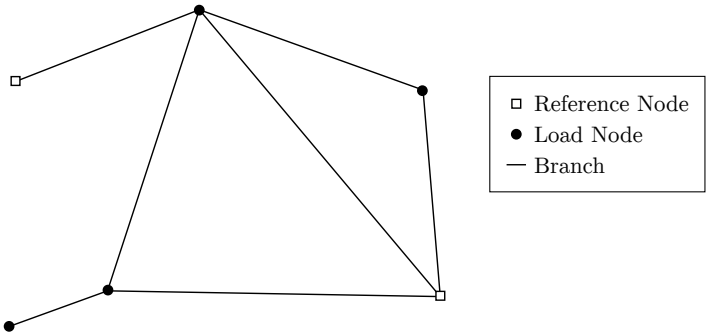

(a) Basic elements of a graph.

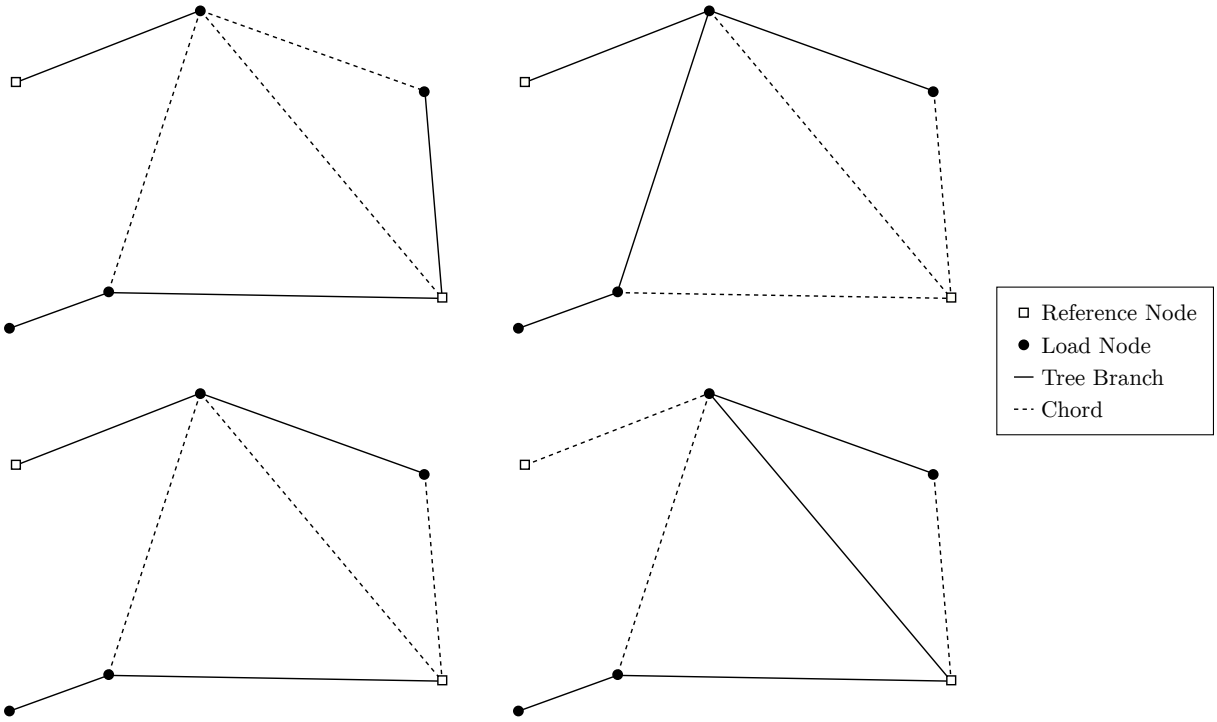

(b) Exemplary dendrites and corresponding chords.

Figure 2.4: Exemplary graph illustrating the basic elements in (a) as well as exemplary dendrites and corresponding chords in (b).

To describe a graph mathematically, different matrices are used. The first is the branch-nodal incidence matrix $\mathbf{A}$, an $n_\mathrm{G} \times m$ matrix with the entries a_{ij}. For this, a direction for each branch is chosen arbitrarily.

$$a_{ij} = \begin{cases} +1 & \text{if branch } j \text{ enters node } i \\ -1 & \text{if branch } j \text{ leaves node } i \\ 0 & \text{if branch } j \text{ is not connected to node } i \end{cases} \tag{2.26}$$

If the nodes are split into load and reference nodes and sorted accordingly, $\mathbf{A}$ can be split into two matrices $\mathbf{A}_1$ ($n_\mathrm{G1} \times m$) and $\mathbf{A}_2$ ($n_\mathrm{G2} \times m$).

$$\mathbf{A} = \begin{bmatrix} \mathbf{A}_1 \\ \mathbf{A}_2 \end{bmatrix} \tag{2.27}$$

The second matrix to describe a graph is the branch-loop incidence matrix $\mathbf{B}$ ($c \times m$) with the entries b_{ij}.

$$b_{ij} = \begin{cases} +1 & \text{if branch } j \text{ has the same direction as loop } i \\ -1 & \text{if branch } j \text{ has the opposite direction as loop } i \\ 0 & \text{if branch } j \text{ is not in loop } i \end{cases} \tag{2.28}$$

Subsequently, all matrices can be split into parts that contain only the tree branches t or chords c, respectively.

$$\mathbf{A} = \begin{bmatrix} \mathbf{A}_\mathrm{t} & \mathbf{A}_\mathrm{c} \end{bmatrix} \tag{2.29}$$

$$\mathbf{A}_1 = \begin{bmatrix} \mathbf{A}_{1\mathrm{t}} & \mathbf{A}_{1\mathrm{c}} \end{bmatrix} \tag{2.30}$$

$$\mathbf{A}_2 = \begin{bmatrix} \mathbf{A}_{2\mathrm{t}} & \mathbf{A}_{2\mathrm{c}} \end{bmatrix} \tag{2.31}$$

$$\mathbf{B} = \begin{bmatrix} \mathbf{B}_\mathrm{t} & \mathbf{B}_\mathrm{c} \end{bmatrix} \tag{2.32}$$

To determine $\mathbf{B}_\mathrm{t}$, the following equation can be used since the loops follow directly from the choice of tree branches and chords.

$$\mathbf{B}_\mathrm{t}^\mathrm{T} = -\mathbf{A}_\mathrm{t}^\mathrm{T} \mathbf{A}_\mathrm{c} \tag{2.33}$$

The next step is to use those matrices to solve the network, that is, to determine the pressures at all nodes and the mass flow rates through all branches under the physical restrictions. According to Osiadacz (1987), the most numerically efficient method is the Newton loop-node method described in the following. Osiadacz (1987) uses volume flow rates to describe the gas flow, but mass flow rates can be used analogously.

First, Kirchhoff's first law has to be considered: The sum of all volume flow rates Q into and out of a node have to equal zero, including the load L for all load nodes.

$$L = \mathbf{A}_1 Q = \mathbf{A}_{1\mathrm{t}} Q_\mathrm{t} + \mathbf{A}_{1\mathrm{c}} Q_\mathrm{c} \tag{2.34}$$

If the volume flow rates in all chords are known, the resulting volume flow rates in

all tree branches can be calculated by combining Equations (2.33) and (2.34) so that Kirchhoff's first law is valid.

$$Q_\mathrm{t} = \mathbf{A}_\mathrm{1t}^{-1} L + \mathbf{B}_\mathrm{t}^\mathrm{T} Q_\mathrm{c} \tag{2.35}$$

Kirchhoff's second law indicates that the sum of pressure losses over a whole loop has to be zero. This also applies to connections between two reference nodes, which forces the known pressures at the reference nodes to be equal. ΔP is the quadratic pressure loss over each branch, $P_1 - P_2 = p_1^2 - p_2^2$.

$$\mathbf{B}\Delta P = 0 \tag{2.36}$$

$$\Delta P = \mathbf{A}^\mathrm{T} P \tag{2.37}$$

The pressure loss could be calculated using Equation (2.21), but it is numerically expensive due to the nonlinearity regarding the pressure and the necessary calculation of the different gas properties. An efficient alternative is the Panhandle 'A' equation for pressure gauges above 7 bar (Osiadacz, 1987)

$$\Phi(Q_i) = \Delta P_i = 18.43 \frac{l_i}{0.9^2 D_i^{4.854}} Q_i^{1.854} \tag{2.38}$$

It is a numerical value equation with ΔP in bar^2, length l in m, diameter D in mm, and volume flow rate Q in m^3/h.

To solve the system of equations, the first-order approximation of the Newton method is applied to $\Phi(Q)$ to calculate the next step $z+1$ using the values at step z:

$$\Phi(Q)^{z+1} = \Phi(Q + \Delta Q)^z \approx \Phi(Q)^z + \mathbf{R}^z \Delta Q^z \tag{2.39}$$

$$\text{with} \qquad \mathbf{R} = \frac{\partial \Phi(Q)}{\partial Q} = \begin{bmatrix} \frac{\partial \Phi_1}{\partial Q_1} & & & \mathbf{0} \\ & \frac{\partial \Phi_2}{\partial Q_2} & & \\ & & \ddots & \\ \mathbf{0} & & & \frac{\partial \Phi_m}{\partial Q_m} \end{bmatrix} = \begin{bmatrix} \mathbf{R}_\mathrm{t} & \mathbf{0} \\ \mathbf{0} & \mathbf{R}_\mathrm{c} \end{bmatrix} \tag{2.40}$$

$$\text{with} \qquad r_{ij} = \begin{cases} 1.854 \cdot 18.43 \dfrac{l_i}{0.9^2 D_i^{4.854}} |Q_i|^{0.854} & \text{if } i = j \\ 0 & \text{if } i \neq j \end{cases} \tag{2.41}$$

Combining all mentioned equations leads to:

$$P_1^{z+1} = -\left(\mathbf{A}_1 \left(\mathbf{R}^z\right)^{-1} \mathbf{A}_1^\mathrm{T}\right)^{-1} \mathbf{A}_1 \left(\mathbf{R}^z\right)^{-1} \left(\Delta P^z + \mathbf{A}_2^\mathrm{T} P_2\right) \tag{2.42}$$

$$\Delta Q_\mathrm{c}^z = \left(\mathbf{R}_\mathrm{c}^z\right)^{-1} \left(-A_\mathrm{c}^\mathrm{T} P^{z+1} - \Delta P_\mathrm{c}^z\right) \tag{2.43}$$

$$Q_\mathrm{c}^{z+1} = Q_\mathrm{c}^z + \Delta Q_\mathrm{c}^z. \tag{2.44}$$

Using Equations (2.35) and (2.42)-(2.44), all values are calculated iteratively until ΔQ_c^z falls under a specified tolerance.

2.4 Aggregation of Fluid Networks

The aggregation of fluid networks serves the purpose of increasing numerical efficiency while still obtaining accurate results. Different methods have arisen in the last decades, mostly in the field of district heating networks.

2.4.1 Aggregation Methods for Gas Networks

Not many resources exist which cover the aggregation of high-pressure gas grids. Some methods are purely mathematical and do not lead to a resulting physical network but just a matrix representation, for example, Benner et al. (2018), so they are not suitable for dynamic simulations with physical models. Other methods only work for linearized gas grid models that might be suitable for low-pressure distribution networks, such as Parkinson et al. (1992), but not high-pressure gas grids. The method of Mohring et al. (2004) focuses on detecting bottlenecks in the gas infrastructure but does not enable the simulation of the whole network.

Since there is no method known which can directly be applied to gas grids and allows the dynamic simulation of a high-pressure gas grid, methods in other fields are investigated. The closest grid type is a district heating network since the physics are similar to gas grids: Here also, a fluid flows through pipes, there are loops, and pressure losses are important. The essential difference is the much higher compressibility of gas compared to water. Also, the heat losses of the pipes are negligible.

2.4.2 Aggregation Methods for District Heating Networks

For district heating networks, the Danish and the German method are the most popular choices, which are compared by Larsen, Bøhm, et al. (2004). Both methods aggregate the network physically-based, that is, a subgrid is aggregated in a manner that the resulting simplified network still has physical properties, for example, pipes with length and diameter. They can reach aggregation grades of up to 99 %, which means that the number of elements in the grid is reduced by 99 %. The biggest flaw of the Danish method (Larsen, Pálsson, et al., 2002) is that it cannot aggregate loops while the German method (Loewen, 2001) is able to do so. Also, the German method considers the pressure drop in each pipe but does not regard the heat losses in the supply and return pipe separately, contrary to the Danish method.

In conclusion, the German method has the characteristics necessary to be applied to gas grids, so it will be presented more in detail.

The German method is based on the following conditions:

- The grid volume and necessary pumping power shall stay constant. The latter requires that the pressure losses remain the same.
- Pressures and temperatures at the nodes as well as the time delays between the nodes, that is, the time the fluid takes to flow from one node to the other, shall not change.
- The sum of heat losses and consumer mass flow rates, as well as heat flow rates, stay the same.

- Specified pipes and nodes shall be excludable from the aggregation.
- Aggregation shall be executable until a specified degree of aggregation is reached.
- The visual representation of the grid shall not change drastically, that is, nodes, which have not been aggregated, shall remain where they originally were.

All conditions based on mass flow rates or pressures can only be ensured using grid computation data from one point in time. The further away the flow situation in the grid is from the chosen aggregation point in time, the larger the expected errors will be.

Ensuring all mentioned conditions, serial, parallel, or terminal pipes as well as loops, can be aggregated, which is described shortly in the following. A detailed description, including the equations, can be found in Loewen (2001).

Serial Pipes

The network topology before and after the aggregation of two serial pipes, P1 and P2, with the same mass flow direction, into one pipe P1′ is shown in Figure 2.5. Note that in this and all following figures, only the supply pipes of the district heating grid are shown. The aggregation is performed for both supply and return pipes in the same way. Nodes and pipes that are modified during the aggregation step are marked with a ′ after aggregation.

The aggregation is achieved by splitting node N2 and adding it to N1 and N3 so that the time delay in pipe P1′ is the same as P1 and P2 together. Also, the resulting pipe is as long as the two serial pipes together, and the diameter, pressure, and heat loss coefficients are chosen so that the grid volume, as well as the pressure and heat losses, stay constant.

Parallel Pipes

Parallel pipes are treated as a particular form of a loop; see Figure 2.6. The ratio of length to diameter is weighted with the mass flow rates and, with the condition of constant grid volume, the length and the diameter of pipe P1′ can be calculated. The pressure and heat loss coefficients are calculated accordingly to reach the same values as for pipes P1 and P2 together.

Terminal Pipes

Terminal pipes can be aggregated into the surrounding grid by combining the terminal pipe P1 with another pipe P2 that meet in one common node N1 and have the same mass flow direction, both either entering or leaving N1, as shown in Figure 2.7. Another condition is that the time delay of pipe P2 has to be smaller than the one of P1. P1′ has the same length as P1, and the diameter is calculated so that the time delays of P1′ and P1 are equal. The length and diameter of P2′ are determined so that P1′ and P2′

Figure 2.5: Topology representation before and after the aggregation of two serial pipes.

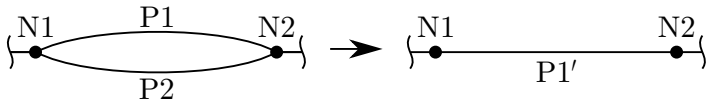

Figure 2.6: Topology representation before and after the aggregation of two parallel pipes.

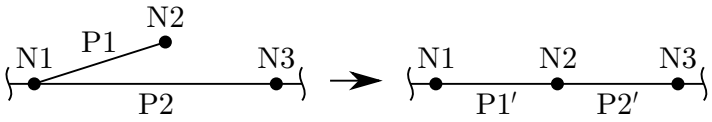

Figure 2.7: Topology representation before and after the aggregation of a terminal pipe.

together have the same length and time delay as P2. Pressure and heat loss coefficients are calculated as in the previous aggregation steps. The resulting serial pipes can then be aggregated in a subsequent step as described above.

If the aggregation is not possible because the time delay of P2 is shorter than the one of P1, the algorithm can be extended to be able to aggregate node N2 in the next pipe to the right of P2 or even further. If the time delays of P1 and P2 are very similar, nodes N2 and N3 can be combined directly to avoid creating serial pipes.

Loops

Loops can be aggregated as long as there is one distinct start and one distinct end point, which split the loop into two branches in which the fluid flows in the same direction. All other nodes are defined as inner nodes.

A loop can be treated in two ways: First, it can be transformed into serial pipes; see Figure 2.8. Second, it can be split into its two branches, see Figure 2.9, but the decision has to be made manually. The first option is more suitable if the loop is in the center of the grid, while the second is more useful if the loop is located in a peripheral area of the grid.

If the loop is supposed to be transformed into serial pipes, the inner nodes are sorted by the time delay between the start node and the corresponding inner node. Each pipe's length is determined by weighing the pipe's length by the time delay of the two pipes that are combined. In the example shown in Figure 2.8, node N2 is moved into pipe P2, splitting it into the pipes P1′ and P2′. Where exactly N2 splits P2, is calculated based on the time delays. The last pipe's length stays the same, and all diameters are then calculated to achieve the desired time delays in each pipe. Heat and pressure loss

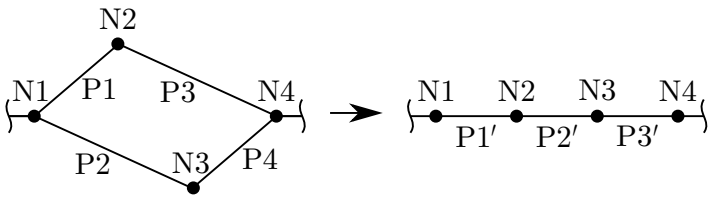

Figure 2.8: Topology representation before and after the aggregation of a loop with four branches into serial pipes.

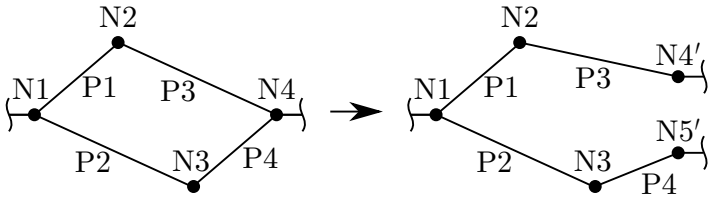

Figure 2.9: Topology representation before and after the split of a loop with four branches.

coefficients are calculated as in the other steps.

If the loop shall be split, the end node N4 and the remaining grid after N4 have to be divided. To reduce the effort and the errors, the remaining grid should only contain one more pipe at most. N4 and the consumers and heat losses in the remaining grid are split according to the mass flow rates in pipes P3 and P4. The lengths and diameters are adjusted to ensure the same time delays and grid volume.

2.5 Power Grids

Heuck et al. (2013) give an overview of all components in an electric supply system. In the following, the essential components for this thesis are shortly presented.

The electric grid is split into several levels, like the gas grid. There are low-voltage (230 V, 400 V), medium-voltage (10 kV, 20 kV), high-voltage (110 kV), and extra-high-voltage (220 kV, 380 kV) levels with typical nominal voltages given in brackets. Transmission lines are part of the high-voltage and extra-high-voltage grid and transport large electric powers over longer distances. Historically, the transmission lines mostly connected large power plants and centers of power consumption. This structure changes slowly with more decentral renewable power generation being integrated into the energy system.

The different voltage levels are connected by power transformers which transform the voltage up or down. The technical principle is based on a certain number of windings for each voltage level coupled by an electromagnetic field.

Large power plants are connected to the power grid using synchronous machines coupled to the turbines of the power plants. A direct current flows through a conductor on the rotating part (rotor) of the generator, which induces a current in the static part (stator). Like that, the mechanical power is transformed into electric power.

3 Modeling, Simulation Setups, and Data

In Section 2.2, different studies have been shown, but none of them covers exactly the demand sectors with the same technologies, which are considered in this thesis, and almost none of the models used in mentioned studies are open-source or use dynamic simulation. Furthermore, none of the studies models the gas grid in detail in combination with the rest of the energy system. That is why an appropriate comparison of different heating technologies and their influence on the rest of the energy system is not possible.

For this reason, own models are created in this thesis, fed with different data sets and combined with aggregation algorithms. How those parts are connected is illustrated in Figure 3.1, and they will be described in Section 3.1.

In Section 3.2, the scenario information and all data for the models are presented.

3.1 Modeling

In this section, all created and used models are described. All of them cover entire Germany, except for the gas grid models, which represent only the gas grid of Northern Germany consisting of the federal states of Schleswig-Holstein, Hamburg, Lower Saxony, Bremen, and Mecklenburg-Western Pomerania to limit the numerical complexity of the models. The considered time span is one year for all models.

The used models shown in Figure 3.1 are split into the following categories:

- Quasi-stationary integrated energy system (IES) model: It covers the entire German energy system without the transportation sector, uses quasi-stationary equations,

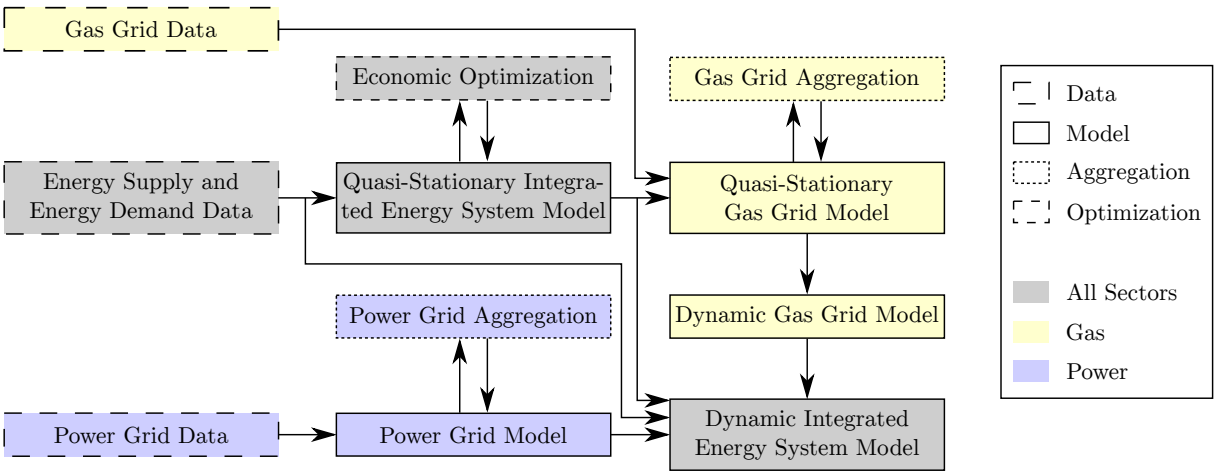

Figure 3.1: Overview of the different models, data sets, and aggregation steps.

and is used to optimize the energy system regarding the cost to find probable configurations of the future German energy system. It is described in Section 3.1.1.

- Quasi-stationary gas grid model: It covers the gas grid of Northern Germany solely as the main part of the considered system and uses quasi-stationary equations as well. The whole implementation is described in Section 3.1.2. To reduce the complexity of the gas grid model and to be able to perform dynamic simulations coupled with the rest of the energy system, an aggregation algorithm is used, which is presented in Section 3.1.3.
- Dynamic gas grid model: Based on the quasi-stationary gas grid model with different aggregation grades, a dynamic gas grid model for Northern Germany is built.
- Power grid model: The German power grid model also has to be aggregated to be combined with the rest of the energy system, and the method is shortly presented in Section 3.1.4.
- Dynamic integrated energy system model: This model is used to perform the final dynamic simulations, and it combines the power and gas grid models with region models representing entire Germany. However, the gas grid has a clear focus on Northern Germany, but it is connected to the rest of Germany. All dynamic component models are described in Section 3.1.5.

To compare and evaluate the different models and scenarios, different key figures are used in Chapter 4, which are described in Section 3.1.6.

3.1.1 Quasi-Stationary Integrated Energy System Model for Optimization

The model described in this section is used to determine probable configurations of a future German integrated energy system by optimizing the system regarding the cost under given assumptions. The three sectors power, heat, and gas are considered, whereas the transportation sector is neglected due to the uncertain development and complex setup. The system is modeled in a quasi-stationary way, so dynamic effects are neglected.

System Overview

In Figure 3.2, a schematic of the system with all considered technologies is shown. The energy storage and conversion technologies in the middle connect the energy input on the left with the final energy demands on the right side.

In the gas sector, it has to be decided first if the main gas in the gas grid is either methane-based or pure hydrogen. Depending on this, either biomethane and natural gas or hydrogen from biomass and hydrogen from natural gas are considered as entering the system from outside. For the latter, hydrogen is produced from natural gas in countries from which Germany imports natural gas at the moment and from gasifying biomass in Germany.

The biogas potential is split into two fractions with different costs: biogas from waste and biogas from energy crops and grassland. To obtain the possible potential of biomethane or hydrogen from biomass, the biogas potential is reduced using efficiencies depending

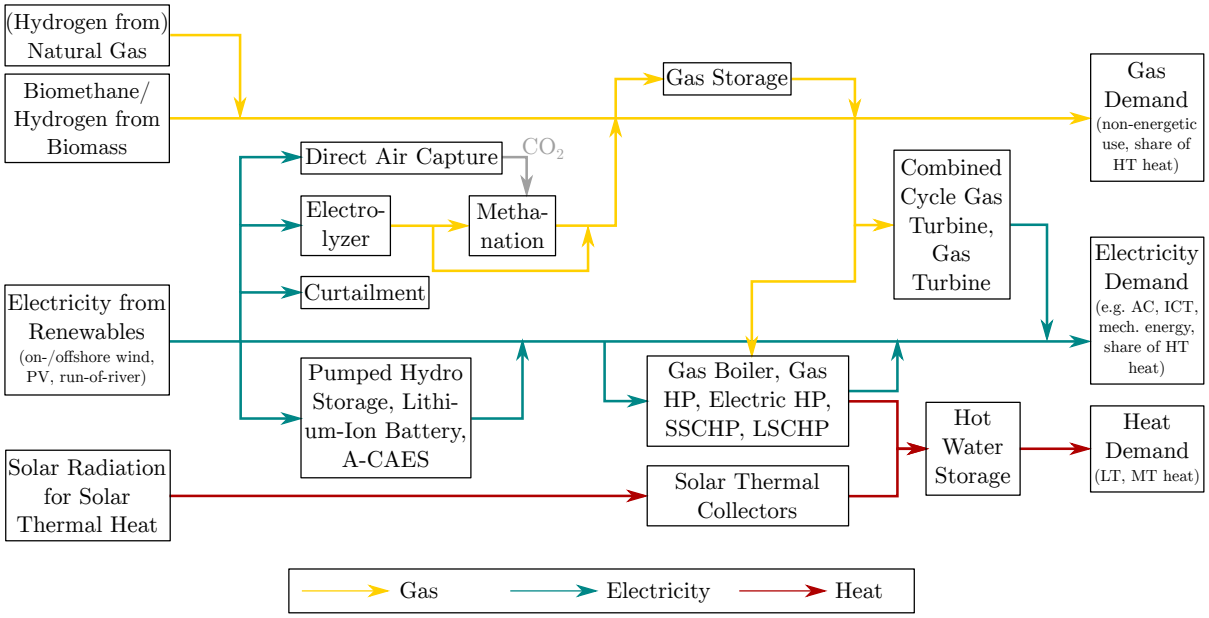

Figure 3.2: General schematic of the quasi-stationary IES model used for optimization. PV: photovoltaics, A-CAES: adiabatic compressed air energy storage, HP: heat pump, SSCHP: small-scale combined heat and power, LSCHP: large-scale combined heat and power, AC: air conditioning, ICT: information and communication technology, LT: low temperature, MT: medium temperature, HT: high temperature

on the process: Either biomethane is produced using anaerobic digestion and biogas cleaning or hydrogen is generated by biomass gasification and conversion to hydrogen.

Also, hydrogen can be produced with electricity using water electrolysis (Power-to-Gas). This hydrogen can either be transported in the gas grid directly or transformed with CO_2 to synthetic natural gas (SNG) using a methanation process. The SNG can be subsequently mixed with natural gas or biomethane without limitations. That is why the entire hydrogen is transformed into SNG directly after the electrolysis. The required CO_2 can be separated from the ambient air using Direct Air Capture (DAC) plants which need power and heat. In the model, the DAC plants always operate simultaneously as the electrolyzers and methanation units. This makes it possible to use the excess heat of those two processes in the DAC plants so that it does not have to be provided externally.

The mixture of natural gas, biomethane, and SNG or hydrogen can then be used to satisfy the final gas demand, to produce power again in combined cycle gas turbine (CCGT) plants or gas turbines (GT), or to generate heat with gas-fired heat producers (gas boilers, gas heat pumps, small or large-scale CHP plants, both heat led). Excess gas can be stored in large-scale gas storage plants and withdrawn again in case of an undersupply of gas.

Alternatively to the heat generation using gas, electric heat pumps (EHP) and flow-type water heaters (for hot water and process heat production) can be used. Furthermore, it is possible to combine those technologies with electric heating rods, gas boilers, or gas heat pumps. Combinations of an EHP with a gas-fired heat producer are called hybrid heating systems. Above a certain temperature (balance point temperature), the EHP produces heat exclusively. Below the balance point temperature, which is part of the optimization, the additional heater supports the electric heat pump. If additional gas-fired heaters are

used, the electric load of the heat generation can be decreased, and in all cases, the EHP can be sized smaller to become more economical. Additionally, in all heating systems, hot water storage tanks are included to match supply and demand, as well as solar thermal collectors, to generate renewable heat.

In the power sector, also pure electric energy storage technologies are considered: pumped hydro storage plants, lithium-ion batteries, and adiabatic compressed air energy storage (A-CAES) plants. Electricity from renewables, which cannot be taken up by the system, is curtailed.

Detailed Model Information

The model is implemented in Matlab (MathWorks Inc., 2021a) and uses a given constant time step of typically one hour. Each technology is represented using charging and discharging efficiencies, standby losses, minimum and maximum powers and energies, maximum gradients, start-up times, and CO_2 emissions. Start-up times are only considered when they are higher than the time step.

All system components are aggregated, so for each technology, there is one large unit in the system, which represents all units in Germany. Accordingly, each power plant type's minimum powers are assumed to be the minimum powers of one power plant. For all other technologies, minimum powers are neglected under the assumption that they consist of a large number of very small units.

Efficiencies are assumed constant for all components since all components are aggregated, and the part load of one, for example, power plant does not significantly affect the overall efficiency. Since the efficiency curve of electrolyzers does not have its maximum at nominal load, an efficiency curve from Kopp et al. (2017) is adapted to reflect the behavior of several plants lumped together. At lower powers than the power with the maximum efficiency, the overall plant is operated at best efficiency because all plants, which are not needed, are turned off. Below 2 % of the nominal load, the efficiency curve declines linearly since all remaining plants are shut off subsequently. The original and modified efficiency curves are depicted in Figure 3.3.

Due to the aggregation, the whole system is concentrated in one point, and thus network congestions cannot be investigated. Transmission losses are neglected except for a constant power grid loss. However, necessary power grid extension due to renewables is accounted for using power-specific values as done by Henning et al. (2012). The model considers low and medium-voltage grid extension due to photovoltaics and onshore wind plants, respectively, as well as undersea cables and high-voltage direct current transmission lines for offshore wind plants. Grid extension necessary for electric heat producers is also considered similarly as for photovoltaics but only if the installed nominal electric power of the heat pumps exceeds that of photovoltaics.

To control the system, all energy storage and conversion technologies are put into a fixed order according to their efficiencies: lithium-ion batteries, pumped hydro storage plants, A-CAES plants, Power-to-Gas plants, CCGT power plants, and gas turbines. The remaining residual load is given consecutively to all technologies as a set point. The initial residual load equals the final power demand and power demand for heating minus the power production from renewables and CHP plants. The remaining negative residual load after the gas turbines is curtailed. Demand-side management is not considered in the model.

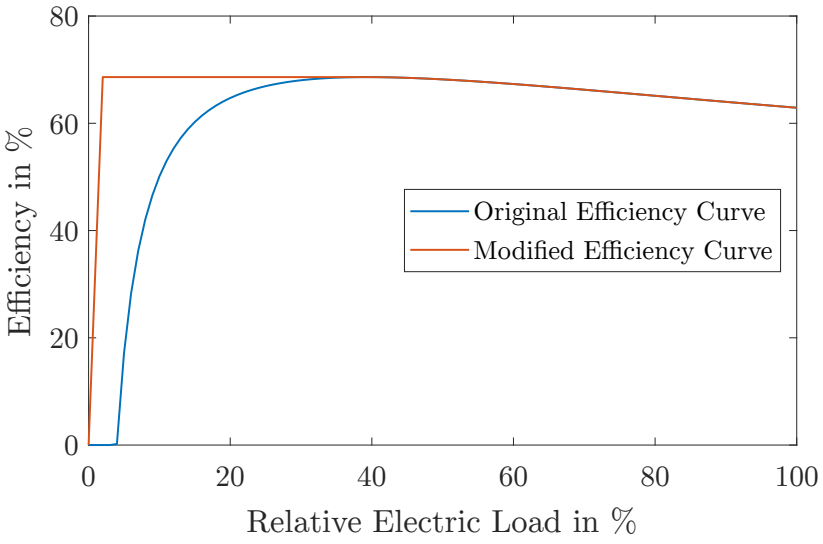

Figure 3.3: Original (Kopp et al., 2017) and modified electrolyzer efficiency curves.

Heating System

The German heating system is modeled in the open-source, equation-based, multi-domain programming language Modelica (Modelica Association, 2021) using the open-source TransiEnt Library (TUHH, 2021). The heating system is easily represented in this way, including dynamic effects. For each heating system configuration, for example, gas boilers, gas heat pumps, or electric heat pumps, one separate model is built. A schematic of the general model is depicted in Figure 3.4. Here, all components are aggregated, so the conventional heat producer represents, for example, all German gas boilers lumped together, and the hot water storage is one large storage working like all German hot water storage tanks together. The inputs and outputs of the hot water storage tank are located at different heights, as shown in the figure, to improve storage usage.

All used models are described in Section 3.1.5. The resulting energy flows across the system boundary, that is, required electricity or gas or generated electricity in the case of CHP plants, can then be multiplied by the share of each configuration and passed to the rest of the system. The energy flows of the hybrid heating systems are composed by combining curves from the simple configurations with just one heat producer according to the chosen balance point temperature.

The pump for the solar thermal collector is controlled so that the outlet temperature reaches the set value, whereas the pump in the circuit of the conventional heat producers, and the electric heating rod if one is used, ensures a minimum set temperature at the top of the storage tank. The control of the pumps on the consumer side, the back-mixing valve, and the electric boiler, if the conventional heat producer is an EHP, is designed so that both circuits' supply and return temperatures are held at their set values.

System Design

To design the system, first, the boundary conditions are set according to Section 3.2. Second, the optimization algorithm picks sizes for all technologies, for example, electric energy storage plants. Based on that, the nominal power of renewable power generators,

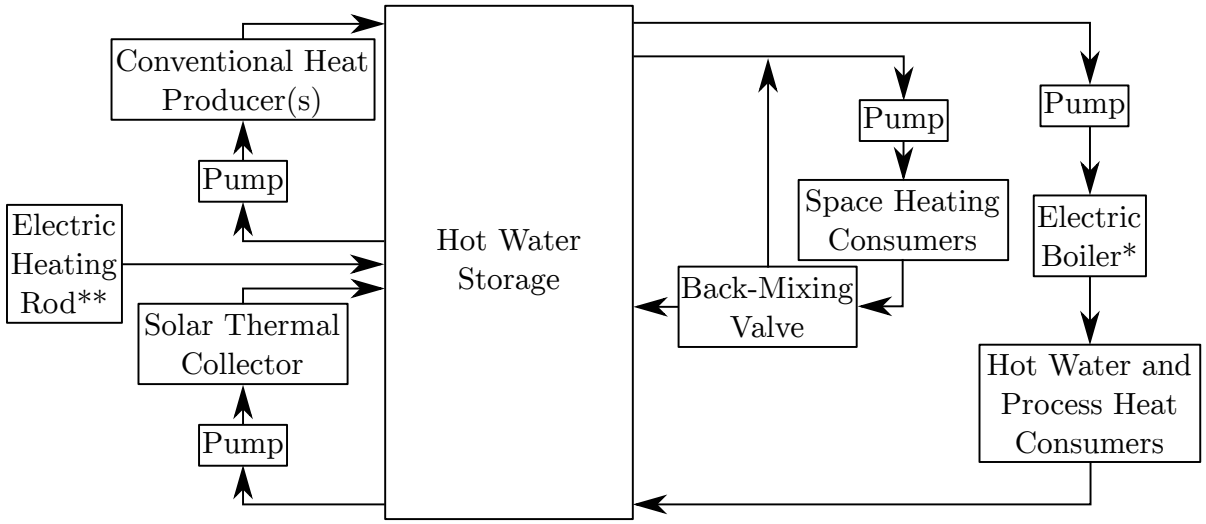

* if an electric heat pump is used as conventional heat producer
** optional

Figure 3.4: Schematic of the general heating system model.

the amount of (hydrogen from) natural gas, and the nominal power of the gas turbines are chosen to satisfy the following requirements:

- The power demand is satisfied at every time instance,
- the overall gas storage volume has the same state of charge (SOC) at the end of the year as at the beginning, and
- the share of renewable energies of the primary energy demand equals the desired value.

This is achieved by sizing the gas turbines so that the electricity demand can be met even in the worst case of highest demand, including power for heating at norm ambient temperature and lowest renewable generation in the year. In accordance with the targeted primary energy consumption, the allowed amount of (hydrogen from) natural gas is calculated using the primary energy consumption without natural gas, including ambient heat used by the heat pumps and the share of renewables. The nominal power of renewable power generators is iterated using the deviation of the state of charge of the overall gas storage volume at the beginning and the end of the year and applying Newton's method. The renewables are split into the different technologies assuming extension paths described in Section 3.2.2.

During the iteration, all formerly named variables are also iterated and checked against given tolerances. If all deviations are below their respective tolerances, the iteration is stopped, and the system is designed for the given parameters. During the optimization, the parameters are adapted by the optimization algorithm, and the design iteration is executed several thousand times until an optimal configuration is found.

System Evaluation

The CO_2 emissions are also determined by the model, including positive as well as negative emissions. The latter is possible when biomethane or SNG are consumed in a non-energetic way where it is assumed that the gases are transformed into a product, and the corresponding CO_2 emissions never enter the atmosphere. Only emissions from the system directly are considered, so upstream emissions from, for example, the extraction of natural gas or the production of components are neglected.

To evaluate the system, the system cost is calculated using the annuity method with full-cost pricing according to VDI 2067 Part 1 (Sep. 2012), that is, all plants are priced as if they are newly built. For this, investment cost, operation and maintenance (O&M) cost, lifetime as well as specific costs for natural gas, biomass, and CO_2 are assumed for the future. Additionally, an interest rate and an observation period are required for the calculation. All required data is given in Section 3.2.7.

The future developments of the prices or other parameters, for example, efficiencies, are either taken from Palzer (2016) or are determined in the same way as Palzer (2016) presumably did in his work. The procedure is not described there, but the following formula gives similar results.

Two data points y_1 and y_2 are needed for the two points in time t_1 and t_2. The exponent v gives the development of the variable y over time t. Examples of possible curves are given in Figure 3.5.

$$y(t) = (y_1 - y_2)\left(\frac{t_2 - t}{t_2 - t_1}\right)^v + y_2 \tag{3.1}$$

It is visible that a higher v leads to a faster decrease of the variable. v is either given in the data directly or determined by curve fitting. That is why minor deviations can occur between the fitted curve and the actual data. For data where only a start and an end value, for example, 2013 and 2050, are given but no data in between, a linear development ($v = 1$) is assumed.

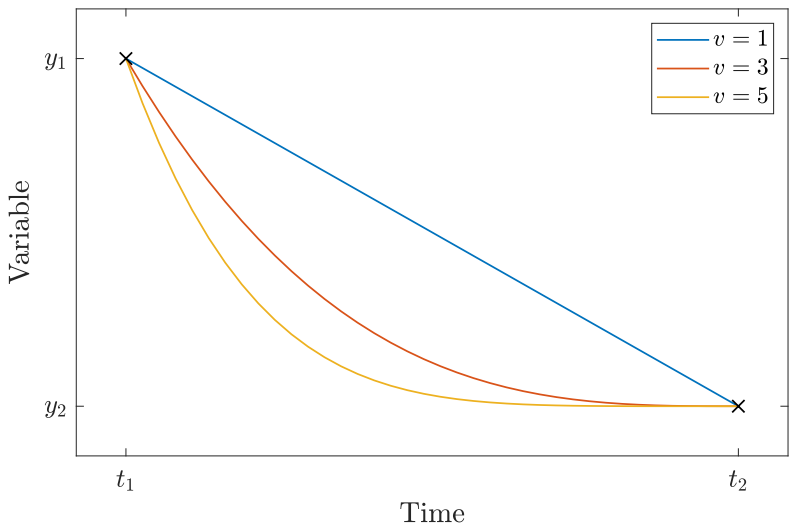

Figure 3.5: Exemplary curves for a variable y over time t with different exponents v.

3.1.2 Quasi-Stationary Gas Grid Computation

The algorithm for the gas grid computation is implemented in Matlab (MathWorks Inc., 2021a). The first step is the pre-processing in which the gas grid structure and demand, production, import, and storage data are transformed into a coherent model. The next step is the actual gas grid computation, where a solution for pressures at the nodes and mass flow rates in the pipes is searched, which complies with the physical laws described in Section 2.3.6.

Prior investigations with the below-described gas grid model, including compressor stations, have shown that the compressor stations are not needed for an ideal control of the gas grid under the assumptions made but are necessary for a real and economic operation of several gas grid operators. Especially for the dynamic simulation, the gas storage plants control the pressure in the gas grid, and that is why the compressor stations are not considered in the following.

The provided gas grid data was not without faults, as described in Section 3.2.4, and there are some assumptions regarding, for example, the gas mass flows between the considered Northern German region and the rest of Germany, see below. That is why there has been continuous feedback to the pre-processing step after conducting the gas grid computation. When the gas grid computation has finished unsuccessfully or with very low or very high node pressures, the results were investigated closely, which enabled finding faults in the data. Adding minor adjustments to the pre-processing, as described below, fixed those faults.

Pre-Processing

First, different options can be set:

- time step between single gas grid computations (default 1 h),
- share of renewables (60 %, 80 %, 100 %),
- if natural gas, biomethane, and SNG or hydrogen are used,
- constant gas temperature and properties of natural gas and hydrogen,
- surface roughness of pipes,
- which node is the reference node for the highest gas grid level (default Dornum in the north west of Lower Saxony where Norwegian natural gas is imported),
- known pressure values (relative to MOP), that is, for known pressure nodes at pressure regulating stations (default 80 % of MOP) or import nodes (default 80 bar for Dornum (Kröcher et al., 2013)),
- pressure start value (relative to MOP) (default 70 % of MOP),
- maximum gas velocity in pipes for calculation of pipe capacities (default 10 m/s for natural gas and 20 m/s for hydrogen), and
- tolerance in GPS coordinates which is used to find nodes (default 0.003°).

The next step is to load the gas grid structure in the form of an export file from ArcGIS (Esri Inc., 2013), and the plausibility is checked by examining if there are any single isolated pipes. If so, they are deleted as well as other pipes which are not relevant for the gas grid computation: import pipes, for example, Nordstream, the OPAL pipeline (since there is no connection to the gas grid of Northern Germany), and very short pipes. The latter are defined as pipes whose length in GPS coordinates is below the set tolerance. Also, in some areas, the topology has to be corrected by either splitting a point because there is no connection or combining points where there is a link that is not in the data. Those points were found and added here manually by analyzing gas grid computation results.

Since the whole gas grid consists of numerous subnetworks which are operated separately and only coupled via pressure regulating stations, it is necessary to identify those subnetworks. This also simplifies the gas grid computation because not the whole gas grid has to be solved as a whole, but the algorithm can start at low MOP levels and subsequently proceed to higher grid levels. The problem is that there is no reliable data about those subnetworks and strictly splitting the gas grid depending on the MOP values leads to a fragmented gas grid since there are many similar but still different values, for example, 64 bar, 67.5 bar, 68 bar, and more values up to 100 bar. That is why the MOP levels 35 bar and 40 bar are combined to 40 bar, and all values above 60 bar are set to 70 bar. However, some pipes can be operated above 70 bar since their original MOP was higher. The subnetworks are then identified using connected pipes with the same MOP. It is important to note that the algorithm does not distinguish between transmission system operators and distribution system operators to enable the integration of biomethane, hydrogen, and SNG from PtG also in areas where there is no transmission gas grid. So, the whole 70 bar gas grid is operated as an entire grid.

In the next step, different manual modifications of pipes are made to avoid problems in the gas grid computation as already mentioned above. The original gas grid data is likely faulty in those cases:

- Single pipes with a different MOP or diameter than the surrounding gas grid are assimilated.
- In some subnetworks at specific time instances, there is an import from the not-considered part of Germany, which leads to too much gas input in those subnetworks. To avoid this, the MOP of the subnetwork is increased to be merged with the surrounding gas grid.
- In some NUTS 3 regions, there is no 70 bar gas grid, so the MOP of certain pipes is increased accordingly to get a connection from the region to that gas grid.
- At certain nodes, the pressures are very high or very low, sometimes even below zero, which hints at too small pipes, so selected pipe diameters are increased. One example is the connection to the underground storage plant Kraak.
- Gasnetz Hamburg GmbH (2021) and Harz Energie Netz GmbH (2021) state much higher average diameters in their gas grids than the values in the data. Since there is no more detailed information, which pipes have which diameter, the average value is used for all pipes of each operator.

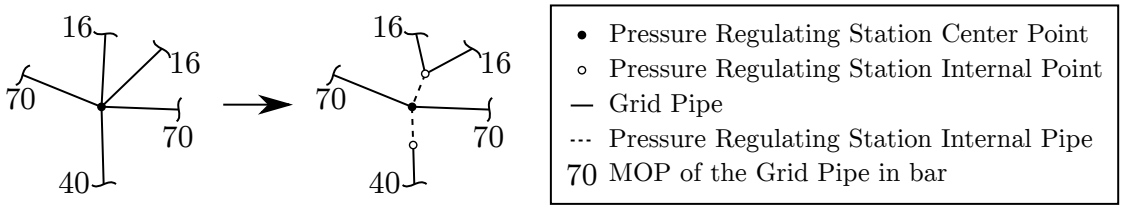

Figure 3.6: Topology representation before and after adding internal pipes and nodes to a pressure regulating station.

- In the future, there is assumed to be a lot of biomethane, hydrogen from biomass and PtG feed-in in the state of Schleswig-Holstein. That is why the pipe capacities are not sufficient, and the diameters are increased. Also, one short connection was added northwest of Hamburg to mitigate a bottleneck.

The next step is to place the pressure regulating stations on nodes where pipes with different MOP values meet. Since unequal pressure values from the different subnetworks would appear in the same node, the node has to be split, and internal pipes are added. An example is shown in Figure 3.6. Those internal pipes do not have a surface roughness like an ordinary gas grid pipe, but the pressure loss results directly from the nodes' pressure difference. The outlet node of a pressure regulating station is also added as a known pressure node with the value relative to the MOP, which was chosen initially.

After that, different data sets are imported. First, the required fluid properties density ρ, dynamic viscosity η, and gas law deviation coefficient K_m of natural gas and hydrogen are modeled using quadratic correlations depending on the integral mean pressure p_m in each pipe as in Equation (2.20). The coefficients for those correlations are imported here.

$$\rho = \alpha_{\rho,1} + \alpha_{\rho,2} p_\mathrm{m} + \alpha_{\rho,3} p_\mathrm{m}^2 \tag{3.2}$$

$$\eta = \alpha_{\eta,1} + \alpha_{\eta,2} p_\mathrm{m} + \alpha_{\eta,3} p_\mathrm{m}^2 \tag{3.3}$$

$$K_\mathrm{m} = \alpha_{K_\mathrm{m},1} + \alpha_{K_\mathrm{m},2} p_\mathrm{m} + \alpha_{K_\mathrm{m},3} p_\mathrm{m}^2 \tag{3.4}$$

Second, the pressure values for known pressure nodes on the 70 bar level are loaded, which are all import nodes. Third, all necessary data for the determination of the mass flow rates at the nodes is imported. This includes the positions of underground gas storage plants and import or export nodes, as well as the corresponding curves. For each NUTS 3 region, the demand curves, as well as biomethane, hydrogen from biomass, and PtG production curves, from the optimization are included. Those curves have to be disaggregated and assigned to the nodes of the gas grid.

To achieve this, first, the curves are interpolated if they are not already in the right time resolution, which is desired for the gas grid computation.

Second, the mass flow rate capacities for the pipes are set. For gas grid pipes, the capacity C is calculated as following using their cross-section $\pi D_i^2/4$, the density ρ at MOP, and the maximum velocity w_max.

$$C_i = \frac{\pi}{4} D_i^2 \rho\left(p_{\mathrm{MOP},i}\right) w_\mathrm{max} \tag{3.5}$$

Pressure regulating stations have zero as lower bound and half the capacity of the

largest connected upstream pipe. The capacities of certain pressure regulating stations are decreased manually to avoid too low pressures.

Third, the gas transfer mass flow rates between Northern Germany and the rest of Germany are determined. Since there is no data about this gas flow, it has to be modeled by taking the gas grid structure into account. According to the transmission gas grid operator in Mecklenburg-West Pomerania ONTRAS (no date), the only entry point into the ONTRAS gas grid from the rest of the gas grid in Northern Germany is via the underground gas storage Kraak. Since ONTRAS does not supply some very western parts of Mecklenburg-Western Pomerania, it is assumed that 98 % of the difference in mass balance in the state are imported from or exported to Brandenburg, south of Mecklenburg-Western Pomerania. It is assumed that the gas exchange between Lower Saxony and the surrounding states in the south closes the mass balance, including all gas import, export, production, consumption, and storage. This results in an inner-German export from Lower Saxony to the rest of Germany for more than 99 % of the hours of the year.

Those overall transfer curves for Lower Saxony and Mecklenburg-Western Pomerania are then split up and assigned to all inner-German transfer nodes, that is, nodes that lie on connections to the rest of Germany, by taking into account the capacities of those transfer pipes. To account for the different tasks of the 70 bar pressure level compared to the lower pressure levels, that is, transmission and distribution, the capacities of the latter are assumed to be 10 % of the respective nominal capacities. Shares of certain pipes are even further reduced to avoid too low pressures. For two transfer pipes between Lower Saxony and North-Rhine Westphalia, the sign of the share has to be switched since those pipes have a higher MOP than the surrounding Northern German gas grid, which means that they work as import, not export pipes, contrary to all others.

Fourth, the mass flow rates of consumption and production at all nodes in the Northern German gas grid are determined by combining the different demand and production categories. Gas consumption of power plants and biogas and PtG feed-in are only assigned to nodes on the highest pressure level in their respective NUTS 3 region. Power plants are usually located there due to their high consumption, and there would be the risk of excess gas supply on lower pressure levels if biogas and PtG feed-in were allocated on those levels. In contrast, mass flow rates related to import or export and storage plants are assigned to the corresponding nodes only, and the gas demand of households, commerce, trade, and services, as well as industry, are allocated to all nodes in the respective NUTS 3 region regardless of their MOP. Within every NUTS 3 region, each demand and production category is assigned proportionally to the largest capacity of connected pipes at each node.

Afterward, the nodal incidence matrix is set up as described in Equation (2.26). If the detailed pressure loss calculation is used, all nodes' pressures must be calculated based on the mass flow rates in all pipes using the detailed Equation (2.22). An efficient way is to choose one known pressure node for each subnetwork as the origin. Then for each load node, the shortest path to the origin is searched, and the pipe data is written into the pressure matrix $\mathbf{X}$. This leads to a vectorized form of Equation (2.22) for a network with n_{G} nodes and m pipes.

$$P = P_{\text{origin}} + \mathbf{X}F \tag{3.6}$$

$$\mathbf{X} = \begin{bmatrix} x_{11} & x_{12} & \cdots & x_{1m} \\ x_{21} & x_{22} & \cdots & x_{2m} \\ \vdots & \vdots & \ddots & \vdots \\ x_{n_{\text{G}}1} & x_{n_{\text{G}}2} & \cdots & x_{n_{\text{G}}m} \end{bmatrix} \tag{3.7}$$

$$x_{ij} = \begin{cases} -\dfrac{16}{\pi^2}\dfrac{l_j}{D_j^5}RT & \text{if pipe } j \text{ is part of the shortest} \\ & \text{path between node } i \text{ and origin} \\ 0 & \text{else} \end{cases} \tag{3.8}$$

$$F = \begin{bmatrix} \dot{m}_1^2 \lambda_1 K_{\text{m},1} \\ \dot{m}_2^2 \lambda_2 K_{\text{m},2} \\ \vdots \\ \dot{m}_m^2 \lambda_m K_{\text{m},m} \end{bmatrix} \tag{3.9}$$

In this case, the most centered known pressure node is selected for each subnetwork. It is found by going through all known pressure nodes, finding the shortest paths to all nodes, and summing up the ratios of length to diameter per pipe for all paths. This reflects the pressure losses over all paths according to Equation (2.9), assuming a constant velocity in the whole subgrid. The known pressure node with the lowest sum of length to diameter ratio is picked as the origin for this subnetwork.

Gas Grid Computation

After the pre-processing, the actual gas grid computation can be done. The algorithm goes through all MOP values in ascending order and through each subnetwork in the MOP level. Like this, the gas grid is solved from bottom to top.

First, the reference nodes or known pressure nodes have to be identified. Those are all nodes on the lower level of a pressure regulating station, all inner-German transfer nodes in Mecklenburg-Western Pomerania since they primarily supply gas to the region, and the two inner-German import nodes in Lower Saxony.

Second, all load nodes are searched, that is, all regular nodes and nodes where there is a pressure regulating station connected, which leads to a lower MOP level. The latter is transformed into a load node since the mass flow rate through the pressure regulating station is known because it leads to an MOP level that has been solved already.

Third, dendrites have to be found to split all pipes into tree branches and chords. The algorithm starts at each reference node and adds all connected branches to the dendrite as long as this step does not create any loops or connections to another dendrite. It gradually continues by adding all connected pipes at the newly added nodes with the same condition and so on until all nodes are included in dendrites. All branches, which are part of a dendrite, are tree branches and all others are chords.

Now, the gas grid can be solved using the equations described in Section 2.3.6 but modified to work for mass flow rates. Based on arbitrary start values for the chords' mass flow rates, the tree branches' gas flow can be calculated using an adapted version of Equation (2.35).

$$\dot{m}_\mathrm{t} = \mathbf{A}_\mathrm{1t}^{-1}\dot{m}_\mathrm{N} + \mathbf{B}_\mathrm{t}^\mathrm{T}\dot{m}_\mathrm{c} \tag{3.10}$$

In the first iterations, the Panhandle 'A' Equation (2.38) is used due to its high numerical efficiency. It also has to be adapted for the use with mass flow rates instead of volume flow rates and SI units. ρ_n is the norm density of the gas.

$$\Phi(Q_i) = \Delta P_i = 18.43 \frac{l_i}{0.9^2 \left(10^{-3} \cdot D_i\right)^{4.854}} \left(\frac{3600 \cdot \dot{m}_i}{\rho_\mathrm{n}}\right)^{1.854} \cdot \left(10^5\right)^2 \tag{3.11}$$

Equations (2.40) and (2.41) are then converted to

$$\mathbf{R} = \frac{\partial \Phi(\dot{m})}{\partial \dot{m}} = \begin{bmatrix} \frac{\partial \Phi_1}{\partial \dot{m}_1} & & & \mathbf{0} \\ & \frac{\partial \Phi_2}{\partial \dot{m}_2} & & \\ & & \ddots & \\ \mathbf{0} & & & \frac{\partial \Phi_m}{\partial \dot{m}_m} \end{bmatrix} \tag{3.12}$$

$$r_{ij} = \begin{cases} 1.854 \cdot 18.43 \dfrac{l_i}{0.9^2 \left(10^{-3} \cdot D_i\right)^{4.854}} \left|\dfrac{3600 \cdot \dot{m}_i}{\rho_\mathrm{n}}\right|^{0.854} \cdot \left(10^5\right)^2 & \text{if } i = j \\ 0 & \text{if } i \neq j. \end{cases} \tag{3.13}$$

If the algorithm detects convergence or clear divergence, as described below, it switches to the use of the detailed pressure loss computation. For this, all node pressures are determined using Equation (3.6) in an iteration loop with Equations (2.13) and (2.14). The Reynolds number is calculated using Equation (2.12), and density, viscosity, and gas law deviation coefficient are determined using the quadratic correlations (Equations (3.2)-(3.4)) with the integral mean pressure in Equation (2.20). The loop iterates until the changes in pressure fall below a specified tolerance, and then, the pressure losses over all pipes are calculated using Equation (2.37).

The next step is to determine the derivative of the detailed pressure loss computation with respect to the mass flow rate, but it cannot be done analytically since the friction factor depends on the mass flow rate in a nonlinear way. That is why it is approximated by varying the mass flow rate slightly by $\pm 10^{-6}\,\mathrm{kg/s}$ and calculating the corresponding pressure loss. Each entry r_{ij} is then approximated by

$$r_{ij} \approx \frac{\Phi\left(\dot{m}_i + 10^{-6}\,\mathrm{kg/s}\right) - \Phi\left(\dot{m}_i - 10^{-6}\,\mathrm{kg/s}\right)}{2 \cdot 10^{-6}\,\mathrm{kg/s}}. \tag{3.14}$$

The new pressures are calculated using Equation (2.42), and afterward, the new mass flow rates can be determined with the following equations.

$$\Delta\dot{m}_\mathrm{c}^z = \left(\mathbf{R}_\mathrm{c}^z\right)^{-1}\left(-A_\mathrm{c}^\mathrm{T} P^{z+1} - \Delta P_\mathrm{c}^z\right) \tag{3.15}$$

$$\dot{m}_\mathrm{c}^{z+1} = \dot{m}_\mathrm{c}^z + \Delta\dot{m}_\mathrm{c}^z \tag{3.16}$$

To limit the mass flow rate fluctuations and help convergence, the mass flow rates are limited using the capacities multiplied by a factor depending on the used gas: 2 for natural gas and 5 for hydrogen. The values were chosen since they facilitated fast convergence.

Convergence of the iteration is detected by evaluating the 1-norm of the average change in mass flow rate per pipe N^z.

$$N^z = \left\| \frac{\Delta \dot{m}_{\mathrm{c}}^z}{m} \right\|_1 \tag{3.17}$$

For $N^z > 10^4\,\mathrm{kg/s}$, the iteration tends to diverge. In that case, the pressure loss calculation is switched from Panhandle 'A' to the more detailed but slower computation. The same is done for $N^z < 10^{-6}\,\mathrm{kg/s}$ if Panhandle 'A' is still used, but if the detailed pressure loss calculation is already used, the iteration converged, and it is stopped.

In some cases, the iteration gets stuck at values of $N^z > 10^{-6}\,\mathrm{kg/s}$, and it was observed that multiplying Equation (3.14) with a factor greater than one can improve the convergence behavior. That is why that factor is multiplied by 10 every time the iteration has not converged after 50 steps.

The last step is to check if any pressure regulating station violates its capacity limitation because the gas grid computation algorithm does not limit the mass flow rates at the reference nodes. In case there is a violation, the mass flow rate of that pressure regulating station is set to the closer bound, that is, zero for negative values or the capacity for higher values, and the algorithm starts again with finding the dendrites.

3.1.3 Aggregation of Gas Grids

Based on the aggregation algorithm of Loewen (2001), the so-called German method, an aggregation method for gas grids is developed and implemented in Matlab (MathWorks Inc., 2021a). The main modification made is the adjustment for changing fluid density which has been neglected by Loewen (2001). Also, algorithms for the aggregation of short pipes and insignificant pipes have been added.

Since heat losses do not play a role in gas grids and the temperature is often assumed to be constant (Cerbe et al., 2017), the temperatures and heat loss coefficients are not considered anymore in the following.

For the implementation in the code, special attention has to be paid to the signs of the mass flow rates at the nodes and in the pipes.

First, some basic equations for the pipe volume V_{P} and the time delay τ_{P}, that is, the time a fluid particle takes to flow through the pipe, are presented, which will be used in the following.

$$V_{\mathrm{P}} = \frac{\pi}{4} D_{\mathrm{P}}^2 l_{\mathrm{P}} \tag{3.18}$$

$$\tau_{\mathrm{P}} = \frac{\dot{m}_{\mathrm{P}}}{V_{\mathrm{P}} \rho_{\mathrm{P}}} \tag{3.19}$$

The last step in every aggregation step is to modify the surface roughness of all modified pipes so that the pressure loss stays the same according to Equation (2.21). Due to the aggregation, the pressure loss may be so low or so high that it is not possible to find a

value for the surface roughness either because it would have to be less than zero or very large compared to the diameter ($k/D_\mathrm{P} > 0.1$). For those cases, a factor f is added to Equation (2.22).

$$p_1^2 - p_2^2 = \frac{16}{\pi^2}\lambda\frac{l_\mathrm{P}}{D_\mathrm{P}^5}RT\dot{m}_\mathrm{P}^2 K_\mathrm{m} f \tag{3.20}$$

With this equation, also negative pressure losses would be possible with $f < 0$, which could occur in some aggregation steps, but that would be numerically unstable, especially in dynamic simulations: With a given inlet pressure at a pipe, an increasing mass flow rate would lead to a decreasing outlet pressure which would again increase the mass flow rate and lead to simulation failure. That is why in some steps, special attention has to be paid to avoid this, as will be described in the respective steps.

Serial Pipes

For the aggregation of serial pipes, as shown in Figure 2.5, the serial pipes must be found first. To achieve that, a loop goes through all remaining nodes of the considered gas grid and analyzes if only two pipes are connected to it, none of those pipes is excluded from aggregation, and the gas flows in the same direction. The latter is ensured by checking the pipes' mass flow rates and the pressures at all nodes. If all those conditions are true, the aggregation is started. If not, the next node is examined.

To calculate the length and the diameter of the resulting pipe, the conditions from Loewen (2001) are used: Pipe P1′ is as long as P1 and P2 together, and the diameter is calculated so that the gas grid volume stays the same.

$$l_{\mathrm{P1}'} = l_\mathrm{P1} + l_\mathrm{P2} \tag{3.21}$$

$$D_{\mathrm{P1}'} = \sqrt{\frac{D_\mathrm{P1}^2 l_\mathrm{P1} + D_\mathrm{P2}^2 l_\mathrm{P2}}{l_\mathrm{P1} + l_\mathrm{P2}}} \tag{3.22}$$

To determine how node N2 is split and added to N1 and N3, the same condition as in Loewen (2001) is applied: The time delay of P1′ is the same as P1 and P2 combined, but the variable density has to be considered.

$$\tau_{\mathrm{P1}'} = \tau_\mathrm{P1} + \tau_\mathrm{P2} \tag{3.23}$$

$$\frac{V_{\mathrm{P1}'}\rho_{\mathrm{P1}'}}{\dot{m}_{\mathrm{P1}'}} = \frac{V_\mathrm{P1}\rho_\mathrm{P1}}{\dot{m}_\mathrm{P1}} + \frac{V_\mathrm{P2}\rho_\mathrm{P2}}{\dot{m}_\mathrm{P2}} \tag{3.24}$$

$$\frac{\frac{\pi}{4}D_{\mathrm{P1}'}^2 l_{\mathrm{P1}'}\rho_{\mathrm{P1}'}}{\dot{m}_{\mathrm{P1}'}} = \frac{\frac{\pi}{4}D_\mathrm{P1}^2 l_\mathrm{P1}\rho_\mathrm{P1}}{\dot{m}_\mathrm{P1}} + \frac{\frac{\pi}{4}D_\mathrm{P2}^2 l_\mathrm{P2}\rho_\mathrm{P2}}{\dot{m}_\mathrm{P2}} \tag{3.25}$$

$$\Rightarrow \qquad \dot{m}_{\mathrm{P1}'} = \frac{D_{\mathrm{P1}'}^2 l_{\mathrm{P1}'}\rho_{\mathrm{P1}'}}{\frac{D_\mathrm{P1}^2 l_\mathrm{P1}\rho_\mathrm{P1}}{\dot{m}_\mathrm{P1}} + \frac{D_\mathrm{P2}^2 l_\mathrm{P2}\rho_\mathrm{P2}}{\dot{m}_\mathrm{P2}}} \tag{3.26}$$

Due to the variable density, Equation (3.26) may lead to mass flow rates less than the smallest or greater than the largest mass flow rate in P1 and P2. This would mean that part of the consumer at N1 is moved to N3′ or vice versa, which should not be part of the aggregation. That is why $\dot{m}_{\mathrm{P1}'}$ is limited accordingly, which leads to a small error in the time delays.

To determine the mass flow rates at nodes N1′ and N3′, the equations from Loewen (2001) can be used.

$$\dot{m}_{\mathrm{N1'}} = \dot{m}_{\mathrm{N1}} + \dot{m}_{\mathrm{P1}} - \dot{m}_{\mathrm{P1'}} \tag{3.27}$$

$$\dot{m}_{\mathrm{N3'}} = \dot{m}_{\mathrm{N3}} + \dot{m}_{\mathrm{P1'}} - \dot{m}_{\mathrm{P1}} \tag{3.28}$$

Parallel Pipes

The aggregation of parallel pipes is shown in Figure 2.6. To find parallel pipes in the gas grid, a loop goes through all pipes and searches parallel pipes, that is, at least two pipes with the same start and end node, respectively. If there are any and none of them is excluded from aggregation, the algorithm proceeds with the main section of the aggregation algorithm. If there are more than two parallel pipes, the first two are picked, and the remaining pipes will be aggregated in the following executions of this algorithm.

To determine the length and the diameter of the resulting pipe, the same equations as in Loewen (2001) can be used since the density is identical in the parallel pipes because inlet and outlet pressure are identical. The length is weighted by the mass flow rates, and the diameter is calculated so that the volume stays constant. At the end, the mass flow rates are added.

$$l_{\mathrm{P1'}} = \sqrt[3]{\left(\frac{\dot{m}_{\mathrm{P1}}}{\dot{m}_{\mathrm{P1}} + \dot{m}_{\mathrm{P2}}}\frac{l_{\mathrm{P1}}}{D_{\mathrm{P1}}} + \frac{\dot{m}_{\mathrm{P2}}}{\dot{m}_{\mathrm{P1}} + \dot{m}_{\mathrm{P2}}}\frac{l_{\mathrm{P2}}}{D_{\mathrm{P2}}}\right)^{2}(l_{\mathrm{P1}}D_{\mathrm{P1}}^2 + l_{\mathrm{P2}}D_{\mathrm{P2}}^2)} \tag{3.29}$$

$$D_{\mathrm{P1'}} = \sqrt[3]{\left(\frac{\dot{m}_{\mathrm{P1}}}{\dot{m}_{\mathrm{P1}} + \dot{m}_{\mathrm{P2}}}\frac{l_{\mathrm{P1}}}{D_{\mathrm{P1}}} + \frac{\dot{m}_{\mathrm{P2}}}{\dot{m}_{\mathrm{P1}} + \dot{m}_{\mathrm{P2}}}\frac{l_{\mathrm{P2}}}{D_{\mathrm{P2}}}\right)^{-1}(l_{\mathrm{P1}}D_{\mathrm{P1}}^2 + l_{\mathrm{P2}}D_{\mathrm{P2}}^2)} \tag{3.30}$$

$$\dot{m}_{\mathrm{P1'}} = \dot{m}_{\mathrm{P1}} + \dot{m}_{\mathrm{P2}} \tag{3.31}$$

Terminal Pipes

The aggregation of terminal pipes is shown schematically in Figure 2.7. To find terminal pipes, first, terminal nodes are searched by examining how many pipes are connected to each node. If one node with just one pipe is found, that pipe is classified as a terminal pipe. In the next step, the algorithm checks that the terminal pipe is not excluded from aggregation and that it is not a serial pipe because then it should be treated by the aggregation of serial pipes first.

Afterward, a loop goes through all pipes, which are connected to the terminal pipes, to find a possible match into which the terminal node can be aggregated: First, the connected pipes are sorted descending by their time delay, and it is checked that there are no parallel pipes so that this step does not prohibit the aggregation of parallel pipes. The connected pipe should not be excluded from aggregation and should have a mass flow rate unequal to zero. Also, the gas in both pipes should flow in the same direction: either enter the common node or leave it. Furthermore, the connected pipe's time delay has to be greater than that of the terminal pipe so that the terminal node can be placed into the connected pipe. To increase the number of terminal pipes which can be aggregated, this time delay condition can be ignored using a flag in the options. In this case, connected pipe's time delay is set to 101 % of the terminal pipe's time delay to force the condition to be true and avoid errors in the following equations. At the end, the pressures at the

nodes are checked to avoid negative pressure losses in any of the new pipes, so the pressure value of the terminal node has to lie between the values of the start and end node. If all conditions are satisfied, the aggregation is started. If not, all other connected pipes are examined, or, after that, the following terminal node is investigated.

For the aggregation, the same conditions as by Loewen (2001) are used: The length is weighted by the time delay, and the mass flow rates in P1 and P2 are added for P1′.

$$l_{\mathrm{P1}'} = l_{\mathrm{P2}} \frac{\tau_{\mathrm{P1}}}{\tau_{\mathrm{P2}}} \tag{3.32}$$

$$l_{\mathrm{P2}'} = l_{\mathrm{P2}} \left(1 - \frac{\tau_{\mathrm{P1}}}{\tau_{\mathrm{P2}}}\right) \tag{3.33}$$

$$\dot{m}_{\mathrm{P1}'} = \dot{m}_{\mathrm{P1}} + \dot{m}_{\mathrm{P2}} \tag{3.34}$$

$$\dot{m}_{\mathrm{P2}'} = \dot{m}_{\mathrm{P2}} \tag{3.35}$$

To calculate the new diameters, the velocity in P1′ should be the same as in P2, and the gas grid volume should not change, as stated by Loewen (2001), but due to the compressibility, the variable density has to be considered. Here, $\rho_{\mathrm{P1}'} = \rho_{\mathrm{P1}}$ holds since the pressures at the nodes stay the same. The equations below use the time delay instead of the mass flow rate to enable its modification, as stated above, so that the time delay condition can be ignored.

$$w_{\mathrm{P1}'} = w_{\mathrm{P2}} \tag{3.36}$$

$$\frac{4\dot{m}_{\mathrm{P1}'}}{\pi D_{\mathrm{P1}'}^2 \rho_{\mathrm{P1}'}} = \frac{4\dot{m}_{\mathrm{P2}}}{\pi D_{\mathrm{P2}}^2 \rho_{\mathrm{P2}}} \tag{3.37}$$

$$\Rightarrow D_{\mathrm{P1}'} = \sqrt{D_{\mathrm{P2}}^2 \frac{\rho_{\mathrm{P2}}}{\rho_{\mathrm{P1}}} \left(1 + \frac{\dot{m}_{\mathrm{P1}}}{\dot{m}_{\mathrm{P2}}}\right)} \tag{3.38}$$

$$= \sqrt{D_{\mathrm{P2}}^2 \frac{\rho_{\mathrm{P2}}}{\rho_{\mathrm{P1}}} \left(1 + \frac{\rho_{\mathrm{P1}} V_{\mathrm{P1}} \tau_{\mathrm{P2}}}{\rho_{\mathrm{P2}} V_{\mathrm{P2}} \tau_{\mathrm{P1}}}\right)} \tag{3.39}$$

$$= \sqrt{D_{\mathrm{P2}}^2 \frac{\rho_{\mathrm{P2}}}{\rho_{\mathrm{P1}}} \left(1 + \frac{\rho_{\mathrm{P1}} l_{\mathrm{P1}} D_{\mathrm{P1}}^2 \tau_{\mathrm{P2}}}{\rho_{\mathrm{P2}} l_{\mathrm{P2}} D_{\mathrm{P2}}^2 \tau_{\mathrm{P1}}}\right)} \tag{3.40}$$

$$D_{\mathrm{P2}'} = \sqrt{D_{\mathrm{P2}}^2 \left(1 - \frac{\rho_{\mathrm{P2}} \tau_{\mathrm{P1}}}{\rho_{\mathrm{P1}} \tau_{\mathrm{P2}}}\right) \left(1 - \frac{\tau_{\mathrm{P1}}}{\tau_{\mathrm{P2}}}\right)^{-1}} \tag{3.41}$$

The new GPS coordinates of node N2 are calculated using the coordinates of N1 and N3 and the length of P1′ and P2′.

Contrary to Loewen (2001), no aggregation of terminal pipes into pipes, which are further away in the gas grid, is implemented to avoid too substantial modifications of the gas grid's geographic structure. Also, no additional algorithm for the case of almost identical time delays of the terminal and connected pipe is integrated since it is not found to be necessary: When the time delay condition is ignored, the most important is that the pressures are consistent, and even without those additional algorithms, high aggregation grades can be achieved.

Loops

Loewen (2001) suggests two different treatments of loops: either conversion into serial pipes or splitting into two branches, but the decision-making cannot be automatized. Here, only the first option is implemented since it is more suitable for highly meshed gas grids and avoids the necessity to pick the kind of treatment for each case manually. An example is shown in Figure 2.8.

Figure 3.7 shows a flowchart of the algorithm. It starts with a search for loops in the remaining gas grid by going through all pipes and looking for the shortest path between the pipe's start and end node without using the pipe itself. This way, small loops are found, which have a higher chance of being aggregated than larger, more complex loops that are not found by this algorithm.

All loops with more than two nodes are gone through in ascending order of the circumference. Then different conditions are checked as described below. If all conditions are satisfied, the aggregation is made, and the next loop is examined until all loops have been checked. Then the loop finding algorithm is started again, and the whole process starts from the beginning. Everything is executed repeatedly until no loop can be aggregated anymore.

The following conditions have to be true to allow the algorithm to aggregate the current loop: First, it is verified that none of the nodes was part of a loop that has been aggregated in a previous step of the current execution. This is necessary because the gas grid structure changed in that area, and the current loop might not exist anymore. Second, all corresponding pipes of the loop are searched and checked that none of the

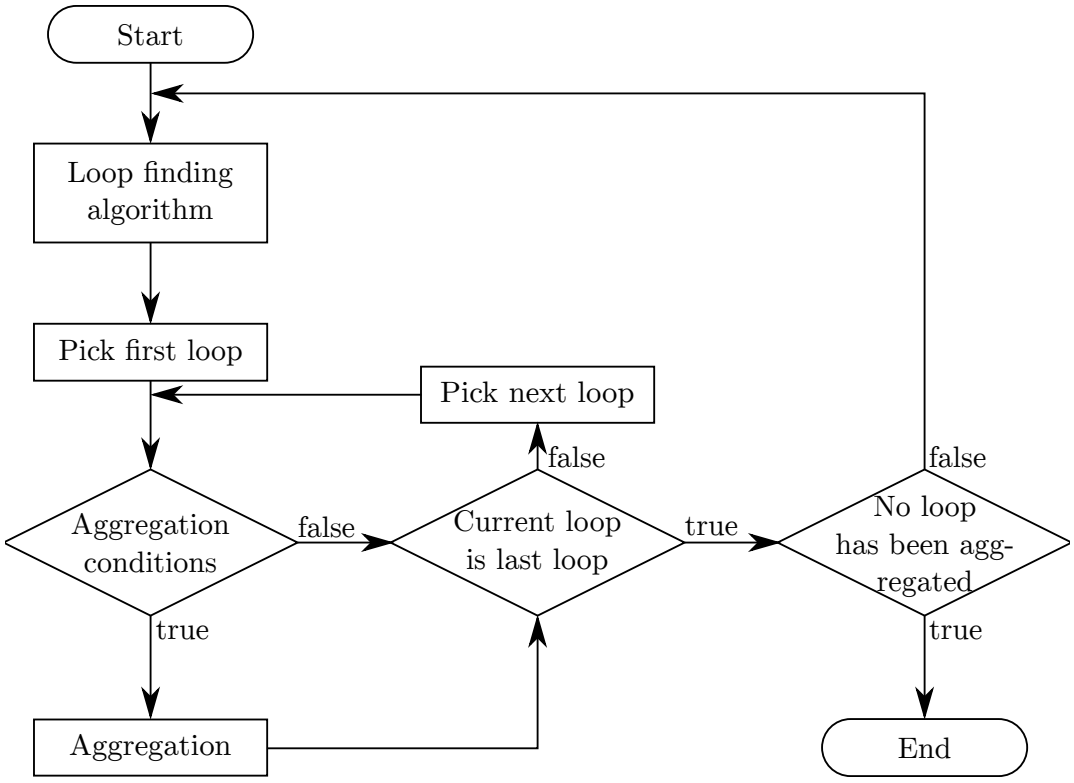

Figure 3.7: Flowchart of the aggregation algorithm for loops.

pipes is excluded from aggregation and all mass flow rates are unequal to zero, which would otherwise lead to problems in the equations. Third, the mass flow directions in all pipes are examined. To aggregate the loop, it has to be split into two paths with the same mass flow direction each, and the paths meet in the common start and end node. Fourth, each path's time delay has to be longer than the other path's time delay without its last pipe, as is stated by Loewen (2001). To avoid negative pressure losses, the nodes are not sorted by time delay as suggested by Loewen (2001) but by pressure. This can lead to negative time delays, which will be treated later.

For the following equations, the pipe indices before aggregation are chosen so that they are already sorted in the order of aggregation, as indicated in Figure 2.8. n_P is the number of pipes in the considered loop, n_P1 and n_P2 are the numbers of pipes in paths 1 and 2 of the loop, respectively. The calculation of time delays is the same as done by Loewen (2001).

$$\tau_{\mathrm{P}i} = \frac{4\dot{m}_{\mathrm{P}i}}{\pi D_{\mathrm{P}i}^2 l_{\mathrm{P}i} \rho_{\mathrm{P}i}} \qquad \forall\, i = 1...n_\mathrm{P} \tag{3.42}$$

$$\tau_{\mathrm{P}1'} = \tau_{\mathrm{P}1} \tag{3.43}$$

$$\tau_{\mathrm{P}i'} = \sum_{j=1}^{i} \tau_{\mathrm{P}j} - \sum_{j=1}^{i-1} \tau_{\mathrm{P}j'} \qquad \forall\, i = 2...n_\mathrm{P} - 2 \tag{3.44}$$

$$\tau_{\mathrm{P}n_\mathrm{P}-1'} = \frac{\dot{m}_{\mathrm{P}n_{\mathrm{P}1}}}{\dot{m}_{\mathrm{P}n_{\mathrm{P}1}} + \dot{m}_{\mathrm{P}n_{\mathrm{P}2}}} \sum_{j=1}^{n_{\mathrm{P}1}} \tau_{\mathrm{P}j} + \frac{\dot{m}_{\mathrm{P}n_{\mathrm{P}2}}}{\dot{m}_{\mathrm{P}n_{\mathrm{P}1}} + \dot{m}_{\mathrm{P}n_{\mathrm{P}2}}} \sum_{j=1}^{n_{\mathrm{P}2}} \tau_{\mathrm{P}j} - \sum_{j=1}^{n_\mathrm{P}-2} \tau_{\mathrm{P}j'} \tag{3.45}$$

Sorting the nodes by pressure may result in negative time delays. In this case, the concerned values are set to 1 s to enable using the following equations. The error is limited to the time delays and does not significantly influence the simulation of the gas grids since the pressures and pressure losses are ensured to stay the same.

If there is a direct connection in the loop, that means one of the paths consists of just one pipe, the length of the remaining pipes is set as the length of all pipes in the not-direct path.

The calculation of the new mass flow rates and lengths is done according to Loewen (2001): The mass flow rates of the combined pipes $\mathrm{P}k_{i1}$ and $\mathrm{P}k_{i2}$ are added, and the lengths are weighted by the time delays. The equation for the diameter also considers the variable density.

$$\dot{m}_{\mathrm{P}i'} = \dot{m}_{\mathrm{P}k_{i1}} + \dot{m}_{\mathrm{P}k_{i2}} \qquad \forall\, i = 1...n_\mathrm{P} - 1 \tag{3.46}$$

$$l_{\mathrm{P}1'} = \frac{\tau_{\mathrm{P}1}}{\sum_{j=1}^{n_\mathrm{P}-1} \tau_{\mathrm{P}j}} \sum_{j=1}^{n_\mathrm{P}} l_{\mathrm{P}j} \tag{3.47}$$

$$l_{\mathrm{P}i'} = \frac{\sum_{j=1}^{i} \tau_{\mathrm{P}j}}{\sum_{j=1}^{n_\mathrm{P}-1} \tau_{\mathrm{P}j}} \sum_{j=1}^{n_\mathrm{P}} l_{\mathrm{P}j} - \sum_{j=1}^{i-1} l_{\mathrm{P}j} \qquad \forall\, i = 2...n_\mathrm{P} - 1 \tag{3.48}$$

$$l_{\mathrm{P}n_\mathrm{P}-1'} = l_{\mathrm{P}n_\mathrm{P}} \tag{3.49}$$

$$D_{\mathrm{P}i'} = \sqrt{\frac{4\dot{m}_{\mathrm{P}i'}\tau_{\mathrm{P}i'}}{\pi \rho_{\mathrm{P}i'} l_{\mathrm{P}i'}}} \qquad \forall\, i = 1...n_\mathrm{P} - 1 \tag{3.50}$$

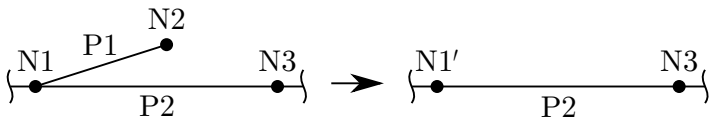

Figure 3.8: Topology representation before and after the aggregation of an insignificant pipe.

Due to the variable density, there is a slight change in the gas grid volume after using the above equations. To ensure constant volume, the diameter is scaled linearly according to the error.

To avoid too extreme changes in the visualization of the gas grid, the GPS coordinates stay the same, that is, N1 = N1′ and so on, and the last node is deleted.

Insignificant Pipes

Loewen (2001) also refers to one source which mentions that terminal pipes can be deleted when pipe length or diameter or the consumption at the end is too small. This attempt was modified and implemented as follows.

The algorithm starts with the same first steps as the algorithm for terminal pipes. If the time delay condition fails and ignoring the condition is not allowed, or the pressure condition is not true, the following steps are executed.

First, the aggregation of insignificant pipes has to be allowed by the current options and, second, the mass flow rate or volume of the pipe has to be below the specified limits. If so, the aggregation is possible, as is illustrated in Figure 3.8: Node N2 and pipe P1 are deleted, and the consumed or fed in gas mass flow rate at N2 is added to N1.

Short Pipes

Also, for short pipes in gas grids, Loewen (2001) names one reference, which states that short pipes can be eliminated as long as they are not bottlenecks in the gas grid. This inspired the following algorithm in which the check for bottlenecks was neglected since the algorithm is designed to minimize errors in time delays and pressure losses and thus covers bottleneck situations as well, as long as the chosen time instance of aggregation covers possible bottlenecks.

To find short pipes, a loop goes through all pipes and checks that the pipe is not excluded from aggregation and is neither a terminal nor a parallel pipe. If the pipe's length is below the specified threshold, it is classified as a short pipe, and the mass flow directions of all connected pipes are examined. Depending on whether the gas in all pipes connected to the start node or the end node, respectively, flows in the same direction and there are no zero mass flows, two different aggregation methods are used. Either the short pipe is aggregated with the connected pipes on one side or it is split in two and aggregated with the corresponding connected pipes.

If the mass flows are unidirectional at one of the nodes, that node is deleted and the short pipe is aggregated with the connected pipes because, like that, the time delays between all nodes can stay the same. An exemplary topology representation is shown in Figure 3.9.

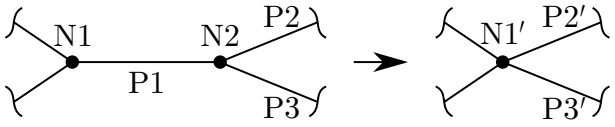

Figure 3.9: Exemplary topology representation before and after the aggregation of a short pipe where N2 and P1 are deleted and pipes P2 and P3 are adapted.

The next step is to check for all connected pipes that the sign of the pressure loss does not change when the node is deleted to avoid negative pressure losses. To increase the number of cases where this is true, it is possible to pick the pressure value of the remaining node N1′: It can either take the value of N1, N2 or the arithmetic mean of those two, and the pressure losses in all affected pipes change accordingly.

If all conditions are true, the following equations for a pipe P1 with nodes N1 and N2, which are aggregated into N1′, are utilized. The n_{P} pipes, which are connected to N2, are called P2...P$n_{\mathrm{P}}+1$. The mass flow rates at the nodes N1 and N2 are simply added, and the time delays of the modified pipes P2′...P$n_{\mathrm{P}}+1'$ are calculated by adding the time delay of the short pipe to the time delay of those pipes since the gas flows are unidirectional. In some cases, the short pipes' time delays are very long due to very small mass flow rates, which can lead to extreme changes in time delays, and thus lengths, for the new pipes, resulting in larger errors in different flow situations. If that is the case, the short pipe's gas velocity is set to a minimum value of 0.1 m/s. The pipe lengths are prolonged according to the time delays, and the diameter is calculated using the equation for the volume with the new density.

$$\dot{m}_{\mathrm{N1}'} = \dot{m}_{\mathrm{N1}} + \dot{m}_{\mathrm{N2}} \tag{3.51}$$

$$\tau_{\mathrm{P}i} = \frac{4\dot{m}_{\mathrm{P}i}}{\pi D_{\mathrm{P}i}^2 l_{\mathrm{P}i} \rho_{\mathrm{P}i}} \qquad \forall\, i = 1...n_{\mathrm{P}}+1 \tag{3.52}$$

$$\tau_{\mathrm{P}i'} = \tau_{\mathrm{P}i} + \tau_{\mathrm{P1}} \qquad \forall\, i = 2...n_{\mathrm{P}}+1 \tag{3.53}$$

$$l_{\mathrm{P}i'} = \frac{\tau_{\mathrm{P}i'}}{\tau_{\mathrm{P}i}} l_{\mathrm{P}i} \qquad \forall\, i = 2...n_{\mathrm{P}}+1 \tag{3.54}$$

$$D_{\mathrm{P}i'} = \sqrt{\frac{4\tau_{\mathrm{P}i}\dot{m}_{\mathrm{P}i}}{\pi l_{\mathrm{P}i} \rho_{\mathrm{P}i'}}} \qquad \forall\, i = 2...n_{\mathrm{P}}+1 \tag{3.55}$$

Due to the variable density, there is a small error in grid volume, which is corrected by slightly adapting the diameter accordingly.

If the gas flows are not unidirectional at neither start and end node, the same procedure is used except that half the short pipe is aggregated into the pipes connected to the start node and the other half to the pipes at the end node by exchanging τ_{P1} for $\tau_{\mathrm{P1}}/2$ in Equation (3.53).

Overall Algorithm

To reduce the error propagation during the aggregation, first, the remaining minor errors from the gas grid computation are corrected by modifying the mass flow rates at the nodes so that Kirchhoff's first law is correct and by adjusting the surface roughness in the pipes so that the pressure losses equal the pressure difference at the nodes.

Afterward, the aggregation can begin. The above-described steps are executed in a particular order to increase the efficiency of the algorithm:

- parallel pipes,
- terminal pipes,
- serial pipes,
- parallel pipes,
- loops,
- serial pipes, and
- parallel pipes.

Since parallel pipes can block several other algorithms, the aggregation algorithm for parallel pipes is always executed when the previous algorithm might have created new parallel pipes. Aggregation of terminal pipes and loops usually results in serial pipes, so the aggregation of serial pipes always follows. After each complete run of the algorithms given above, the aggregated gas grid data is saved to a file. Also, it is checked if at least one node or pipe has been aggregated. If so, all algorithms are started again in that order. If not, the aggregation of short pipes is executed with the current limit, which starts at 10 m. If no short pipes can be aggregated, certain algorithms are activated or limits are increased as listed below, and all algorithms are started again until no aggregation happened again and the next option is set. The options are:

1. The time delay condition (time delay of terminal pipe has to be less than the time delay of the connected pipe) is ignored from now on for the aggregation of terminal pipes.
2. The aggregation of insignificant pipes is activated, which is part of the algorithm for the aggregation of terminal pipes. The limits for mass flow rate and volume for identifying insignificant pipes are set to 10^{-10} kg/s and 100 m^3, respectively.
3. The maximum length for the aggregation of short pipes is increased, first to 1000 m and then in 1000 m steps.

The aggregation stops if either a specified number of pipes has been reached or no aggregation has been made in the last run through all algorithms, all options have been activated, and the maximum length for the aggregation of short pipes has reached its ultimate limit of 100 km.

3.1.4 Aggregation of Power Grids

For the aggregation of the power grid, the algorithm of Heckel et al. (2020) implemented in Matlab (MathWorks Inc., 2021a) is used. The method is split into two steps: First, nodes with low electric distances are clustered together to reduce the total number of nodes. Nodes with high power production or consumption are excluded from elimination

to reduce the resulting error. Second, the transmission lines for the new nodes have to be found. This is done by combining the lines of the same type which connected the different nodes before by creating several parallel transmission lines with averaged properties.

These two steps are executed until the desired number of nodes has been reached.

3.1.5 Models for Dynamic Simulation

In this section, all models for the dynamic simulations are described, first the component models and then the dynamic IES model. Except for the superstructure, all models are part of the open-source TransiEnt Library (TUHH, 2021), and only a short description will be given here.

The TransiEnt Library is written in the open-source programming language Modelica (Modelica Association, 2021). It is an object-oriented, equation-based, and acausal language that allows physical modeling with a high grade of reusability. Differential equations can be included in the models so that dynamic effects can be considered. Furthermore, multi-domain systems can be built so that, for example, the power, heat, and gas sector can be represented in one system model. As simulation environment, Dymola (Dassault Systèmes, 2021) is used.

For all models, the following sign convention applies: All flows, for example, mass flow rates, heat flow rates, electric powers, have a negative sign when leaving the respective component and a positive sign when entering it.

Pipe

The pipe model is based on the discretizable pipe model in the ClaRa Library (TLK-Thermo, XRG, et al., 2021). The modeling approach follows the finite volume method for a one-dimensional flow, and the media properties are provided by the TILMedia Library (TLK-Thermo and ift, 2021). Each of the n_{CV} control volumes contains dynamic mass balances for the entire fluid, Equations (3.56) and (3.57), mass balances for the n_{comp} components of the fluid, Equations (3.58)-(3.62), as well as an energy balance, Equations (3.63)-(3.66) (TLK-Thermo, XRG, et al., 2021). Here, the mass flow rates are positive if they flow in the direction of increasing i. The variables with the indices inlet, in and outlet, in enter the inlet or outlet of the pipe from the outside.

$$\frac{\mathrm{d}\rho_i}{\mathrm{d}t} V_i = \dot{m}_i - \dot{m}_{i+1} \qquad \forall\, i = 1...n_{\mathrm{CV}} \tag{3.56}$$

$$\frac{\mathrm{d}\rho_i}{\mathrm{d}t} = p_i \left.\frac{\partial \rho_i}{\partial p_i}\right|_{h_i,\xi_i} + h_i \left.\frac{\partial \rho_i}{\partial h_i}\right|_{p_i,\xi_i} + \sum_{j=1}^{n_{\mathrm{comp}}-1} \xi_{i,j} \left.\frac{\partial \rho_i}{\partial \xi_i}\right|_{p_i,h_i} \qquad \forall\, i = 1...n_{\mathrm{CV}} \tag{3.57}$$

$$\frac{\mathrm{d}\xi_{i,j}}{\mathrm{d}t} m_{\mathrm{CV},i} = \left(\dot{\Xi}_{i,j} - \dot{m}_i \xi_{i,j}\right) - \left(\dot{\Xi}_{i+1,j} - \dot{m}_{i+1} \xi_{i+1,j}\right) \qquad \forall \begin{matrix} i = 1...n_{\mathrm{CV}}, \\ j = 1...n_{\mathrm{comp}} - 1 \end{matrix} \tag{3.58}$$

$$\sum_{j=1}^{n_{\mathrm{comp}}} \xi_{i,j} = 1 \qquad \forall\, i = 1...n_{\mathrm{CV}} \tag{3.59}$$

$$\dot{\Xi}_{1,j} = \begin{cases} \dot{m}_1 \xi_{\mathrm{inlet,in},j} & \text{if } \dot{m}_1 \geq 0 \\ \dot{m}_1 \xi_{1,j} & \text{if } \dot{m}_1 < 0 \end{cases} \qquad \forall\, j = 1...n_{\mathrm{comp}} - 1 \tag{3.60}$$

$$\dot{\Xi}_{i,j} = \begin{cases} \dot{m}_i \xi_{i-1,j} & \text{if } \dot{m}_i \geq 0 \\ \dot{m}_i \xi_{i,j} & \text{if } \dot{m}_i < 0 \end{cases} \qquad \forall \begin{matrix} i = 2...n_{\mathrm{CV}}, \\ j = 1...n_{\mathrm{comp}} - 1 \end{matrix} \tag{3.61}$$

$$\dot{\Xi}_{n_{\mathrm{CV}}+1,j} = \begin{cases} \dot{m}_{n_{\mathrm{CV}}+1} \xi_{n_{\mathrm{CV}}+1,j} & \text{if } \dot{m}_{n_{\mathrm{CV}}+1} \geq 0 \\ \dot{m}_{n_{\mathrm{CV}}+1} \xi_{\mathrm{outlet,in},j} & \text{if } \dot{m}_{n_{\mathrm{CV}}+1} < 0 \end{cases} \qquad \forall\, j = 1...n_{\mathrm{comp}} - 1 \tag{3.62}$$

$$\frac{\mathrm{d}h_i}{\mathrm{d}t} m_{\mathrm{CV},i} = \dot{H}_i - \dot{H}_{i+1} + \dot{Q}_i + \frac{\mathrm{d}p_i}{\mathrm{d}t} V_i - \frac{\mathrm{d}\rho_i}{\mathrm{d}t} h_i V_i \qquad \forall\, i = 1...n_{\mathrm{CV}} \tag{3.63}$$

$$\dot{H}_1 = \begin{cases} \dot{m}_1 h_{\mathrm{inlet,in}} & \text{if } \dot{m}_1 \geq 0 \\ \dot{m}_1 h_1 & \text{if } \dot{m}_1 < 0 \end{cases} \tag{3.64}$$

$$\dot{H}_i = \begin{cases} \dot{m}_i h_{i-1} & \text{if } \dot{m}_i \geq 0 \\ \dot{m}_i h_i & \text{if } \dot{m}_i < 0 \end{cases} \qquad \forall\, i = 2...n_{\mathrm{CV}} \tag{3.65}$$

$$\dot{H}_{n_{\mathrm{CV}}+1} = \begin{cases} \dot{m}_{n_{\mathrm{CV}}+1} h_{n_{\mathrm{CV}}+1} & \text{if } \dot{m}_{n_{\mathrm{CV}}+1} \geq 0 \\ \dot{m}_{n_{\mathrm{CV}}+1} h_{\mathrm{outlet,in}} & \text{if } \dot{m}_{n_{\mathrm{CV}}+1} < 0 \end{cases} \tag{3.66}$$

To this model, different simplifications were applied, and the pressure loss model was exchanged for a more exact formulation.

If the gas composition is constant, Equations (3.58)-(3.62) can be left out. Also, if only one component is freely variable, for example, when hydrogen is injected into natural gas with otherwise constant composition, all other components are dependent on this one free component and can be calculated using their default mass fraction $\xi_{i,j,\mathrm{def}}$. This aspect can be generalized for all indices $j_{\mathrm{comp,free}}$ of the free components, and all, except one, indices of the dependent components $j_{\mathrm{comp,dep-1}}$ in Equations (3.67) and (3.68), which replace Equation (3.58). This leads to a reduction of the so-called states, that is, the variables whose time derivatives appear in the system of equations, which results in increased numerical efficiency.

$$\frac{\mathrm{d}\xi_{i,j}}{\mathrm{d}t} m_{\mathrm{CV},i} = \left(\dot{\Xi}_{i,j} - \dot{m}_i \xi_{i,j}\right) - \left(\dot{\Xi}_{i+1,j} - \dot{m}_{i+1} \xi_{i+1,j}\right) \qquad \forall \begin{matrix} i = 1...n_{\mathrm{CV}}, \\ j = j_{\mathrm{comp,free}} \end{matrix} \tag{3.67}$$

$$\xi_{i,j} = \frac{1 - \sum\limits_{z=j_{\mathrm{comp,free}}} \xi_{i,z}}{1 - \sum\limits_{z=j_{\mathrm{comp,free}}} \xi_{i,z,\mathrm{def}}} \xi_{i,j,\mathrm{def}} \qquad \forall \begin{matrix} i = 1...n_{\mathrm{CV}}, \\ j = j_{\mathrm{comp,dep-1}} \end{matrix} \tag{3.68}$$

Despite these simplifications, all components' gas properties still have to be computed by the TILMedia Library. That is why the mixture of natural gas and hydrogen is simplified to be a methane-hydrogen mixture to reduce the computation time for the gas properties. The error is negligible since the assumed Russian natural gas has a methane content of 98.3 vol% (Cerbe et al., 2017).

In case of the common simplification of an isothermal flow, that is, for ideal heat transfer between the gas and a constant pipe wall and ground temperature or for negligible temperature changes, Equation (3.69) replaces Equations (3.63)-(3.66).

$$T_i = T_{\mathrm{ground}} \quad \forall\, i = 1...n_{\mathrm{CV}} \tag{3.69}$$

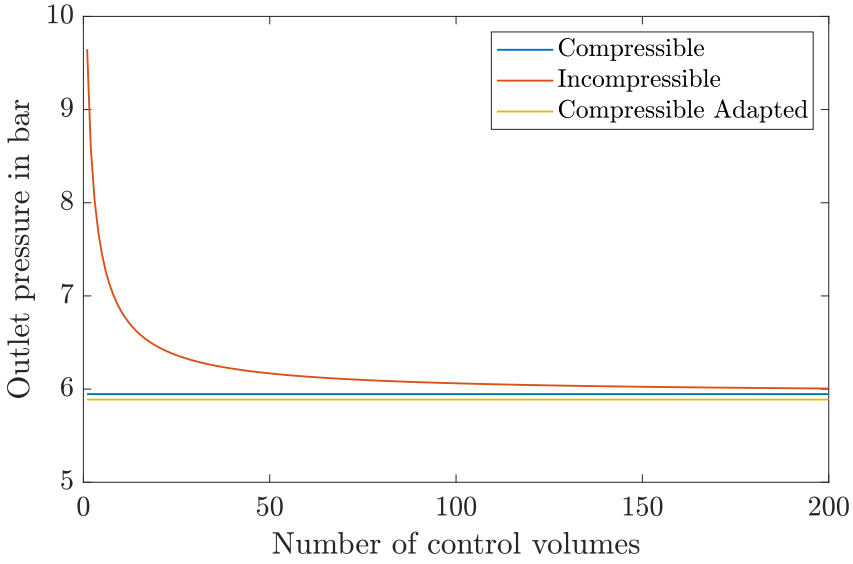

Figure 3.10: Comparison of different implementations of the pressure loss calculation for exemplary conditions of $D = 0.5\,\mathrm{m}$, $l = 100\,\mathrm{km}$, $k = 0.1\,\mathrm{mm}$, $\dot{m} = 17\,\mathrm{kg/s}$, $p_1 = 17.013\,\mathrm{bar}$, and $f = 1$.

The dynamic viscosity is needed for the pressure loss calculation, as explained in Section 2.3.5, but the TILMedia Library does not provide the value. Since the dynamic viscosity does not strongly depend on the pressure, its influence on the pressure losses is small, and to avoid nonlinear equations, linear correlations depending on the pressure, temperature, and composition are used.

$$\eta_{\mathrm{m},i} = \alpha_{\eta,1} + \alpha_{\eta,2} p_{\mathrm{m},i} + \alpha_{\eta,3} T_{\mathrm{m},i} + \sum_{j=1}^{n_{\mathrm{comp}}-1} \alpha_{\eta,3+j} \xi_{\mathrm{m},i,j} \qquad \forall\, i = 1...n_{\mathrm{CV}} \tag{3.70}$$

The pressure loss over the whole pipe is split into pressure losses between the control volumes and, if desired, into a pressure loss before the first control volume, a pressure loss after the last control volume, or both. Switching on the pressure losses at the inlet and outlet can improve numerical performance. Since the gas flow in the pipe is compressible, Equation (2.21) should be used. This leads to a strongly nonlinear system of equations, and the compressibility factor is needed, which is not provided by the TILMedia Library. That is why the compressible pressure loss calculation is compared to the incompressible pressure loss calculation in Equation (2.15) which requires no compressibility factor and leads to a less nonlinear system of equations. For this, the changes of density in each control volume are neglected. As can be seen in an example shown in Figure 3.10 (red line), that equation only leads to exact results of the outlet pressure when a high discretization is used because otherwise, the density changes are not negligible. However, a high number of control volumes leads to slow simulations.

That is why Equation (2.23) is adapted by applying Boyle's law in Equation (2.17) and transforming the ideal gas density back into the real gas density.

$$p_1 - p_2 = \frac{8}{\pi^2} \lambda \frac{l}{D^5} \frac{1}{\rho_{\mathrm{m,arithm}}} \dot{m}^2 \frac{K_{\mathrm{m}}}{K_{\mathrm{m,arithm}}} \tag{3.71}$$

To avoid the nonlinearity in Equation (2.20) for the integral mean pressure and the gas law deviation coefficient, which is not provided by the TILMedia Library, $K_\mathrm{m} \approx K_\mathrm{m,arithm}$ is approximated. For Equation (3.70) and the calculation of Re for λ, also $p_\mathrm{m} \approx p_\mathrm{m,arithm}$, $T_\mathrm{m} \approx T_\mathrm{m,arithm}$, $\xi_\mathrm{m} \approx \xi_\mathrm{m,arithm}$, $\rho_\mathrm{m} \approx \rho_\mathrm{m,arithm}$ and $\eta_\mathrm{m} \approx \eta_\mathrm{m,arithm}$ is assumed. To adopt the modification of the pressure losses from the aggregation, the factor f is added as done for Equation (3.20).

$$p_1 - p_2 = \frac{8}{\pi^2}\lambda\frac{l}{D^5}\frac{1}{\rho_\mathrm{m,arithm}}\dot{m}^2 f. \tag{3.72}$$

As shown in Figure 3.10 (yellow line), this gives good results while avoiding a strongly nonlinear system of equations.

A parameter study over a wide variety of inlet pressures, pipe diameters, pipe lengths, mass flow rates, and surface roughness values showed that high deviations between the compressible and adapted incompressible computation only occur for high inlet pressures, that is, 70 bar and above, and at the same time very low outlet pressures, that is, close to 1 bar. Those values do not appear in regular operation, and the error in pressure loss was below 0.01 % for more than 75 % of investigated parameter sets for natural gas and 82 % for hydrogen.

Since Equation (3.72) is still nonlinear, numerical problems can occur, especially around zero mass flow, which slows down the simulations. To avoid that, a linearization is used below a specified pressure loss threshold (TUHH, 2021).

Junction

The junction consists of one volume with a desired number of ports, and the model contains mass and component mass balances as well as an energy balance similar to the pipe model. Also, the same simplifications for changing compositions and isothermal conditions can be applied. For improved numerical behavior in some situations, simple pressure losses at the ports can be turned on, which depend linearly on the mass flow rate through the port.

Gas Storage

The gas storage plants are represented by a very simple model. Energy for compression and expansion is neglected since it is small compared to the enthalpy of the gas and all other components work isothermal. The gas storage volume itself contains a mass balance for the entire fluid and $n_\mathrm{comp} - 1$ component mass balances.

$$\frac{\mathrm{d}m_\mathrm{CV}}{\mathrm{d}t} = \dot{m}_\mathrm{inlet} + \dot{m}_\mathrm{outlet} \tag{3.73}$$

$$\frac{\mathrm{d}m_{i,\mathrm{CV}}}{\mathrm{d}t} = \dot{m}_{i,\mathrm{inlet}} + \dot{m}_{i,\mathrm{outlet}} \qquad \forall\, i = 1...n_\mathrm{comp} - 1 \tag{3.74}$$

The gas storage plants are controlled so that the pressure of the corresponding node equals the set pressure under the restrictions of the gas storage capacity and maximum injection and withdrawal capacity. The set pressure is composed of two parts: First, a nominal value $p_\mathrm{stor,set,nom}$ which depends on a base pressure value $p_\mathrm{stor,set,base}$, the average

residual gas demand or production in the region over the whole year $\dot{m}_{\mathrm{res,region}}$, and a factor f_{stor}.

$$p_{\mathrm{stor,set,nom}} = p_{\mathrm{stor,set,base}} + \dot{m}_{\mathrm{res,region}} f_{\mathrm{stor}} \tag{3.75}$$

This ensures that the pressure is generally lower in a region with high demand and low production so that the gas automatically flows into that region. The second part is variable and depends on the state of charge of the storage $\mathrm{SOC}_{\mathrm{stor}}$ and a bandwidth Δp_{bw} so that the storage is charged less when it is almost full.

$$p_{\mathrm{stor,set}} = p_{\mathrm{stor,set,nom}} + (\mathrm{SOC}_{\mathrm{stor}} - 0.5)\, \Delta p_{\mathrm{bw}} \tag{3.76}$$

Power Plant

The power plants' power output is limited by a minimum and maximum power and a maximum gradient while turned on. Start-up times are not modeled; it is assumed that the power plants are always prepared for a start-up with perfect foresight. Dynamics are reflected by a first-order block for the internal dynamics and an inertia for the turbine and the generator.

All power plants of the same kind in one region are represented by one model, which behaves like several separate power plant blocks. The efficiency is assumed constant since the part load of one power plant only marginally affects the overall efficiency if all other power plants are operated at nominal load.

Each power plant, including the run-of-river power plants, can provide primary balancing power controlled by a P controller and limited by maximum possible power and maximum power gradient.

Power-to-Gas Plant

The main component of the PtG plant is the electrolyzer which is modeled using first-order dynamics and the efficiency curve as depicted in Figure 3.3.

If SNG shall be produced, the methanation plant is directly operated in parallel with the electrolyzer. The required CO_2 is provided by a DAC plant which is modeled using a constant electric efficiency. As for the quasi-stationary IES model for optimization, it is assumed that the waste heat from the PtG plant can be used here. The DAC plant always separates as much CO_2 as is needed for the methanation at the moment.

The methanation plant is modeled in a simplified way: A P controller feeds as much hydrogen as possible directly into the gas grid without violating the maximum hydrogen fraction. The remaining hydrogen, which is supposed to be transformed into SNG, reacts entirely with the supplied CO_2, and the produced water vapor is separated so that only methane leaves the plant.

Heat Components

The model of the hot water storage is a vertically discretized cylinder with a given number of water ports through which water can be added or taken at specified heights. Water is exchanged between adjacent control volumes depending on buoyancy and heat conduction,

and to the outside, heat losses are modeled using a constant heat loss coefficient. Water properties are used from the TILMedia Library (TLK-Thermo and ift, 2021).

For the solar collector, first, the solar radiation onto a tilted surface has to be determined. Based on that, the heat flow rate transferred to the water in the solar collector is calculated, considering the efficiency, heat capacity and possible soiling of the collector, reflection of the radiation on the ground, and heat losses to the environment. The mass flow rate is controlled using a matched-flow operation, that is, between the minimum and maximum values depending on the outlet temperature.

The gas boiler, electric boiler, electric heating rod, and small-scale CHP plants have constant efficiency, and the electric and gas-fired heat pumps use COP curves depending on the ambient temperature (source of ambient heat) and the set outlet temperature. All heat producers and consumers are ideally controlled to reach a specified outlet temperature.

The large-scale CHP plant is modeled similarly to the power plants but with added heat output depending on and limited by an efficiency field. It is combined with a peak gas boiler to reduce the cost. The CHP plant is operated heat-led, so it provides the heat when demanded. However, a buffer hot water storage is used for large-scale solar collectors.

More details about the modeling and the control of the heating system can be found in Bode et al. (2018) and Bode et al. (2019) (without the utilization of excess power in the heating system).

Electric Components

The power grid components are all quasi-stationary models, which means there is no dynamic implemented in the components but only in the power producers, for example, the rotating mass in a power plant. The transmission line is modeled as a two-port representation with active and reactive power losses. The power transformers have a fixed turn ratio with power losses, and the generator model is a linear model with power losses. The inertia is included in the power plant model, and detailed modeling of currents and voltages is not necessary since voltage stability is not regarded.

The electric energy storage plants are modeled using a maximum power gradient as well as minimum and maximum energy capacities. For A-CAES and pumped hydro storage plants, constant maximum powers and efficiencies are used for charging and discharging. For the lithium-ion battery plants, maximum charging and discharging power, as well as the efficiency depending on the nominal efficiency, are determined using curves from the TransiEnt Library (TUHH, 2021). Self-discharge is accounted for with a percental loss of the current energy capacity.

Superstructure

The model, which represents the regions of Northern Germany, is called superstructure. It contains all renewable energy producers and final energy consumers as well as all conversion technologies, that is, PtG and power plants, and storage technologies, that is, electric energy storage and gas storage plants.

Within the superstructures, no power or gas grid is modeled; the whole grid representation lies outside of the regions. So, all submodels of the superstructure are directly

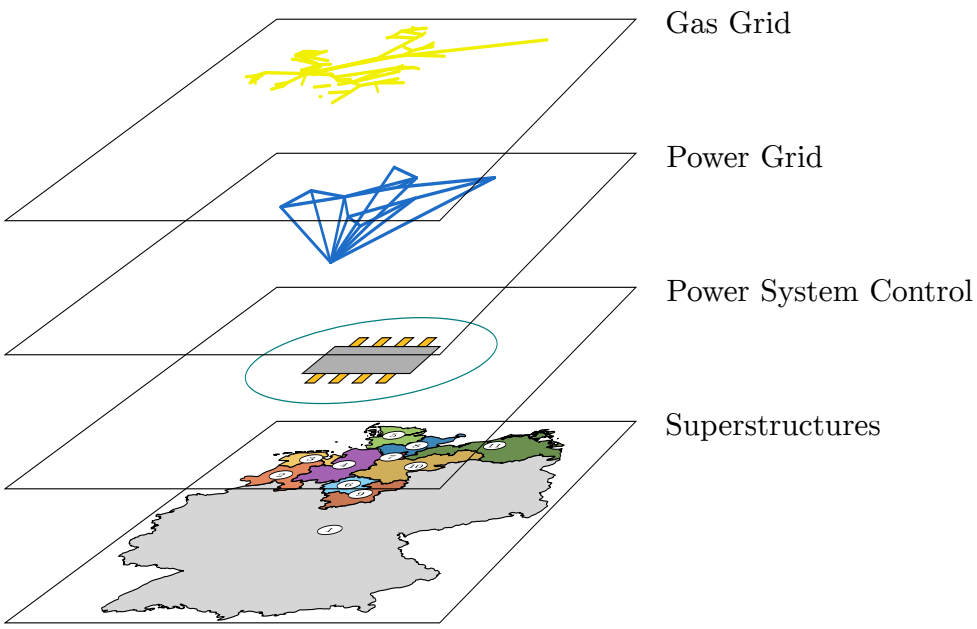

Figure 3.11: The main components of the dynamic integrated energy system model.

connected to the electric or gas interfaces or so-called ports through which the information will be given to other parts of the dynamic IES model. Only for numerical reasons, small pressure losses or short transmission lines are added, which do not significantly influence the results but speed up the simulations.

Power System Control

The power system control decides in which order the residual load is covered by the different technologies. First, it calculates the residual load by comparing current renewable power production and power consumption in each region. Then, the regional residual load is primarily covered following the given merit order of technologies. If it is not possible to match supply and demand in one region due to limited powers or capacities, the residual load is passed to the other regions, also following the merit order of technologies and, within those, the merit order of regions.

To ensure a stable operation of the power grid, also secondary balancing power is provided by all plants. The necessary balancing power is determined using a PI controller based on the deviation of the power grid frequency from its nominal value of 50 Hz. This value is added to the residual load to be supplied by the available plants.

Dynamic IES Model

The dynamic IES model consists of four components: superstructures, power grid, gas grid, and power system control, illustrated in Figure 3.11. Since the aggregation algorithms for the power and gas grid work differently, there are differences between how the regions are connected to the grids. The power grid has one node for each superstructure, so every superstructure is connected to one power grid node, whereas the gas grid is more detailed, so each superstructure is linked to several nodes.

That is why each Northern German superstructure has five different gas ports, one each for power plants, PtG plants, gas storage plants, local demand, and biomethane or hydrogen from biomass. Since each region contains demand, production, and storage of several nodes, those aggregated mass flows must be matched to the gas grid nodes. So, each category's total gas flow must be split according to the share of gas grid node utilization. This is done by connecting each of those ports to the gas grid ports with a fixed share based on the yearly share of gas flow through that connection in the quasi-stationary computations.

Since there is no detailed information on how Northern Germany is connected to the rest of Germany, the superstructure in the south has just one gas port combining all gas flows. From the gas grid to the superstructures, the pressures are given with the same shares.

3.1.6 Key Figures for System Evaluation

In this section, the key figures are described, which will be used in Chapter 4 to evaluate and compare the results of the different models. First, the key figures concerning the gas grid will be described and, second, the figures for the power grid.

Gas Grid

The aggregation grade G shows how much of the gas grid has been eliminated by aggregation. That is why the number of remaining pipes $n_{\mathrm{P,rem}}$ and nodes $n_{\mathrm{N,rem}}$ is compared to the numbers before aggregation $n_{\mathrm{P,nonagg}}$ and $n_{\mathrm{N,nonagg}}$.

$$G = 1 - \frac{n_{\mathrm{P,rem}} + n_{\mathrm{N,rem}}}{n_{\mathrm{P,nonagg}} + n_{\mathrm{N,nonagg}}} \tag{3.77}$$

To compare the quasi-stationary and dynamic gas grid model as well as the different steps of aggregation, the mean error $e_{\mathrm{m},p,i}$ and the standard deviation $\sigma_{p,i}$ (MathWorks Inc., 2021a) of the pressure values are calculated for each node i. The indices 1 and 2 represent the two simulations that are compared, and n_{step} is the number of equidistant time steps calculated by the quasi-stationary gas grid model.

$$e_{\mathrm{m},p,i} = \frac{1}{n_{\mathrm{step}}} \sum_{j=1}^{n_{\mathrm{step}}} \left(p_{i,j,1} - p_{i,j,2}\right) \tag{3.78}$$

$$\sigma_{p,i} = \sqrt{\frac{1}{n_{\mathrm{step}} - 1} \sum_{j=1}^{n_{\mathrm{step}}} \left| \left(p_{i,j,1} - p_{i,j,2}\right) - e_{\mathrm{m},p,i} \right|} \tag{3.79}$$

During aggregation, the pipe length changes according to the aggregation algorithm. Since the algorithm aims to reduce the error in pressure and mass flow rate in the gas grid, it might result in very large or small values that do not reflect the actual distance of the pipe's inlet and outlet. To use the pipe length for further calculations, even after aggregation, an equivalent length $l_{\mathrm{eq},i}$ is calculated for each pipe i based on the pipe's mass flow rate capacity, which is well-contained by the aggregation algorithm.

$$V_{\mathrm{P},i} = \frac{\pi}{4} D_{\mathrm{P},i}^2 l_{\mathrm{P},i} \tag{3.80}$$

$$D_{\mathrm{eq},i} = \sqrt{\frac{4C_i}{\pi \rho \left(p_{\mathrm{MOP},i}\right) w_{\max}}} \tag{3.81}$$

$$l_{\mathrm{eq},i} = \frac{4V_{\mathrm{P},i}}{\pi D_{\mathrm{eq},i}^2} \tag{3.82}$$

In the following equations, $l_{\mathrm{eq},i}$ will be used instead of $l_{\mathrm{P},i}$ for aggregated gas grids.

The gas grid capacity $\Gamma_{\mathrm{gas,grid}}$ shows how large the gas grid is and which amount of gas could be transported using all n_{P} pipes. It is defined as energetic capacity related to NCV times pipeline length.

$$\Gamma_{\mathrm{gas,grid}} = \sum_{i=1}^{n_{\mathrm{P}}} C_i H_{\mathrm{i,n}} l_{\mathrm{P},i} \tag{3.83}$$

The utilized pipe capacity $u_{\mathrm{P},i}$ for each pipe i is a dimensionless value that reflects how much of the pipe's capacity is used.

$$u_{\mathrm{P},i} = \frac{|\dot{m}_i|}{C_i} \tag{3.84}$$

Comparing the actually transported gas flow times length to the gas grid capacity results in the utilized gas grid capacity $u_{\mathrm{grid,gas}}$.

$$u_{\mathrm{grid,gas}} = \frac{\sum_{i=1}^{n_{\mathrm{P}}} |\dot{m}_i| \, H_{\mathrm{i,n}} l_{\mathrm{P},i}}{\Gamma_{\mathrm{gas,grid}}} \tag{3.85}$$

The required gas grid extension $\Gamma_{\mathrm{gas,grid,ext}}$, which is needed to keep a working gas grid, is determined by first calculating the required extension of each pipeline $\Gamma_{\mathrm{gas,P,ext}}$. This is done by comparing the maximum mass flow rate to the mass flow rate capacity. If it exceeds the mass flow rate capacity, gas grid extension is necessary.

$$\Gamma_{\mathrm{gas,P,ext},i} = \begin{cases} \left(\dot{m}_{\max,i} - C_i\right) H_{\mathrm{i,n}} l_{\mathrm{P},i} & \text{if } \dot{m}_{\max,i} > C_i \\ 0 & \text{if } \dot{m}_{\max,i} \leq C_i \end{cases} \tag{3.86}$$

$$\Gamma_{\mathrm{gas,grid,ext}} = \sum_{i=1}^{n_{\mathrm{P}}} \Gamma_{\mathrm{gas,P,ext},i} \tag{3.87}$$

Power Grid

The nominal electric power $P_{\mathrm{el,nom,tl},i}$ of a transmission line i is calculated using the maximum possible current $I_{\mathrm{max,tl},i}$ and nominal voltage $U_{\mathrm{nom,tl},i}$ of the transmission line assuming zero phase angle (Heuck et al., 2013).

$$P_{\mathrm{el,nom,tl},i} = \sqrt{3} U_{\mathrm{nom,tl},i} I_{\mathrm{max,tl},i} \tag{3.88}$$

The power grid capacity $\Gamma_{\text{power,grid}}$ of a power grid containing n_{tl} transmission lines is defined analogously to $\Gamma_{\text{gas,grid}}$ with the length $l_{\text{tl},i}$ of each transmission line.

$$\Gamma_{\text{power,grid}} = \sum_{i=1}^{n_{\text{tl}}} P_{\text{el,nom,tl},i} l_{\text{tl},i} \tag{3.89}$$

Furthermore, also the required power grid extension $\Gamma_{\text{power,grid,ext}}$ is defined similarly. The maximum occurring power in the year in each transmission line i is compared to its nominal value and if it exceeds it, power grid extension is required.

$$\Gamma_{\text{power,tl,ext},i} = \begin{cases} \left(P_{\text{el,max,tl},i} - P_{\text{el,nom,tl},i}\right) l_{\text{tl},i} & \text{if } P_{\text{el,max,tl},i} > P_{\text{el,nom,tl},i} \\ 0 & \text{if } P_{\text{el,max,tl},i} \leq P_{\text{el,nom,tl},i} \end{cases} \tag{3.90}$$

$$\Gamma_{\text{power,grid,ext}} = \sum_{i=1}^{n_{\text{tl}}} \Gamma_{\text{power,tl,ext},i} \tag{3.91}$$

3.2 Simulation Setups and Data

In this section, the scenario information and data for all models is presented: The scenarios, which are simulated using the dynamic IES model, are defined in Section 3.2.1. Afterward, the energy supply and demand data is described. It contains information about renewable energy generation, biogas potential, and natural gas import, see Section 3.2.2, as well as power, heat, and gas demand, see Section 3.2.3. The gas and power grid data is presented in Sections 3.2.4 and 3.2.6 before specific data for each of the models (quasi-stationary IES model for optimization, quasi-stationary and dynamic gas grid model as well as dynamic IES model) is described in Sections 3.2.7-3.2.9.

3.2.1 Scenario Definition

For the scenarios, three different shares of renewable primary energy input are set for the considered system: 60 %, 80 %, and 100 %. Based on the German government's goals (BMWi, 2018), this approximately correlates with the years 2040, 2045, and 2050 since the transportation sector is neglected and its defossilization is assumed especially complex. That is why the shares of renewables are higher for the considered system than the German government's goals.

Since it is unclear if rather SNG or hydrogen will dominate the gas transport in the future, both options are compared. The scenarios are referred to as 60 % RE H2, 60 % RE SNG, 80 % RE H2, and so on.

Additional to the years and renewable shares, also the heating technologies are varied. Based on the optimization results, different variations towards higher use of either gas or power for heating are investigated.

3.2.2 Energy Supply

In this section, the energy supply data for the three sectors in Germany is presented, which is used for the quasi-stationary IES model for optimization and the dynamic IES model. For the simulations, it is not only crucial to have a timely resolution but also

a spatial one. For the latter, the NUTS 3 regions of Germany as of the end of 2015 (Regionalstatistik, 2021a) are chosen.

Renewable Power Production

In the power sector, the only exogenous energy input is renewable power production. Onshore and offshore wind turbines, as well as photovoltaics and run-of-river plants, are considered, and their power production has been modeled by Schülting (2021): The technologies are modeled for each local administrative unit (LAU, Gemeinde) and can be aggregated into the respective NUTS 3 regions afterward. The base for the model is weather data from the German weather service for the year 2015 (Baldauf et al., 2014) and assumed nominal power expansion paths for each technology, taking into account the current development and local potential. Power production from each technology is calculated using characteristic curves.

The resulting local power production curves are used except for run-of-river plants to account for time-varying production. The constant production profile is exchanged for the curve from Ziems et al. (2012), which is scaled for full load hours from 50Hertz et al. (2017) and technical potential from Henning et al. (2015).

Solar Radiation for the Heat Sector

As an input to the heat sector, solar radiation is modeled using weather data of the year 2015 from Baldauf et al. (2014). Direct normal and horizontal irradiance curves for each LAU are weighted by each LAU's respective heat demand in 2050 to obtain a representative value for Germany to be used in the dynamic model of the heating system.

In this model, the solar collector area is chosen so that the assumed potential is reached. It is derived for the considered years by linearly interpolating between the actually produced energy of 8.9 $\mathrm{TWh_{th}}$ in 2018 (Umweltbundesamt, 2020) and an estimation for a system with 100 % renewable energies. The latter is based on the study by Henning et al. (2015), who optimized the energy system for renewable shares of 80 % to 90 %, which resulted in the use of approximately 50 $\mathrm{TWh_{th}}$ of solar thermal energy in households and commerce, trade, and services on average over all scenarios and 25 $\mathrm{TWh_{th}}$ in the industry. Since Bürger et al. (2016) describe the value for the industry already as the maximum potential, the first value is roughly scaled to 100 % of renewables which leads to an overall solar thermal energy of 85 $\mathrm{TWh_{th}}$.

Natural Gas

Natural gas entering the German gas grid is either produced within Germany or imported from other countries. Also, Germany plays a significant role in Europe as a transit country, so large amounts of gas just pass through the country.

For the considered years, German indigenous production of natural gas is assumed to have reduced to zero since linearly extrapolating the projection of FNB Gas (2019) leads to the end of production in 2038.

In the current gas network development plan (FNB Gas, 2019), LNG (Liquefied Natural Gas) terminals are planned to be built, but due to their uncertain development regarding the climate goals, LNG imports are neglected. For the import and export of natural gas

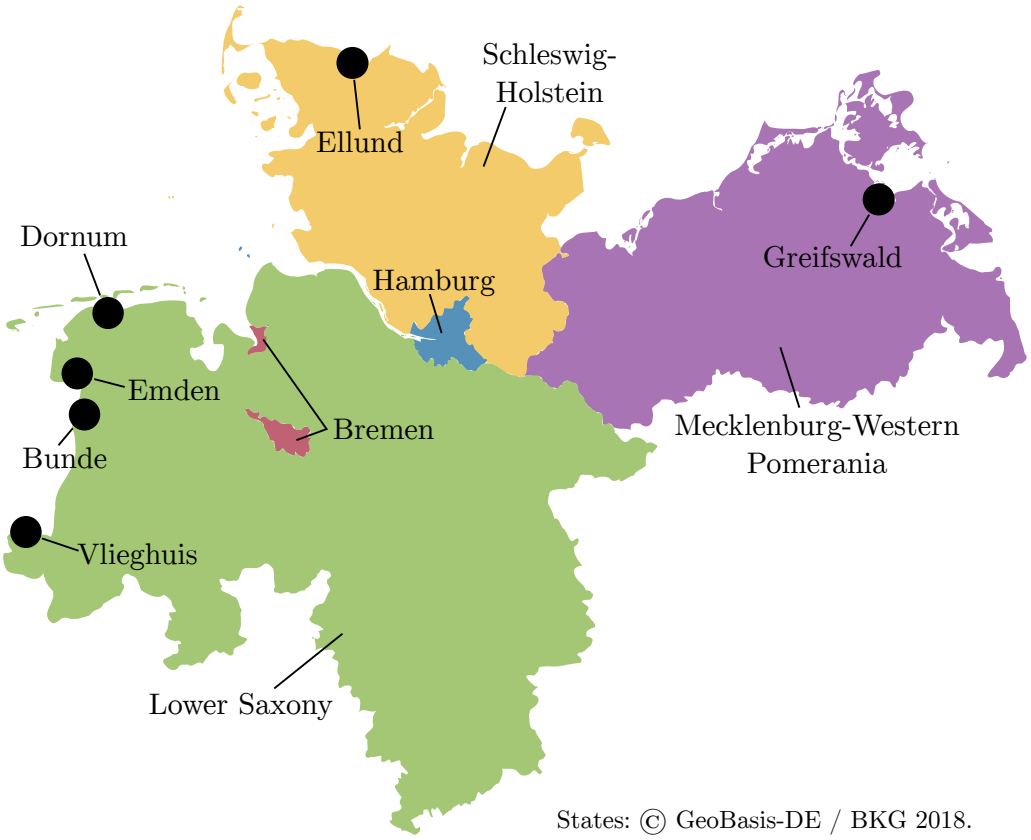

Figure 3.12: Map showing the federal states and all import and export nodes in Northern Germany (ENTSOG, 2014).

through pipelines, Northern Germany currently has cross-border interconnection points with the following countries: Netherlands (Bunde, Vlieghuis), Norway (Emden, Dornum), Denmark (Ellund), and Russia (Greifswald) (ENTSOG, 2014). The points are shown on a map of Northern Germany in Figure 3.12. Natural gas is constantly imported from Russia and Norway and imported from or exported to the Netherlands and Denmark. The node Vlieghuis is neglected since the gas flow is very small compared to the other nodes (ENTSOG, 2014). The future natural gas import and export for each point is derived by linearly extrapolating the Ten Year Network Development Plan (ENTSOG and ENTSO-E, 2018) until 2050.

Assuming the Minimum Scenario, that is, minimum exports in line with the climate goals, Norwegian exports will decline by more than 84 % until 2050 compared to 2018. A share of those exports is imported to Germany. Since the gas arrives at the different points, Emden and Dornum, the developments at each point have to be considered by investigating the change in transferred gas in the last years. From 2015 to 2018, the yearly imported gas amounts through the point Emden have reduced by more than 65 %, whereas the yearly import through Dornum stayed almost constant (ENTSOG, 2014). So, it is assumed that in the considered future years, Emden will not be used anymore and all the gas from Norway will be imported through Dornum.

In contrast, Russian exports are projected to only drop by 32 % until 2030 compared to 2018 and stay constant afterward. Since this is not in accordance with the climate goals,

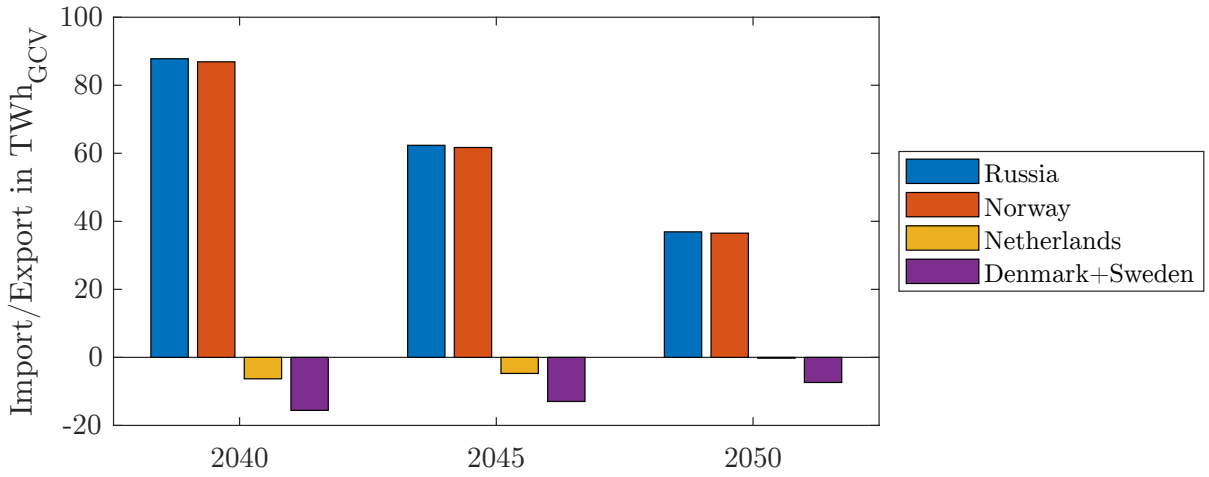

Figure 3.13: Projected import to (positive) or export from (negative) Northern Germany in the considered years.

the same import reduction as for Norway is assumed. For the imports from Russia, only the node Greifswald and the gas flow through the NEL are considered. There also exists the OPAL and the EUGAL (in construction), which transport the gas directly south, but there is no connection to Northern Germany (FNB Gas, 2019).

Denmark only has cross-border interconnection points with Germany and Sweden, and Sweden is only connected to Denmark (ENTSOG, 2014). Neglecting LNG imports and possible future connections to other countries, it is assumed that Denmark and Sweden import the entire missing natural gas from Germany. The same is assumed for the Netherlands since the two countries are closely connected in terms of natural gas. There are also connections between the Netherlands and Belgium, but they are neglected due to the uncertain development of demand and production in all connected countries.

In the next step, the residual gas demand has to be determined for Denmark, Sweden, and the Netherlands by extrapolating demand as well as indigenous, biogas, and PtG production of each country according to the scenario Global Climate Action in ENTSOG (2018a) and ENTSOG (2018b). Production and demand are then balanced and the residual demand is calculated.

In Figure 3.13, the imports and exports to or from Northern Germany are listed for the considered years. It is apparent that the sum of imports and exports in 2050 is not zero, so Northern Germany still imports natural gas. However, all of it will be exported, most of it in the south of Germany to other neighboring countries. In contrast, in 2040 and 2045, the natural gas import to Northern Germany is not sufficient for entire Germany, so more natural gas will be imported directly to the rest of Germany. One option is Greifswald and the pipelines OPAL and EUGAL, as mentioned above.

The curves of the imports and exports over a year are assumed constant, as is approximately the case for the import from Russia and Norway nowadays (ENTSOG, 2014), so each receiving country will have to take care of storing the gas appropriately.

Biogas

The amount of biogas used in the IES is determined by the optimization but limited by its potential. For the spatially resolved simulations, a biogas potential for each NUTS 3 region is required, but there is no open data available. Beil et al. (2019) consider a lot of different substrates which can be fermented in a biogas plant and determine their potential, including a projection until 2030: animal manure, energy crops, grassland, bio-waste container, garden and park waste, organic share in municipal waste, and more. The data for the remaining categories is mostly proprietary, and the majority of biogas potentials are small, so they are not considered in the following. For the other categories, the methodology of Beil et al. (2019) is adapted and combined with open data, which was more detailed in some cases. Since there is always at least one data set missing to completely follow the methodology of Beil et al. (2019) for the first three categories, the total values are scaled to the given biogas potentials. The values are projected until 2030, as done by Beil et al. (2019), and no further extrapolation is made due to the uncertain development. So, the biogas potential of 2030 is also used for the years 2040 to 2050.

Animal Manure For the generation of animal manure, cattle, pigs, and poultry are considered. The numbers of cattle and pigs for each NUTS 3 region in 2016 are taken from Regionalstatistik (2021g), but the numbers for poultry are not available for each NUTS 3 region but only for each federal state in 2016 (DESTATIS, 2021b). It is assumed that they correlate with the numbers of cattle and pigs, so the number of poultry per state is split into NUTS 3 regions with the same share per state as cattle and pigs. The total amount of manure is calculated using the specific values from SMEKUL (2021).

The projection is conducted by determining the average change rate for each animal in each state from 2001 to 2016 using DESTATIS (2021b) and linearly extrapolating the livestock until 2030. If a value falls below zero, it is set to zero for the following years. It is assumed that the biogas yield from each kind of animal manure is the same. The last step is scaling the total values to the given value from Beil et al. (2019) to obtain the same total biogas potential for Germany in 2030 of 38.1 $\mathrm{TWh_{GCV}}$, see Figure 3.14.

Energy Crops First, the complete harvest of all types of wheat, sugar beet, and silage maize is calculated by multiplying the arable land per NUTS 3 region in 2016 from Regionalstatistik (2021f) with the average specific harvest between 2013 and 2017 per NUTS 3 region from Regionalstatistik (2021h). The split between winter and spring barley is done using data for the federal states in 2016 from DESTATIS (2021a).

Second, each plant's harvest is multiplied with the respective specific biogas yield from Bundesrepublik Deutschland (2012). To determine how much of the energy crops can actually be used for biogas production in the future, the potentials of energy crops for each federal state from Majer et al. (2013) (Basis-U-Szenario) are used. It is assumed that the development for each NUTS 3 region is the same as for the corresponding federal state, and the total value for Germany is scaled to the value of 135.8 $\mathrm{TWh_{GCV}}$ given by Beil et al. (2019) for 2030. The spatial distribution is shown in Figure 3.15.

Grassland The biogas potential from grassland is determined similarly to the biogas potential from energy crops. First, each NUTS 3 region's permanent grassland areas in

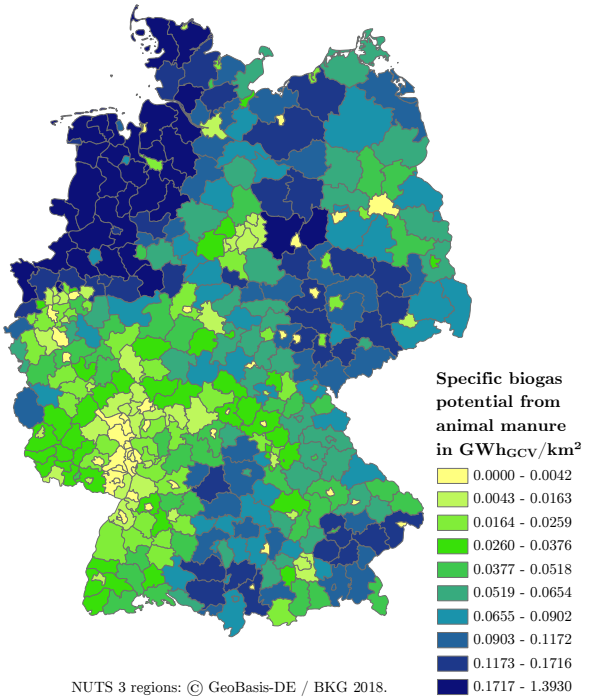

Figure 3.14: Specific biogas potential from animal manure in 2030.

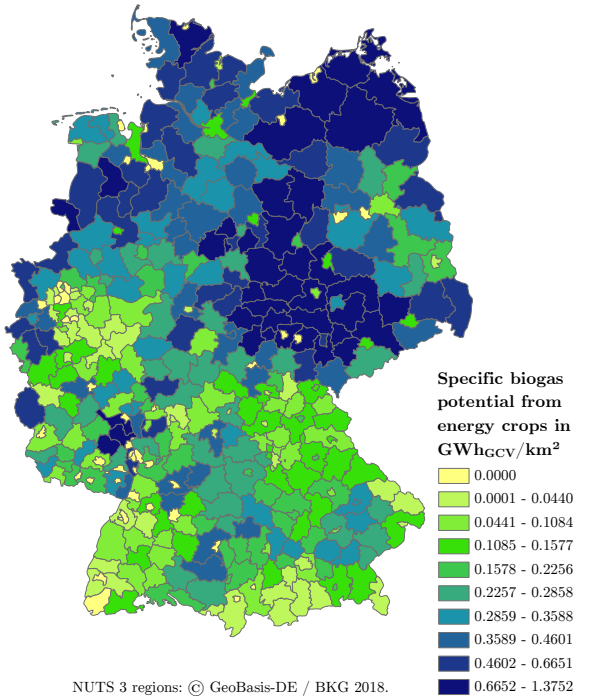

Figure 3.15: Specific biogas potential from energy crops in 2030.

2016 are taken from Regionalstatistik (2021e) and projected using the grassland potentials for each federal state from Majer et al. (2013). Negative values are set to zero, and the total value is scaled to the value of Beil et al. (2019) for Germany in 2030 (108.0 TWh$_{GCV}$), see Figure 3.16.

Bio-Waste Container The total amount of bio-waste collected in bio-waste containers in each NUTS 3 region in 2015 is listed in Regionalstatistik (2021c). It is converted to the total biogas potential by multiplying it with the yield and gross calorific value given by Beil et al. (2019), which results in 3.7 TWh$_{GCV}$.

To project this biogas potential until 2030, first, the total expected amount of bio-waste in Germany is linearly extrapolated using data for Germany from 2013 to 2017 (Regionalstatistik, 2021c). According to that, bio-waste availability rises from 4.57 Mt in 2015 to 6.86 Mt in 2030.

Second, the amount of bio-waste per inhabitant is calculated using population data for each NUTS 3 region in 2015 from Regionalstatistik (2021b). Third, the local development of bio-waste generation in each NUTS 3 region has to be determined. Thus, it is assumed that regions with a high bio-waste generation per capita stay like that since the inhabitants already have access to bio-waste containers and separate the garbage well. In contrast, regions with low specific values might not even have access to bio-waste containers but might get access in the near future. To account for that development, a minimum specific bio-waste generation is searched iteratively, which is set for all regions with lower bio-waste amounts so that the total bio-waste availability for Germany is reached. This leads to a value of 71.5 kg/a per inhabitant. Multiplied with the specific biogas yield and the gross calorific value from Beil et al. (2019), this results in 5.6 TWh$_{GCV}$. A map of Germany with the biogas potential from bio-waste is shown in Figure 3.17.

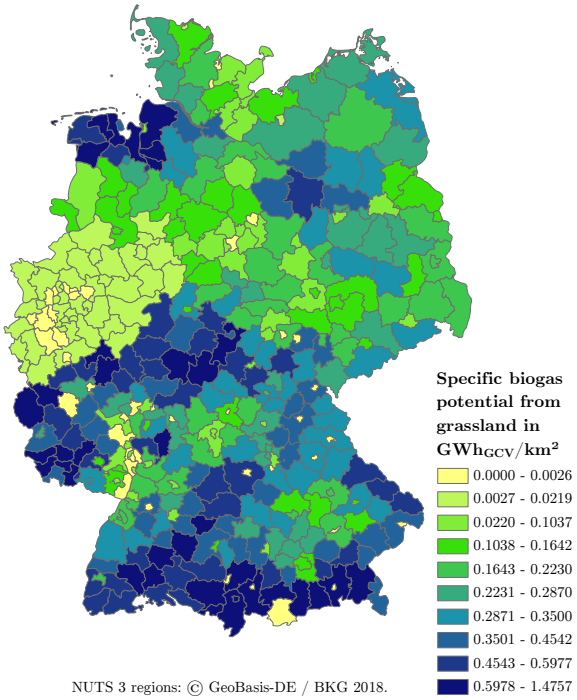

Figure 3.16: Specific biogas potential from grassland in 2030.

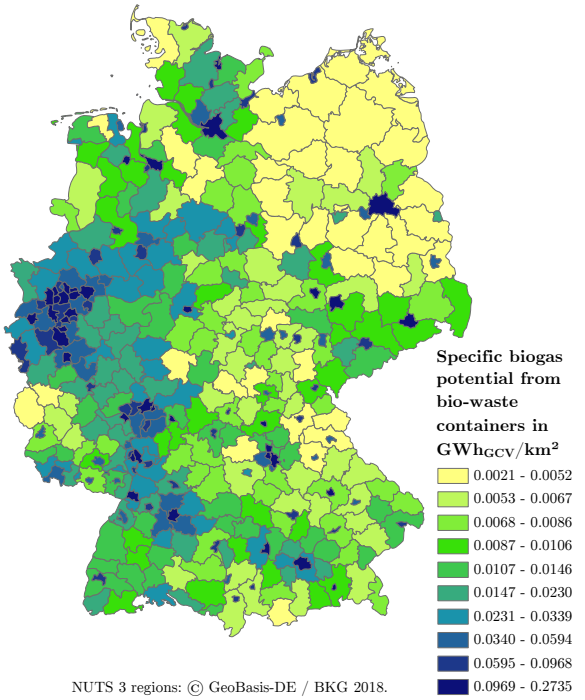

Figure 3.17: Specific biogas potential from bio-waste containers in 2030.

Garden and Park Waste The determination of the biogas potential from garden and park waste is conducted similarly to the biogas potential from bio-waste: The total amount of garden and park waste was 5.10 Mt in 2015 (Regionalstatistik, 2021c) and is projected to be 7.53 Mt in 2030, which results in 2.4 TWh_{GCV} biogas in 2015 and 3.6 TWh_{GCV} in 2030 with a minimum waste generation of 78.3 kg/a per capita.

Additionally, roadside vegetation is also considered: First, the length of all streets in each federal state as of January 1, 2016 (DESTATIS, 2021c) is combined with the mowed areas next to the streets, the amount of grass per m^2, the biogas yield and gross calorific values from Beil et al. (2019). This leads to a biogas yield of 0.4 TWh_{GCV}, which is assumed constant over the years since the total street length does not vary significantly over the years. The amount of biogas potential per state is then disaggregated to the NUTS 3 regions using the traffic areas from Regionalstatistik (2021d).

The total biogas potential from garden and park waste is illustrated in Figure 3.18.

Organic Share in Municipal Waste First, the amount of municipal waste in each NUTS 3 region has to be determined. Regionalstatistik (2021c) gives values for each NUTS 3 region in 2015 for municipal and bulky waste together. That is why the values are scaled so that the sum equals the value for municipal waste from Beil et al. (2019), assuming that the ratio of municipal to bulky waste is the same in each region.

Second, the organic fraction in the municipal waste is calculated based on the shares given by Beil et al. (2019) depending on the type of region, that is, if it is a city, and if there are bio-waste containers available. The total producible biogas from that organic fraction is determined using the yield and gross calorific value from Beil et al. (2019) which results in 3.6 TWh_{GCV}.

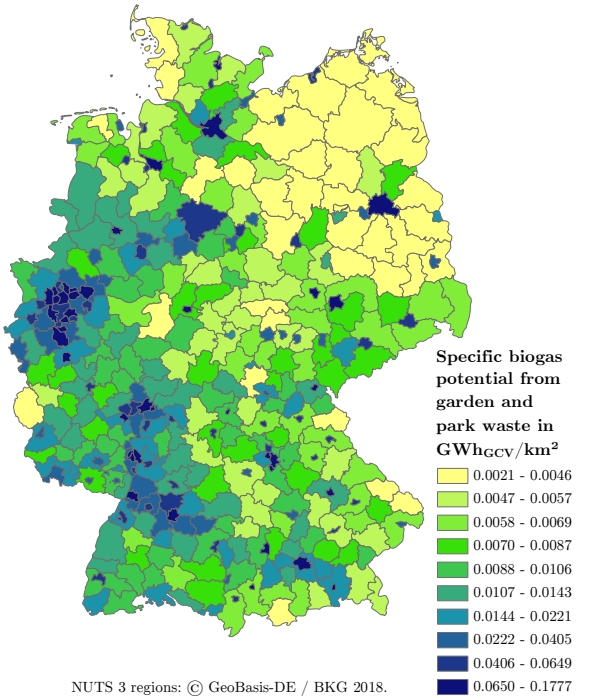

Figure 3.18: Specific biogas potential from garden and park waste in 2030.

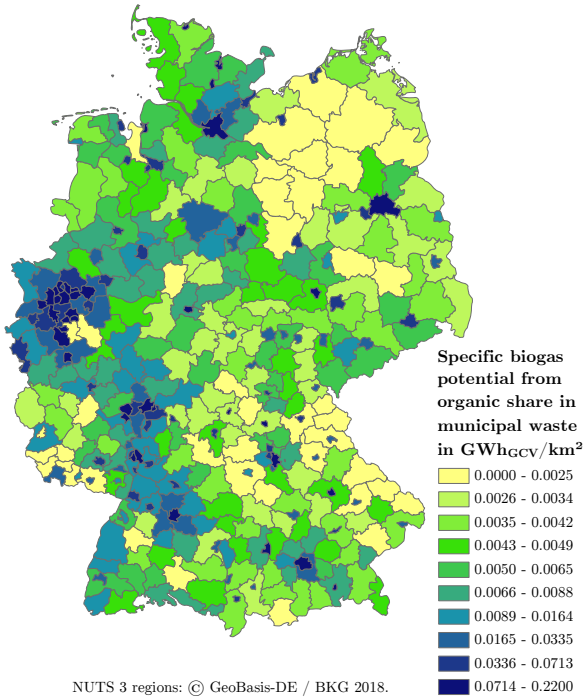

Figure 3.19: Specific biogas potential from organic share of municipal waste in 2030.

In the last step, the value is projected until 2030 by projecting the amount of municipal waste to the value from Beil et al. (2019) and assuming that every NUTS 3 region has access to a bio-waste container until then. This leads to a total value of 3.2 TWh_{GCV}, and a map is shown in Figure 3.19.

Summary The projected biogas potential sums up to a value of 294.7 TWh_{GCV}, but by far the largest share of 83 % is based on energy crops and grassland for which the land competes with food production. That is why only 50 % of the respective biogas potentials are considered for the optimization, which results in a biogas potential of 172.8 TWh_{GCV}. A map with the assumed total biogas potential in 2030 is shown in Figure 3.20, and Table A.7 in the appendix lists the biogas potential of every category for each NUTS 3 region.

3.2.3 Energy Demand

The energy demands of the three sectors power, heat, and gas are represented by their respective final energy demands. Different energy applications from BMWi (2019) are matched with the sectors by determining that, for example, mechanical energy should be generated using electricity in the future since most of the renewable energies produce electricity, so it is the most efficient. For the share of process heat, which is already supplied by electricity nowadays, it is assumed that it remains like that. However, for the share of process heat produced using oil, gas, coal, or others nowadays, it is unclear if it is possible to substitute those energy carriers with electricity due to the required

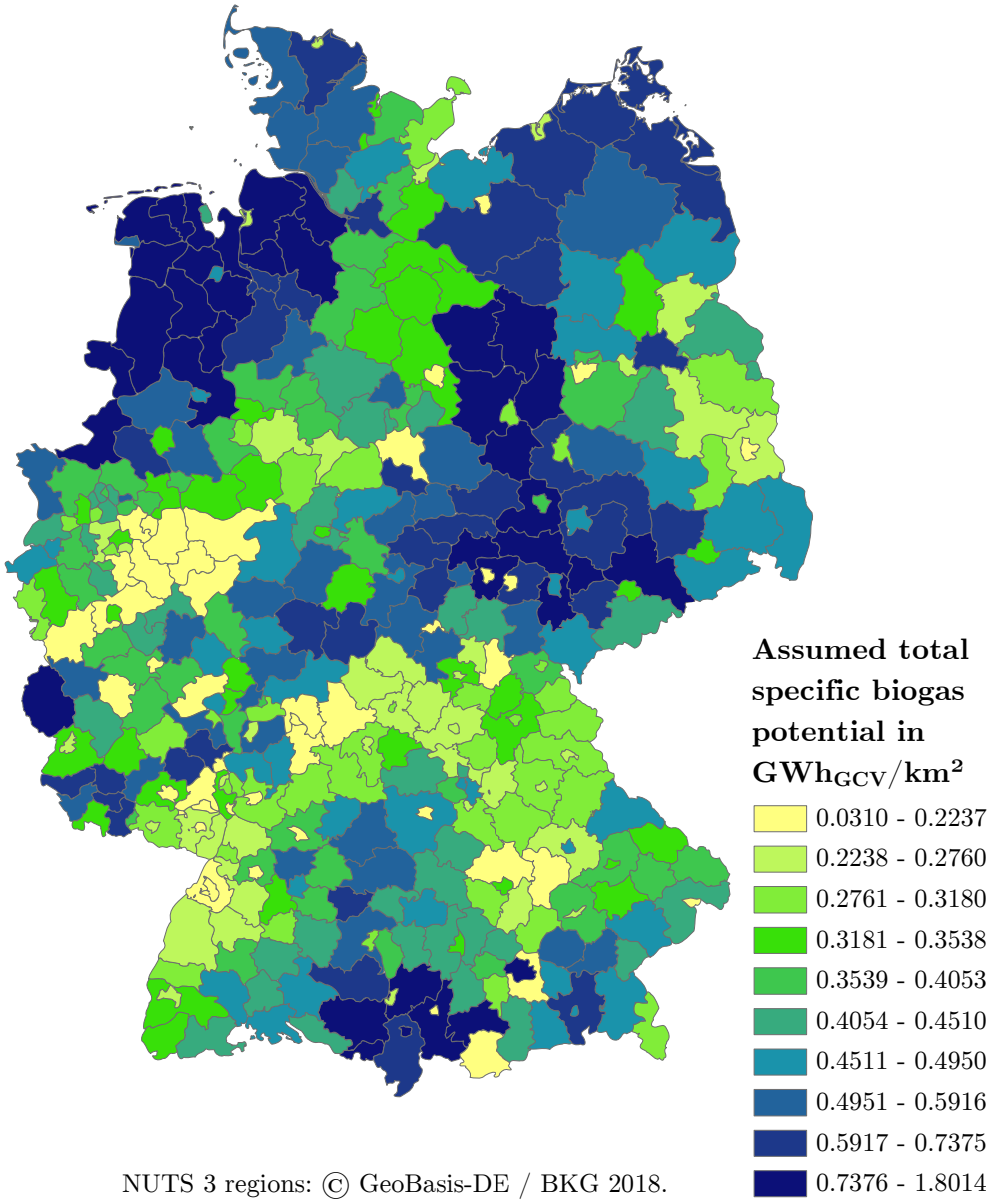

Figure 3.20: Assumed total specific biogas potential in 2030 with 50 % of the biogas potential from energy crops and grassland.

temperature level. That is why that process heat is split into fixed shares of each 50 % electricity and gas. The matched applications and energy sectors are listed below.

- Power: air-conditioning, other cooling energy, mechanical energy, information and communication technology, lighting, process heat (electricity), share of process heat (oil, gas, coal, others)
- Heat: space heating, hot water, process heat (district heating, renewables)
- Gas: non-energetic demand, share of process heat (oil, gas, coal, others)

The calculation of the yearly power, process heat and gas demand of the base year 2015 is based on the data from BMWi (2019) in combination with assumed efficiencies of 35 %

for oil or gas to power and 95 % for oil, gas, district heating, coal, renewables or others to heat since the values of the original energy carrier have to be converted to the final energy.

In the next step, the power and gas demand are projected into the future, using change rates for each use of energy for the trend scenario of Schlesinger et al. (2014). The yearly heat demand is determined using a more complex model, which is described below as well as the determination of the curves for each sector.

Electricity

A very detailed description of the modeling of the electricity demand curves can be found in Schülting (2021); only a short description is given here.

First, the temperature-dependent share of power consumption is filtered from the German power consumption curve since it results from space heating which is already included in the heat demand curve. Second, this overall German final power demand curve is synthesized using standard load profiles, and with those, load profiles for each consumer group are assembled. Combining those load profiles with certain statistical values, for example, power consumption per inhabitant or employee in an economic branch, leads to power demand curves for each LAU, which are aggregated to the respective NUTS 3 regions.

Since a specific share of process heat is supposed to be supplied by electricity in the future, that share is added to the profile. The description of how that process heat demand curve is determined can be found below.

Heat

The heat demand curves used here were developed by Zimmermann et al. (2020). An updated version is published in Zimmermann (2021). The heat demand of households is modeled bottom-up with a complex building model that goes through different transformation steps, such as renovation, depending on the age of the buildings and other factors. For the sectors commerce, trade and services, and industry, a top-down approach is used, based on heat demands for Germany, which are disaggregated depending on the numbers of employees in different branches of the economy. To eliminate the effect of different weather conditions in different parts of Germany, the space heating demand in all sectors is corrected with the degree day number. Based on those yearly demands, the curves are created using standard load profiles combined with constant loads.

Gas

The final gas demand consists of a share of the high-temperature process heat demand described above and the non-energetic utilization of gas which is modeled using data from the project DemandRegio (Gotzens et al., 2020).

The code and data of Gotzens et al. (2020) are utilized to determine the total gas demand in the industry: The weather data from 2015 is used for consistency with the power and heat data, and 2035 is picked as the target year since it is the most future year in the study and a further extrapolation is too uncertain. First, the spatially and temporally distributed gas demand for each industrial sector is calculated, which is projected until

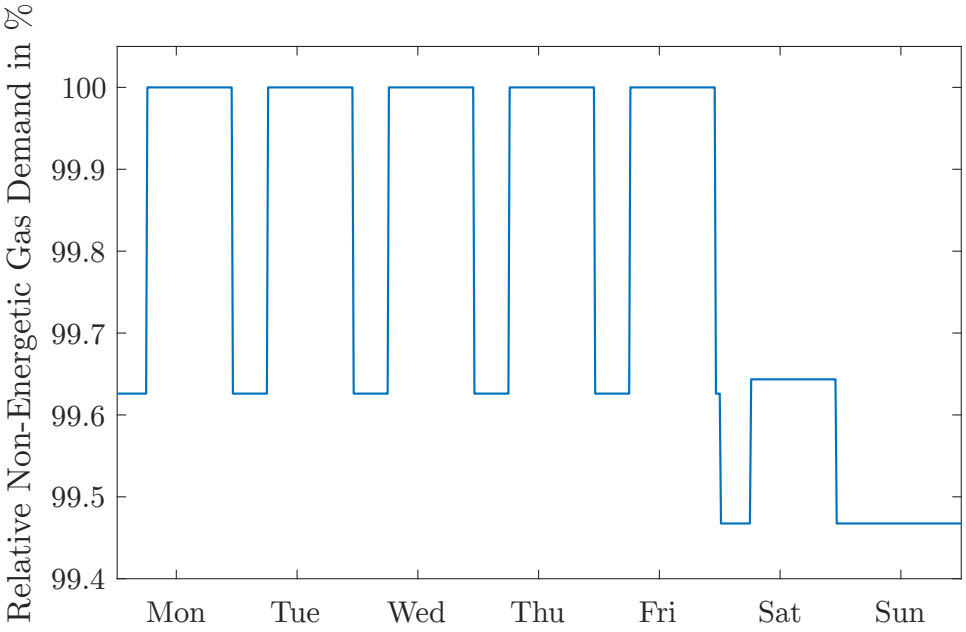

Figure 3.21: Relative curve of the German non-energetic gas demand over a week in 2035.

2035 according to forecasted numbers of employees for each industrial branch. Since there are no well-established standard load profiles for the industry, its gas consumption is modeled using different shift types (one, two, or three shifts per day) and week types (five, six, or seven-day week) which are assigned to each industrial sector.

Based on that, the non-energetic gas demand in each NUTS 3 region can be determined by using the shares of non-energetic gas demand for each industrial sector given by Gotzens et al. (2020). Because most of the processes considered here are almost continuous processes, the non-energetic gas demand only fluctuates by less than 1 % due to the different weekdays and the different shifts, see Figure 3.21.

3.2.4 Gas Grid Data

The gas grid data used here is based on the digital map from Verlag Glückauf GmbH et al. (2010) and cannot be shown in its raw form due to the limitations of the license. For different reasons, the data cannot be used directly for the simulations but has to undergo mostly manual pre-processing first: The data only includes an MOP value for 29 % of the pipes or 40 % of all pipe kilometers, the map was updated for the last time in 2010, and there have been some mistakes which were found by the gas grid computation, for example, wrong diameters in certain pipes (one large pipeline with one small diameter segment).

In a first step, MOP values are added manually for all pipes by investigating the surrounding gas grid and taking values from surrounding pipes with the same operator or diameter or based on detailed gas grid maps from operators. Afterward, the gas grid development plans from 2012 on have been searched for relevant gas grid extensions, which were then added to the gas grid (NEL (FNB Gas, 2013), DEUDAN (FNB Gas, 2015),

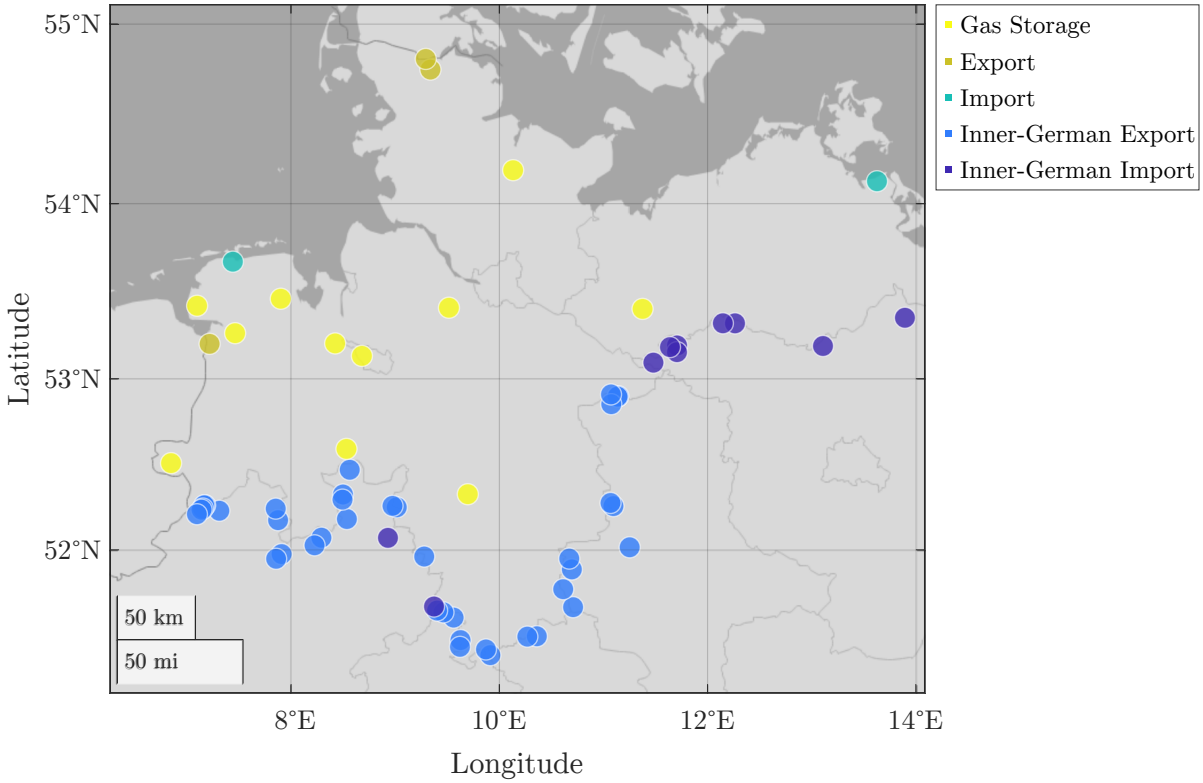

Figure 3.22: Locations of special nodes in the Northern German gas grid.

NOWAL (FNB Gas, 2017)). Like this, new and large pipelines are included in the gas grid data, but smaller projects are neglected since there is no publicly available data.

In the gas grid computation in Section 3.1.2, certain nodes have special functions in the grid, namely storage, import, export, and inner-German import and export nodes. Figure 3.22 shows all those nodes on a map. In comparison to Figure 3.12, the import and export nodes Emden and Vlieghuis are eliminated since it is assumed that they will not be used in the future, as described in Section 3.2.2. The storage plants are mapped on the gas grid structure, so some nodes are moved or combined. Also visible are the locations of the inner-German import nodes, which are primarily located in Mecklenburg-Western Pomerania but in Lower Saxony as well.

3.2.5 Gas Storage Data

The storage data is combined from two sources, EID Energie Informationsdienst GmbH (2019) and gie (2018). The first contains detailed information about all gas storage plants in Germany and only storage and maximum withdrawal but no maximum injection capacities. The second source contains working gas volumes as well as maximum injection and withdrawal capacities but some storage plants are clustered together depending on the operators. That is why both sources are combined: The data from gie (2018) is used to create a correlation between injection and withdrawal capacity, which is shown in Figure 3.23. A linear regression analysis shows that, on average, the injection capacity is 59.77 % of the withdrawal capacity, with an R-square value of 0.8848.

All values are then converted to masses and mass flow rates, respectively, based on the

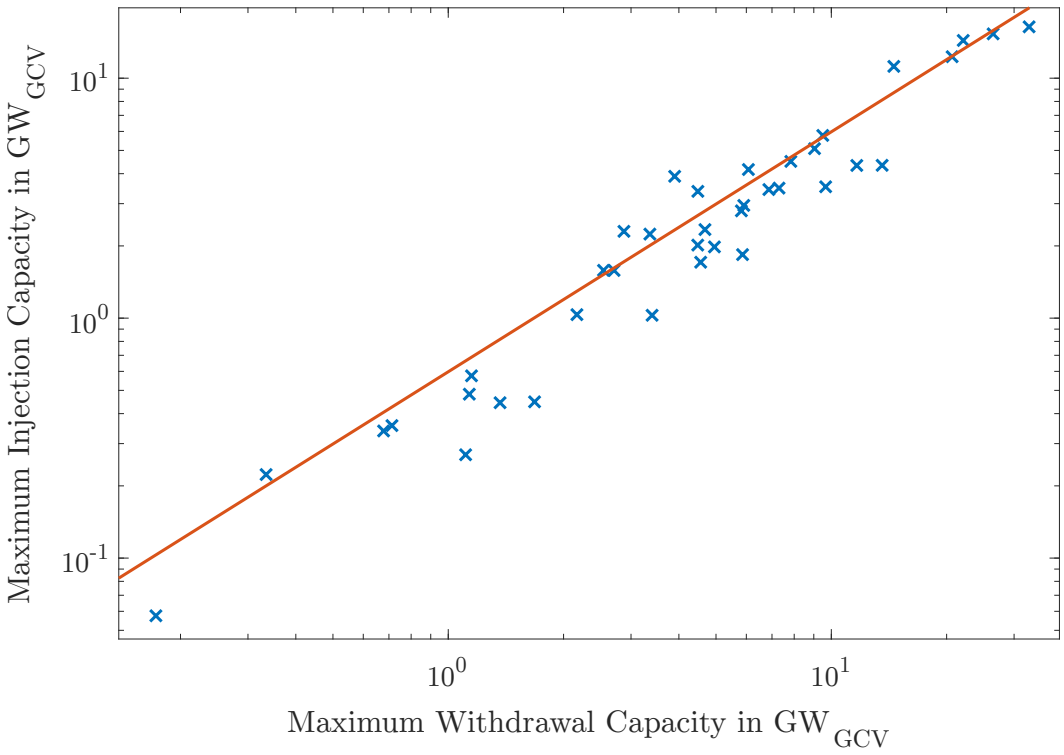

Figure 3.23: Correlation between maximum injection and withdrawal capacity of the gas storage plants according to gie (2018).

gross calorific value given in EID Energie Informationsdienst GmbH (2019) and the norm density for a natural gas with the same GCV from Cerbe et al. (2017). In the last step, the gas storage plants are assigned to their NUTS 3 region, and all values are listed in Table 3.1.

3.2.6 Power Grid Data

The used power grid data for the German high-voltage and extra-high-voltage level is taken from Meinecke et al. (2019), and coupling capacities with neighboring countries are neglected since only the German energy system is considered. To account for near-future power grid extension, the plans from 50Hertz et al. (2016) are considered.

3.2.7 Quasi-Stationary Integrated Energy System Model for Optimization

To design the conventional heat producers in the heating system, such as electric heat pumps or gas boilers, the average norm ambient temperature for Germany is determined. It is calculated based on the norm ambient temperature for each zip code area from DIN/TS 12831-1 (Apr. 2020), which were mapped to the LAUs and weighted by their heat consumption in 2050, resulting in $-11.01\,°C$. The heat producers are then designed using the heat demand profiles from Zimmermann et al. (2020) with that temperature. For systems with an electric boiler, it is designed to provide the share of heating from set storage top temperature to supply temperature of hot water and process heat.

Table 3.1: Data of gas storage plants in Germany based on EID Energie Informationsdienst GmbH (2019) and gie (2018).

NUTS 3 region	Storage Capacity in kg	Maximum Injection Capacity in kg/s	Maximum Withdrawal Capacity in kg/s
01002	$5.969 \cdot 10^7$	13.76	23.03
03241	$2.943 \cdot 10^8$	70.19	117.44
03251	$3.648 \cdot 10^9$	330.33	552.67
03359	$9.119 \cdot 10^7$	41.29	69.08
03452	$1.277 \cdot 10^8$	38.54	64.48
03456	$7.129 \cdot 10^8$	59.18	99.02
03457	$2.019 \cdot 10^9$	407.41	681.62
03461	$2.553 \cdot 10^8$	61.94	103.63
03462	$3.678 \cdot 10^9$	684.06	1144.48
04011	$1.782 \cdot 10^8$	71.57	119.74
05170	$1.467 \cdot 10^8$	44.04	73.69
05554	$2.866 \cdot 10^9$	918.04	1535.95
06432	$6.632 \cdot 10^7$	13.76	23.03
06433	$1.119 \cdot 10^8$	18.58	31.09
06631	$9.119 \cdot 10^7$	13.76	23.03
07311	$7.461 \cdot 10^7$	17.89	29.94
08226	$2.487 \cdot 10^7$	6.19	10.36
08436	$8.290 \cdot 10^6$	4.13	6.91
09175	$3.026 \cdot 10^8$	33.03	55.27
09183	$8.290 \cdot 10^8$	165.16	276.33
09187	$1.302 \cdot 10^9$	133.51	223.37
09371	$5.969 \cdot 10^7$	13.08	21.88
12064	$8.290 \cdot 10^7$	19.27	32.24
13076	$2.147 \cdot 10^8$	55.05	92.11
15081	$2.893 \cdot 10^8$	123.19	206.10
15088	$9.616 \cdot 10^8$	159.38	266.66
15089	$1.595 \cdot 10^9$	350.97	587.21
16065	$5.140 \cdot 10^7$	8.53	14.28

The heating curve for the heating system is modeled as a linear curve between the supply and return temperatures of 45 °C and 35 °C, respectively, at the weighted norm ambient temperature and supply and return temperatures of 20 °C at an ambient temperature of 20 °C. The set temperature of the control for the solar thermal collector is 75 °C, and the top volume temperature is used to control the heat flow provided by the heat producer. Its set value is 45.5 °C for systems with an electric heat pump so that it is working efficiently and can always provide the heat for space heating. For the process heat and hot water demand, the electric boiler raises the temperature from there to the desired value. For systems with other heat producers, 60 °C is assumed since no electric boiler is used, and the efficiency of the heat producers does not depend on the temperature except for the gas-fired heat pump. The set supply temperature of each heat producer is 0.5 K above

that value and is used for the mass flow rate control. The supply and return temperatures for hot water and process heat are set to 60 °C and 10 °C to avoid legionella growth and assuming that the water is consumed entirely and new water is taken from the water grid.

The heat loss coefficient of the hot water storage is chosen to have the same losses as the number of small hot water storage tanks with the same volume. The small hot water storage tanks have a height of 2 m and a diameter of 1 m.

The technical and economic data for the optimization can be found in the appendix in Tables A.1-A.6. The observation period is chosen to be 20 years and the interest rate 7 %. Price changes during the observation period are neglected; the prices change only depending on the starting year of the period.

To evaluate the emission reduction of the resulting future systems, the emissions of SNG and natural gas are calculated based on the specific emission value of natural gas of 202 g_{CO_2}/kWh_{NCV} (ffe, 2010) and set in relation to the emissions in 1990 (Umweltbundesamt, 2019). Emissions in the upstream chain of natural gas are not considered. The power grid losses are presumed to be 25.8 TWh_{el} from Bundesnetzagentur (2016) and assumed constant for the future.

The described model is then optimized using the Optimization Toolbox (MathWorks Inc., 2021b). The model is very complex, with up to 26 optimization variables that highly compete, especially the different heating and electric energy storage technologies. To achieve an efficient optimization behavior, the algorithms `surrogateopt` and `patternsearch` are executed after each other. Both algorithms work best when all optimization variables have the same order of magnitude, so they are all scaled accordingly.

3.2.8 Quasi-Stationary Gas Grid Model

Gas Properties

Since most of the natural gas imported into Germany nowadays comes from Russia (ENTSOG, 2014), the properties of Russian natural gas, according to Cerbe et al. (2017), are used for the simulations with natural gas. All relevant properties for natural gas and hydrogen are listed in Table 3.2. Since different compositions cannot be accounted for by the quasi-stationary gas grid model, biomethane and SNG have the same composition as the natural gas.

To determine the coefficients for quadratic correlations for density, dynamic viscosity, and gas law deviation coefficient in Equations (3.2)-(3.4), curve fitting with a second degree polynomial depending on the pressure was applied to property values from REF-

Table 3.2: Properties of natural gas and hydrogen according to Cerbe et al. (2017) and TLK-Thermo and ift (2021).

Property	Unit	Natural Gas	Hydrogen
Norm Density	kg/m_n^3	0.74	0.089 89
Net Calorific Value	$kW\,h/m_n^3$	10.036	2.995
Gross Calorific Value	$kW\,h/m_n^3$	11.1	3.540
Specific Gas Constant	$J/(kg\,K)$	509.0	4124.4

Table 3.3: Coefficients for the quadratic correlations to calculate density, dynamic viscosity, and gas law deviation coefficient for Russian natural gas and pure hydrogen based on NIST (2018).

Property	Coefficient	Unit	Natural Gas	Hydrogen
Density	$a_{\rho,1}$	$\mathrm{kg/m^3}$	$-2.375 \cdot 10^{-2}$	$5.690 \cdot 10^{-4}$
	$a_{\rho,2}$	$\mathrm{kg/(m^3\,Pa)}$	$6.933 \cdot 10^{-6}$	$8.554 \cdot 10^{-7}$
	$a_{\rho,3}$	$\mathrm{kg/(m^3\,Pa^2)}$	$1.628 \cdot 10^{-13}$	$-4.944 \cdot 10^{-15}$
Dynamic Viscosity	$a_{\eta,1}$	$\mathrm{Pa\,s}$	$1.061 \cdot 10^{-5}$	$8.587 \cdot 10^{-6}$
	$a_{\eta,2}$	s	$1.030 \cdot 10^{-13}$	$6.901 \cdot 10^{-15}$
	$a_{\eta,3}$	s/Pa	$2.039 \cdot 10^{-20}$	$6.831 \cdot 10^{-22}$
Gas Law Deviation	$a_{K_\mathrm{m},1}$	-	1.003	$9.994 \cdot 10^{-1}$
Coefficient	$a_{K_\mathrm{m},2}$	1/Pa	$-2.271 \cdot 10^{-8}$	$6.023 \cdot 10^{-9}$
	$a_{K_\mathrm{m},3}$	$\mathrm{1/Pa^2}$	$3.585 \cdot 10^{-16}$	$1.973 \cdot 10^{-17}$

PROP (NIST, 2018). Pressure values were varied from 1 bar to 100 bar, and the correlation resulted in R-square values of above 0.9999. All coefficients can be found in Table 3.3.

Gas Grid

For the isothermal flow of the gas, a constant temperature of 10 °C is chosen. Before aggregating the gas grid, all pipes have the surface roughness of transmission pipes according to Cerbe et al. (2017) of 0.1 mm.

Disaggregation

Several results of the optimization are used in the gas grid computation afterward, that is, gas consumption for heating and power plants, gas production from PtG, and the injection and withdrawal curve of the gas storage plants. Before allocating the curves to the gas grid's nodes, they have to be disaggregated first, that is, split into the NUTS 3 regions or directly assigned to specific nodes. In general, the disaggregation is based on the assumption that the plants or components work the same in the different regions. This means that they have the same curve, which is simply split into the regions or nodes using constant shares.

The gas consumption for heating is split according to the yearly heat demand of each NUTS 3 region for 2050, whereas the gas storage injection and withdrawal curve is disaggregated with regard to the storage capacity at each storage node. For the H2 scenarios, only salt caverns are considered as gas storage plants. Gas consumption for power plants in each NUTS 3 region is determined by splitting the overall curve according to the currently installed power plant capacity from Hofmann et al. (2019), assuming that future power plants will still be located in the same regions because the required infrastructure exists already.

The PtG plants are assumed to be built in NUTS 3 regions with much excess power over the year. So first, the residual load is calculated by subtracting the final electric demand and electric demand for heating from the renewable power production in each

region. According to their share of the yearly excess electric energy in Germany, the overall PtG gas production is then assigned to each NUTS 3 region.

3.2.9 Dynamic Models

Gas Properties

In the dynamic models, the fluid properties are supplied by the TILMedia Library (TLK-Thermo and ift, 2021) except for the dynamic viscosity; that is why Equation (3.70) is used. To account for different constant temperatures and varying compositions of the methane-hydrogen mixture, property values from REFPROP (NIST, 2018) for 5 °C to 15 °C, pressure values from 1 bar to 100 bar, and hydrogen admixtures from 0 vol% to 100 vol% are used to fit the linear curve. For the simulations with pure hydrogen, also a curve-fitting with data for hydrogen in the same temperature and pressure range is performed. It results in R-square values of 0.8728 for the methane-hydrogen mixture and 0.9958 for hydrogen, and all coefficients are listed in Table 3.4.

Since the fluid in the gas grid is modeled as a methane-hydrogen mixture, it is assumed that the biomethane only consists of methane and there is no remaining CO_2.

Gas Grid

For the simulation of the gas grid, a linearization below pressure losses of 0.01 bar is chosen for hydrogen scenarios and 0.1 bar for SNG scenarios. This only leads to minor errors but results in a reasonable speed up in simulation time. Each pipe only contains one control volume since it was shown in Section 3.1.5 that it is sufficient to get good results.

Junctions between the pipes account for the mixing of the different gas flows. Each junction's size is chosen according to the node's importance: The node capacity is calculated for each node by adding the capacities of all connected pipes and the absolute average value of consumption and production at the node. Those values are divided by the mean value of all node capacities and multiplied by the average junction volume. It is chosen to be on average 100 m^3 for the simulations to compare the quasi-stationary and dynamic models. This only leads to an increase in gas grid volume by approximately 5 % for the non-aggregated gas grid, which strongly decreases with higher aggregation grades due to the sinking number of nodes. For numeric reasons, the average volume is increased to 1000 m^3 for the simulations with the aggregated gas grid in the dynamic IES model, which enlarges the gas grid by approximately 2.5 %. To avoid numerical problems due to

Table 3.4: Coefficients for the linear correlations to calculate the dynamic viscosity for a methane-hydrogen mixture and pure hydrogen based on NIST (2018).

Coefficient	Unit	Methane-Hydrogen Mixture	Hydrogen
$a_{\eta,1}$	Pa s	$3.498 \cdot 10^{-7}$	$2.772 \cdot 10^{-6}$
$a_{\eta,2}$	s	$1.043 \cdot 10^{-13}$	$1.378 \cdot 10^{-14}$
$a_{\eta,3}$	Pa s/K	$2.716 \cdot 10^{-8}$	$2.050 \cdot 10^{-8}$
$a_{\eta,4}$	Pa s	$2.807 \cdot 10^{-6}$	-

very small junction volumes, the minimum possible value is 1 % of the average junction volume.

Additionally, the two inner-German import nodes in Lower Saxony are treated in a particular way. They both constantly import gas from the rest of Germany with the same curve as all other transfer nodes but with a different sign. Additionally, the subsequent networks are very small, so there is a high risk of too low pressures at those nodes. That is why one boundary condition each is connected to those nodes, which delivers a small ideal mass flow rate to keep the node pressure constant. This only leads to a small error in the transferred gas flow rate of less than 0.2 %.

Gas Storage Plants

The installed gas storage capacities, including injection and withdrawal capacities, are assigned by splitting the values from the optimization proportional to the currently installed capacities. For the H2 scenarios, only salt caverns are considered as gas storage plants. If larger capacities are required, it is assumed that the capacities are also expanded proportionally to the current values. Since the gas storage plants control the pressure in the model, critical situations with very low or high pressures can occur when a gas storage plant is empty, full, or at the mass flow rate limits. To avoid those problems, the storage and the maximum injection and withdrawal capacities are scaled by factor 1.2, which gives the model more flexibility.

Furthermore, the nominal pressure set values for each aggregated gas storage per region are determined based on Equation (3.75) with $p_{\mathrm{stor,set,base}} = 80\,\mathrm{bar}$ and $f_{\mathrm{stor}} = 1500\,\mathrm{Pa\,s/kg}$. The bandwidth of the set pressure in Equation (3.76) is chosen to be $\Delta p_{\mathrm{bw}} = 20\,\mathrm{bar}$.

Energy Conversion Plants

In the power plant and electrolyzer models, time constants of 2 s and 10 s, respectively, are only used for numeric reasons. The limitations of the power plants are already comprised in the gradient limiter and the reaction time of the electrolyzers is very fast.

Furthermore, for the SNG scenarios, a maximum hydrogen feed-in of 20 vol% is assumed in accordance with the goals of DVGW (2019).

Regions

Due to the model's complexity, not every NUTS 3 region can be represented by one superstructure, but the regions have to be aggregated. This is done using an algorithm developed by Schülting (2021): First, all regions, which are not part of Northern Germany, are aggregated so that the rest of Germany is part of the model, but the highest resolution is used in Northern Germany. Second, a loop goes through all remaining regions and always combines the two adjacent regions with the smallest combined final electric load until the specified number of regions is reached. To prevent oddly shaped, for example, very long, regions, the growth in length in latitude and longitude of the regions is also considered and prevents some aggregation steps. The resulting ten regions are shown in Figure 3.24. The eleventh region (number 1) is the rest of Germany, which is left out here.

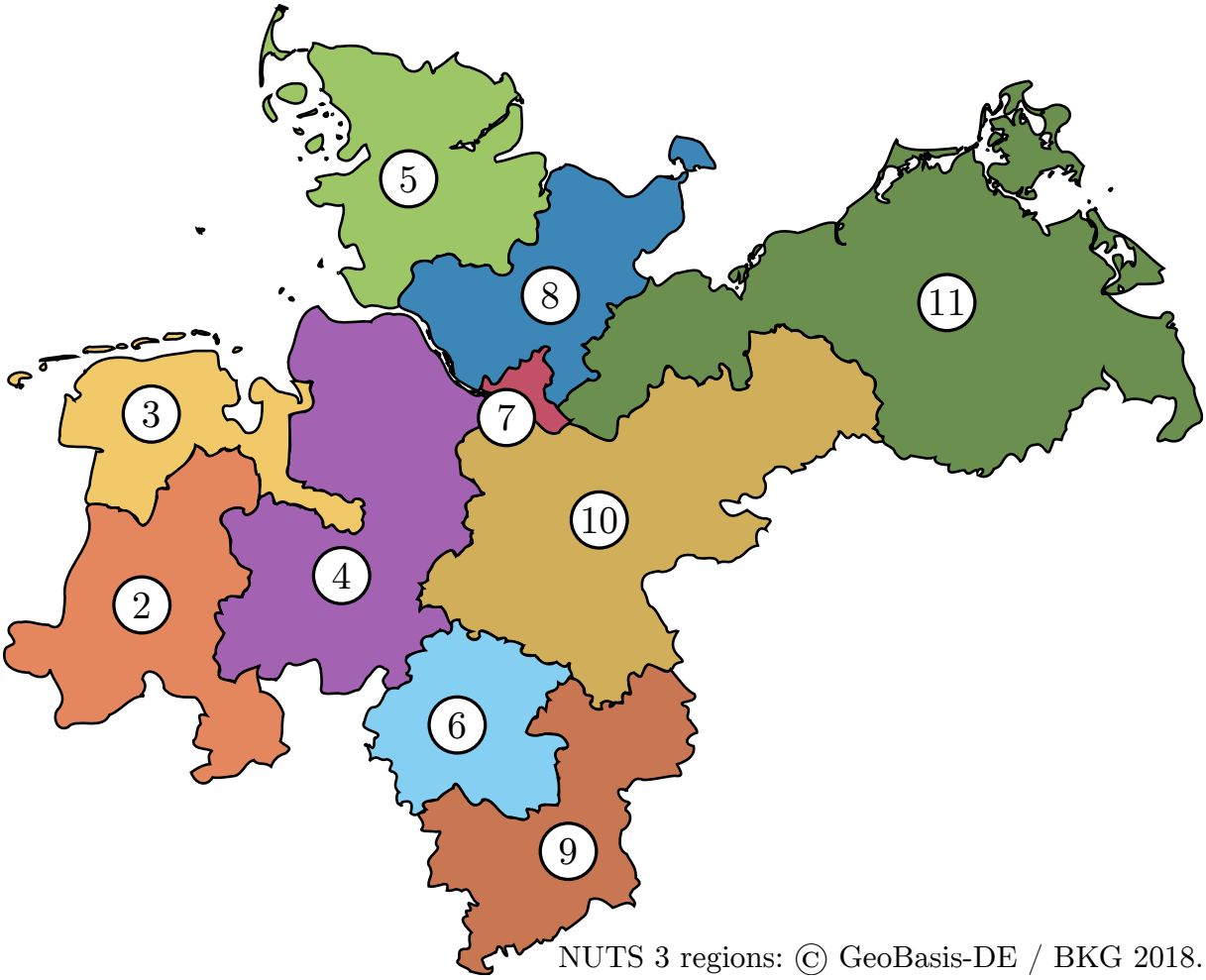

NUTS 3 regions: © GeoBasis-DE / BKG 2018.

Figure 3.24: The aggregated regions of Northern Germany. Region 1 (not shown here) is the rest of Germany.

4 Results

In this chapter, the results of the different models are presented, starting with the optimization of the quasi-stationary IES model in Section 4.1. Section 4.2 shows the results of the quasi-stationary gas grid model and, in Section 4.3, the results of the aggregation algorithm and the derived aggregated dynamic gas grid models are presented. The findings of the dynamic IES model are shown in Section 4.4.

4.1 Design of the Integrated Energy System

In this section, the results of the quasi-stationary IES model, which was used by the optimization, are presented. First, the results of the quasi-stationary model are compared with a dynamic model in Section 4.1.1 and, in Section 4.1.2, the optimal system configurations, which were found by the optimization, are presented. The results of the sensitivity analysis and the variations of the heating technologies are shown in Section 4.1.3 and Section 4.1.4, respectively.

4.1.1 Comparison of Quasi-Stationary and Dynamic Integrated Energy System Model

First, it has to be checked that the quasi-stationary IES model, with which the IES is economically optimized, adequately reflects the dynamic IES model's behavior. For that purpose, one arbitrary configuration including all considered technologies is simulated with both models and compared. The dynamic IES model has no spatial resolution here so that only the differences between quasi-stationary and dynamic modeling are examined. Since all components somehow depend on the power sector, any deviations between the models would be visible by examining the electric powers. Figure 4.1 shows the results for powers of different components in one period of the year. In general, the results match well, but some appearing deviations will be explained in the following.

The solver, which solves the system of equations of the dynamic model, uses a variable time step to resolve all necessary dynamic effects. It depends on the system's dynamics at the current simulation time: If fast changes occur, a small step size is chosen, whereas large steps are made if the system is close to a steady state. In contrast, the quasi-stationary IES model uses a fixed time step given by the user. Figure 4.1a shows deviations for the battery storage plants due to the variable time step. When the state of charge falls below a threshold due to self-discharge, the battery is quickly charged again with maximum power. In the quasi-stationary simulations, this charging process is spread out over the whole time step, which leads to a much smaller charging power which is not visible in the figure.

For the pumped hydro storage plants, shown in Figure 4.1b, as well as A-CAES and CCGT power plants, which are not shown here, the simulations match very well. In

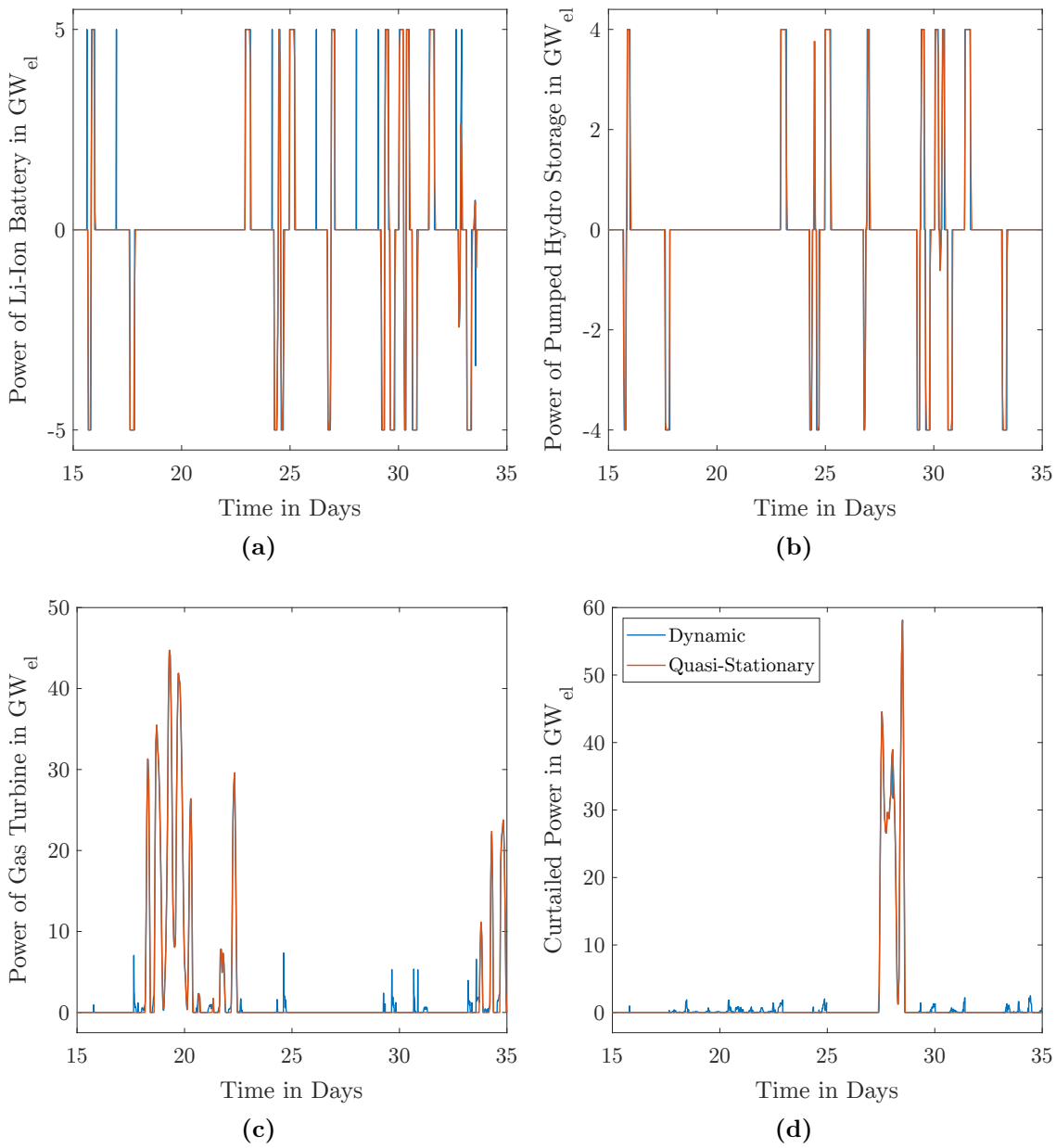

Figure 4.1: Comparison of the results of the dynamic and quasi-stationary IES model for the electric powers of different components: (a) lithium-ion battery storage plant, (b) pumped hydro storage plant, (c) gas turbine plant, and (d) curtailment of renewables. The storage plants are charged for positive powers and discharged for negative powers.

contrast, Figures 4.1c and 4.1d show deviations of several GW_{el} for the gas turbines and curtailment of renewables. Those discrepancies result from the accumulation of minor deviations in all technologies, which come first in the merit order, for example, the time constants and gradient limitations of the CCGT power plants. Since the gas turbine is the last technology in the merit order and the remaining excess power is curtailed, the deviations appear here. All in all, the results match very well, so the quasi-stationary IES model can be used for optimization.

4.1.2 Optimal System Configuration

All Scenarios

The optimization was conducted for all scenarios with 60 %, 80 %, and 100 % renewable energies and either SNG or hydrogen. The optimization algorithm has found the combination of electric heat pumps with gas boilers, in the following called EHPGB, to be optimal in all scenarios. Despite their high overall efficiency, small and large-scale CHP plants are not considered by the optimization algorithm since they are implemented to be operated heat-led. So, the plants produce power in times of high heat demand, which is not needed to that extent at that time and would have to be stored. This is found to be not economical by the optimization algorithm. Furthermore, pumped hydro storage and A-CAES plants are never chosen but only lithium-ion batteries or even no electric energy storage in the H2 scenarios.

The optimization leads to zero emissions for the H2 scenarios since no natural gas is used. For the SNG scenarios, emission reductions of 86.7 %, 93.9 %, and 100.6 % compared to 1990 are achieved, which complies with the German government's goals, bearing in mind that the transportation sector is not included here. More than 100 % emission reduction in 2050 means that negative emissions are reached by using CO_2 from the atmosphere for biogas or SNG production and then using the biomethane or SNG in a non-energetic way that the CO_2 stays within the product.

Figure 4.2 shows the nominal electric powers of all components in the scenarios, and, in Figure 4.3, the amount of biomethane or hydrogen from biomass input, storage capacities, the balance point temperature of EHPGB, and the total system cost are depicted.

The nominal electric power of renewable power generators increases strongly with an increasing renewable share and almost doubles going from 60 % to 100 % renewables. Despite the lower efficiency of Power-to-Gas in the systems with SNG due to the additional methanation, less renewable power is needed than for H2 scenarios. This effect can be explained by fewer used hydrogen from biomass than biomethane due to higher cost: Only the potential of biogas from waste is used for the H2 scenarios, whereas the full potential is exploited in the SNG scenarios.

Lithium-ion batteries are only used in systems with SNG, and their nominal powers and storage capacities rise exponentially with a rising share of renewables. Due to the high efficiency of the batteries and the low efficiency and high power-specific but low energy-specific cost of PtG with methanation, both technologies supplement each other. For the H2 scenarios, the PtG plants are more efficient and less expensive due to the missing methanation, making batteries unnecessary.

Also, the nominal Power-to-Gas plant powers follow an exponential growth even though no PtG is used in 60 % RE SNG. However, nominal electrolyzer powers are always higher for the H2 scenarios because the missing electric energy storage plants are replaced by Power-to-Gas-to-Power (PtGtP) plants, that is, Power-to-Gas and re-electrification. Also, more gas has to be produced since less hydrogen from biomass is used than biomethane in the SNG scenarios.

The sums of CCGT power plants and gas turbines are similar for SNG and H2 scenarios, and they stay almost constant for the different shares of renewables. However, there is a shift from CCGT power plants to GT due to fewer operating hours, which favors GT despite the worse efficiency because of lower cost.

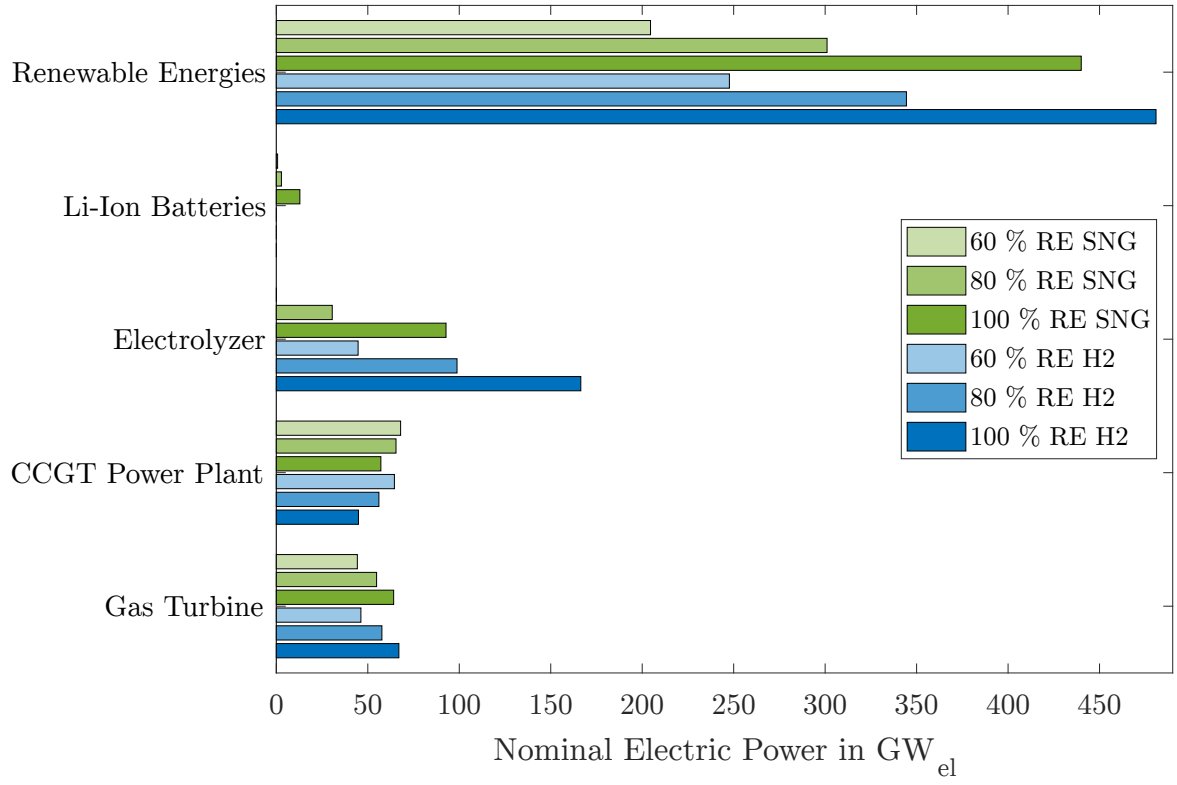

Figure 4.2: Nominal electric powers of the different technologies resulting from the optimization for all scenarios.

Even though more hydrogen and SNG are produced from excess electricity with a rising share of renewables, the required gas storage capacities reduce since the energy demand decreases in all sectors. This is also reflected in the bivalence point temperature for EHPGB, which sinks with growing renewable energy share. This means that the fraction of supplied energy by the electric heat pump increases and the gas boiler produces less heat. Additionally, the heat demand as such decreases due to better insulation standards.

For the cost, there is no clear tendency. For the SNG scenarios, the cost increase, whereas for the H2 scenarios, they decrease with a rising share of renewables. Additionally, the cost of the H2 scenarios is always higher for the same share of renewables except for 100 % renewables. To explain the different cost development, the cost fractions are shown in Figure 4.4.

Cost for most of the components are very similar between H2 and SNG scenarios, but the biggest differences lie in the cost for biomethane or hydrogen from biomass, (hydrogen from) natural gas, PtG plants, gas storage plants, and cost for CO_2 certificates.

Expenses for biomethane are higher for the SNG scenarios, but the total cost for natural gas is much lower than for hydrogen from natural gas: For the H2 scenarios, the natural gas is converted into hydrogen first, which approximately doubles the price. That is why the H2 scenarios have higher overall costs for 60 % and 80 % renewables. Additionally, the costs for gas storage plants in the H2 scenarios are higher due to the factor in Equation (2.8).

Another difference is the higher cost for PtG and CO_2 certificates in the SNG scenarios. The H2 scenarios have no CO_2 emissions and thus no expenses for the certificates, but the

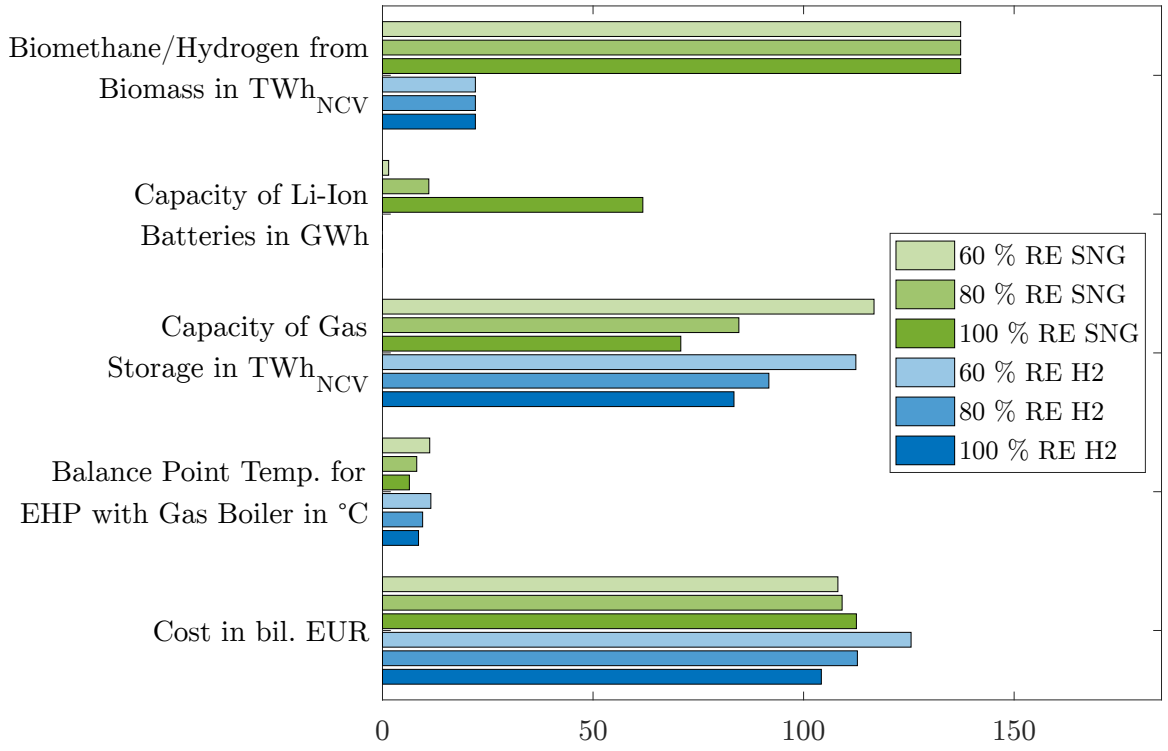

Figure 4.3: Biomethane or hydrogen from biomass input, storage capacities, hybrid heating system's balance point temperature, and total system cost resulting from the optimization for all scenarios.

SNG scenarios do, which causes roughly half the cost of natural gas. Also, PtG plants are much more expensive due to the additional methanation and DAC plants. This results in increasing costs for rising shares of renewables.

It is important to note that the cost for the rededication of the natural gas grid to hydrogen or the erection of a new hydrogen grid have not been considered here and might change the relation between SNG and H2 scenarios.

100 % RE SNG

In the following, the exemplary scenario 100 % RE SNG will be presented in more detail. Figure 4.5 shows the flow scheme for this scenario; all others are shown in Figures A.1-A.5 in the appendix. The flow schemes show the yearly energies and maximum powers which enter and leave every component and enable the investigation of overall efficiencies or full load hours. For example, it can be calculated with the given energies and powers that the CCGT and GT power plants only have full load hours of 1443 h and 164 h, respectively, whereas the electrolyzer has 3365 h.

Also, it is visible that the amount of curtailment reaches up to 113.4 GW_{el} and a total of 45.6 TWh_{el} for the respective share of renewables which is more than 4.8 % of the generated renewable electricity. It is important to note that this amount was part of the optimization, so it is the economic optimum: It is cheaper to curtail this much electricity instead of building electrolyzer, methanation, and DAC plants more than twice the size just to use 15 % more electricity in the PtG plant.

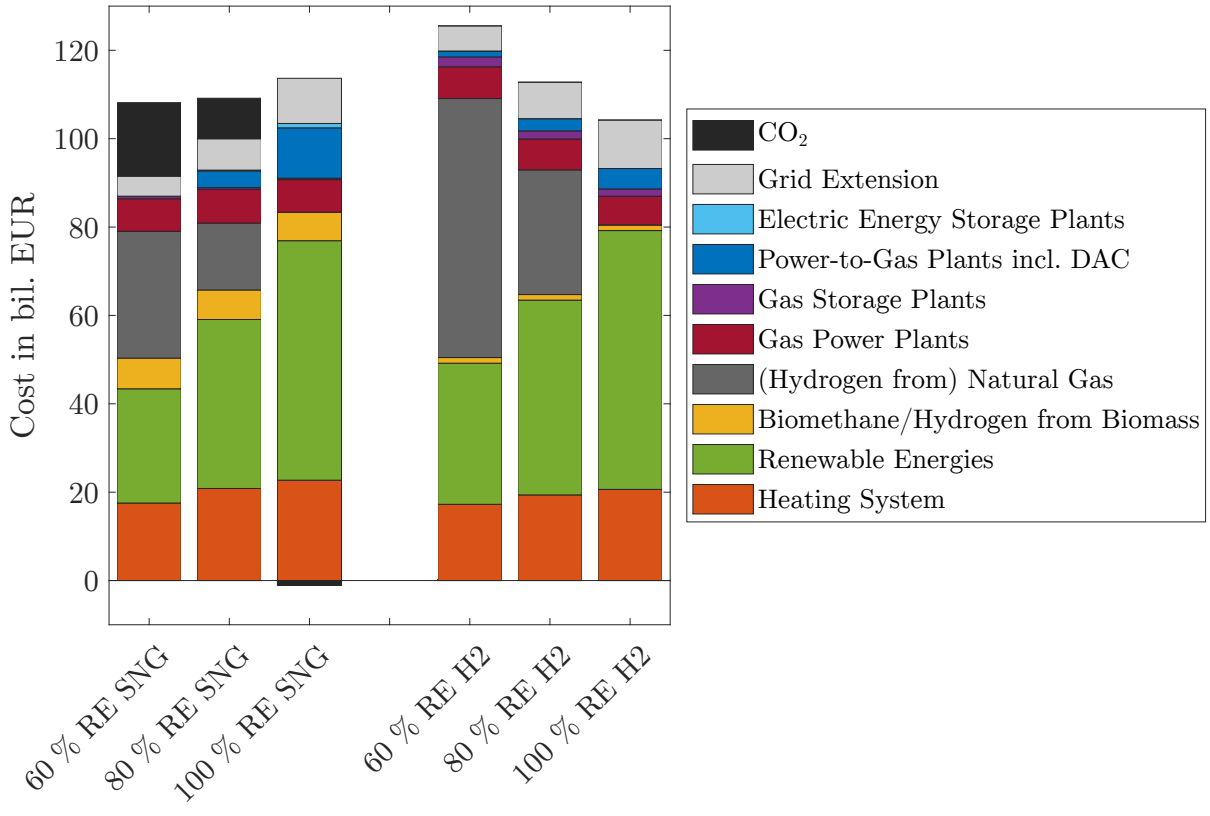

Figure 4.4: Cost fractions of the total system cost for different shares of renewables and the use of SNG or hydrogen.

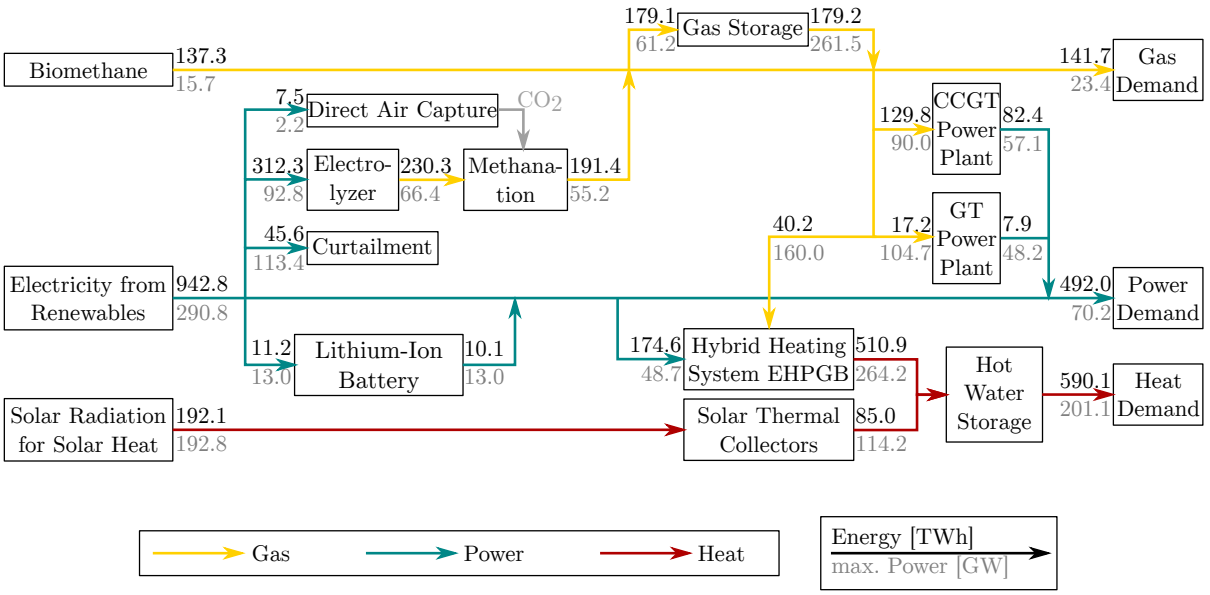

Figure 4.5: Flow scheme of the IES for 100 % RE SNG.

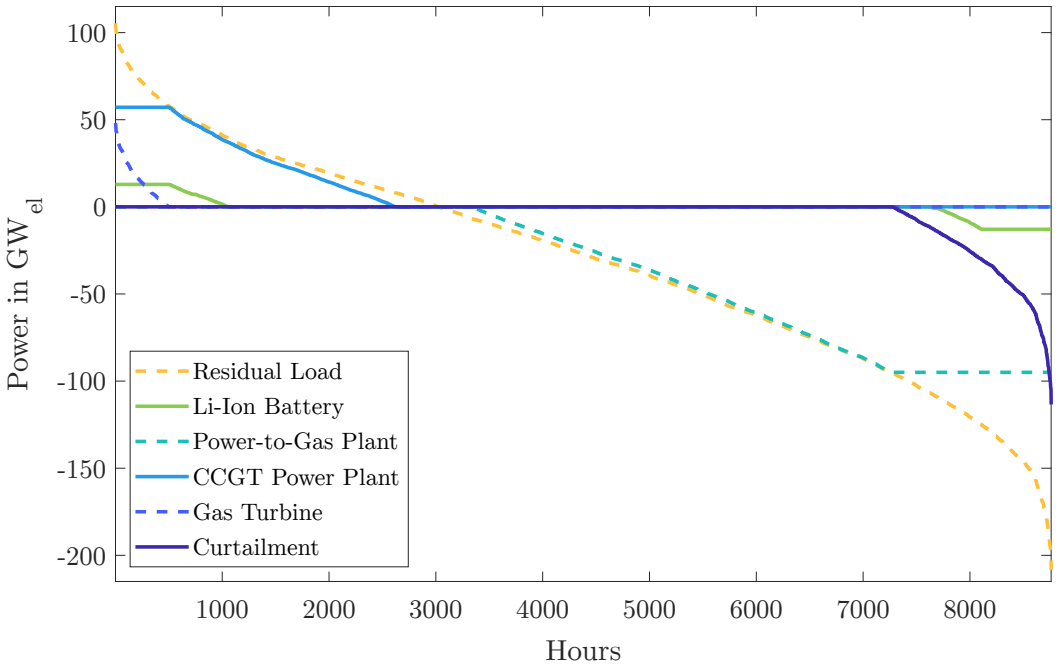

Figure 4.6: Sorted annual load curves of the residual load, all storage technologies, and curtailment for 100 % RE SNG.

To analyze how the different storage technologies are used, Figure 4.6 shows the sorted annual curves of the residual load, the different storage options, and curtailment. Positive residual loads of more than 100 GW_{el} occur, which are covered mainly by the CCGT power plant (82 % of the yearly energy), followed by the lithium-ion battery (10 %) and the gas turbine plant (8 %). Negative residual loads can reach up to 200 GW_{el}, and the majority is used by the PtG plant (85 %) or stored in the lithium-ion battery (3 %), and the remaining 12 % are curtailed.

Due to the differing fluctuations of energy supply and demand, the systems's essential components are the storage units and, thereof, mostly the electric energy storage plants. In this system, those are the lithium-ion battery plants and the PtGtP plants. However, they are operated in fundamentally different ways due to their different technical parameters: A battery has high efficiency but a certain self-discharge, so it is an appropriate short-term storage technology. In contrast, the PtGtP technology has a comparatively low round-trip efficiency but no self-discharge and low storage capacity cost compared to batteries, making it a suitable long-term storage.

To illustrate the operation of the storage technologies, Figures 4.7 and 4.8 show their respective heat maps, that is, electric power at each hour and day over a year. Charging is marked in yellow and discharging in blue. It is visible that the batteries are not operated for most of the year, represented by the turquoise areas in the figure, because they are either full or empty and are primarily used to move excess photovoltaics power in the middle of summer days to the evening. The PtGtP plants are operated differently. Long periods of up to twelve days in winter and primarily sunny hours in the summer are used to charge the gas storage to be able to discharge it during dark periods with no wind of up to 5.5 days. However, it is important to note here that this illustrates how the PtGtP plant is operated. Not the entire amount of SNG is re-electrified, and also part of the biomethane is used in the power plants.

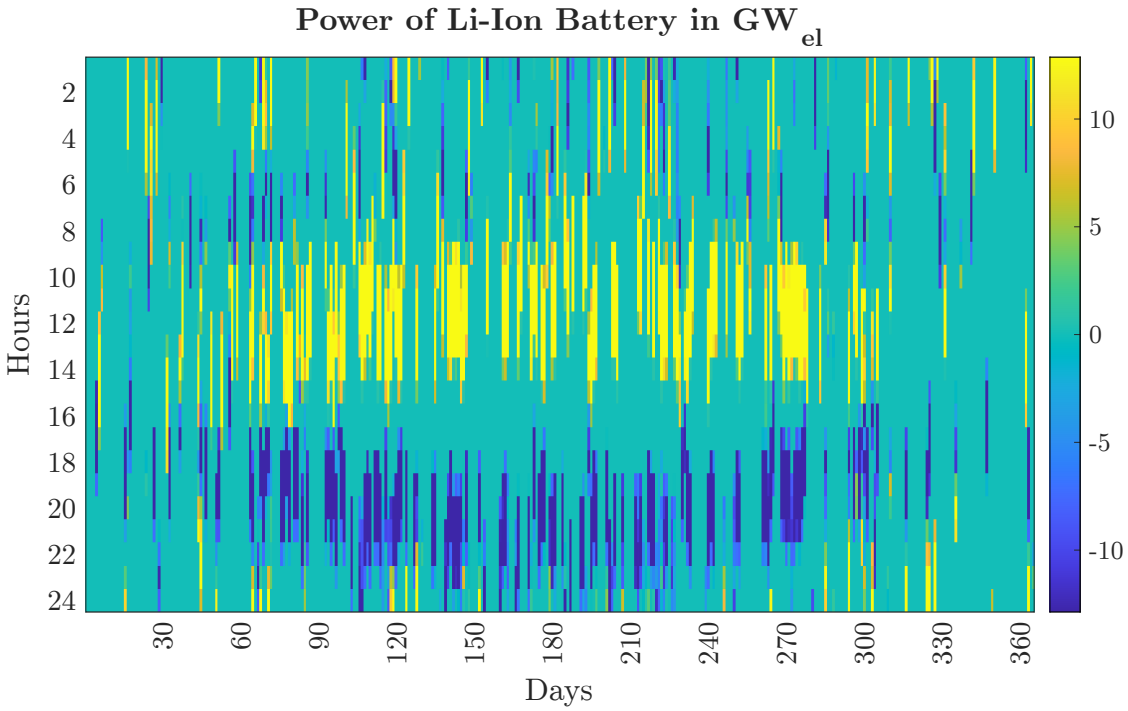

Figure 4.7: Heat map of the electric power of the lithium-ion batteries for 100 % RE SNG. Positive powers charge the batteries and negative powers discharge them.

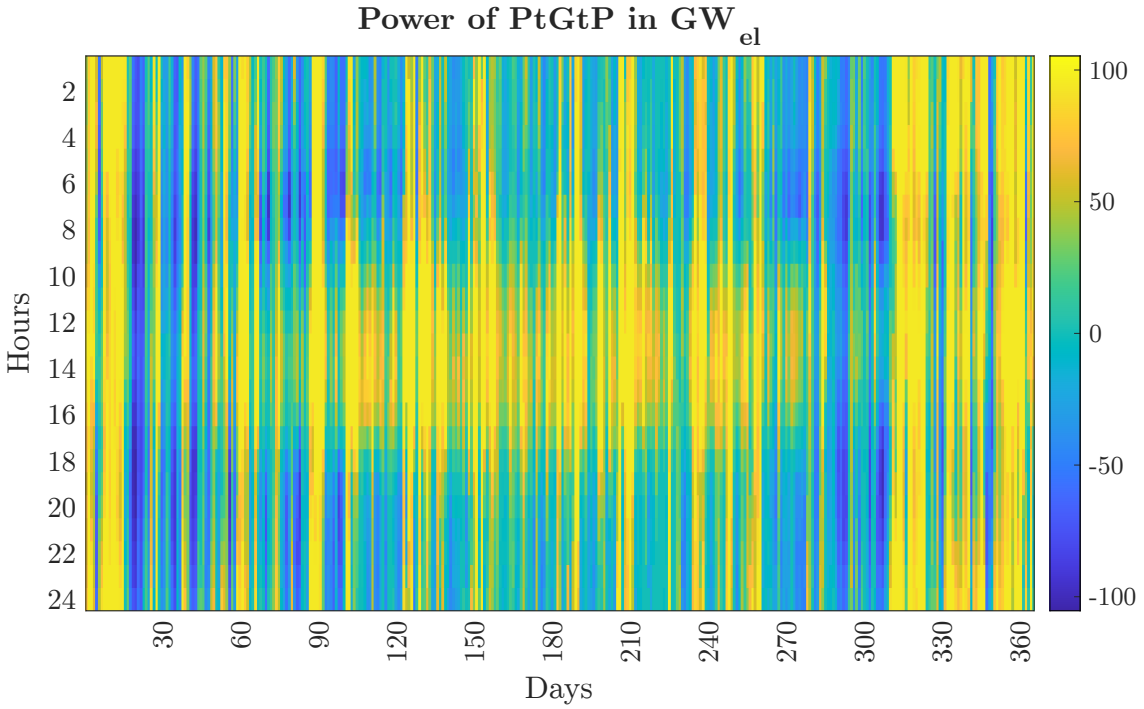

Figure 4.8: Heat map of the electric power of the Power-to-Gas-to-Power storage system for 100 % RE SNG. The electrolyzer is operated with positive powers and the power plants with negative powers.

4.1.3 Sensitivity Analysis

Since many assumptions have been made for the optimization, especially for costs far in the future, a sensitivity analysis is conducted to investigate how sensitive the results are to those assumptions. For this purpose, all capital cost values are varied depending on their assumed cost reduction until 2050. So, if one component's price is assumed to be half the cost of today, the optimization is executed with a grid of 16 points over the interval of no cost reduction down to a quarter of the cost.

In general, it can be stated that the choice of heating system is very stable: All sensitivity analyses showed that the hybrid heating system consisting of an electric heat pump and a gas boiler (EHPGB) is the most economical even if the cost of competing heat producers are reduced. Only the balance point temperature changes depending on the change in cost for the power or gas sector.

Furthermore, the choice of electric energy storage is very distinct: If one is used, it is a lithium-ion battery plant in all cases. Also, the extent to which biomethane and natural gas or hydrogen from biomass and natural gas are used stays fairly constant. All in all, most of the cost values show only a small influence on the results; some examples of sensitive values are shown in the following. In some cases, certain variation points are eliminated from the plots since the optimization algorithm did not find a valid solution. This is characterized by strongly deviating values from the adjacent points. The curves for lithium-ion battery storage capacity and the heating system's balance point temperature remain a bit unsteady since those values are highly sensitive to the competition in the group of electric energy storage and heating technologies, respectively. For improved visibility, the reference point, where the factor equals 1, is marked in all plots as a filled diamond.

There is strong competition between the electric energy storage technologies and the PtG technology, and the storage capacity cost for lithium-ion batteries is forecasted to reduce significantly. So, there is a high sensitivity towards that cost which is shown in Figure 4.9 for 60 % RE. For the SNG scenario, only a slight increase in cost suffices to push the batteries completely out of the system, but their role substantially increases when the cost reduce even more than projected: storage capacity and nominal power grow by factor 59 and 21, respectively, when the cost is a quarter of the assumed value. The effect is stronger for the SNG than the H2 scenario, but even for the latter, batteries will be used when the cost decrease at least 45 % more than assumed. Despite the big change for the batteries in those cases, the rest of the system only slightly changes, including renewable power generators, PtG plants, power plants, and cost.

After investigating a change in battery storage capacity cost, an important component of the other major storage technology, the PtG plant, is examined. In Figure 4.10, the sensitivity analysis for the power-specific cost of PtG plants for 100 % RE is shown. For the SNG scenario, it also includes a variation of the methanation plant cost. It is visible that changing the PtG plant cost strongly influences the overall system cost, especially for the SNG scenario due to the high cost of the entire PtG plant. Increased PtG plant cost reduces the plant's size, which means less hydrogen or SNG is produced. Thus, the heating system's balance point temperature shifts towards electricity which requires more renewable power and CCGT power plants. Also, the nominal battery power and storage capacity change significantly for the SNG scenario, whereas, for the H2 scenario, no batteries are used, even for a PtG plant cost increase by factor 4.

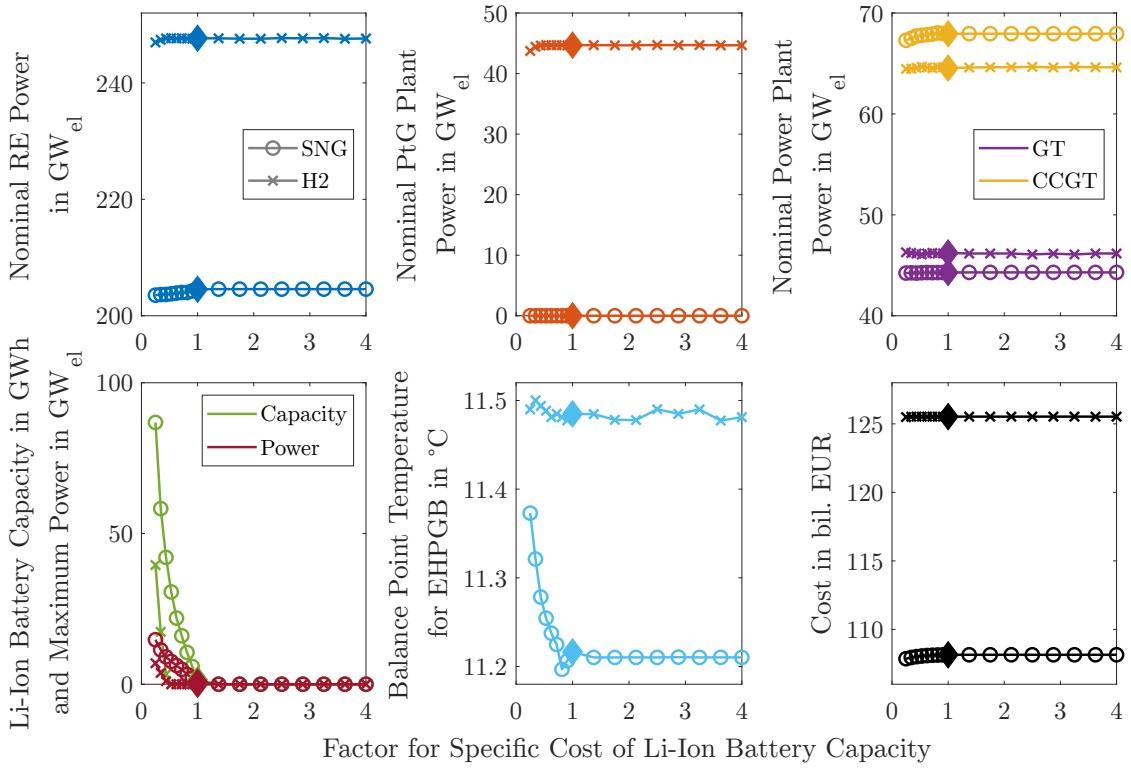

Figure 4.9: Sensitivity analysis for the cost of lithium-ion battery storage capacity for 60 % RE.

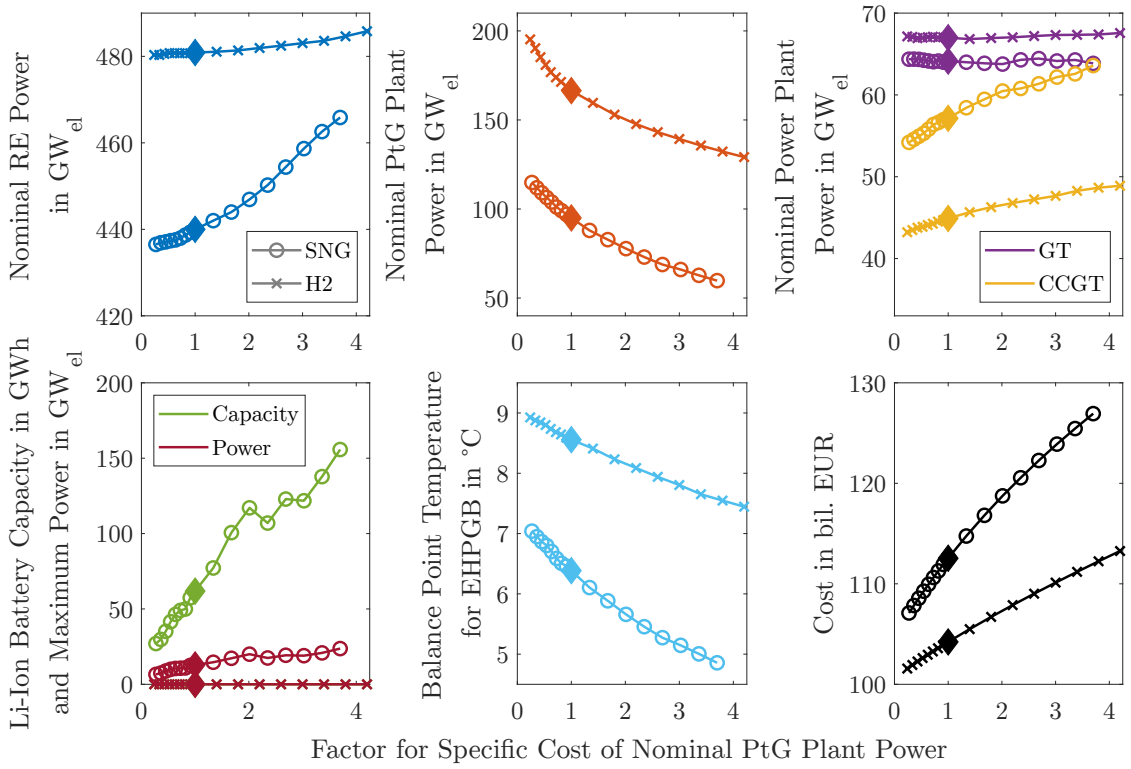

Figure 4.10: Sensitivity analysis for the cost of nominal electric PtG plant power for 100 % RE.

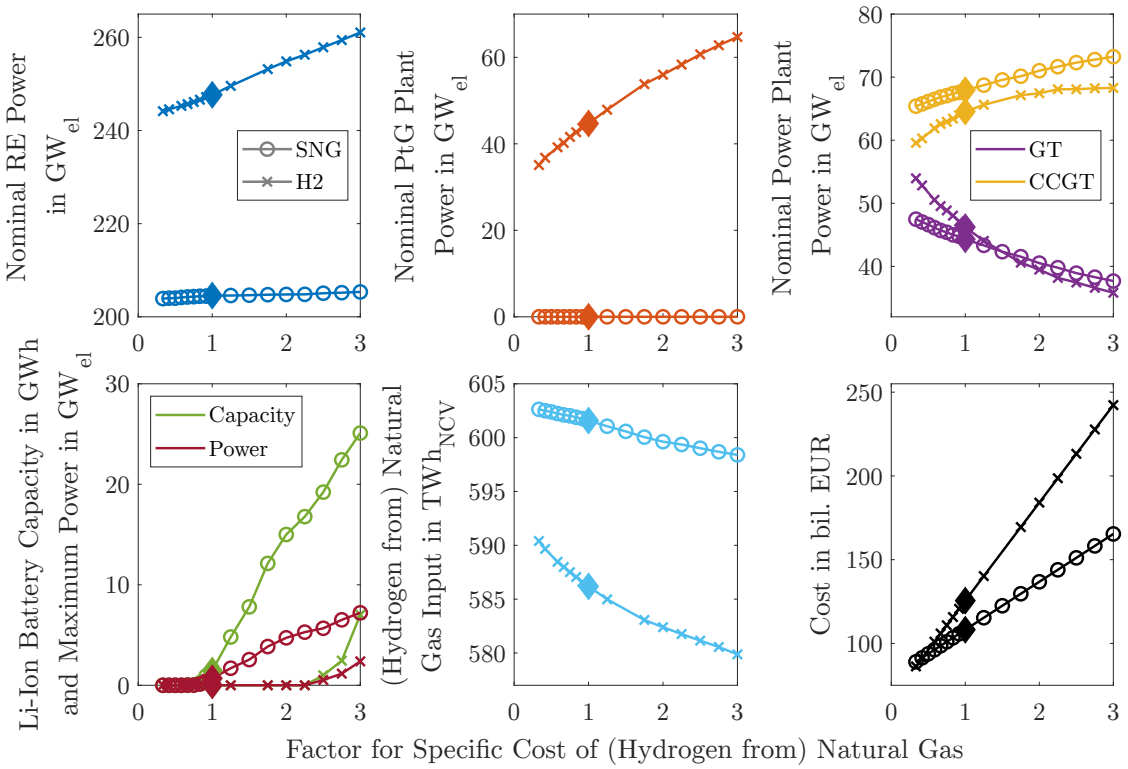

Figure 4.11: Sensitivity analysis for the cost of (hydrogen from) natural gas for 60 % RE.

Also, the development of cost for natural gas is uncertain, especially for hydrogen from natural gas. Figure 4.11 shows the sensitivity analysis for this element for 60 % RE. The H2 scenario is more sensitive since the cost for hydrogen from natural gas makes up a larger share of the overall cost. However, the input of natural gas or hydrogen from natural gas only reduces slightly by 0.5 % and 1 % for a cost increase by factor 3 for the SNG and H2 scenario, respectively. In contrast, the overall system cost almost doubles for the H2 scenario and increases by 50 % for the SNG scenario. The reduced amount of natural gas is substituted by shifting towards more efficient but also more expensive power plants, that is, CCGT plants, as well as battery storage plants. The latter happens stronger for the SNG scenario since in the H2 scenario, also more PtG is used, which requires more renewable power.

Also, some other assumptions are varied to examine their influence on the optimization results: The speed of renewable power extension for photovoltaics plants as well as onshore and offshore wind turbines is each multiplied by values between zero and three. Furthermore, the share of high-temperature process heat supplied by gas and the assumptions for the potential of biogas from energy crops and grassland are varied between 0 % and 100 %.

The results are the most sensitive towards the variation of power extension of photovoltaics compared to onshore and offshore wind. Figure 4.12 shows the results of the sensitivity analysis for it for 100 % RE. If the rate of extension is increased, it leads to a rise in nominal renewable electric power since photovoltaic plants have lower full load hours than the other power generation technologies. So, more nominal electric power has

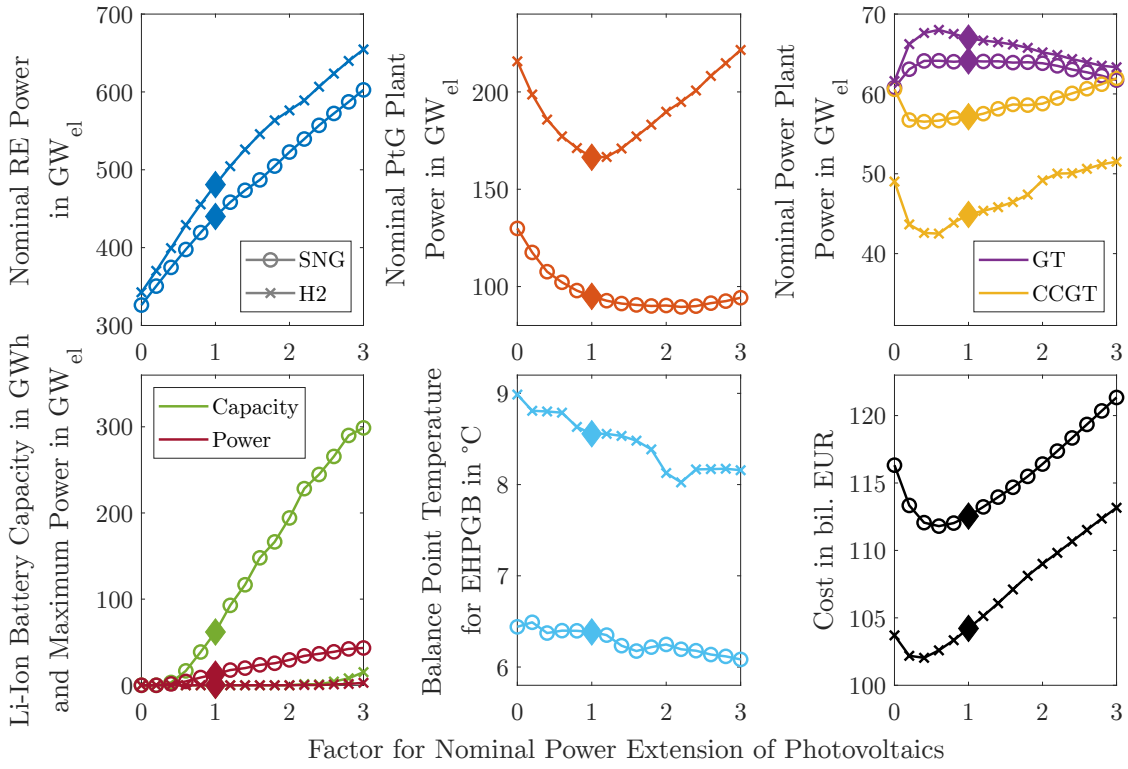

Figure 4.12: Sensitivity analysis for the rate of photovoltaics power extension for 100 % RE.

to be installed to generate the same energy. Also, it results in larger lithium-ion battery plants due to the necessity to shift renewable power from day to night. Even in the H2 scenario, lithium-ion batteries are used from factor 2.5 on. The heating system's balance point temperature moves slightly towards lower values, so more electricity is used in the system. Regarding the cost and nominal PtG as well as power plant power, there is no clear picture: The PtG plant size increases for both lower and higher PV extension rates since both lead to an increased seasonality of renewable power production. Wind turbines produce much electricity in winter, whereas photovoltaics plants generate large amounts in summer. Both lead to a higher seasonal storage demand which also influences the required power plant sizes. Due to those different effects, the overall cost rise for low and high PV extension rates. However, the chosen extension rate is close to the economic optimum.

Another interesting sensitivity is found when varying the share of high-temperature process heat provided by gas, shown in Figure 4.13 for 100 % RE. Interestingly, the cost increase for the SNG scenario whereas they reduce for the use of hydrogen which can be explained with the different cost for both gases: For the H2 scenario, it is cheaper to use hydrogen for heat generation than electricity, whereas, for the SNG scenario, the SNG is more expensive than electricity. For both scenarios, the heating system's balance point temperature reduces with an increasing share since the gas is used for the high-temperature process heat in that case. Larger PtG plants produce more gas, and fewer power plants are used since the overall power consumption sinks due to the reduced need for power for process heat. More renewable power is needed for the SNG scenario when the

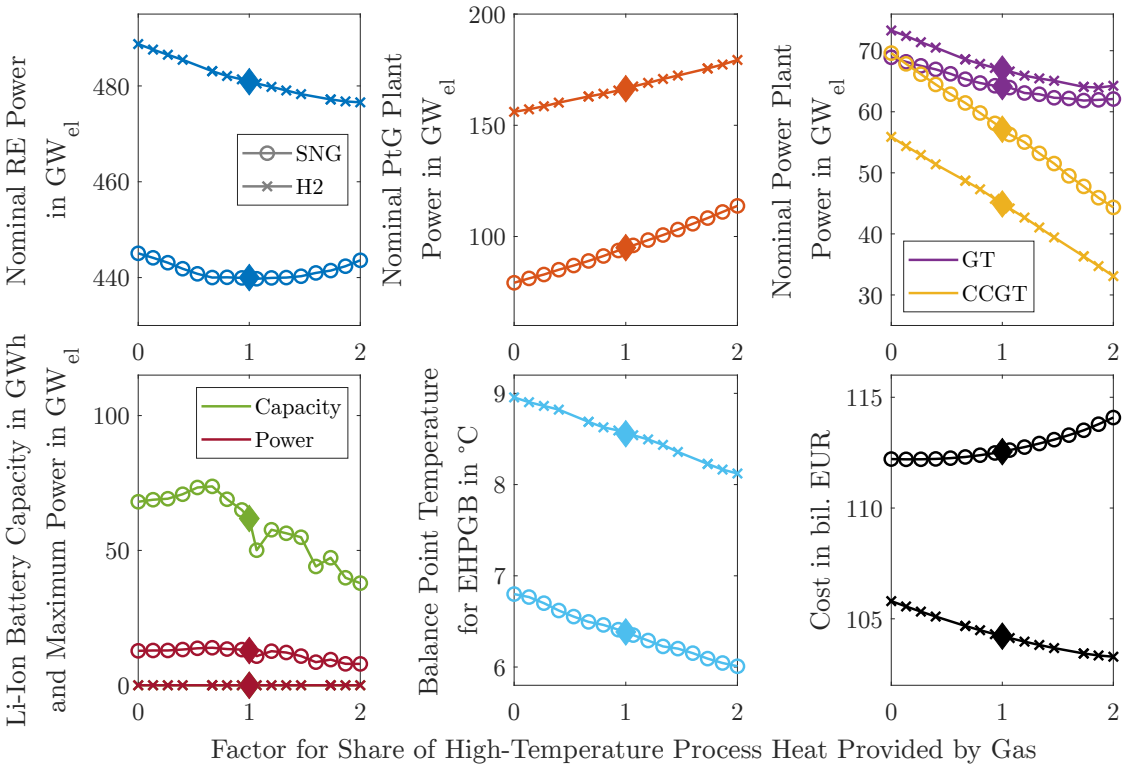

Figure 4.13: Sensitivity analysis for the share of high-temperature process heat provided by gas for 100 % RE.

share is both reduced and increased, which can be explained as follows: For lower process heat provision by gas, curtailment increases since fewer PtG plants are used, whereas the overall efficiency decreases for higher shares of gas-fired process heat provision due to the low efficiency of PtG with methanation. The chosen share, so factor 1, leads to the lowest required nominal renewable electric power, whereas for the H2 scenario, the value reduces with an increasing share. The battery plant size for the SNG scenario does not show a clear tendency as well. It sinks for both higher and lower shares of gas utilization for high-temperature process heat.

Varying the biogas potential in a sensitivity analysis has a different effect for each scenario, depending on the extent of biogas usage in the system. For scenarios using the full potential, the changed potential is still fully exploited. This leads to a shift from renewable power and natural gas to biogas. Scenarios, which only use the share of biogas from garbage, remain the same.

4.1.4 Variations of Heating Technologies

The hybrid heating system with an electric heat pump and a gas boiler (EHPGB) was found to be the best option for the heating technologies. It combines the currently most common heating technologies in Germany: an electric heat pump combined with an electric heating rod (EHPEHR) and a gas boiler (GB). Figure 4.14 illustrates the clear advantage of the hybrid heating system over purely electric or gas-fired heat production. It shows the gas and power demand for heating in 2050 for the peak hours for the three

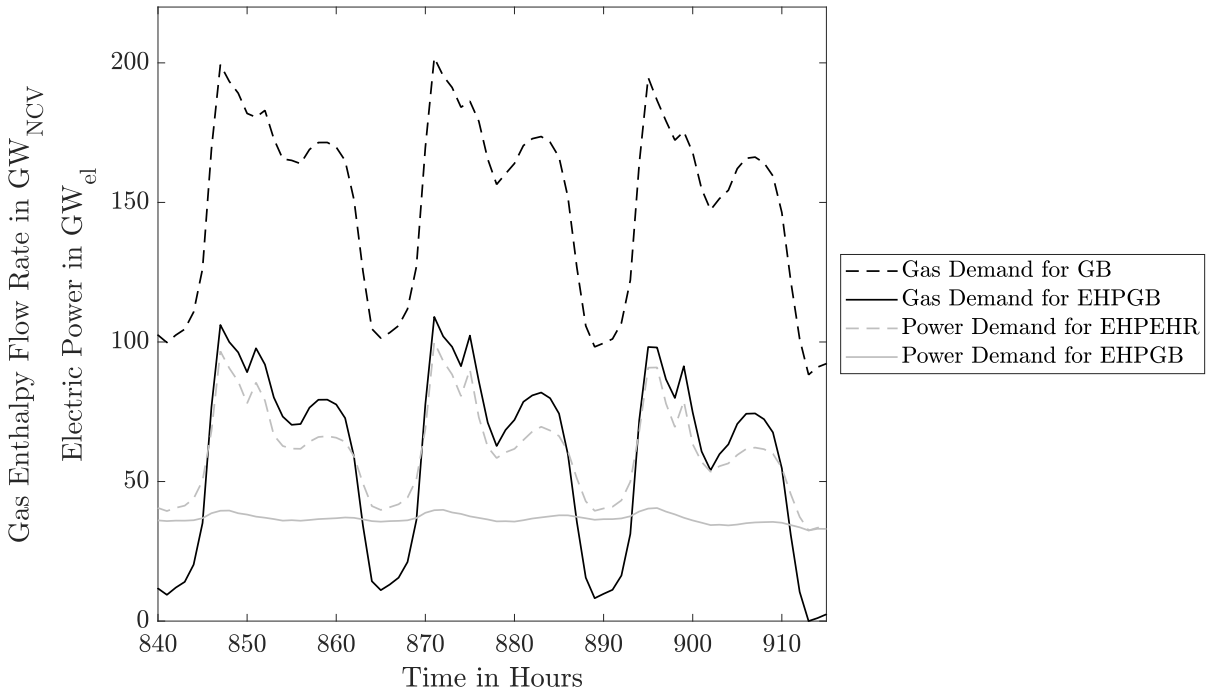

Figure 4.14: Gas and power demand for heating in 2050 for the peak hours depending on the heating technology.

considered heating technologies. EHPGB consumes gas and power but both with highly reduced peaks compared to the purely gas-fired or electrically-driven technologies: It reduces the gas peak demand by 92.8 GW_{NCV} or 46.0 % compared to GB and the power demand by 60.1 GW_{el} or 60.1 % compared to EHPEHR. That explains why it was found to be the optimal heating technology by the optimization algorithm. This effect is even more substantial when the temperatures drop down to, for example, the norm ambient temperature all over Germany instead of −5.5 °C on average in the coldest hour in Germany as in the considered weather data.

To investigate the influence of more power or gas consumption for heating on the IES, variations are considered combining the hybrid heating system with either electric heat pumps and electric heating rods or gas boilers. The following heating technology mixes are considered: 100 % EHPEHR (called 100_0_0), 50 % EHPEHR and 50 % EHPGB (50_50_0), 100 % EHPGB (0_100_0), 50 % EHPGB and 50 % GB (0_50_50) and 100 % GB (0_0_100).

Figure 4.15 shows the key results of the economically optimized variations; the detailed results are shown in Tables A.8-A.13 in the appendix. The nominal renewable power continues the trend, which was already visible in Figure 4.2: The H2 scenarios need more renewable power than the SNG scenarios, and the required nominal renewable electric power increases strongly with a rising share of renewables. Also, it is visible that it expands greatly when gas boilers are used since the gas is mostly produced via PtG using renewable power.

The figure also shows the year in which it is expected to reach the required nominal renewable electric power for each variation, assuming the nominal renewable power extension path presented in Section 3.2.2. Especially the variations including gas boilers

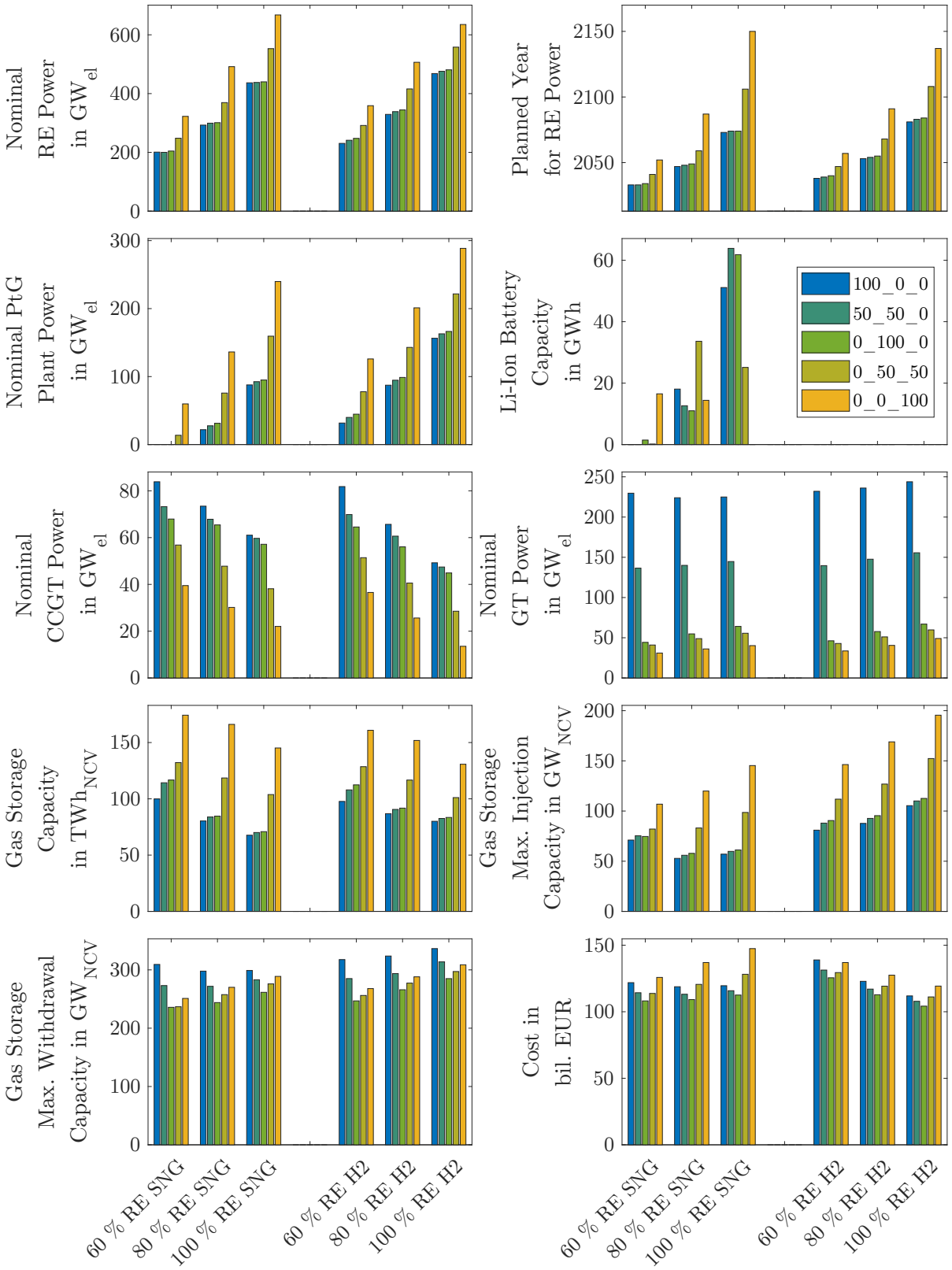

Figure 4.15: Overview of the optimization results of the variations of the heating technologies.

clearly exceed the possible nominal renewable electric power for the respective year (2040, 2045, 2050), going up to the year 2150 for 2050. The extension rates have to rise strongly to reach that amount of nominal renewable power, but the high values might lead to acceptance problems in the population. However, the variations 100_0_0, 50_50_0, and 0_100_0 require very similar values of nominal renewable electric power, which will be for the 60 % RE scenarios until 2040 but not for higher shares. Also, here, the extension needs to speed up, especially when considering that the transportation sector is not included in the model.

The nominal electric PtG power shows the same tendency as the nominal renewable power: It also strongly increases with more renewables and more gas use in the heat sector. All variations employ PtG plants except for 60 % RE SNG 100_0_0, 50_50_0 and 0_100_0. Interestingly, none of the variations including hydrogen uses battery plants, and the SNG scenarios mostly use them, but there is no clear tendency. This might result from the optimization algorithm not finding the absolute optimum due to the competition between PtG and the batteries, even though, for each variation, five optimization runs have been conducted. However, the storage capacities also strongly increase with a rising share of renewables for SNG 100_0_0, 50_50_0, and 0_100_0.

For the power plants, an interesting effect can be seen. The 100_0_0 variations show a very high need for power plants of up to 314 GW_{el} to be able to provide enough power for heat generation at norm ambient temperature. That is more than three times the nominal installed conventional power plant power in 2018, which was 102 GW_{el} (Bundesnetzagentur, 2020), so a large number of power plants would have to be built just to provide electricity for extreme cold spells. In contrast, the total required nominal electric power plant power across all variations can go down to 62 GW_{el} for 100 % RE SNG 0_0_100 since much less re-electrification is required for the scenarios employing gas boilers.

However, the necessary gas storage demand rises with an increasing share of renewables since much gas is used in winter, but it is produced via PtG and biogas production or imported throughout the year. So, a large amount of seasonal gas storage is required. It reaches values between 67.7 TWh_{NCV} and 174.3 TWh_{NCV} for the SNG scenarios and between 80.1 TWh_{NCV} and 160.9 TWh_{NCV} for the H2 scenarios. In comparison, today's natural gas storage capacity is roughly 214 TWh_{NCV} (EID Energie Informationsdienst GmbH, 2019) which equals approximately 47 TWh_{NCV} for hydrogen storage using the factor from Equation (2.8) or even just 29 TWh_{NCV} considering only salt cavern storage plants. So, the current storage capacities in Germany are not sufficient for any of the H2 scenarios.

The required maximum injection capacity of gas storage plants develops similarly to the gas storage capacity. However, it does not exceed today's maximum injection capacity of 164 GW_{NCV} based on EID Energie Informationsdienst GmbH (2019) for the SNG scenarios. In contrast, the H2 scenarios need more maximum injection capacity with 81.03-195.3 GW_{NCV} compared to today approximately 36 GW_{NCV} if all natural gas storage plants were converted to hydrogen and assuming the factor from Equation (2.8).

Contrary to the injection, the maximum withdrawal capacity is always the lowest for 0_100_0 and increases for both higher shares of GB or EHPEHR. Again, the values lie below today's value of 275 GW_{NCV} for SNG scenarios, but all H2 scenarios clearly exceed the equivalent value of 60 GW_{NCV}.

The total system cost given as the annuity differs strongly between the variations. The extreme configurations 100_0_0 and 0_0_100 lead to much higher cost than the hybrid

heating system 0_100_0. The most extreme differences can be found for 100 % RE SNG, where 0_0_100 increases the system cost compared to 0_100_0 by 34.9 bil. EUR, which equals a cost increase by 31 %.

4.2 Quasi-Stationary and Dynamic Gas Grid Computation

This section presents the results of the quasi-stationary and dynamic gas grid computations of the non-aggregated gas grid. In Section 4.2.1, the spatially resolved gas consumption and production are shown to illustrate how the general gas flow will be. In Section 4.2.2, the results of the quasi-stationary gas grid computation are shown, and the results from the quasi-stationary and dynamic computations are compared in Section 4.2.3.

4.2.1 Spatially Resolved Gas Consumption and Production

To get a better impression of the load situation in the gas grid, in Figure 4.16, map representations of gas consumption and production as well as a balance of both are shown for scenario 100 % RE SNG 0_100_0. Since the biomethane potential is fully exploited, it is not displayed here and can be found in Figure 3.20. The maps for the other years and variations look similar and, thus, are not shown here.

In Figure 4.16a, it can be seen that the consumption without power plants is focused in and around cities or metropolitan areas since the population density is high and industrial centers exist there. Also, the power plants are located in those areas, as shown in Figure 4.16b, but sometimes they are rather in the outskirts of a densely populated area, for example, in the Rhein-Ruhr area in Western Germany.

In contrast, the PtG plants are located in places with high cumulative negative residual load over the year, so in rural areas with a lot of renewable power production. This is shown in Figure 4.16c: The production is mainly centered in Schleswig-Holstein, Lower Saxony, and Mecklenburg-Western Pomerania in the north of Germany, where many wind parks are installed and the population density is relatively low. In contrast, Bavaria in the southeast only has low production capacities due to comparatively low installed nominal renewable power.

Combining gas consumption and production, including biomethane, reveals from where to where the gas has to flow through the gas grid, see Figure 4.16d. The balance is dominated by the differences between rural areas with a high potential for PtG and biogas and the densely populated areas with high gas consumption, including power plants. Also, a strong gradient from north to south is visible, so significant gas flows are expected in this direction. Additionally, gas is imported in the north in Dornum and Greifswald, which amplifies this effect.

4.2.2 Pressures in the Gas Grid

To judge the flow situation in the gas grid, the pressures can be investigated. Figure 4.17 shows the pressures in the highest gas grid level at the 463rd hour of the year (January 20, 7:00 am) for scenario 100 % RE H2 0_100_0. To simplify the illustration, only every

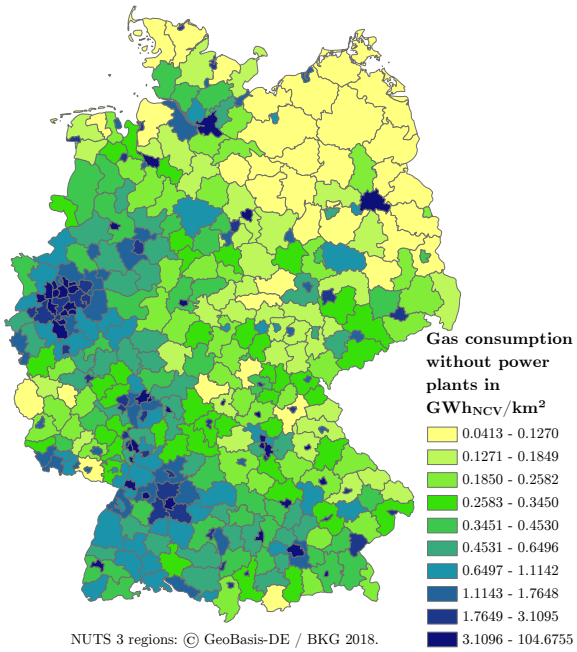

(a) Gas consumption without power plants.

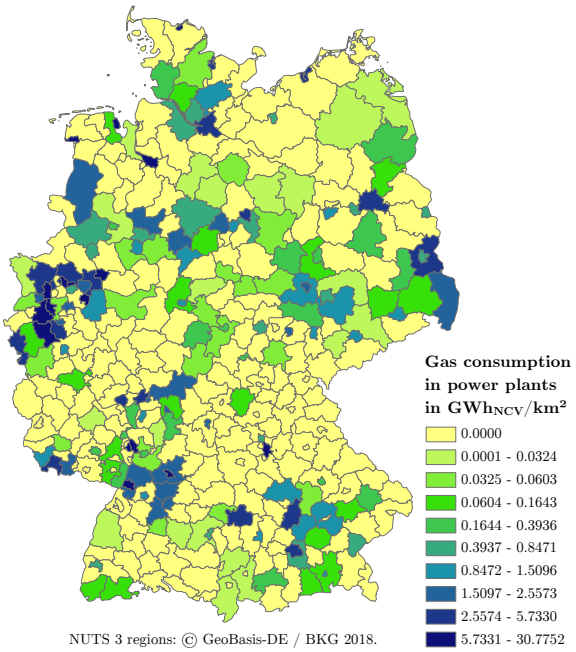

(b) Gas consumption of power plants.

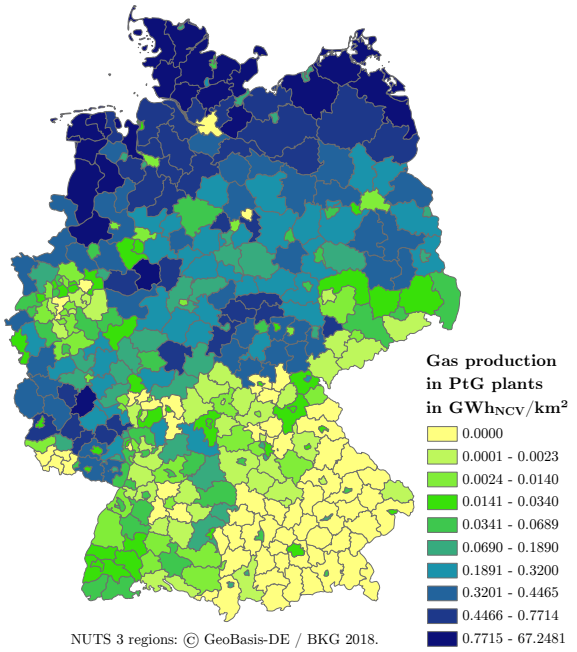

(c) Gas production of PtG plants.

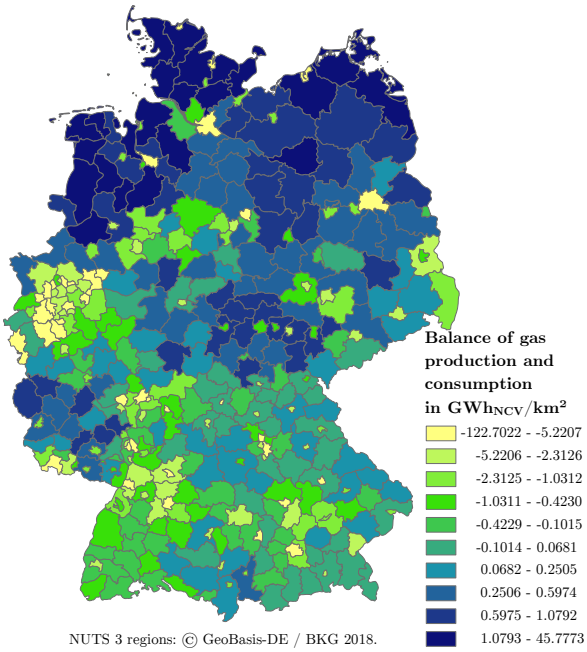

(d) Balance of gas production (positive) and consumption (negative).

Figure 4.16: Map representation of (a) gas consumption without power plants, (b) gas consumption of power plants, (c) gas production from PtG and (d) a balance, also including biomethane for 100 % RE SNG 0_100_0.

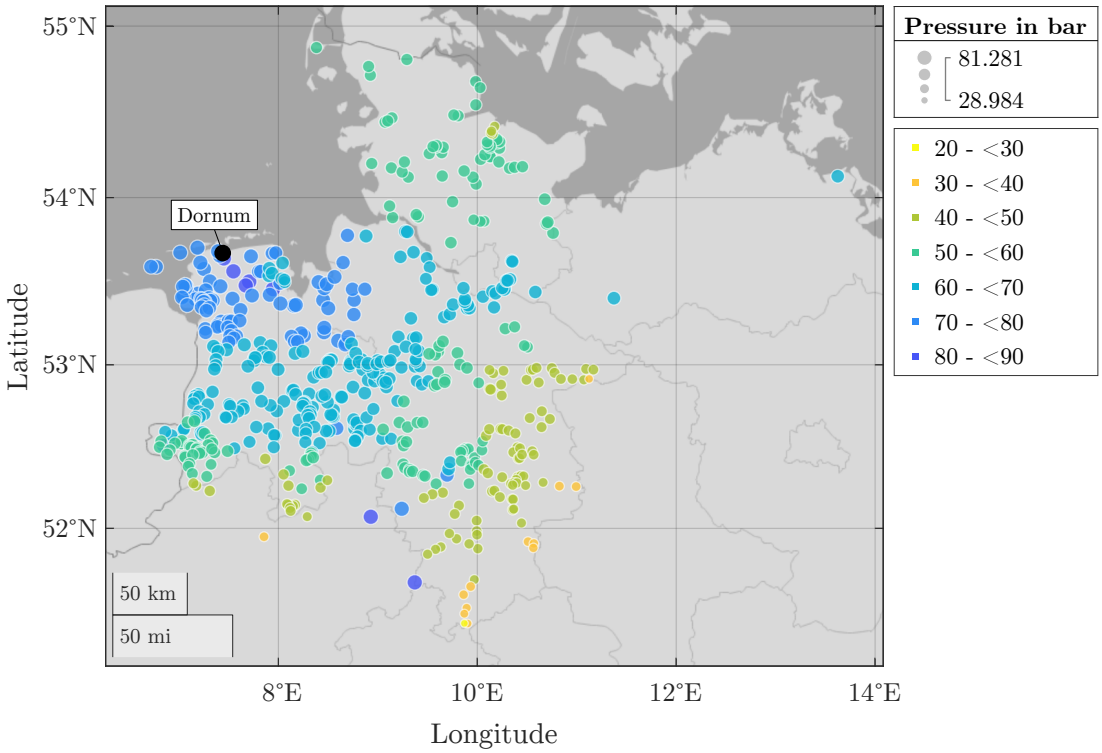

Figure 4.17: Pressure values at every third node of the highest gas grid level at the 463rd hour for 100 % RE H2 0_100_0 (low-pressure situation).

third node is shown. At this point in time, the mean of all pressure values reaches its minimum, so it is the hour where the gas grid is closest to reaching its transport capacity. It is important to note here that Mecklenburg-Western Pomerania has a connection to the gas grid but mostly on lower pressure levels. That is why there are only a few nodes in this state.

For the H2 scenario in Figure 4.17, minimum values of approximately 29 bar occur, mostly at the border of Northern Germany to the rest of Germany. This is due to the large distance to the known pressure node in Dornum in the northwest of Lower Saxony. That is where the high values of above 80 bar lie. The nodes in the south of Lower Saxony with high pressure values are the inner-German import nodes and the connected nodes. Figure A.6 in the appendix shows the same for the SNG scenario, which is less critical with pressures down to 59 bar due to the different density and NCV of natural gas compared to hydrogen. In general, certain minimum pressures have to be maintained at the gas transfer stations to supply the connected lower grid levels, of which the most relevant have MOPs of 16 bar, 25 bar, and 40 bar. However, the gas grids can often be operated with much lower pressures, so an evaluation is complex, but a necessary minimum pressure of 25 bar in the whole grid is assumed.

It is important to mention here that the pressure in most parts of the gas grid lies above the assumed MOP of 70 bar since the known pressure node was set to 80 bar to be able to compute the gas grid for the different scenarios. However, many pipes, especially in the northwest of Lower Saxony, have MOP values of up to 100 bar. Also, in actual grid operation, the gas grid pressure could be decreased so that the MOP is exceeded nowhere

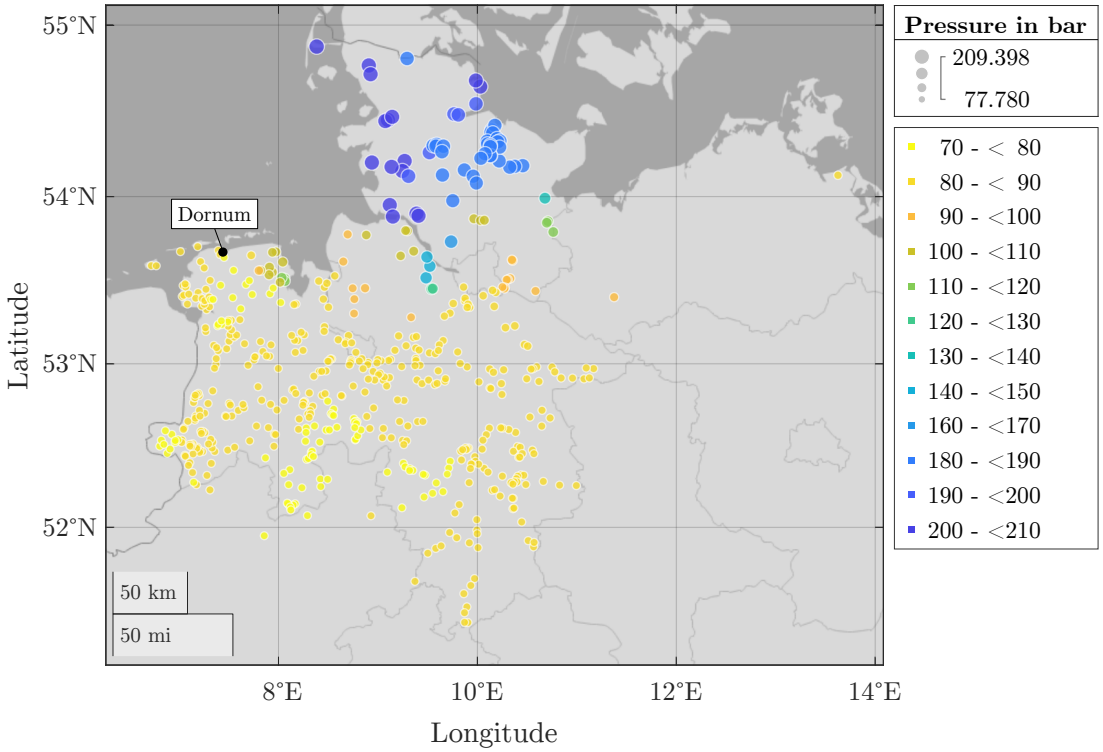

Figure 4.18: Pressure values at every third node of the highest gas grid level at the 5628th hour for 100 % RE H2 0_100_0 (high-pressure situation).

in the gas grid, as long as the smallest pressure values do not reach critical values.

To examine a high-pressure situation, in Figure 4.18 and Figure A.7 in the appendix, the pressures for scenarios 100 % RE 0_100_0 are shown for the 5628th hour (August 23, 12:00 am), which features the highest mean pressure value. Again, the flow situation is more critical for hydrogen (Figure 4.18) than for SNG (Figure A.7), and the lowest pressure values are reached close to the border of Northern Germany to the rest of Germany. However, both scenarios show very high pressures in Schleswig-Holstein due to the high PtG input resulting from very high renewable power generation. This leads to pressures above 106 bar for the SNG scenario and almost 210 bar for the H2 scenario. Those values are too high and require gas grid extension between Schleswig-Holstein and Lower Saxony to be able to transport those large gas quantities.

For scenarios with 100_0_0, a lot of power has to be produced in gas power plants for electric heat generation, and for 0_0_100 scenarios, the gas boilers require much gas. That is why the gas grid computation fails at critical hours of the year for certain H2 scenarios, and a few nodes reach pressures below 1 bar. However, none of the 0_100_0 scenarios is concerned. Those low pressures are shown in Figure 4.19 for 100 % RE H2 100_0_0. It is visible that the low pressures not only occur at the border to the rest of Germany but also in the northwest of Lower Saxony and in Schleswig-Holstein since power plants are located there. This problem could be solved by extending the gas grid or using compressor stations. However, this clearly shows that hybrid heat generation using electricity and gas combined leads to a less critical gas grid operation due to lower gas demand.

This is emphasized by Figure 4.20, which shows a box plot of the pressures at all nodes

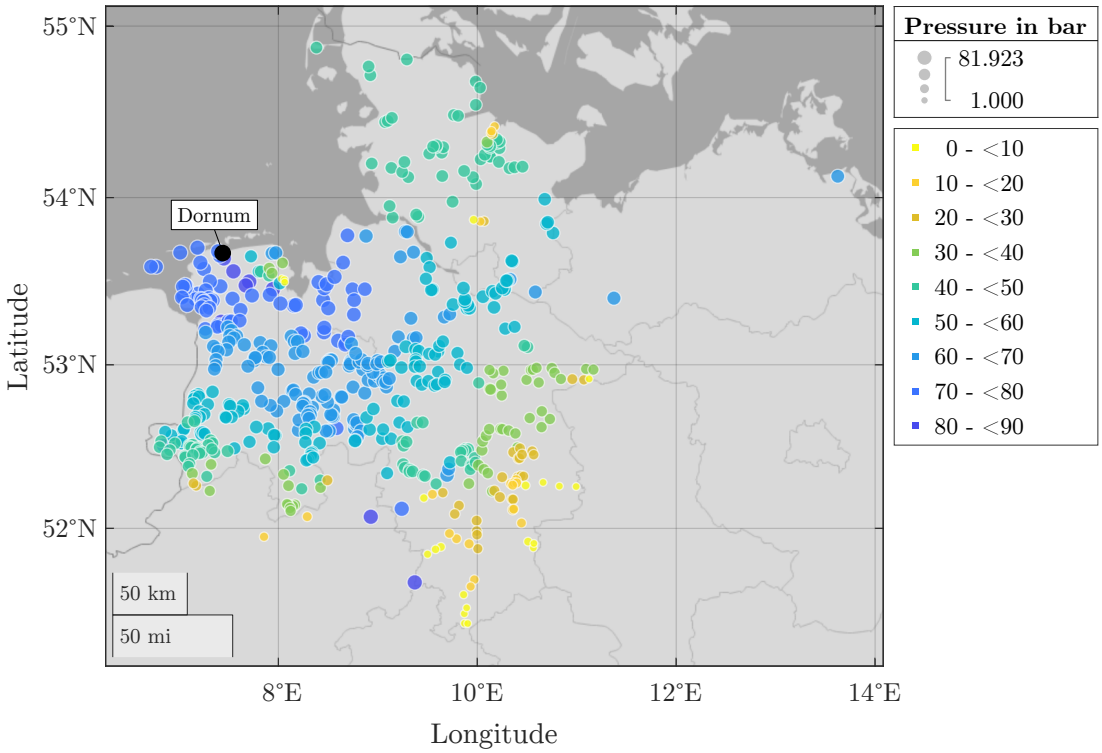

Figure 4.19: Pressure values at every third node of the highest gas grid level at the 463rd hour for 100 % RE H2 100_0_0 (low-pressure situation).

at the 463rd hour. The red line represents the median of all values, whereas the blue box shows the 25th and 75th percentile. The whiskers indicate the minimum and maximum values. This way, it is possible to visualize a large amount of data and its distribution. It is noticeable that the pressure values are always the highest for 0_100_0 across all shares of renewables. 100_0_0 leads to the lowest pressures. The same applies to the use of hydrogen compared to SNG due to its lower density and, thus, higher velocity and pressure loss.

Figure 4.21 shows the same box plot but for the 5628th hour, so the high-pressure situation. Due to very high maximum values, the plot is cut, and the maximum values are written at the top of the plot. This indicates increasing maximum pressures due to rising PtG generation linked to higher shares of renewables and more extensive use of gas in the heat sector. Also, it emphasizes the aforementioned effect: The flow situation is the most critical, due to low pressures, for the 0_0_100 scenarios. Also, for each H2 scenario, the pressures are always more extreme than for the respective SNG scenario, so the minimum values are lower and the maximum values are higher.

4.2.3 Comparison of Quasi-Stationary and Dynamic Gas Grid Computation

In this section, the results of the quasi-stationary and dynamic gas grid computation are compared. As an example, scenario 60 % RE H2 0_100_0 is chosen.

First, the mean error in pressure over the whole year according to Equation (3.78) lies

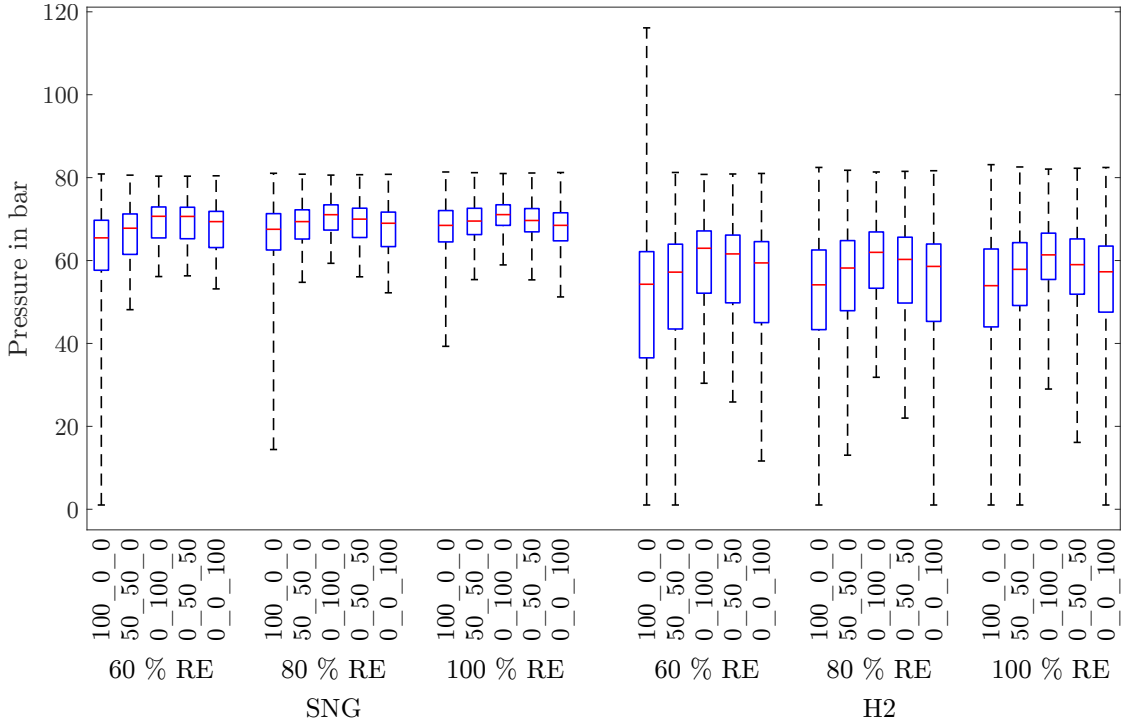

Figure 4.20: Box plot of the pressure values at all nodes of the highest gas grid level at the 463rd hour.

between −0.04 bar and 0.02 bar and has a median close to zero. So, the mean error is minimal. More interesting is the standard deviation of each node over the whole year according to Equation (3.79) since errors can still occur even though the mean values are the same. The standard deviation ranges from almost 0 bar up to 1.8 bar, which means that there is one point that deviates on average by 1.8 bar. Related to the MOP, this equals 2.6 %.

Figure 4.22 depicts each node's standard deviation, which has a standard deviation greater than 0.8 bar on a map. This reveals that the error rises with an increasing distance from the known pressure node in Dornum. In the south of Lower Saxony and the north of Schleswig-Holstein, the highest values occur.

This can be explained by the considered dynamic effects in the dynamic simulation: Due to the volume of the gas grid, dampening of the changes in pressure occur, which are neglected by the quasi-stationary computation. This can be illustrated with Figure 4.23, which depicts the pressure curves during the high load period at the node with the highest standard deviation. It shows that the curve of the quasi-stationary simulation reacts to demand changes with higher peaks in pressure due to its inherent negligence of the dampening effects. The dynamic simulation reflects the more physical behavior. Compared to the quasi-stationary simulation, it looks slightly delayed and with lower peaks comparable to a delay in a first-order differential equation.

Next to the pressures, also the mass flow rates play an important role in a gas grid operation. To examine the differences in mass flow rates, the utilized grid capacity is calculated for each hour of the year according to Equation (3.85). Investigating the distribution reveals that the median is almost identical, with 15.3 % for the quasi-stationary

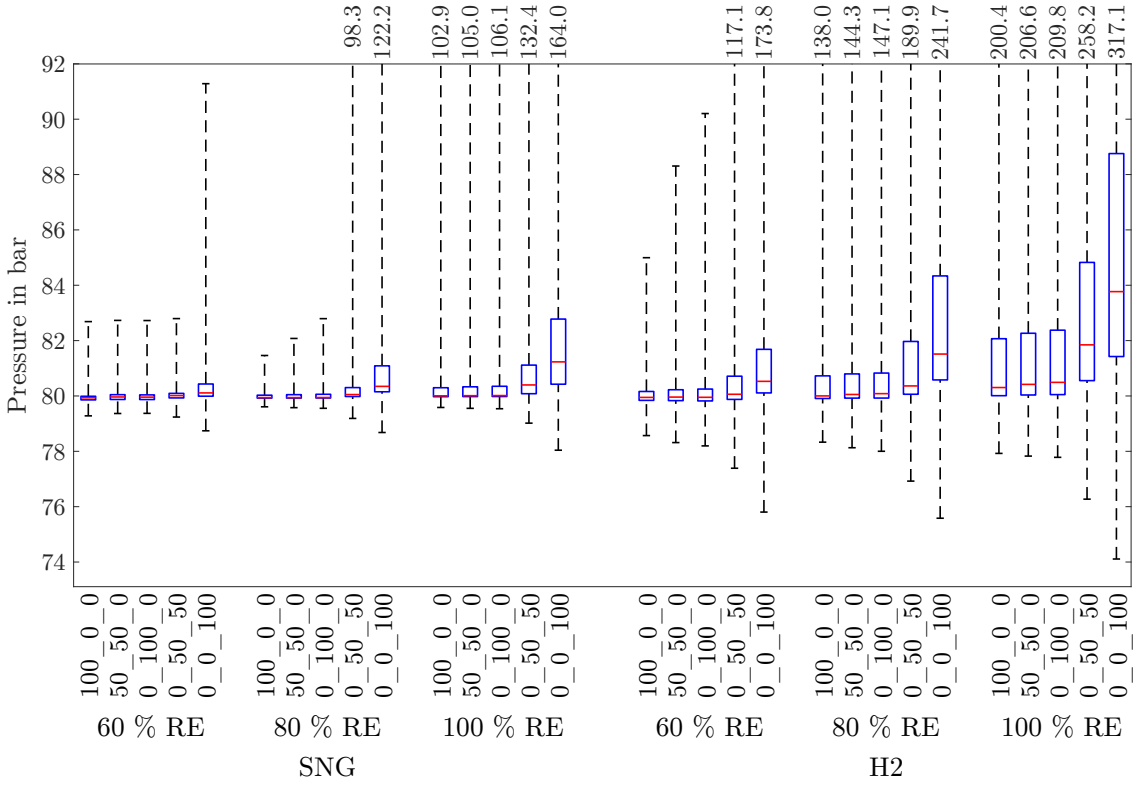

Figure 4.21: Box plots of the pressure values at all nodes of the highest gas grid level at the 5628th hour. The values at the top indicate the maximum value if it exceeded the shown range of the plot.

and 15.2 % for the dynamic simulations. Also, minimum (10.4 % vs. 10.0 %) and maximum (57.9 % vs. 53.6 %) values are very similar.

In the next step, the gas grid extension additional to the existing 44 000 GW_{NCV} km for hydrogen is determined according to Equation (3.87). Following the quasi-stationary gas grid computation, 8450 GW_{NCV} km of gas pipelines would have to be added, whereas the dynamic gas grid simulation only indicates 7526 GW_{NCV} km. This confirms that the dynamic simulation considers the dampening and does not reach as high or low peaks as the quasi-stationary computation.

In conclusion, it can be stated that the dynamic and quasi-stationary gas grid computation match well since the fundamental physics are the same. The most significant difference lies in the dynamic change of pressure, leading to a delay at nodes far away from the known pressure node. This also shows that the quasi-stationary grid computation covers the worst case, and the dynamic simulation can show the available grid buffer in actual operation.

4.3 Aggregation of the Gas Grid

For the aggregation of the gas grid, the results of the gas grid computation will be used. Therefore, an appropriate point in time needs to be found at which the aggregation algorithm will use the mass flow rate and pressure values. Since the total gas demand,

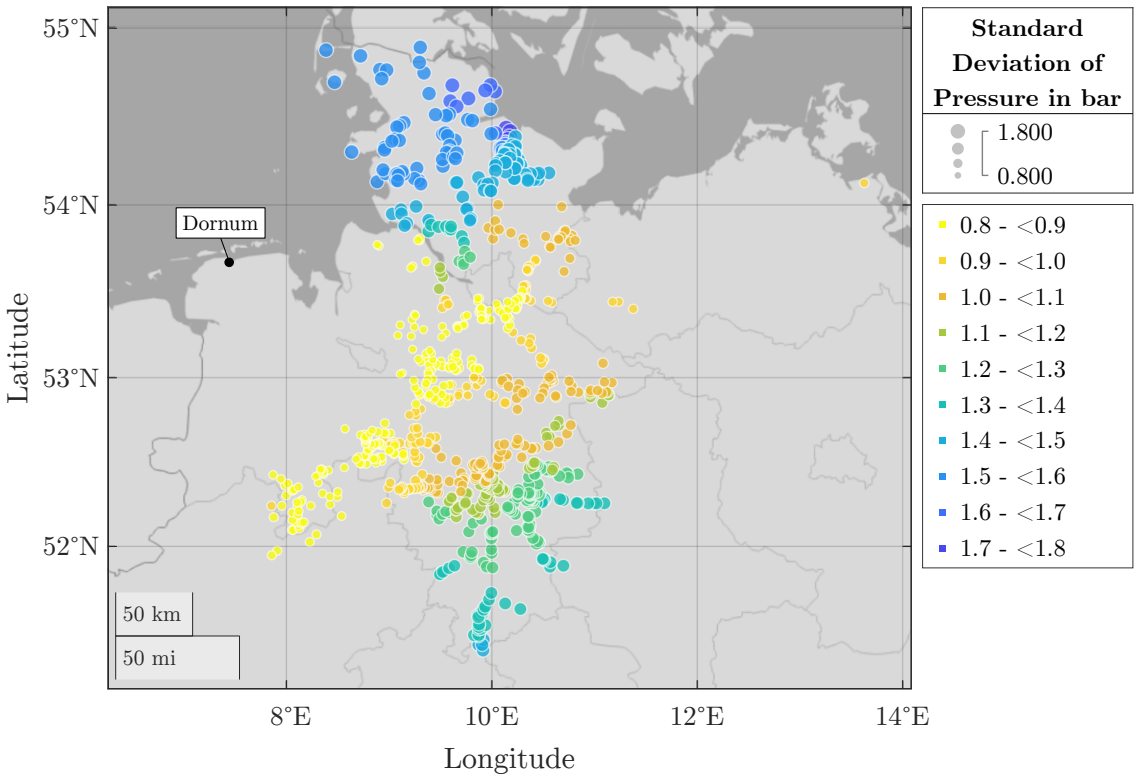

Figure 4.22: Map representation of the standard deviation in pressure of all nodes with values of more than 0.8 bar over the whole year with 60 % RE H2 0_100_0.

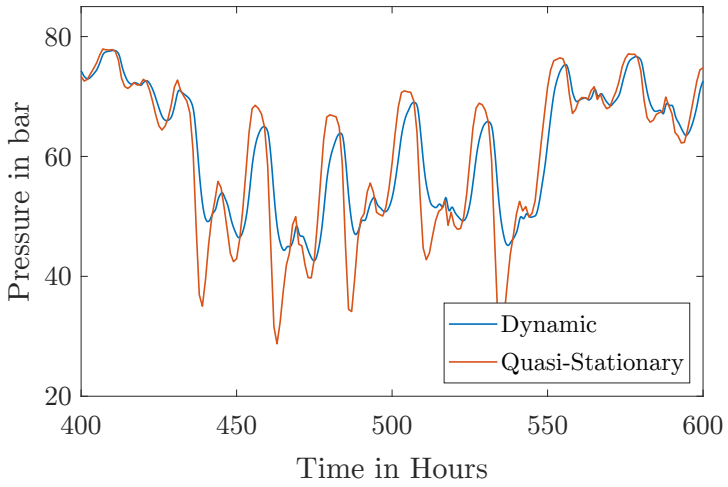

Figure 4.23: Comparison of the pressure in the node with the highest standard deviation in pressure for 60 % RE H2 0_100_0.

including power plants, is the highest at the 464th hour of the year, this results in the lowest absolute pressure values in the gas grid. To minimize the errors, which are especially critical at this point in time due to the very low pressures, this hour was chosen for every scenario. Since the pressure and mass flow rate values in the gas grid differ from one scenario to the other, the gas grid is aggregated for each scenario separately to reduce the resulting error.

However, as shown in Section 4.2.2, the gas grid computation for certain scenarios and hours results in pressures below 1 bar, which means that the results are not adequate for the aggregation. That is why, in those cases, the closest hour for which the gas grid computation did not fail was chosen. Like this, for every scenario, an appropriate point in time for aggregation can be found between the 462nd and the 467th hour.

In the following, the results of the aggregation will be presented. Pressures and mass flow rates in the gas grid result from dynamic simulation of the concerning gas grid.

4.3.1 Changes in the Gas Grid Structure

First, the gas grid structure changes during different steps of the aggregation are shown in Figure 4.24 for scenario 60 % RE H2 0_100_0. The color shows the average utilized pipe capacity according to Equation (3.84). It is visible that the aggregation algorithm significantly reduces the number of pipes and, thus, the complexity of the gas grid. An aggregation grade of 98.2 % according to Equation (3.77) is reached at the end of the aggregation. Also, from a graphical comparison, one can see that the gas grid utilization stays similar in the different areas, so this information is contained. The connections to the rest of Germany are particularly highly utilized, which is linked to the significant gas transfer. Also, high grid utilization can be seen in the west of Lower Saxony, where large gas storage plants are located.

To illustrate the effect of the gas grid reduction on numerical complexity, in Figure 4.25, the changes of CPU time and number of loops over aggregation grade are shown. All values are relative to the non-aggregated grid. The number of pipes and nodes equals the number of states in the dynamic model since in each pipe or junction volume the pressure appears as a state. The states are the variables for which the solver tries to solve the system of equations, and reducing the states usually reduces the CPU time.

The aggregation almost proportionally reduces the CPU time according to the reduction of states, so the aggregation reaches its goal by making the model faster. However, the CPU time reduction is even slightly stronger than proportional, illustrated by the angle bisector. This can be explained by the additional reduction of loops in the gas grid. At first, the reduction of loops is slower than proportional but speeds up with higher aggregation grades, simplifying the gas grid even more than the pure reduction of pipes and nodes. The original highest gas grid level has 570 loops at 2237 pipes compared to 2 loops at 35 pipes which equals a reduction of 99.6 %, which is higher than the corresponding aggregation grade and leads to a CPU time reduction of 99.4 %.

4.3.2 Pressures in the Gas Grid

In the next step, the changes in the pressure values at the nodes after aggregation will be investigated. Due to the design of the aggregation algorithm, the pressures at the

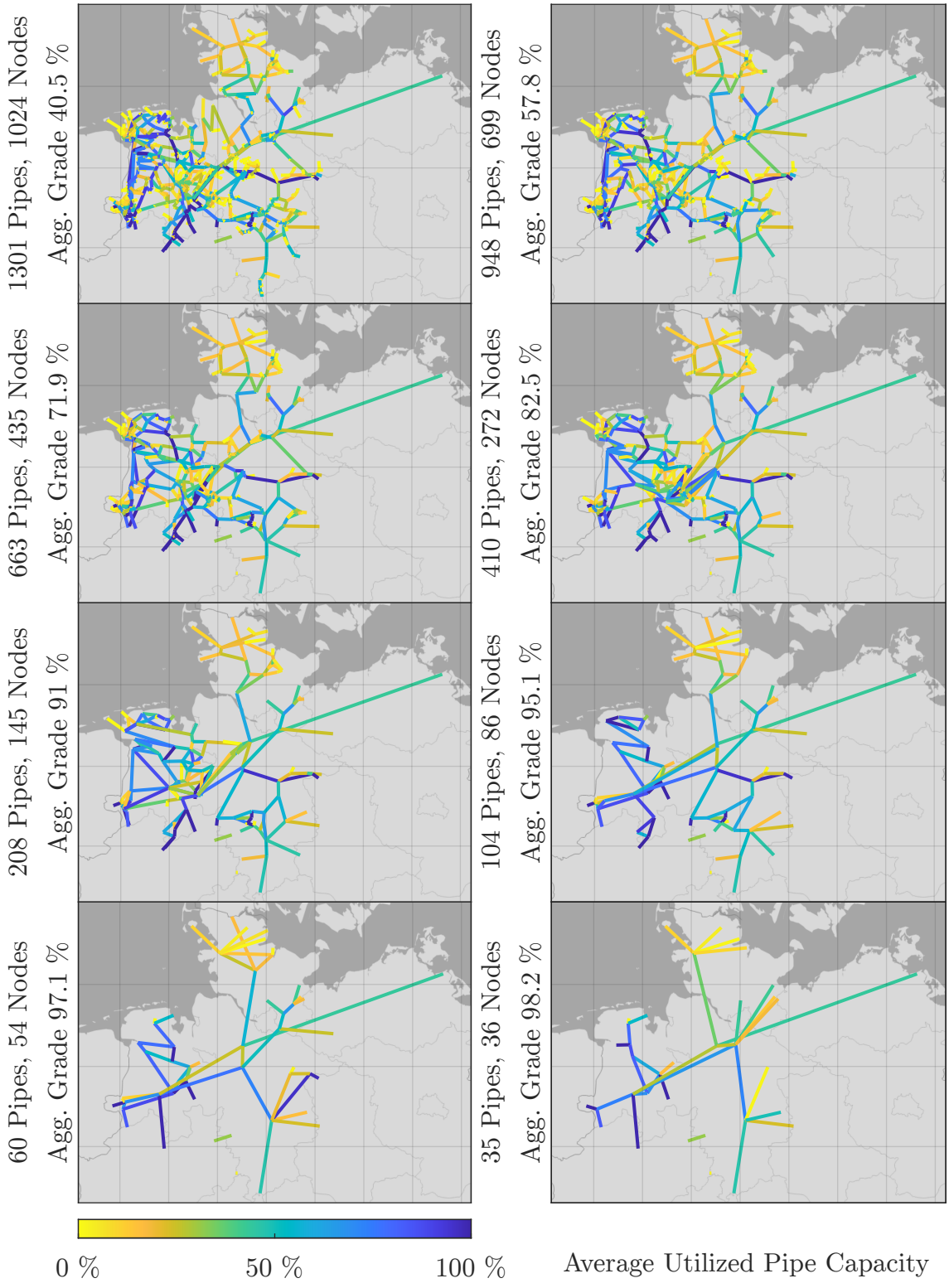

Figure 4.24: Map representation of the gas grid structure at different aggregation steps for 60 % RE H2 0_100_0. The color marks the average utilized pipe capacity.

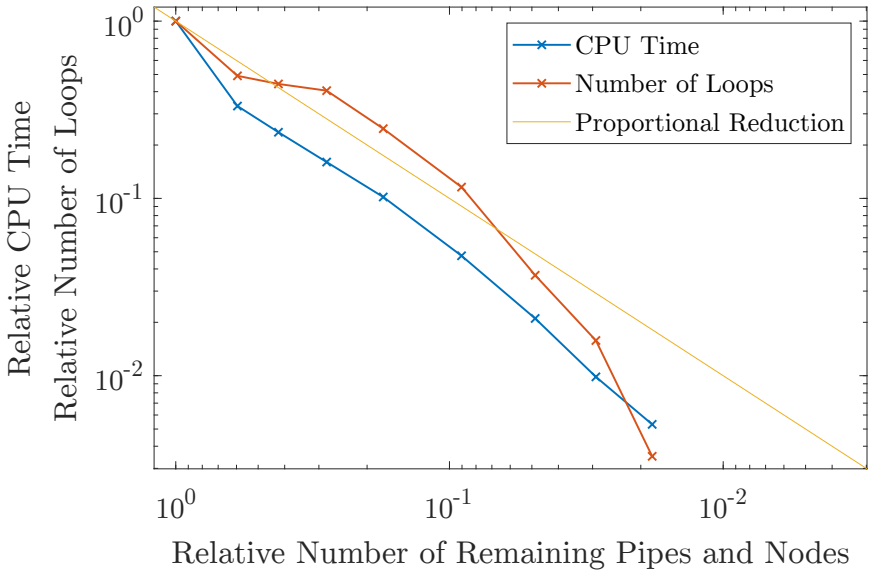

Figure 4.25: Relative CPU time and number of loops over relative number of remaining pipes and nodes for different aggregation grades for 60 % RE H2 0_100_0.

nodes are still the same at the time instance whose data was used for the aggregation. An exception can be deviations due to the aggregation of short pipes when the pressure at the nodes is adapted to avoid negative pressure losses. However, at other times, there will be errors since the flow situation will be different than at the time instance of aggregation.

To illustrate that, Figure 4.26 depicts the resulting errors over a whole year for scenario 60 % RE H2 0_100_0. For different aggregated grids, the remaining nodes' pressure values are compared to their original values in the non-aggregated gas grid. Figure 4.26a depicts the standard deviation in the pressure of all nodes according to Equation (3.79). Its minimum, maximum, and median values increase with the declining number of pipes with minor exceptions. Furthermore, Figure 4.26b shows the mean error in pressure according to Equation (3.78). The values are similar between 1301 and 208 pipes, but the absolute error increases stronger from 104, and especially from 35 pipes on. This equals aggregation grades of 95.1 % and 98.2 %, respectively. Starting at 35 pipes, the absolute values of the minimum and maximum jump to -1 bar and 3 bar, respectively, so much larger errors occur. It is important to note here that those are values over a whole year, so the exact deviations can be much higher.

Figure 4.27 shows the pressure at the node with the highest standard deviation, which is located close to Kiel in Schleswig-Holstein, for different aggregation steps. It is noticeable that the error is not zero at the time instance based on whose data the gas grid was aggregated, that is, the 464th hour (marked in red). This is linked to the aggregation of short pipes where the node's pressure is adapted in certain cases. However, the deviation is comparatively small, also at other time instances. The largest error occurs for the gas grid with 35 pipes due to the significant simplifications.

If the standard deviation and mean error in pressure are compared between the scenarios over different aggregation grades, it can be seen that the tendency is the same: The errors increase with higher aggregation grades. Furthermore, higher shares of renewables as well as hydrogen compared to SNG lead to larger errors. Also, the heating system 0_100_0

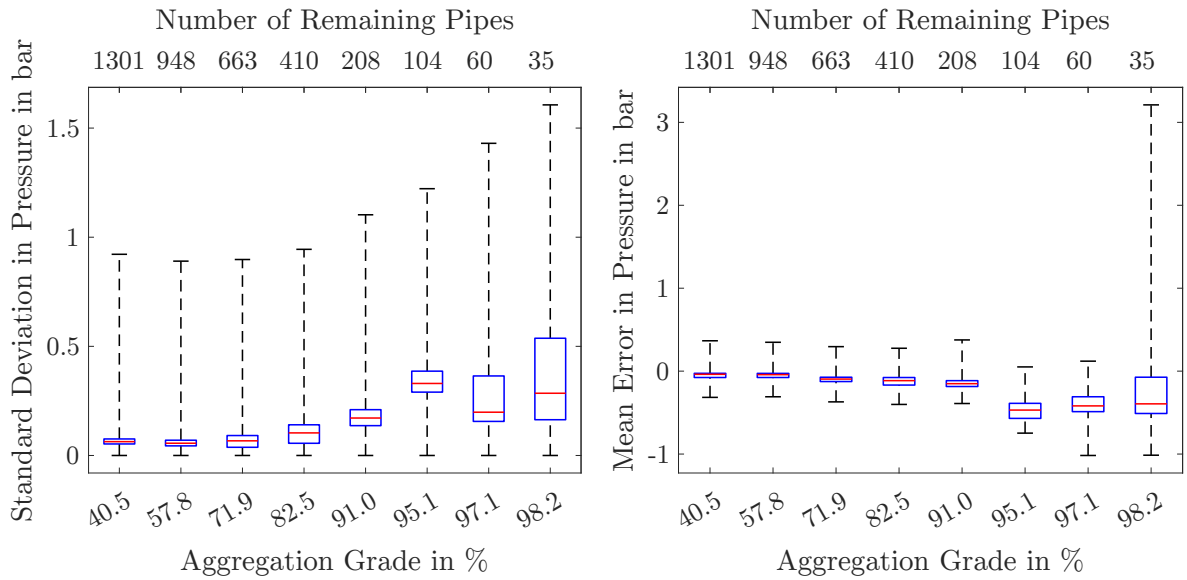

(a) Standard deviation. **(b)** Mean error.

Figure 4.26: Box plots of the standard deviation and mean error in pressure for different aggregation steps for 60 % RE H2 0_100_0.

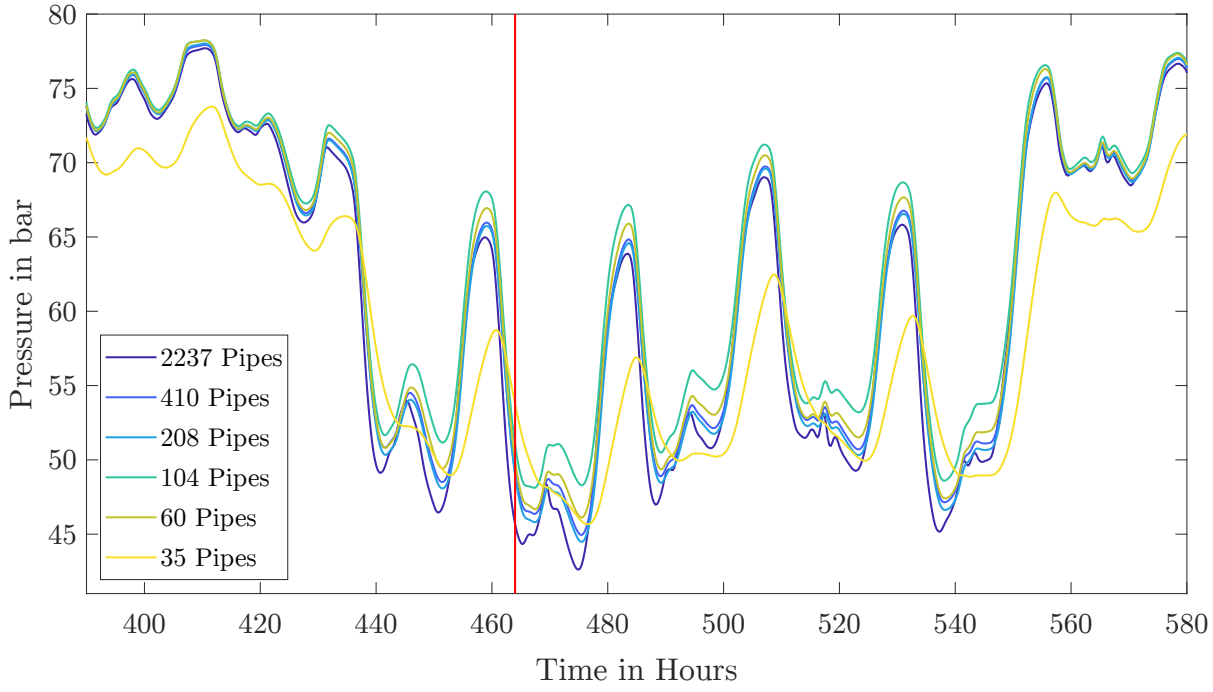

Figure 4.27: Pressure at the node with the highest standard deviation for different aggregation steps for 60 % RE H2 0_100_0. The time instance based on whose data the gas grid was aggregated is marked in red.

results in the smallest errors. This leads to the following conclusion: The higher the gas grid utilization, the larger the errors. This is caused by increased gas use in the heat sector or power plants and extended fluctuating gas production in PtG plants.

4.3.3 Required Gas Grid Extension

One essential result of the gas grid model is the required gas grid extension to sustain a working gas grid in the future according to the scenarios. Since the aggregation strongly simplifies the gas grid, the model must not significantly lose precision in predicting the required gas grid extension. That is why this value was calculated for each of the aggregation steps of scenario 60 % RE H2 0_100_0 and depicted in Figure 4.28.

Despite the considerable simplification of the gas grid, until 208 pipes, the value stays quite the same. However, aggregating the gas grid further leads to larger errors of 41.5 % for 104 pipes and 73.6 % for 60 pipes compared to the non-aggregated gas grid. The errors can be explained by the combination of pipes with high and low utilized capacity, which prohibits the detection of pipes operated at the limit. The more pipes are aggregated, the more significance this effect gains. Nevertheless, it is crucial to see the absolute error values in relation to the current gas grid capacity for hydrogen, which is 44 000 GW_{NCV} km. So, an error of, for example, 382 GW_{NCV} km for the gas grid with 104 pipes resembles less than 1 % of the gas grid capacity.

Comparing the required gas grid extension over different scenarios, as shown in Table 4.1, reveals that the values are much higher for H2 scenarios and increase for higher shares of renewables in most cases. Also, the extended use of both electricity and gas in the heat sector requires more gas grid capacity. A more thorough analysis of this aspect is done in Section 4.4.1.

Figure 4.29 shows how the relative errors in gas grid extension develop with higher aggregation grades. For the SNG scenarios in Figure 4.29a, the relative errors are already relatively high for low aggregation grades. Also, most scenarios reach relative errors of

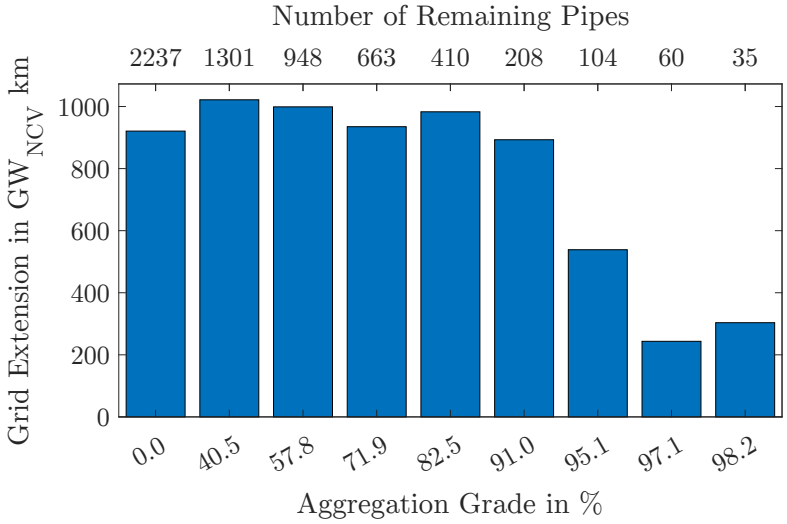

Figure 4.28: Required gas grid extension for different aggregation steps for 60 % RE H2 0_100_0.

Table 4.1: Required gas grid extension based on the dynamic simulation of the non-aggregated gas grid. For the H2 100_0_0 scenarios, the simulations failed due to too low pressures.

Required Gas Grid Extension in GW_{NCV} km				
		100_0_0	0_100_0	0_0_100
SNG	60 % RE	109.7	25.7	35.8
	100 % RE	75.6	43.1	651.8
H2	60 % RE	-	920.8	2625.1
	100 % RE	-	3894.5	7423.1

−100 % at aggregation grades above 95 %, which means no gas grid extension is required. However, those extreme values have to be seen in relation to the absolute required gas grid extension values in Table 4.1, which are very low for most SNG scenarios. For scenario 100 % RE SNG 0_0_100, the SNG scenario with the highest required gas grid extension shown here, has comparatively low relative errors up to aggregation grades just above 95 %.

The relative errors for the H2 scenarios show a similar behavior; see Figure 4.29b. The 100_0_0 variations are not shown because the simulations failed since too low pressures in the gas grid occur due to aggregation errors and high gas grid utilization. The relative error is maximum 22.6 % until more than 90 % of the gas grid have been aggregated, which resembles a gas grid with approximately 200 pipes. For 100 pipes or aggregation grades of approximately 95 %, the relative error ranges from 23.24 % to 42.6 %. Afterward, relative errors of up to 85.6 % occur.

In conclusion, the aggregation leads to high relative errors for small values of required gas grid extension. However, the relative errors are comparatively small for aggregation grades of 90 % and rise strongly afterward.

4.4 Dynamic Simulation of the Integrated Energy System

Section 4.3 showed that the errors increase with higher aggregation grades, but the CPU time reduces significantly. In the next step, the gas grid will be combined with the rest of the IES. For this, an aggregation grade has to be chosen at which the precision of the gas grid model and its numerical efficiency keep a good balance. The gas grid aggregation was executed for each scenario, and a gas grid with approximately 100 pipes was chosen, which approximately equals an aggregation grade of 95 %.

The dynamic IES models for the H2 scenarios take 29-40 h to simulate, whereas the SNG scenario models take 54-119 h using the solver `Radau IIa` with a tolerance of 10^{-5} on a desktop computer with an Intel® i7-8700 CPU and 32 GB RAM. The difference between SNG and H2 scenarios results from the additional gas properties, which have to be calculated for methane, as well as the lithium-ion batteries and the more complex PtG plants used in most SNG scenarios.

The gas storage plants in the regions play a crucial role in the simulation since they control the pressure at the respective nodes. The pressure at the gas storage within the region is attempted to equal the set pressure according to Equation (3.76). However, the

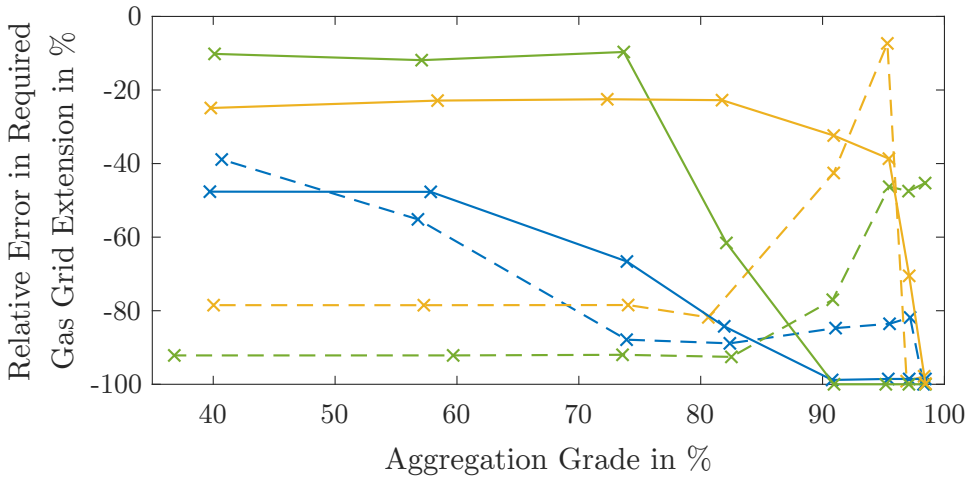

(a) SNG scenarios.

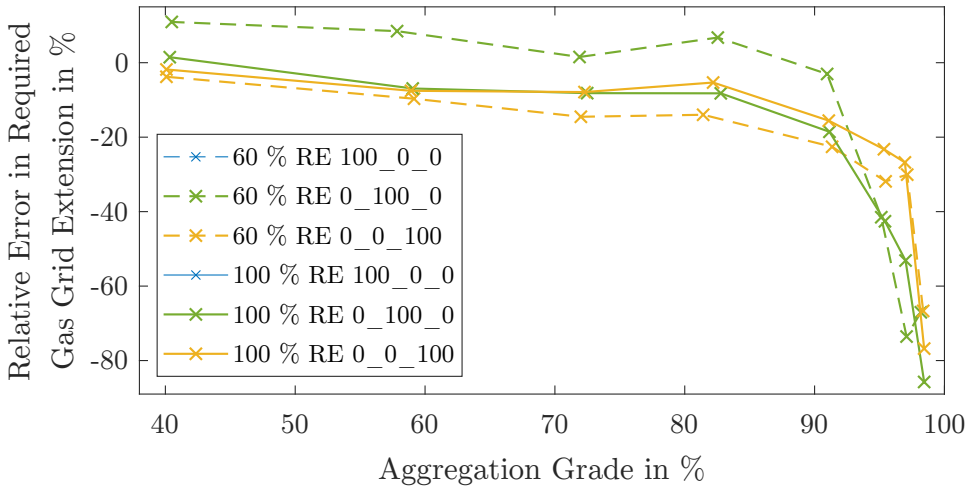

(b) H2 scenarios.

Figure 4.29: Relative error of required gas grid extension over different aggregation grades for selected scenarios.

gas storage capacity as well as the injection and withdrawal capacity limitations apply. That is why the pressure at certain nodes reached values below 1 bar, leading to simulation failure. To avoid this, there are two options: First, the gas storage volume in Region 10 can be increased since it is the only gas storage in the east of Northern Germany and it is comparatively small. However, it plays a significant role for the gas pressure in this region and can lead to too low pressures when the gas storage is empty. So, for 60 % RE SNG 0_0_100, 80 % RE SNG 50_50_0, and 80 % RE SNG 0_0_100 it is increased by factor 5 and for 80 % RE SNG 100_0_0, 100 % RE H2 100_0_0, and 100 % RE H2 50_50_0 by factor 2 compared to the other simulations. Second, the maximum injection and withdrawal capacities of the gas storage plant in Region 10 can be increased. This helps if the pressure falls too low because the withdrawal capacity is limited. So it is increased by factor 1.5 for 80 % RE SNG 0_0_100 and by factor 1.2 for 80 % RE SNG 50_50_0 to ensure a stable gas grid operation.

4.4.1 Required Gas Grid Extension

Figure 4.30 shows the required gas grid extension over all variations for the dynamic IES model. It also includes the results for the non-aggregated quasi-stationary gas grid model and the dynamic aggregated gas grid model with 100 pipes. To distinguish the missing simulation of the aggregated dynamic gas grid model of scenario 60 % RE H2 100_0_0, which did not work due to too low pressures, from zero values, it is marked with a short red bar. For better comparison, the same scale is used for all H2 and SNG scenarios, respectively.

As shown in Section 4.2.3, the quasi-stationary and dynamic gas grid simulations match well, but the dynamic simulations are a bit dampened, so lower required gas grid extension is expected. Also, the required gas grid extension decreases with higher aggregation grades, as has been presented in Section 4.3.3. That is why the required gas grid extension is always lower for the simulation of the aggregated grid with 100 pipes. One outlier is scenario 60 % RE SNG 50_50_0 due to higher deviations resulting from the aggregation.

For most scenarios, the required gas grid extension values based on the results of the dynamic IES model also lie below the values for the aggregated gas grid model or at a similar level. This can be explained by the function of the gas storage plants: In the gas grid models without the rest of the IES, the gas storage plants are operated by curves given by the optimization, whereas in the dynamic IES model, they are controlled according to the gas grid pressure at the respective nodes. This leads to a gas grid operation that is more adapted to the flow situation in the gas grid. Also, the operation of the power plants and PtG plants is modeled in more detail in the dynamic IES model since the power and gas production depends on each region's local residual load. In contrast, in the gas grid models without the rest of the IES, the power plants and PtG plants are also simply following the curve given by the optimization. So, the consideration of the whole system has a benefit since less gas grid extension is sufficient for most of the scenarios.

Only for all H2 0_0_100 scenarios and 60 % RE SNG 100_0_0, the required gas grid extension based on the dynamic IES model is much higher than for the aggregated dynamic gas grid model. The differences between the scenarios can be explained by the following: For the quasi-stationary and dynamic gas grid models without the rest of the IES, the required gas grid extension is mostly driven by the demand during cold spells in winter. Especially the gas transfer to the rest of Germany requires a lot of grid capacity, as can be seen in Figure 4.24. For the dynamic IES model, the required gas grid extension is mostly caused by two effects: First, it can also be caused by the demand during cold spells, then the gas grid extension values are smaller or very similar. This is due to the more advanced control of the gas storage plants, which considers the pressure and leads to better use of the gas grid capacity. Second, gas storage injection can require a lot of gas grid capacity. With an increasing gas use in the heat sector, the required gas storage and injection capacities increase, see Figure 4.15. At the beginning and middle of the year, it can occur that the gas storage volumes in the rest of Germany are full, which represent roughly half of the whole German gas storage capacity. Then, the gas storage plants in the northwest of Lower Saxony take up large quantities of gas from all over Germany, especially from PtG from Schleswig-Holstein. This leads to the required gas grid extension, especially when the heat sector demands much gas, such as in the 0_0_100 scenarios. For 60 % RE SNG 100_0_0, the reason for the high value of required gas grid extension lies in the high gas demand of power plants to supply electricity for heating during the cold spell.

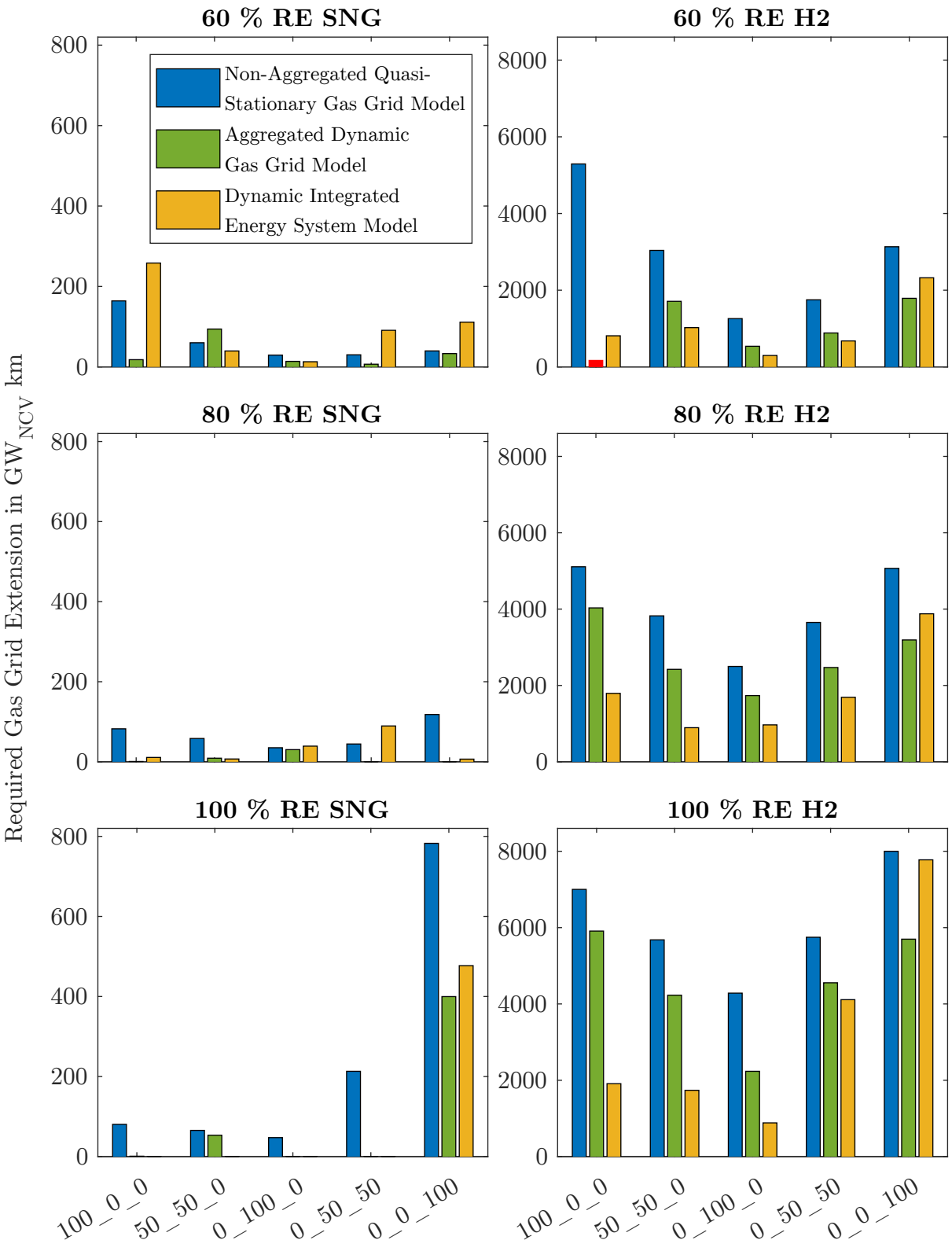

Figure 4.30: Required gas grid extension resulting from the different models for all scenarios. Failed simulations are marked in red.

Due to the different properties of the gases, there is a striking difference between the SNG and H2 scenarios: For SNG, there is either no or just a small amount of gas grid extension necessary. The maximum value based on the dynamic IES model is 477 GW_{NCV} km, whereas, for H2, it is 7776 GW_{NCV} km. For both H2 and SNG, the maximum values occur for 100 % RE 0_0_100. However, this extension should be regarded as related to the current gas grid capacity of 88 000 GW_{NCV} km for SNG and 44 000 GW_{NCV} km for hydrogen. This merely resembles a gas grid extension by 0.5 % for SNG and 17.7 % for hydrogen, respectively, which is much less than for the power grid, as presented in Section 4.4.2.

Furthermore, for all scenarios, the non-aggregated quasi-stationary gas grid model resulted in the lowest gas grid extension values for variation 0_100_0 and increasing values towards either more use of power or gas in the heat sector. The dynamic IES model confirms this in most cases. However, for 80 % RE H2, scenario 50_50_0 has a slightly lower value than 0_100_0. For the SNG scenarios, the required gas grid extension values are mostly very small and, thus, lie very close to each other. That is why 0_100_0 is mostly close to the minimum. The minimum values for each renewable share occur at 60 % RE SNG 0_100_0, 80 % RE SNG 0_0_100 and for 100 % RE SNG 100_0_0-0_50_50.

To illustrate where the gas grid needs to be extended, Figure 4.31 shows the gas grid of exemplary H2 scenarios where the color marks the gas grid extension. The clear difference between the 60 % and 100 % RE scenarios is visible, as well as the discrepancy between the variation of heating technologies in each renewable share category. The gas grid extension focuses on two areas: First, the connection between Schleswig-Holstein and Lower Saxony to integrate the high production of hydrogen from PtG into the gas grid. Second, the connection of the gas storage plants in the northwest of Lower Saxony so that they can take up excess gas. The rest of the gas grid either does not have to be extended or just to a minor extent.

4.4.2 Required Power Grid Extension

Figure 4.32 shows the required power grid extension for all scenarios calculated from data from the dynamic IES model according to Equation (3.91). The required power grid extension increases with the rising use of gas in the heat sector since then also the amount of PtG increases. This necessitates extensive transport of renewable electric power and, thus, a lot of power grid extension. For 100 % RE, the power grid extension also rises for increasing use of power for heating since power plants need to produce much electricity during cold spells. This causes a high need for power transmission lines as well.

Another trend is that the required power grid extension increases with higher shares of renewables since, in general, the use of electricity, especially for PtG, rises. H2 scenarios require more power grid extension in all variations since the power grid extension is mainly coupled to the amount of renewable generation, which is higher for H2 scenarios than the respective SNG scenarios. Only for 100 % RE 0_0_100, the SNG scenario needs more power grid extension than the H2 scenario since more renewable power is required for the SNG scenario due to very high amounts of demanded SNG.

The minimum values of required power grid extension lie between 100_0_0 and 0_100_0 for all scenarios, so in the direction of increased use of power in the heat sector.

Relative to the original transmission grid capacity of 4100 GW_{el} km, the power grid

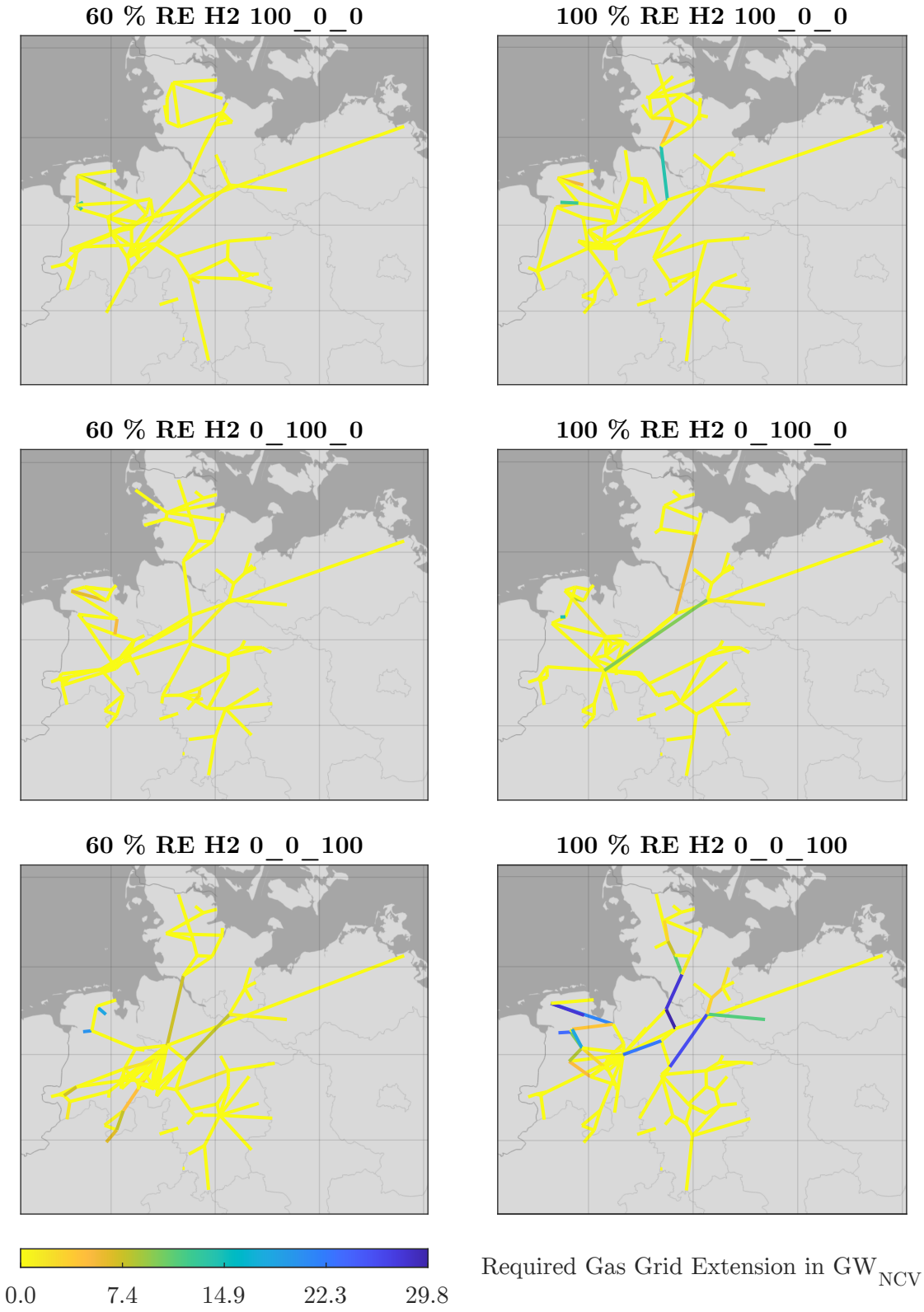

Figure 4.31: Maps of the required gas grid extension resulting from the dynamic IES models for selected H2 scenarios.

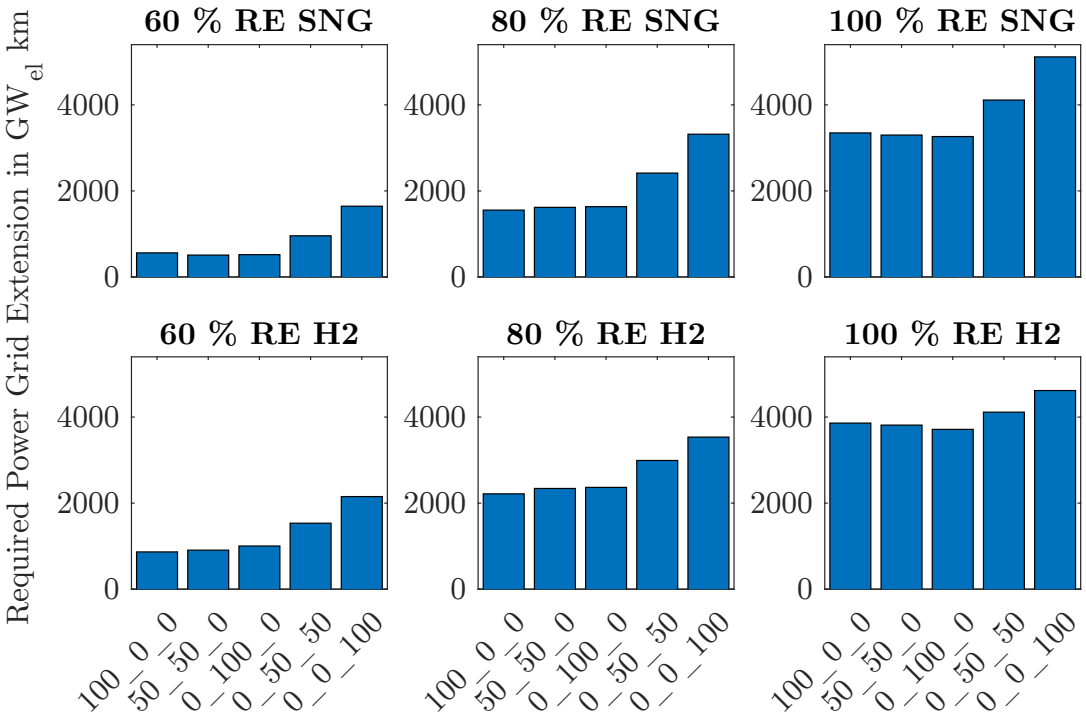

Figure 4.32: Required power grid extension for all scenarios.

extension ranges from 12.4 % to 124.8 %. So, the power grid has to be extended to a much larger extent than the gas grid for all scenarios.

Figure 4.33 shows the required power grid extension on a map for selected H2 scenarios. Note that only the transmission lines that have to be extended are depicted here. In general, it is visible that most of the extension is required in the north-south direction, especially from the regions with high renewable generation in Schleswig-Holstein and the northwest of Lower Saxony to the south of Germany. This effect is more substantial for more extensive gas use in the heat sector as well as higher shares of renewables due to the enormous rise in renewable power generation. The SNG scenarios show very similar results.

4.4.3 Cost for Gas and Power Grid Extension

To truly compare the grid extension in both grids, the annuities are calculated according to VDI 2067 Part 1 (Sep. 2012) using cost assumptions listed in Table 4.2. For the gas pipelines, a diameter of 600 mm is assumed since this represents approximately the average diameter of the existing highest gas grid level. For the power transmission lines, new erections of 380 kV double circuit lines with 4000 A maximum current, comparable to typical projects in 50Hertz et al. (2021a), are assumed. To connect the power transmission line to the surrounding power grid, power transformers for 110/380 kV and the required switch fields are added at the beginning and end of each new transmission line.

The resulting costs are shown in Figure 4.34. It is clear that the power grid extension dominates the cost in all scenarios but especially in the SNG scenarios since almost no gas grid extension is necessary. However, even for the H2 scenarios, the cost for power grid

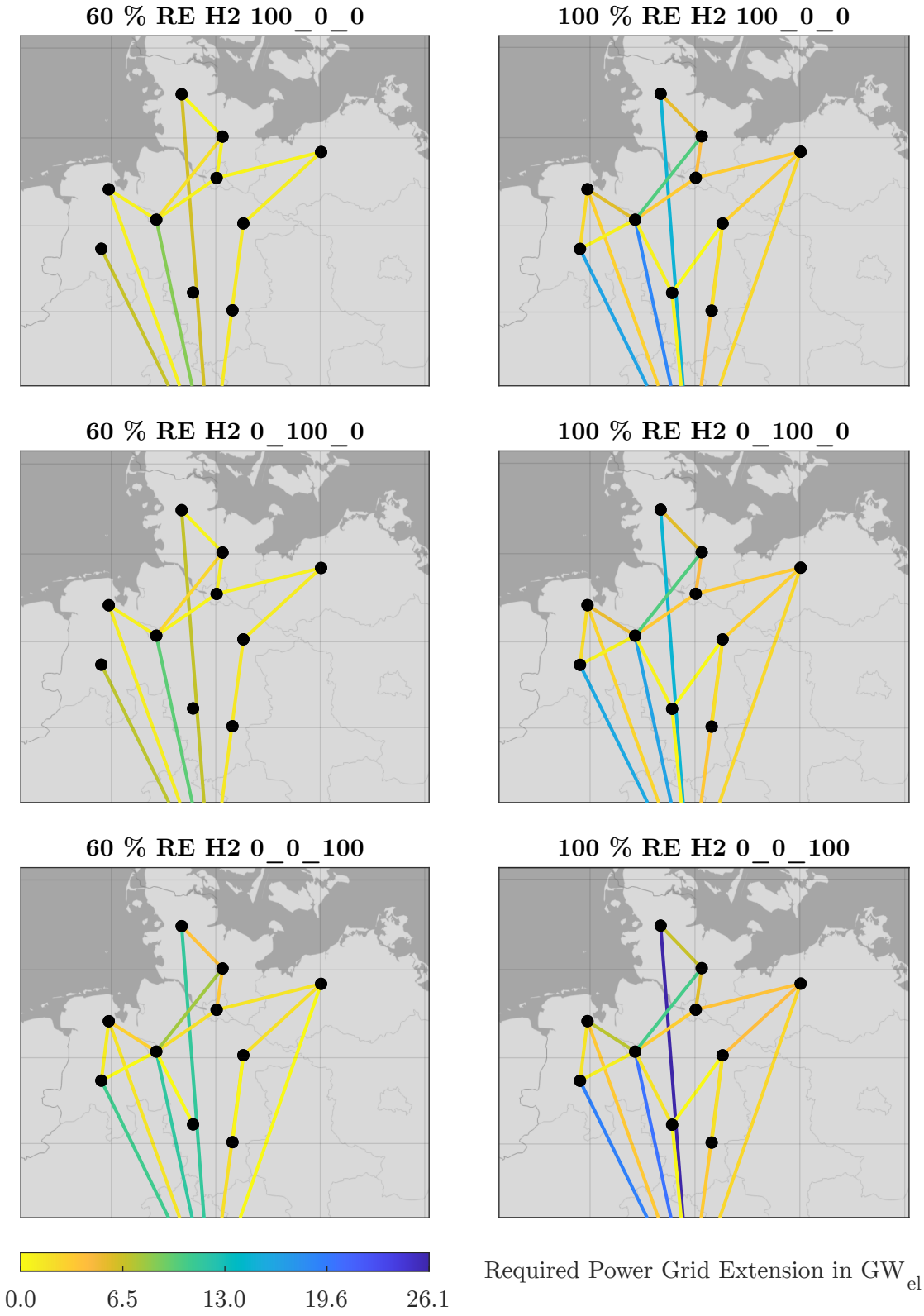

Figure 4.33: Maps of the required power grid extension resulting from the dynamic IES models for selected H2 scenarios.

Table 4.2: Assumptions for the calculation of gas and power grid extension cost.

	Value	Source
Gas Pipeline		
Capital cost	1720 EUR/m	FNB Gas (2020)
Yearly O&M cost	2.5 %	Sterchele et al. (2020b)
Lifetime	30 a	Sterchele et al. (2020b)
Power Transmission Line		
Capital cost	2500 EUR/m	50Hertz et al. (2021b)
Power Transformer		
Capital cost	17 EUR/kW_{el}	50Hertz et al. (2021b)
Switch Field		
Capital cost	4.9 mil. EUR	50Hertz et al. (2021b)
All Power Components		
Yearly O&M cost	3.0 %	Sterchele et al. (2020b)
Lifetime	40 a	Sterchele et al. (2020b)

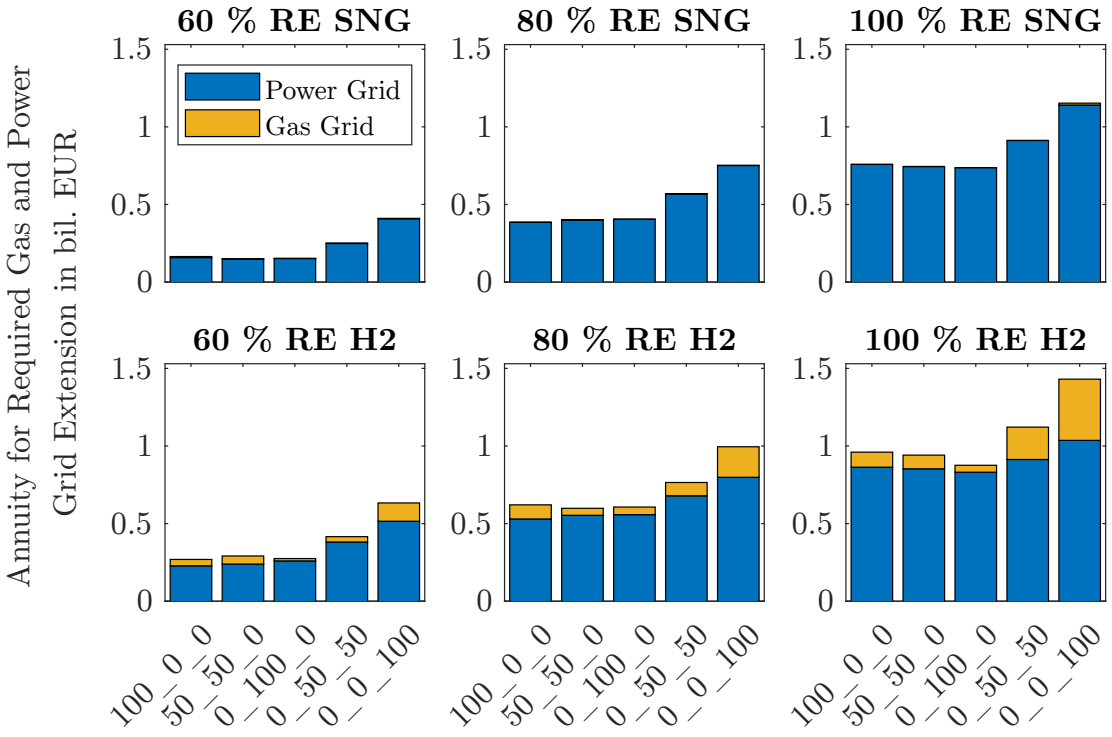

Figure 4.34: Cost for required extension of power and gas grids for all scenarios.

extension makes up 72.4-94.9 % of the cost. Also, the H2 scenarios always have higher costs than the respective SNG scenarios.

The total cost of grid extension is lowest for 0_100_0 for 100 % RE H2 and SNG. For 60 % RE SNG and 80 % RE H2, 50_50_0 has slightly lower cost, and for 60 % RE H2 and 80 % RE SNG, even 100_0_0 has the lowest grid extension cost. Nonetheless, for most scenarios, the cost of the variations 100_0_0-0_100_0 are very similar.

However, it has to be noted here that the gas grid extension focuses on Northern Germany, whereas the power grid extension covers the entire country. Nevertheless, assuming that the gas grid extension in Northern Germany is representative for the rest of Germany, this would simply scale up the cost in all scenarios with the same factor. Even this would not significantly change the relation of the variations to each other, and the qualitative results would stay the same.

Nevertheless, to consider the whole system, the costs have to be compared, including the overall cost of the IES in Figure 4.15. The cost difference between the optimal 0_100_0 scenarios and the respective 50_50_0 and 0_50_50 scenarios range between 3.3 bil. EUR and 15.6 bil. EUR. However, the differences in cost for grid extension between the variations are all less than 0.6 bil. EUR. So they are so low that they do not outbalance the differences in overall system cost. That is why, even considering the grid extension cost, 0_100_0 (100 % EHPGB) stays the most economical option for 60 % to 100 % renewables. Also, hydrogen has not lost its cost-benefit for 100 % RE, and SNG is less expensive for 60 % and 80 % RE.

5 Summary and Outlook

Aiming at CO_2 emission reductions of up to 95 % until 2050 compared to 1990 (BMWi, 2018), a significant change of the German energy system is imminent. To quantify the effects of certain parts of the energy system, different models are developed and used in this thesis. The overall model covers the sectors power, heat, and gas excluding transportation with 60 %, 80 %, and 100 % renewable energies in the considered integrated energy system. A particular focus is laid on the gas sector in Northern Germany, where the gas grid is modeled in detail.

First, an optimization is developed to find economical configurations of the German future integrated energy system. This includes a variety of energy storage and heating technologies as well as different power plants. For Power-to-Gas plants, options with and without methanation are considered to investigate the use of either SNG or hydrogen in the gas grid.

The economic optimization finds hybrid heating systems consisting of electric heat pumps and gas boilers (EHPGB) to be the most cost-effective. A sensitivity analysis shows that this is a very robust result, and just the ratio of consumed gas to power changes slightly. Lithium-ion batteries are the only electric energy storage plant type used but exclusively in scenarios with Power-to-Gas with methanation. Power-to-Gas and gas power plants are needed to a large extent, as well as renewable power generators. For all technologies, but particularly renewable power generators, an extensive and fast nominal power and storage capacity expansion is necessary to enable the system to integrate such high shares of renewables. The comparison of either hydrogen or SNG in the gas grid shows that the cost is lower for SNG for 60 % and 80 % renewables, but hydrogen is more economical at 100 % renewables due to various effects.

Additional to the optimal case of EHPGB, variations of the composition of the heating technologies in the system are considered and economically optimized: exclusively gas boilers or electric heat pumps as well as balanced mixes of each technology with EHPGB. With those variations, the effect of different heating technologies with different extents of power and gas use for heating on the integrated energy system are investigated.

Second, a computation of the Northern German gas grid is implemented and parametrized with the optimization results. This enables the investigation of how the different shares of renewables and heating technologies, as well as the use of either hydrogen or SNG, influence the operation of the gas grid. An aggregation algorithm is developed to reduce the complexity of the gas grid and enable integration into the dynamic integrated energy system model.

The gas grid computation revealed that using hydrogen in the gas grid instead of SNG is more critical since lower pressures are reached due to different gas properties. This effect gets more extreme for the extended use of either power or gas in the heat sector, especially during cold spells where both heating technologies increase the gas demand. Electric heat pumps indirectly cause higher gas consumption due to the high power demand, which is satisfied by gas power plants.

Comparing dynamic and quasi-stationary gas grid computation shows that both match very well, but the dynamic simulation includes the dampening of the gas grid. This results in a more realistic behavior with less extreme peaks and better use of the gas grid capacity. However, quasi-stationary computations work well for worst-case investigations.

Also, the simulations of the aggregated gas grid models lead to good results compared to the non-aggregated model. First, the aggregation algorithm can reduce the number of pipes of the gas grid by more than 98 %. Also, over a large range of aggregation grades, the results, including the required gas grid extension, match well even for aggregation grades of 90 % or even higher for certain scenarios. However, the errors increase stronger for higher aggregation grades. On the one hand, the errors increase with fewer remaining pipes, but on the other hand, the computation time reduces drastically, which is necessary to couple the gas grid with the rest of the integrated energy system.

Third, the aggregated gas grid model is integrated into the dynamic integrated energy system model, which includes all energy producers and consumers, storage and conversion plants as well as an aggregated power grid. Using this model, the optimization results can be verified in a spatially resolved, dynamic model. Furthermore, the required grid extension for the gas and power grid can be determined.

For the gas grid, the results of the required grid extension from the dynamic IES model match well with the values from the quasi-stationary and aggregated gas grid models. In most cases, the calculated required extension is lower for the dynamic integrated energy system model than for the gas grid models. So, considering the entire system, including the energy grids and all technologies, is important since it gives more detailed results, and the gas grid models often overestimate the required grid extension. The gas grid is mostly sufficient for all SNG scenarios; only minor extension is necessary. More gas grid extension is required for scenarios with hydrogen due to the different gas properties compared to SNG. However, for EHPGB, the gas grid extension values are lowest or close to the minimum values.

Looking at the power grid extension shows similar results. EHPGB often requires the least power grid extension compared to the other heating technologies. However, in some cases, the power grid capacity has to be more than doubled.

Interestingly, the extensive use of gas by gas boilers to produce heat does stress not only the gas grid but also the power grid due to the increased demand for Power-to-Gas. This necessitates high transmission capacities both in the power and the gas grid. The same applies to a high share of electric heat producers combined with a high share of renewables. The heat producers require large power plants to provide the power during cold spells, which need a suitable power and gas grid connection as well as gas from Power-to-Gas.

Calculating the cost of both grid extensions shows that the power grid extension dominates the cost. Adding them to the overall system cost enables a more detailed comparison. However, the system cost without the grid and the grid extension cost are both lowest for EHPGB in most cases, or the cost difference does not outbalance the cost difference of the rest of the system. So, the consideration of grid extension does not significantly change the optimal solution.

Different model aspects could be investigated in the future and might lead to a better understanding of the integrated energy system. An alternative to gas grid extension is the erection of compressor stations, which were so far neglected in the model. Also,

considering the whole German gas grid might be beneficial to cover the gas grid extension in the whole grid. Furthermore, the investigation of separate SNG and hydrogen grids can be worthwhile since it depends on the renewables' share if using hydrogen or SNG is more economical. This way, the benefits of both gases can be combined.

For both, power and gas sector, the calculated grid extension only considers the highest grid level and neglects the distribution grid. Especially in the power sector, the distribution within the region is not limited by the power grid capacity, which could be added to investigate further the effect of electric heat producers on the power grid.

Also, not only economic and ecological aspects but also the resilience of the integrated energy system should be examined to evaluate the security of supply in the future in detail. In this context, the dynamic simulation can provide detailed time-resolved insight into the propagation of disturbances not only within the gas grid but also to the connected sectors. The developed algorithms and models provide a solid basis for those possible enhancements.

All in all, the use of hybrid heating systems is beneficial for the integrated energy system, not only regarding the cost but also for the minimization of power and gas grid capacity and an increase in consumer flexibility. Hybrid heating systems can help transform the German energy system efficiently to limit the effects of climate change.

Bibliography

50Hertz et al. (2016). *Punktmaßnahmen im NEP 2025. Begleitdokument zum Netzentwicklungsplan Strom 2025, Version 2015*. Technical report. Berlin, Dortmund, Bayreuth, Stuttgart: 50Hertz Transmission GmbH, Amprion GmbH, TenneT TSO GmbH, TransnetBW GmbH. URL: https://www.netzentwicklungsplan.de/sites/default/files/paragraphs-files/Begleitdokument_NEP_2025_Punktmassnahmen.pdf.

– (2017). *Netzentwicklungsplan Strom 2030, Version 2017. Zweiter Entwurf*. Technical report. Berlin, Dortmund, Bayreuth, Stuttgart: 50Hertz Transmission GmbH, Amprion GmbH, TenneT TSO GmbH, TransnetBW GmbH. URL: https://www.netzentwicklungsplan.de/sites/default/files/paragraphs-files/NEP_2030_2_Entwurf_Teil1.pdf.

– (2021a). *Netzentwicklungsplan Strom 2035, Version 2021. Erster Entwurf der Übertragungsnetzbetreiber*. Technical report. Berlin, Dortmund, Bayreuth, Stuttgart: 50Hertz Transmission GmbH, Amprion GmbH, TenneT TSO GmbH, TransnetBW GmbH. URL: https://www.netzentwicklungsplan.de/sites/default/files/paragraphs-files/NEP_2035_V2021_1_Entwurf_Teil1.pdf.

– (2021b). *Netzentwicklungsplan Strom 2035, Version 2021. Kostenschätzungen*. Technical report. Berlin, Dortmund, Bayreuth, Stuttgart: 50Hertz Transmission GmbH, Amprion GmbH, TenneT TSO GmbH, TransnetBW GmbH. URL: https://www.netzentwicklungsplan.de/sites/default/files/paragraphs-files/NEP_2035_2021_1_Entwurf_Kostenschaetzungen_0.pdf.

Amid, A et al. (2016). "Seasonal storage of hydrogen in a depleted natural gas reservoir". In: *International Journal of Hydrogen Energy* 41.12, pages 5549–5558. DOI: 10.1016/j.ijhydene.2016.02.036.

Andresen, Lisa (2019). "Evaluation of energy storage in integrated energy systems". PhD Thesis. Hamburg University of Technology. ISBN: 978-3-8439-4502-8.

Andresen, Lisa et al. (2018). "Dynamic simulation of different transport options of renewable hydrogen to a refinery in a coupled energy system approach". In: *International Journal of Hydrogen Energy* 43.42, pages 19600–19614. DOI: 10.1016/j.ijhydene.2018.08.111.

Baldauf, Michael et al. (2014). *Kurze Beschreibung des Lokal-Modells Kürzestfrist COSMO-DE (LMK) und seiner Datenbanken auf dem Datenserver des DWD*. Technical report. Offenbach: Deutscher Wetterdienst. URL: https://www.dwd.de/SharedDocs/downloads/DE/modelldokumentationen/nwv/cosmo_de/cosmo_de_dbbeschr_version_2_3_201406.pdf?__blob=publicationFile&v=5.

Beil, Michael et al. (2019). *Schlussbericht zum Verbundvorhaben: Effiziente Mikro-Biogasaufbereitungsanlagen (eMikroBGAA)*. Technical report.

Kassel, Leipzig, Berlin: Fraunhofer IEE, DBFZ Deutsches Biomasseforschungszentrum gGmbH, DBI Gas- und Umwelttechnik GmbH.
URL: https://www.fnr-server.de/ftp/pdf/berichte/22402411.pdf.

Benndorf, Rosemarie et al. (2014).
Treibhausgasneutrales Deutschland im Jahr 2050 (Climate Change 07/2014).
Technical report. Dessau-Roßlau: Umweltbundesamt.
URL: https://www.umweltbundesamt.de/sites/default/files/medien/378/publikationen/07_2014_climate_change_dt.pdf.

Benner, Peter et al. (2018). "A Direct Index 1 DAE Model of Gas Networks".
In: *Reduced-Order Modeling (ROM) for Simulation and Optimization.* Springer, pages 99–119. DOI: 10.1007/978-3-319-75319-5.

Benthin, Jörn et al. (2020). *Integrierte Betrachtung von Strom-, Gas- und Wärmesystemen zur modellbasierten Optimierung des Energieausgleichs- und Transportbedarfs innerhalb der deutschen Energienetze.* Technical report.
Oberhausen, Essen: Fraunhofer UMSICHT, GWI Gas- und Wärme-Institut Essen e.V.
URL: https://www.gwi-essen.de/fileadmin/user_upload/IntegraNet_0324027_Abschlussbericht.pdf.

Bernath, Christiane et al. (2017).
Langfristszenarien für die Transformation des Energiesystems in Deutschland. Modul 1: Hintergrund, Szenarioarchitektur und übergeordnete Rahmenparameter.
Technical report. Karlsruhe, Aachen, Heidelberg: Fraunhofer ISI, Consentec GmbH, ifeu Institut für Energie- und Umweltforschung Heidelberg GmbH.
URL: https://www.bmwi.de/Redaktion/DE/Downloads/B/berichtsmodul-1-hintergrund-szenarioarchitektur-und-uebergeordnete-rahmenparameter.pdf?__blob=publicationFile&v=4.

BMWi (2018). *Die Energie der Zukunft. Sechster Monitoring-Bericht zur Energiewende. Berichtsjahr 2016.* Technical report.
Berlin: Bundesministerium für Wirtschaft und Energie.
URL: https://www.bmwi.de/Redaktion/DE/Publikationen/Energie/sechster-monitoring-bericht-zur-energiewende.pdf?__blob=publicationFile&v=39.

– (2019). *Zahlen und Fakten. Energiedaten.*
Bundesministerium für Wirtschaft und Energie.
URL: http://www.bmwi.de/Redaktion/DE/Artikel/Energie/energiedaten-gesamtausgabe.html (visited on 06/20/2019).

– (2020). *Zahlen und Fakten. Energiedaten.*
Bundesministerium für Wirtschaft und Energie.
URL: http://www.bmwi.de/Redaktion/DE/Artikel/Energie/energiedaten-gesamtausgabe.html (visited on 12/15/2020).

Bode, Carsten et al. (2018). "Dynamic Simulation and Comparison of Different Configurations for a Coupled Energy System with 100 % Renewables".
In: *Energy Procedia* 155, pages 412–430. DOI: 10.1016/j.egypro.2018.11.037.

– (2019). "Influence of Excess Power Utilization in Power-to-Heat Units on an Integrated Energy System with 100 % Renewables". In: *Proceedings of the 13th International Modelica Conference, Regensburg, Germany, March 4–6, 2019.* 157. Linköping Electronic Conference Proceedings, pages 413–422.
DOI: 10.3384/ecp19157413.

Breyer, Christian et al. (2013).
Vergleich und Optimierung von zentral und dezentral orientierten Ausbaupfaden zu einer Stromversorgung aus erneuerbaren Energien in Deutschland. Technical report.
Berlin: Reiner Lemoine Institut gGmbH.
URL: https://reiner-lemoine-institut.de/wp-content/publications/0_Vergleich_und_Optimierung_zentral_und_dezentral_071_100EE/Breyer2013.pdf.

Bründlinger, Thomas et al. (2018). *dena-Leitstudie Integrierte Energiewende. Impulse für die Gestaltung des Energiesystems bis 2050*. Technical report.
Berlin: dena Deutsche Energie-Agentur.
URL: https://www.dena.de/fileadmin/dena/Dokumente/Pdf/9262_dena-Leitstudie_Integrierte_Energiewende_Ergebnisbericht.pdf.

Bundesnetzagentur (2016). *Bericht. Monitoringbericht 2016*. Technical report.
Bonn: Bundesnetzagentur für Elektrizität, Gas, Telekommunikation, Post und Eisenbahnen and Bundeskartellamt.
URL: https://www.bundesnetzagentur.de/SharedDocs/Mediathek/Monitoringberichte/Monitoringbericht2016.pdf?__blob=publicationFile&v=2.

– (2020). *Bericht. Monitoringbericht 2020*. Technical report.
Bonn: Bundesnetzagentur für Elektrizität, Gas, Telekommunikation, Post und Eisenbahnen and Bundeskartellamt.
URL: https://www.bundesnetzagentur.de/SharedDocs/Mediathek/Berichte/2020/Monitoringbericht_Energie2020.pdf?__blob=publicationFile&v=5.

Bundesrepublik Deutschland (2012).
Biomasseverordnung vom 21. Juni 2001 (BGBl. I S. 1234), die zuletzt durch Artikel 5 Absatz 10 des Gesetzes vom 24. Februar 2012 (BGBl. I S. 212) geändert worden ist.

– (2020). *Atomgesetz in der Fassung der Bekanntmachung vom 15. Juli 1985 (BGBl. I S. 1565), das zuletzt durch Artikel 3 des Gesetzes vom 7. Dezember 2020 (BGBl. I S. 2760) geändert worden ist*.

Bürger, Veit et al. (2016).
Klimaneutraler Gebäudebestand 2050 (Climate Change 06/2016). Technical report.
Dessau-Roßlau: Umweltbundesamt.
URL: https://www.umweltbundesamt.de/sites/default/files/medien/378/publikationen/climate_change_06_2016_klimaneutraler_gebaeudebestand_2050.pdf.

Cerbe, Günter et al. (2017).
Grundlagen der Gastechnik. Gasbeschaffung - Gasverteilung - Gasverwendung. 8th ed.
München: Carl Hanser Verlag. ISBN: 978-3-446-44966-4.

Crotogino, Fritz et al. (2001).
Huntorf CAES: More than 20 Years of Successful Operation. Technical report.
Orlando, Florida: KBB GmbH, E.ON Kraftwerke Bremen.
URL: http://www.fze.uni-saarland.de/AKE_Archiv/AKE2003H/AKE2003H_Vortraege/AKE2003H03c_Crotogino_ea_HuntorfCAES_CompressedAirEnergyStorage.pdf.

Dassault Systèmes (2021). *DYMOLA Systems Engineering*.
URL: https://www.3ds.com/products-services/catia/products/dymola/ (visited on 03/29/2021).

DESTATIS (2021a). *41141-0003: Landwirtschaftliche Betriebe mit Ackerland, Fläche: Deutschland, Jahre, Ackerkulturen, Größenklassen des Ackerlandes*.

Statistisches Bundesamt. URL: https://www-genesis.destatis.de/genesis/online?operation=table&code=41141-0003 (visited on 01/21/2021).

DESTATIS (2021b). *41311-0002: Gehaltene Tiere: Bundesländer, Jahre, Tierarten*. Statistisches Bundesamt. URL: https://www-genesis.destatis.de/genesis/online?operation=table&code=41311-0002 (visited on 01/21/2021).

– (2021c). *46271-0003: Straßenlänge: Bundesländer, Stichtag, Straßenklasse/Ortslage*. Statistisches Bundesamt. URL: https://www-genesis.destatis.de/genesis/online?operation=table&code=46271-0003 (visited on 01/21/2021).

DIN/TS 12831-1 (Apr. 2020). *Verfahren zur Berechnung der Raumheizlast – Teil 1: Nationale Ergänzungen zur DIN EN 12831-1, mit CD-ROM*. DIN Deutsches Institut für Normung e.V.

DVGW (2019). "Wasserstoff - CO2-freier Wasserstoff als Schlüsselelement für die Energiewende und den Klimaschutz". In: *energie | wasser-praxis kompakt* November. URL: https://www.dvgw.de/medien/dvgw/leistungen/publikationen/ewp-kompakt-wasserstoff.pdf.

DVGW Arbeitsblatt G 260 (Mar. 2013). *Gasbeschaffenheit*. DVGW Deutscher Verein des Gas- und Wasserfaches e.V.

DVGW Arbeitsblatt G 262 (Sep. 2011). *Nutzung von Gasen aus regenerativen Quellen in der öffentlichen Gasversorgung*. DVGW Deutscher Verein des Gas- und Wasserfaches e.V.

EEX (2019). *EEX Emissions market / Primary Market Auction*. European Energy Exchange AG. URL: https://www.eex.com/fileadmin/EEX/Downloads/EUA_Emission_Spot_Primary_Market_Auction_Report/Archive_Reports/emission-spot-primary-market-auction-report-2019-data.xls (visited on 03/17/2021).

EID Energie Informationsdienst GmbH (2019). "Untertage Gasspeicherung in Deutschland". In: *ERDÖL ERDGAS KOHLE* 135.11, pages 415–420. DOI: 10.19225/191101.

Elsner, Peter, Manfred Fischedick, et al. (2015). *Flexibilitätskonzepte für die Stromversorgung 2050. Technologien - Szenarien - Systemzusammenhänge (Analyse aus der Schriftenreihe Energiesysteme der Zukunft)*. Technical report. München. URL: https://www.acatech.de/publikation/flexibilitaetskonzepte-fuer-die-stromversorgung-2050-technologien-szenarien-systemzusammenhaenge/download-pdf?lang=de.

Elsner, Peter and Dirk Uwe Sauer (2015). *Energiespeicher. Technologiesteckbrief zur Analyse "Flexibilitätskonzepte für die Stromversorgung 2050" (Schriftenreihe Energiesysteme der Zukunft)*. Technical report. München: Nationale Akademie der Wissenschaften Leopoldina, acatech – Deutsche Akademie der Technikwissenschaften, Union der deutschen Akademien der Wissenschaften. URL: https://www.acatech.de/wp-content/uploads/2018/03/ESYS_Technologiesteckbrief_Energiespeicher.pdf.

ENTSOG (2014). *ENTSOG - Transparency Platform*. European Network of Transmission System Operators for Gas. URL: https://transparency.entsog.eu (visited on 01/20/2021).

– (2018a). *TYNDP 2018 Final Scenario Report Demand*. Technical report. Brussels: European Network of Transmission System Operators for Gas.

URL: https://www.entsog.eu/sites/default/files/entsog-migration/publications/TYNDP/2018/ENTSOG_TYNDP_2018_Scenario_Report_Demand.xlsx.
– (2018b). *TYNDP 2018 Final Scenario Report Supply*. Technical report. Brussels: European Network of Transmission System Operators for Gas. URL: https://www.entsog.eu/sites/default/files/entsog-migration/publications/TYNDP/2018/entsog_tyndp_2018_Final_Scenario_Report_Supply.xlsx.
ENTSOG and ENTSO-E (2018). *TYNDP 2018. Scenario Report. Main Report*. Technical report. Brussels: European Network of Transmission System Operators for Gas, European Network of Transmission System Operators for Electricity. URL: https://entsog.eu/sites/default/files/entsog-migration/publications/TYNDP/2018/entsos_tyndp_2018_Final_Scenario_Report.pdf.
Esri Inc. (2013). *ArcGIS*. URL: https://www.arcgis.com/index.html (visited on 01/19/2021).
European Commission (2018). *A Clean Planet for all. A European strategic long-term vision for a prosperous, modern, competitive and climate neutral economy. COM(2018) 773 final*. Brussels. URL: https://eur-lex.europa.eu/legal-content/EN/TXT/PDF/?uri=CELEX:52018DC0773&from=EN.
Fasihi, Mahdi et al. (2019). "Techno-economic assessment of CO2 direct air capture plants". In: *Journal of Cleaner Production* 224, pages 957–980. DOI: 10.1016/j.jclepro.2019.03.086.
Fette, Max et al. (2020). *Multi-Sektor-Kopplung. Modellbasierte Analyse der Integration erneuerbarer Stromerzeugung durch die Kopplung der Stromversorgung mit dem Wärme, Gas- und Verkehrssektor. Endbericht*. Technical report. Bremen: Fraunhofer IFAM, DLR Deutsches Zentrum für Luft- und Raumfahrt e.V., GWI Gas- und Wärme-Institut Essen e.V. URL: https://www.gwi-essen.de/fileadmin/dateien/abschlussberichte/2020/MuSeKo-Endbericht-2020-08-31.pdf.
ffe (2010). *Basisdaten zur Bereitstellung elektrischer Energie*. Technical report. Forschungsstelle für Energiewirtschaft e.V. URL: https://www.ffe.de/download/wissen/186_Basisdaten_Energietraeger/Basisdaten_von_Energietraegern_2010.pdf.
FNB Gas (2013). *Netzentwicklungsplan Gas 2012 der deutschen Fernleitungsnetzbetreiber*. Technical report. Berlin: Vereinigung der Fernleitungsnetzbetreiber Gas e.V. URL: https://www.fnb-gas.de/media/130310_netzentwicklungsplan_gas_2012.pdf.
– (2015). *Netzentwicklungsplan Gas 2015*. Technical report. Berlin: Vereinigung der Fernleitungsnetzbetreiber Gas e.V. URL: https://www.fnb-gas.de/media/2015_11_13_nep-gas-2015.pdf.
– (2017). *Netzentwicklungsplan Gas 2016-2026*. Technical report. Berlin: Vereinigung der Fernleitungsnetzbetreiber Gas e.V. URL: https://www.fnb-gas.de/media/2017_10_16_nep-gas-2016-2026_1.pdf.
– (2019). *Netzentwicklungsplan Gas 2018-2028*. Technical report. Berlin: Vereinigung der Fernleitungsnetzbetreiber Gas e.V. URL: https://www.fnb-gas.de/media/2019_03_20_nep-gas-2018-2028_final_1_1.pdf.

FNB Gas (2020). *Netzentwicklungsplan Gas 2020-2030. Entwurf*. Technical report. Berlin: Vereinigung der Fernleitungsnetzbetreiber Gas e.V. URL: https://www.fnb-gas.de/media/fnb_gas_2020_nep_entwurf_de.pdf.

Gasnetz Hamburg GmbH (2021). *Strukturdaten*. URL: https://www.gasnetz-hamburg.de/fuer-unternehmen/netzzugang-nutzung/strukturdaten (visited on 01/19/2021).

gie (2018). *Storage Map 2018. Existing & Planned Infrastructure*. Brussels: Gas Infrastructure Europe. URL: https://www.gie.eu/download/maps/2018/GIE_STOR_2018_A0_1189x841_FULL_FINAL.pdf.

Görner, Klaus et al. (2016). *Konventionelle Kraftwerke. Technologiesteckbrief zur Analyse "Flexibilitätskonzepte für die Stromversorgung 2050" (Schriftenreihe Energiesysteme der Zukunft)*. Technical report. München: Nationale Akademie der Wissenschaften Leopoldina, acatech – Deutsche Akademie der Technikwissenschaften, Union der deutschen Akademien der Wissenschaften. URL: https://www.acatech.de/wp-content/uploads/2018/03/ESYS_Technologiesteckbrief_Konventionelle_Kraftwerke.pdf.

Gotzens, Fabian et al. (2020). *DemandRegio. Harmonisierung und Entwicklung von Verfahren zur regionalen und zeitlichen Auflösung von Energienachfragen. Abschlussbericht*. Technical report. Berlin, Jülich, München: Forschungszentrum Jülich, Technische Universität Berlin, ffe Forschungsstelle für Energiewirtschaft e.V. URL: https://www.ffe.de/attachments/article/735/DemandRegio_Abschlussbericht.pdf.

Harz Energie Netz GmbH (2021). *Veröffentlichungen*. URL: https://www.harzenergie-netz.de/de/Kopfnavigation/Unternehmen/Veroeffentlichungen/ (visited on 01/19/2021).

Heckel, Jan-Peter et al. (2020). "Investigation of the Voltage Stability in the Integrated Energy System of Northern Germany". In: *NEIS 2020; Conference on Sustainable Energy Supply and Energy Storage Systems, Hamburg, Germany, September 14-15, 2020*. Berlin, Offenbach: VDE VERLAG GmbH, pages 185–190. ISBN: 978-3-8007-4954-6.

Heinemann, N et al. (2018). "Hydrogen storage in porous geological formations - onshore play opportunities in the midland valley (Scotland , UK)". In: *International Journal of Hydrogen Energy* 43, pages 20861–20874. DOI: 10.1016/j.ijhydene.2018.09.149.

Henning, Hans-Martin et al. (2012). *100 % erneuerbare Energien für Strom und Wärme in Deutschland*. Technical report. Freiburg: Fraunhofer ISE. URL: https://www.ise.fraunhofer.de/content/dam/ise/de/documents/publications/studies/studie-100-erneuerbare-energien-fuer-strom-und-waerme-in-deutschland.pdf.

– (2015). *Was kostet die Energiewende? Wege zur Transformation des deutschen Energiesystems bis 2050*. Technical report. Freiburg: Fraunhofer ISE. URL: https://www.ise.fraunhofer.de/content/dam/ise/de/documents/presseinformationen/2015/Fraunhofer-ISE_Transformation-Energiesystem-Deutschland_final_19_11.pdf.

Heuck, Klaus et al. (2013). *Elektrische Energieversorgung. Erzeugung, Übertragung und Verteilung elektrischer Energie für Studium und Praxis*. 9th ed. Wiesbaden: Springer Vieweg. DOI: 10.1007/978-3-8348-9761-9.

Hofmann, Fabian et al. (2019). *FRESNA/powerplantmatching: powerplantmatching v.0.4.1*. DOI: 10.5281/zenodo.3358985.

Homann, Klaus, Thomas Hüwener, et al., editors (2017). *Handbuch der Gasversorungstechnik. Logistik - Infrastruktur - Lösungen*. 1st ed. Essen: Vulkan Verlag. ISBN: 978-3-8356-7299-4.

Homann, Klaus, Rainer Reimert, et al. (2013). *The Gas Engineer's Dictionary. Supply Infrastructure from A to Z*. München: DIV Deutscher Industrieverlag GmbH. ISBN: 978-3-8356-3214-1.

Keith, David W et al. (2018). "A Process for Capturing CO2 from the Atmosphere". In: *Joule* 2, pages 1573–1594. DOI: 10.1016/j.joule.2018.05.006.

Klocke, Bernhard et al., editors (2020). *Handbuch der Gasverwendungstechnik. Greening of gas - Technologien für die Energiewende*. 2nd ed. Essen: Vulkan Verlag. ISBN: 978-3-8356-7372-4.

Klotz, Eva-Maria et al. (2014). *Potenzial- und Kosten-Nutzen-Analyse zu den Einsatzmöglichkeiten von Kraft-Wärme-Kopplung (Umsetzung der EU-Energieeffizienzrichtlinie) sowie Evaluierung des KWKG im Jahr 2014*. Technical report. Basel, Bremen, Karlsruhe, Rastatt: Prognos AG, Fraunhofer IFAM, Institut für Ressourceneffizienz und Energiestrategien IREES, BHKW-Consult. URL: https://www.prognos.com/sites/default/files/2021-01/141001_prognos_bmwi_bericht_kwk.pdf.

Kopp, M. et al. (2017). "Energiepark Mainz: Technical and economic analysis of the worldwide largest Power-to-Gas plant with PEM electrolysis". In: *International Journal of Hydrogen Energy* 42.19, pages 13311–13320. DOI: 10.1016/j.ijhydene.2016.12.145.

Kröcher, Uwe et al. (2013). *Potenzialstudie Energieregion Nordwest. Studie im Rahmen des Projektes Hansa Energy Corridor (HEC)*. Technical report. Oldenburg, Hannover: Arbeitsgruppe für regionale Struktur- und Umweltforschungs GmbH,CIMA - Institut für Regionalwirtschaft, regio gmbh - Institut für Regionalentwicklung und Informationssysteme. URL: https://www.regio-gmbh.de/fileadmin/documents/Energieregion_Nordwest.pdf.

Larsen, Helge V, Benny Bøhm, et al. (2004). "A comparison of aggregated models for simulation and operational optimisation of district heating networks". In: *Energy Conversion and Management* 45, pages 1119–1139. DOI: 10.1016/j.enconman.2003.08.006.

Larsen, Helge V, Halldór Pálsson, et al. (2002). "Aggregated dynamic simulation model of district heating networks". In: *Energy Conversion and Management* 43, pages 995–1019. DOI: 10.1016/S0196-8904(01)00093-0.

Loewen, Achim (2001). *Entwicklung eines Verfahrens zur Aggregation komplexer Fernwärmenetze (UMSICHT-Schriftenreihe Band 29)*. Stuttgart: Fraunhofer IRB Verlag. ISBN: 978-3-8167-5909-2. URL: http://publica.fraunhofer.de/eprints/urn_nbn_de_0011-n-68946.pdf.

Majer, Stefan et al. (2013). *Biomassepotenziale und Nutzungskonkurrenzen. Kurzstudie im Rahmen der Wissenschaftlichen Begleitung, Unterstützung und Beratung des BMVBS in den Bereichen Verkehr und Mobilität mit besonderem Fokus auf Kraftstoffen und Antriebstechnologien sowie Energie und Klima*. Technical report. Leipzig: DLR Deutsches Zentrum für Luft- und Raumfahrt e.V. Institut für Verkehrsforschung, ifeu Institut für Energie- und Umweltforschungs Heidelberg GmbH, LBST Ludwig-Bölkow-Systemtechnik GmbH, DBFZ Deutsches Biomasseforschungszentrum gGmbH.
URL: https://www.bmvi.de/SharedDocs/DE/Anlage/G/MKS/mks-kurzstudie-nutzungskonkurrenzen.pdf?__blob=publicationFile.

MathWorks Inc. (2021a). *MATLAB*.
URL: https://www.mathworks.com/products/matlab.html (visited on 01/19/2021).

– (2021b). *MATLAB Optimization Toolbox*.
URL: https://www.mathworks.com/products/optimization.html (visited on 01/19/2021).

Meinecke, Steffen et al. (2019).
SimBench - Dokumentation. Dokumentationsversion DE-1.0.0. Technical report. Kassel, Aachen, Dortmund: Universität Kassel, Fraunhofer IEE, RWTH Aachen University, Technische Universität Dortmund. URL: https://simbench.de/wp-content/uploads/2019/08/simbench_documentation_de.pdf.

Modelica Association (2021). *Modelica and the Modelica Association*.
URL: https://www.modelica.org/ (visited on 01/19/2021).

Mohring, Jan et al. (2004).
"Automated Model Reduction of Complex Gas Pipeline Networks".
In: *PSIG Annual Meeting, Pipeline Simulation Interest Group*.

NIST (2018).
REFPROP 10.0. Reference Fluid Thermodynamic and Transport Properties.
URL: https://www.nist.gov/srd/refprop (visited on 01/19/2021).

Nitsch, Joachim et al. (2012). *Langfristszenarien und Strategien für den Ausbau der Erneuerbaren Energien in Deutschland bei Berücksichtigung der Entwicklung in Europa und global. Schlussbericht*. Technical report.
Stuttgart, Kassel, Teltow: DLR Deutsches Zentrum für Luft- und Raumfahrt, Fraunhofer IWES, IFNE Ingenieurbüro für neue Energien.
URL: https://elib.dlr.de/76043/1/leitstudie2011_bf.pdf.

ONTRAS (no date). *ONTRAS Netzkarte*.
URL: https://www.ontras.com/fileadmin/Dokumente_Publikationen/Allgemeine_Informationen/DE/ONTRAS_Netzkarte.pdf.

Osiadacz, Andrzej J (1987). *Simulation and analysis of gas netzworks*.
London: E. & F.N. Spon Ltd. ISBN: 0-419-12480-2.

Packer, Neil et al. (2018). *Conventional and Alternative Power Generation*. 1st ed.
West Sussex: John Wiley & Sons, Ltd. ISBN: 9781119479376.

Palzer, Andreas (2016). *Sektorübergreifende Modellierung und Optimierung eines zukünftigen deutschen Energiesystems unter Berücksichtigung von Energieeffizienzmaßnahmen im Gebäudesektor*. Stuttgart: Fraunhofer Verlag.
ISBN: 978-3-8396-1041-1.

Parkinson, Jonathan S et al. (1992).
"Systems modelling and control applied to a low-pressure gas distribution network".
In: *Proceedings of the Institution of Mechanical Engineers, Part E: Journal of Process Mechanical Engineering* 206, pages 35–44.

Purr, Katja et al. (2019). *Wege in eine ressourcenschonende Treibhausgasneutralität. RESCUE - Studie (Climate Change 36/2019).* Technical report.
Dessau-Roßlau: Umweltbundesamt. URL: https://www.umweltbundesamt.de/sites/default/files/medien/376/publikationen/rescue_studie_cc_36-2019_wege_in_eine_ressourcenschonende_treibhausgasneutralitaet.pdf.

Recknagel, Hermann et al. (2017). *Taschenbuch für Heizung und Klimatechnik.*
Edited by Otto Ginsberg et al. 78th ed.
München: DIV Deutscher Industrieverlag GmbH. ISBN: 978-3-8356-7284-0.

Regionalstatistik (2021a).
11111-02-01-4-B: Zahl der Gemeinden - Stichtag 31.12. - regionale Ebenen.
Statistische Ämter des Bundes und der Länder.
URL: https://www.regionalstatistik.de/genesis/online?operation=table&code=11111-02-01-4-B (visited on 01/21/2021).

– (2021b). *12411-01-01-4: Bevölkerung nach Geschlecht - Stichtag 31.12. - regionale Tiefe: Kreise und krfr. Städte.* URL: https://www.regionalstatistik.de/genesis/online?operation=table&code=12411-01-01-4 (visited on 01/21/2021).

– (2021c).
32121-01-02-4: Haushaltsabfälle - Jahr - regionale Tiefe: Kreise und krfr. Städte.
Statistische Ämter des Bundes und der Länder.
URL: https://www.regionalstatistik.de/genesis/online?operation=table&code=32121-01-02-4 (visited on 01/21/2021).

– (2021d). *33111-01-01-4: Bodenfläche nach Art der tatsächlichen Nutzung - Stichtag 31.12. - Kreise und kreisfr. Städte (bis 2015).*
Statistische Ämter des Bundes und der Länder.
URL: https://www.regionalstatistik.de/genesis/online?operation=table&code=33111-01-01-4 (visited on 01/21/2021).

– (2021e).
41141-01-01-4: Landwirtschaftliche Betriebe und deren landwirtschaftlich genutzte Fläche (LF) nach Kulturarten - Jahr - regionale Tiefe: Kreise und krfr. Städte.
Statistische Ämter des Bundes und der Länder.
URL: https://www.regionalstatistik.de/genesis/online?operation=table&code=41141-01-01-4 (visited on 01/21/2021).

– (2021f). *41141-02-02-4: Anbau auf dem Ackerland in landwirtschaftlichen Betrieben nach Fruchtarten - Jahr - regionale Tiefe: Kreise und krfr. Städte.*
Statistische Ämter des Bundes und der Länder.
URL: https://www.regionalstatistik.de/genesis/online?operation=table&code=41141-02-02-4 (visited on 01/21/2021).

– (2021g). *41141-03-01-4: Landwirtschaftliche Betriebe mit Viehhaltung und Zahl der Tiere - Stichtag - regionale Tiefe: Kreise und krfr. Städte.*
Statistische Ämter des Bundes und der Länder.
URL: https://www.regionalstatistik.de/genesis/online?operation=table&code=41141-03-01-4 (visited on 01/21/2021).

Regionalstatistik (2021h). *41241-01-03-4: Erträge ausgewählter landwirtschaftlicher Feldfrüchte - Jahressumme - regionale Tiefe: Kreise und krfr. Städte.* Statistische Ämter des Bundes und der Länder. URL: https://www.regionalstatistik.de/genesis/online?operation=table&code=41241-01-03-4 (visited on 01/21/2021).

Repenning, Julia et al. (2015). *Klimaschutzszenario 2050. 2. Endbericht.* Technical report. Berlin, Karlsruhe: Öko-Institut e.V., Fraunhofer ISI. URL: https://www.oeko.de/oekodoc/2451/2015-608-de.pdf.

Reuß, Markus Eduard (2019). "Techno-ökonomische Analyse alternativer Wasserstoffinfrastruktur". In: *Schriften des Forschungszentrums Jülich. Reihe Energie & Umwelt/Energy & Environment.* Edited by Forschungszentrum Jülich GmbH. Volume 467. Jülich. ISBN: 978-3-95806-414-0. URL: https://juser.fz-juelich.de/record/864486/files/Energie_Umwelt_467.pdf.

Robinius, Martin, Peter Markewitz, et al. (2020). "Wege für die Energiewende. Kosteneffiziente und klimagerechte Transformationsstrategien für das deutsche Energiesystem bis zum Jahr 2050". In: *Schriften des Forschungszentrums Jülich. Reihe Energie & Umwelt/Energy & Environment.* Volume 499. Jülich. ISBN: 978-3-95806-483-6. URL: https://juser.fz-juelich.de/record/877960/files/Energie_Umwelt_499.pdf?version=1.

Robinius, Martin, Alexander Otto, et al. (2017). "Linking the Power and Transport Sectors — Part 2: Modelling a Sector Coupling Scenario for Germany". In: *Energies* 10.957. DOI: 10.3390/en10070957.

Schlesinger, Michael et al. (2014). *Entwicklung der Energiemärkte – Energiereferenzprognose. Endbericht.* Technical report. Basel, Köln, Osnabrück: Prognos AG, Energiewirtschaftliches Institut an der Universität zu Köln, Gesellschaft für Wirtschaftliche Strukturforschung mbH. URL: https://www.bmwi.de/Redaktion/DE/Publikationen/Studien/entwicklung-der-energiemaerkte-energiereferenzprognose-endbericht.pdf?__blob=publicationFile&v=7.

Schmitz, Gerhard (2020). *Technische Thermodynamik.* 10th ed. Essen: Vulkan Verlag. ISBN: 978-3-8027-3136-5.

Schülting, Oliver (2021). *Vergleich von Power-to-X-Konzepten zur Sektorenkopplung bei hohen regenerativen Anteilen.* Göttingen: Cuvillier Verlag. ISBN: 978-3-7369-7434-0.

Senkel, Anne et al. (2021). "Quantification of the resilience of integrated energy systems using dynamic simulation". In: *Reliability Engineering and System Safety* 209, page 107447. DOI: 10.1016/j.ress.2021.107447.

SMEKUL (2021). *Dungeinheitenschlüssel.* Sächsisches Staatsministerium für Energie, Klimaschutz, Umwelt und Landwirtschaft. URL: https://www.landwirtschaft.sachsen.de/dungeinheitenschluessel-15620.html (visited on 01/21/2021).

Sørensen, Bent (2017). *Renewable Energy.* 5th ed. London: Elsevier Ltd. ISBN: 978-0-12-804567-1.

Sterchele, Philip et al. (2020a). *Wege zu einem klimaneutralen Energiesystem – Die deutsche Energiewende im Kontext gesellschaftlicher Verhaltensweisen.* Technical report. Freiburg: Fraunhofer ISE. URL: https://www.ise.fraunhofer.de/content/dam/ise/de/documents/publications/studies/Fraunhofer-ISE-Studie-Wege-zu-einem-klimaneutralen-Energiesystem.pdf.

– (2020b). *Wege zu einem klimaneutralen Energiesystem – Die deutsche Energiewende im Kontext gesellschaftlicher Verhaltensweisen - Anhang zur Studie.* Technical report. Freiburg: Fraunhofer ISE. URL: https://www.ise.fraunhofer.de/content/dam/ise/de/documents/publications/studies/Anhang-Studie-Wege-zu-einem-klimaneutralen-Energiesystem.pdf.

Sterner, Michael and Ingo Stadler, editors (2019). *Handbook of Energy Storage.* 2nd ed. Berlin: Springer-Verlag. DOI: 10.1007/978-3-662-55504-0.

Sterner, Michael, Martin Thema, et al. (2014). *Stromspeicher in der Energiewende. Untersuchung zum Bedarf an neuen Stromspeichern in Deutschland für den Erzeugungsausgleich, Systemdienstleistungen und im Verteilnetz.* Technical report. Berlin: Agora Energiewende. URL: https://static.agora-energiewende.de/fileadmin2/Projekte/2013/speicher-in-der-energiewende/Agora_Speicherstudie_Web.pdf.

Stolzenburg, Klaus et al. (2014). *Integration von Wind-Wasserstoff-Systemen in das Energiesystem. Abschlussbericht.* Technical report. Berlin: Planungsgruppe Energie und Technik GbR PLANET, fachhochschule lübeck PROJEKT-GMBH, Fraunhofer ISI, Fachhochschule Stralsund Institut für Energie und Umwelt e.V., KBB Underground Technologies GmbH. URL: https://edocs.tib.eu/files/e01fn16/872792943.pdf.

Tietze, Vanessa et al. (2015). "Comparison of hydrogen and methane storage by means of a thermodynamic analysis". In: *International Journal of Hydrogen Energy* 40.35, pages 11530–11537. DOI: 10.1016/j.ijhydene.2015.04.154.

TLK-Thermo and ift (2021). *TILMedia Suite.* TLK-Thermo GmbH and Institut für Thermodynamik, Technische Universität Braunschweig. URL: https://www.tlk-thermo.com/index.php/en/software/tilmedia-suite (visited on 01/19/2021).

TLK-Thermo, XRG, et al. (2021). *ClaRa.* TLK-Thermo GmbH, XRG Simulation GmbH, and Hamburg University of Technology. URL: https://claralib.com/index.php?lang=en (visited on 01/19/2021).

TUHH (2021). *TransiEnt Library.* Hamburg University of Technology. URL: https://www.tuhh.de/transient-ee/en/ (visited on 01/19/2021).

Umweltbundesamt (2019). *National Trend Tables for the German Atmospheric Emission Reporting. 1990 - 2017. Final version reporting period 2019.* Dessau-Roßlau. URL: https://www.umweltbundesamt.de/sites/default/files/medien/361/dokumente/2018_12_19_em_entwicklung_in_d_trendtabelle_thg_v1.0.1_0.xlsx.

– (2020). *Time series for the development of renewable energy sources in Germany.* Technical report. Dessau-Roßlau. URL: https://www.erneuerbare-energien.de/EE/Redaktion/DE/Downloads/zeitreihen-zur-entwicklung-der-erneuerbaren-energien-in-deutschland-1990-2019-en.pdf?__blob=publicationFile&v=12.

United Nations (2015). *Paris Agreement*. Paris. URL: https://unfccc.int/files/essential_background/convention/application/pdf/english_paris_agreement.pdf.

Vattenfall GmbH (2018). *Wasserkraft in Deutschland*.
URL: https://corporate.vattenfall.de/uber-uns/geschaftsfelder/erzeugung/wasserkraft/wasserkraft-in-deutschland-psw/ (visited on 01/08/2018).

VDI 2067 Part 1 (Sep. 2012).
Economic efficiency of building installations. Fundamentals and economic calculation.
Verein Deutscher Ingenieure.

Verlag Glückauf GmbH et al. (2010).
Gasversorgungsnetze in Deutschland - digitale Karte. Essen, Dortmund.

Viessmann (2019). *Datenblatt Vitosol 100-FM/-F*.
Allendorf: Viessmann Werke GmbH & Co. KG. URL: https://www.viessmann.de/content/dam/vi-brands/DE/Produkte/Solarsysteme/Vitosol-100-FM/DB-5784083_Vitosol_100-FM_SV1F_SH1F_Vitosol_100-F_SV1B_SH1B.pdf/_jcr_content/renditions/original.media_file.download_attachment.file/DB-5784083_Vitosol_100-FM_SV1F_SH1F_Vitosol_100-F_SV1B_SH1B.pdf.

– (2020). *Technologie-Broschüre. Hybrid-Lösungen*. Technical report.
Allendorf (Eder): Viessmann Deutschland GmbH. URL: https://www.viessmann.de/content/dam/vi-brands/DE/PDF/Technologien/pr-hybrid-loesungen.pdf.

Wärme Hamburg (2020). *Erzeugungsanlagen*.
URL: https://waerme.hamburg/erzeugungsanlagen (visited on 03/17/2020).

Zech, Konstantin et al. (2014).
DBFZ Report Nr. 19. Hy-NOW - Evaluierung der Verfahren und Technologien für die Bereitstellung von Wasserstoff auf Basis von Biomasse. Endbericht. Technical report.
Leipzig: DBFZ Deutsches Biomasseforschungszentrum gGmbH, LBST Ludwig-Bölkow-Systemtechnik GmbH, Fraunhofer ISI. URL: https://www.dbfz.de/fileadmin/user_upload/Referenzen/DBFZ_Reports/DBFZ_Report_19.pdf.

Ziems, Christian et al. (2012). *Kraftwerksbetrieb bei Einspeisung von Windparks und Photovoltaikanlagen - Abschlussbericht zum Forschungsvorhaben*. Technical report.
Rostock: VGB PowerTech, Universität Rostock.
URL: https://www.vgb.org/vgbmultimedia/333_Abschlussbericht-p-5968.pdf.

Zimmermann, Tobias (2021). *Beitrag des Wärmesektors zur Reduzierung der CO2-Emissionen in Energiesystemen mit Sektorenkopplung*.
Göttingen: Cuvillier Verlag. ISBN: 978-3-7369-7521-7.

Zimmermann, Tobias et al. (2020).
"Auswirkungen verschiedener Sektorenkopplungspfade auf die elektrische Residuallast in Systemen mit hoher fluktuierender Einspeisung".
In: *16. Symposium Energieinnovation, 12.-14.02.2020, Graz/Austria*. Graz.

A Appendix

A.1 Input Parameters

Table A.1: Economical and technical assumptions for renewable energy generators. Yearly O&M cost are given in percentage of the capital cost.

Technology	Unit	2040	2045	2050	Source
Offshore Wind Plant					
Capital cost	EUR/kW$_{el}$	2494	2337	2251	Palzer (2016)
Yearly O&M cost	%	3.03	3.03	3.03	Palzer (2016)
Lifetime	a	20	20	20	Palzer (2016)
Onshore Wind Plant					
Capital cost	EUR/kW$_{el}$	1401	1400	1400	Palzer (2016)
Yearly O&M cost	%	3.4	3.4	3.4	Palzer (2016)
Lifetime	a	22.5	22.5	22.5	Palzer (2016)
Photovoltaics Plant					
Capital cost	EUR/kW$_{el}$	597	576	571	Palzer (2016)
Yearly O&M cost	%	1.96	1.96	1.96	Palzer (2016)
Lifetime	a	30	30	30	Palzer (2016)
Run-of-River Plant					
Capital cost	EUR/kW$_{el}$	1600	1600	1600	Palzer (2016)
Yearly O&M cost	%	2	2	2	Palzer (2016)
Lifetime	a	50	50	50	Palzer (2016)
Full load hours	h	3989	3989	3989	50Hertz et al. (2017)
Technical potential	GW$_{el}$	5.3	5.3	5.3	Henning et al. (2015)
Relative yearly production profile					Ziems et al. (2012)
Decentral Solar Thermal Collector					
Capital cost	EUR/m^2	163	162	162	Palzer (2016)
Yearly O&M cost	%	1.3	1.3	1.3	Palzer (2016)
Lifetime	a	30	30	30	Palzer (2016)
Technical parameters					Viessmann (2019)
Central Solar Thermal Collector					
Capital cost	EUR/m^2	108	106	106	Palzer (2016)
Yearly O&M cost	%	1.4	1.4	1.4	Palzer (2016)
Lifetime	a	30	30	30	Palzer (2016)

Continued on next page

Table A.1 – continued from previous page

Technology	Unit	2040	2045	2050	Source
Technical parameters					Viessmann (2019)
Biogas Plant					
Capital cost	EUR/kW$_{\text{NCV,upgr. gas}}$	836	827	826	Palzer (2016)
Yearly O&M cost	%	5	5	5	Palzer (2016)
Lifetime	a	20	20	20	Palzer (2016)
Biogas Upgrading Unit					
Capital cost	EUR/kW$_{\text{NCV,upgr. gas}}$	296	286	284	Palzer (2016)
Yearly O&M cost	%	5	5	5	Palzer (2016)
Lifetime	a	20	20	20	Palzer (2016)
Efficiency related to NCV	%	88	88	88	Palzer (2016)
Yearly Availability	h	8400	8400	8400	Palzer (2016)
Biomass to Hydrogen Plant					
Capital cost	EUR/kW$_{\text{NCV}}$	1917	1886	1882	Palzer (2016)
Yearly O&M cost	%	6	6	6	Palzer (2016)
Lifetime	a	20	20	20	Palzer (2016)
Efficiency related to NCV	%	48	48	48	Palzer (2016)
Yearly Availability	h	8000	8000	8000	Palzer (2016)

Table A.2: Economical and technical assumptions for Power-to-Gas and power plant technologies. Yearly O&M cost are given in percentage of the capital cost.

Technology	Unit	2040	2045	2050	Source
Electrolyzer					
Capital cost	EUR/kW$_{\text{el}}$	213	202	200	Palzer (2016)
Yearly O&M cost	%	4	4	4	Palzer (2016)
Lifetime	a	18.1	18.4	18.5	Elsner and Sauer (2015)
Efficiency related to NCV	%	77.6	78.3	78.5	Elsner and Sauer (2015)
Relative efficiency curve					Modified version of Kopp et al. (2017)
Electrolyzer and Methanation Unit					
Capital cost	EUR/kW$_{\text{el}}$	843	805	800	Palzer (2016)
Yearly O&M cost	%	2.5	2.5	2.5	Palzer (2016)
Lifetime	a	24.4	24.9	25.0	Elsner and Sauer (2015)
Efficiency of methanation unit related to NCV	%	83.1	83.1	83.1	TUHH (2021)

Continued on next page

Table A.2 – continued from previous page

Technology	Unit	2040	2045	2050	Source
Low Temperature Direct Air Capture Plant					
Capital cost	EUR a/t_{CO_2}	215	201	199	Fasihi et al. (2019)
Yearly O&M cost	%	4	4	4	Fasihi et al. (2019)
Lifetime	a	30	30	30	Fasihi et al. (2019)
Specific power demand	kWh_{el}/t_{CO_2}	1281	1182	1102	Fasihi et al. (2019)
Specific heat demand	kWh_{th}/t_{CO_2}	202	192	182	Fasihi et al. (2019)
Combined Cycle Gas Turbine Plant					
Capital cost	EUR/kW_{el}	700	700	700	Görner et al. (2016)
Yearly O&M cost	%	3	3	3	Görner et al. (2016)
Lifetime	a	32.5	32.5	32.5	Görner et al. (2016)
Efficiency related to NCV	%	63.1	63.3	63.5	Görner et al. (2016)
Smallest unit	MW_{el}	100	100	100	Own assumption
Minimum load	%	45.6	46.6	47.5	Görner et al. (2016)
Maximum load gradient	$\%P_{el,nom}$/min	10.1	10.3	10.5	Görner et al. (2016)
Start up time (hot)	min	24.4	24.9	25.5	Görner et al. (2016)
Gas Turbine					
Capital cost	EUR/kW_{el}	375	375	375	Görner et al. (2016)
Yearly O&M cost	%	3.5	3.5	3.5	Görner et al. (2016)
Lifetime	a	50	50	50	Görner et al. (2016)
Efficiency related to NCV	%	43.8	44.9	46.0	Görner et al. (2016)
Smallest unit	MW_{el}	50	50	50	Own assumption
Minimum load	%	14	14	14	Görner et al. (2016)
Maximum load gradient	$\%P_{el,nom}$/min	100	100	100	Görner et al. (2016)
Start up time (hot)	min	3	3	3	Görner et al. (2016)

Table A.3: Economical and technical assumptions for heating technologies. Yearly O&M cost are given in percentage of the capital cost.

Technology	Unit	2040	2045	2050	Source
Large-Scale Combined Heat and Power CCGT Plant					
Capital cost	EUR/kW$_{el}$	1250	1250	1250	Görner et al. (2016)
Yearly O&M cost	%	2.8	2.8	2.8	Palzer (2016)
Lifetime	a	32.5	32.5	32.5	Palzer (2016)
Nominal electric and thermal load					TUHH (2021) (CHP CCGT plant "Fortuna")
Efficiency field					TUHH (2021) (CHP CCGT plant "Fortuna")
Maximum load gradient	$\%P_{el,nom}$/min	10.1	10.3	10.5	Görner et al. (2016)
Start up time (hot)	min	60	60	60	Görner et al. (2016)
Ratio of nominal thermal load of CHP CCGT plant to peak load boiler	-	2	2	2	Wärme Hamburg (2020)
Small-scale Combined Heat and Power Plant					
Capital cost	EUR/kW$_{el}$	2989	2975	2973	Klotz et al. (2014), relative cost reduction from Palzer (2016)
Yearly O&M cost	%	1.45	1.45	1.45	Klotz et al. (2014)
Lifetime	a	10	10	10	Klotz et al. (2014)
Electric efficiency	%	32	32	32	Klotz et al. (2014)
Thermal efficiency	%	60	60	60	Klotz et al. (2014)
Electric Heat Pumps					
Capital cost	EUR/kW$_{th}$	1006	978	956	Palzer (2016)
Yearly O&M cost	%	3.5	3.5	3.5	Palzer (2016)
Lifetime	a	20	20	20	Palzer (2016)
Performance Curve					Palzer (2016)
Electrode Boiler and Electric Heating Rod					
Capital cost	EUR/kW$_{th}$	70	70	70	Elsner and Sauer (2015)
Yearly O&M cost	%	2	2	2	Elsner and Sauer (2015)
Lifetime	a	15	15	15	Elsner and Sauer (2015)
Efficiency	%	99	99	99	Elsner and Sauer (2015)
Gas Heat Pump					
Capital cost	EUR/kW$_{th}$	894	823	800	Palzer (2016)
Yearly O&M cost	%	1.5	1.5	1.5	Palzer (2016)
Lifetime	a	20	20	20	Palzer (2016)
Performance Curve					Palzer (2016)

Continued on next page

Table A.3 – continued from previous page

Technology	Unit	2040	2045	2050	Source
Gas Boiler					
Capital cost	EUR/kW$_{th}$	175	175	175	Palzer (2016)
Yearly O&M cost	%	2	2	2	Palzer (2016)
Lifetime	a	20	20	20	Palzer (2016)
Efficiency related to NCV	%	98	98	98	Elsner and Sauer (2015)

Table A.4: Economical and technical assumptions for storage technologies. Yearly O&M cost are given in percentage of the capital cost.

Technology	Unit	2040	2045	2050	Source
Pumped Hydro Storage Plant					
Capital cost	EUR/kW$_{el}$	850	850	850	Elsner, Fischedick, et al. (2015)
	EUR/kWh	50	50	50	Elsner, Fischedick, et al. (2015)
Yearly O&M cost	%	1.2	1.2	1.2	Elsner, Fischedick, et al. (2015)
Lifetime	a	80	80	80	Palzer (2016)
Charging efficiency	%	88	88	88	Elsner, Fischedick, et al. (2015)
Discharging efficiency	%	89	89	89	Elsner, Fischedick, et al. (2015)
Maximum load gradient	%$P_{el,nom}$/min	60	60	60	Vattenfall GmbH (2018)
Technical power potential	GW$_{el}$	8.6	8.6	8.6	Benndorf et al. (2014)
Technical capacity potential	GWh	52.12	52.12	52.12	Calculated using Benndorf et al. (2014) with scaled up power from above
Adiabatic Compressed Air Energy Storage Plant					
Capital cost	EUR/kW$_{el}$	663	658	658	Elsner and Sauer (2015)
	EUR/kWh	25.0	24.0	23.5	Elsner and Sauer (2015)
Yearly O&M cost	%	1	1	1	Elsner, Fischedick, et al. (2015)
Lifetime	a	40	40	40	Elsner, Fischedick, et al. (2015)
Charging efficiency	%	87.8	88.1	88.4	Elsner and Sauer (2015)
Discharging efficiency	%	78.7	79.0	79.2	Elsner and Sauer (2015)

Continued on next page

Table A.4 – continued from previous page

Technology	Unit	2040	2045	2050	Source
Maximum load gradient	$\%P_{\mathrm{el,nom}}$/min	10	10	10	Own assumption (CAES plants can be used for minute reserve (Crotogino et al., 2001))
Minimum SOC	%	60	60	60	Elsner, Fischedick, et al. (2015)
Battery Storage Plant					
Capital cost	EUR/$\mathrm{kW_{el}}$	45.3	45.0	45.0	Elsner and Sauer (2015)
	EUR/kWh	145.0	145.0	145.0	Elsner and Sauer (2015)
Yearly O&M cost	%	1	1	1	Elsner, Fischedick, et al. (2015)
Lifetime	a	21.2	21.8	22.0	Elsner and Sauer (2015)
Charging efficiency	%	94.4	94.7	94.9	Elsner and Sauer (2015)
Discharging efficiency	%	94.4	94.7	94.9	Elsner and Sauer (2015)
Maximum load gradient	$\%P_{\mathrm{el,nom}}$/min	∞	∞	∞	Own assumption
Self-discharge rate	%/month	3.22	3.05	3.00	Elsner and Sauer (2015)
Minimum SOC	%	0	0	0	Elsner and Sauer (2015)
Minimum SOC	%	100	100	100	Elsner and Sauer (2015)
Decentral Hot Water Storage Tanks					
Capital cost	EUR/$\mathrm{m^3}$	1091	1053	1040	Palzer (2016)
Yearly O&M cost	%	1.3	1.3	1.3	Palzer (2016)
Lifetime	a	20	20	20	Palzer (2016)
Height	m	2	2	2	Own assumption
Diameter	m	1	1	1	Own assumption
Relative heights of entries and exits					Recknagel et al. (2017)
Heat transmission coefficient of storage wall	W/($\mathrm{m^2\,K}$)	0.5	0.5	0.5	Own assumption
Central Hot Water Storage Tanks					
Capital cost	EUR/$\mathrm{m^3}$	124	121	120	Palzer (2016)
Yearly O&M cost	%	1	1	1	Palzer (2016)
Lifetime	a	40	40	40	Palzer (2016)
Height	m	50	50	50	Own assumption
Relative heights of entries and exits					Recknagel et al. (2017)
Heat transmission coefficient of storage wall	W/($\mathrm{m^2\,K}$)	0.5	0.5	0.5	Own assumption

Continued on next page

Table A.4 – continued from previous page

Technology	Unit	2040	2045	2050	Source
Gas Storage Plants for Natural Gas, SNG, and Biomethane					
Capital cost	EUR/kg	0.604	0.604	0.604	Stolzenburg et al. (2014) (Green field salt cavern with 500 000 m^3 with density values from TLK-Thermo and ift (2021))
Yearly O&M cost	%	2	2	2	Stolzenburg et al. (2014)
Lifetime	a	30	30	30	Stolzenburg et al. (2014)
Gas Storage Plants for Hydrogen					
Capital cost	EUR/kg	6.237	6.237	6.237	Stolzenburg et al. (2014) (Green field salt cavern with 500 000 m^3 with density values from TLK-Thermo and ift (2021))
Yearly O&M cost	%	2	2	2	Stolzenburg et al. (2014)
Lifetime	a	30	30	30	Stolzenburg et al. (2014)

Table A.5: Cost assumptions for power grid extension due to renewables and electric heat pumps. Yearly O&M cost are given in percentage of the capital cost.

	Unit	2040	2045	2050	Source
Undersea Cable for Offshore Wind Plants					
Capital cost	EUR/$kW_{el,nom,offshore}$	430	430	430	Henning et al. (2012)
Yearly O&M cost	%	3	3	3	Sterchele et al. (2020b)
Lifetime	a	40	40	40	Henning et al. (2012)
High-Voltage Direct Current Transmission Line for Offshore Wind Plants					
Capital cost	EUR/$kW_{el,nom,offshore}$	200	200	200	Henning et al. (2012)
Yearly O&M cost	%	3	3	3	Sterchele et al. (2020b)
Lifetime	a	40	40	40	Sterchele et al. (2020b)
Medium-Voltage Grid Extension for Onshore Wind Plants					
Capital cost	EUR/$kW_{el,nom,onshore}$	180	180	180	Sterchele et al. (2020b)
Yearly O&M cost	%	3	3	3	Sterchele et al. (2020b)
Lifetime	a	40	40	40	Sterchele et al. (2020b)
Low-Voltage Grid Extension for Photovoltaics and Electric Heat Pumps					
Capital cost	EUR/$kW_{el,nom,pv/EHP}$	140	140	140	Henning et al. (2012)
Yearly O&M cost	%	3	3	3	Sterchele et al. (2020b)
Lifetime	a	40	40	40	Henning et al. (2012)

Table A.6: Cost assumptions for different energy carriers and CO_2.

	Unit	2040	2045	2050	Source
Garbage (for Biogas Production)					
Energy-specific cost	EUR/$MWh_{NCV,upgr.\,gas}$	11.4	11.4	11.4	Palzer (2016)
Biomass (for Biogas Production)					
Energy-specific cost	EUR/$MWh_{NCV,upgr.\,gas}$	42.4	40.1	37.9	Palzer (2016)
Natural Gas					
Energy-specific cost	EUR/MWh_{NCV}	47.7	51.9	56.3	Palzer (2016)
Hydrogen from Natural Gas					
Energy-specific cost	EUR/MWh_{NCV}	100	100	100	Assumption based on approximate price of hydrogen from PtG in the system
CO_2					
Mass-specific cost	EUR/t_{CO_2}	143.5	171.8	200.0	Interpolation between the average value of 2019 (EEX, 2019) and an upwardly corrected value for 2050 from Schlesinger et al. (2014)

A.2 Biogas Potential

Table A.7: Biogas potential in GWh_{GCV} for each NUTS 3 region in Germany.

	Biogas Potential in GWh_{GCV} from					
NUTS 3 Region	Animal Manure	Energy Crops	Grass-land	Bio-Waste Container	Garden and Park Waste	Organic Share in Municipal Waste
01001	0.28	0.00	0.74	5.05	3.39	4.10
01002	2.47	4.70	0.00	14.47	9.64	10.49
01003	6.00	26.62	11.49	12.79	8.54	10.20
01004	3.22	15.27	0.00	5.73	3.15	5.26
01051	206.04	684.22	321.45	13.31	6.55	6.65
01053	83.65	537.05	84.09	12.95	8.72	9.37
01054	376.19	915.21	502.28	9.63	8.44	9.28
01055	77.29	523.98	86.86	11.72	8.95	10.09
01056	67.81	223.94	122.21	24.15	12.52	15.91
01057	98.77	503.83	96.34	11.58	5.75	5.79
01058	315.96	1304.10	359.15	34.97	12.53	11.07
01059	397.80	1485.90	335.20	12.19	9.72	7.37
01060	163.36	696.56	156.29	21.17	11.75	13.15
01061	201.62	485.23	252.79	9.15	5.98	5.15
01062	75.95	314.61	73.97	17.34	10.14	12.61
02000	4.09	82.53	296.33	104.98	67.57	103.89
03101	1.54	52.29	18.40	14.76	10.61	8.34
03102	2.51	136.83	0.00	5.94	5.14	3.70
03103	2.41	32.31	0.00	11.46	4.99	5.83
03151	79.20	668.52	219.74	11.07	8.11	8.99
03153	20.13	238.17	61.53	8.12	5.83	6.24
03154	10.05	359.40	61.58	6.10	4.22	2.93
03155	91.94	414.28	151.42	9.38	6.59	4.16
03157	16.92	412.85	54.02	12.58	5.64	4.79
03158	9.47	523.46	31.47	13.60	5.28	5.96
03159	93.21	300.36	213.43	20.11	14.44	12.53
03241	145.89	949.68	312.00	67.22	95.70	52.48
03251	664.40	1102.49	372.42	34.90	10.18	8.44
03252	56.04	351.49	74.76	8.71	17.65	6.44
03254	41.44	829.03	69.68	19.14	11.78	11.07
03255	48.60	140.97	112.65	4.23	3.41	2.01
03256	303.49	616.80	209.01	7.65	13.87	4.70
03257	63.87	260.92	78.64	20.67	10.34	3.01
03351	128.39	513.56	181.21	10.45	9.54	6.22
03352	774.32	946.82	1237.42	11.64	9.65	11.26
03353	141.98	336.53	294.80	14.57	16.47	10.29
03354	89.32	404.02	202.16	2.94	6.31	1.56
03355	107.18	392.00	263.75	10.61	9.75	6.95

Continued on next page

Table A.7 – continued from previous page

NUTS 3 Region	Biogas Potential in GWh_{GCV} from Animal Manure	Energy Crops	Grass-land	Bio-Waste Container	Garden and Park Waste	Organic Share in Municipal Waste
03356	188.35	243.80	416.33	8.29	4.98	4.54
03357	713.28	1363.59	676.53	9.59	13.71	7.25
03358	220.47	574.75	354.35	9.49	7.62	5.31
03359	380.85	551.29	497.67	11.75	10.58	5.90
03360	92.65	623.66	116.69	9.94	4.88	3.95
03361	238.84	324.94	232.81	7.91	5.97	4.74
03401	13.89	0.00	30.58	5.02	2.97	3.53
03402	18.60	11.11	50.72	2.98	2.13	1.61
03403	8.96	0.00	31.35	12.83	6.44	4.65
03404	17.23	16.73	16.55	9.54	8.65	6.62
03405	12.45	0.00	47.63	4.46	3.04	4.16
03451	263.94	327.80	332.77	13.14	5.44	4.39
03452	387.33	375.97	715.27	18.68	8.54	5.28
03453	1398.56	992.96	196.30	12.41	7.57	5.23
03454	1491.05	1572.61	260.42	18.77	31.07	11.14
03455	253.20	158.41	486.97	18.70	4.28	5.45
03456	577.32	667.84	137.59	7.97	13.03	3.87
03457	402.00	275.32	828.56	9.84	7.51	6.85
03458	389.12	604.14	247.73	11.19	5.88	5.13
03459	990.87	975.87	296.98	21.03	28.96	11.63
03460	1132.91	500.90	120.15	8.70	9.22	3.66
03461	327.54	116.54	825.06	7.96	3.98	1.74
03462	226.68	202.11	404.98	3.36	2.78	3.36
04011	7.17	0.00	310.14	32.74	21.30	22.53
04012	0.19	0.00	5.47	6.70	4.39	8.00
05111	0.50	8.36	0.45	35.96	23.64	28.13
05112	1.38	3.08	0.57	28.85	19.06	26.89
05113	1.98	0.00	0.61	34.22	22.51	29.12
05114	4.16	0.00	0.40	13.22	8.82	14.01
05116	3.88	60.35	0.35	23.77	10.26	12.17
05117	0.44	0.00	0.36	9.94	6.58	8.51
05119	0.34	1.78	0.11	12.39	8.20	13.06
05120	3.05	0.00	0.46	6.43	4.27	5.80
05122	1.45	0.00	0.40	9.32	6.16	9.72
05124	3.59	3.57	0.89	20.56	13.51	17.83
05154	340.80	586.58	10.24	28.34	13.12	11.26
05158	7.23	50.95	1.88	28.39	18.97	22.29
05162	13.38	261.60	1.49	33.57	18.12	25.28
05166	82.24	209.64	2.01	27.66	12.06	12.88
05170	161.54	338.77	8.55	27.17	19.00	19.17
05314	0.00	2.82	0.26	18.73	12.39	15.15

Continued on next page

Table A.7 – continued from previous page

NUTS 3 Region	Biogas Potential in GWh_{GCV} from Animal Manure	Energy Crops	Grass-land	Bio-Waste Container	Garden and Park Waste	Organic Share in Municipal Waste
05315	0.00	0.26	0.34	62.29	40.86	65.53
05316	1.88	7.20	0.55	9.60	7.56	8.64
05334	43.03	130.72	6.85	43.93	25.92	27.56
05358	24.18	468.90	3.06	24.79	11.17	9.39
05362	6.10	342.41	0.83	42.45	18.78	22.09
05366	56.64	195.35	12.33	21.46	9.07	8.12
05370	68.12	396.29	2.28	14.83	13.39	8.27
05374	73.91	37.28	12.93	16.06	12.05	0.00
05378	24.13	1.58	4.86	16.61	11.26	0.00
05382	57.90	177.10	10.18	60.33	24.66	21.14
05512	19.31	0.00	0.64	8.85	4.65	8.05
05513	2.27	0.00	0.18	15.29	11.16	15.56
05515	20.36	76.77	1.04	18.21	12.28	10.16
05554	717.90	768.44	6.75	37.18	18.83	11.00
05558	461.42	359.50	3.58	30.31	9.46	4.95
05562	115.32	143.73	2.66	36.29	24.87	32.67
05566	628.57	635.81	7.75	39.13	19.21	12.86
05570	473.38	421.72	4.50	31.98	12.01	9.33
05711	10.71	43.52	0.81	19.56	13.09	12.79
05754	199.90	270.42	5.67	26.78	14.83	9.64
05758	45.60	138.84	1.26	17.05	10.31	7.01
05762	158.06	389.54	6.67	15.66	6.89	2.83
05766	73.35	303.25	4.36	30.19	14.70	8.46
05770	197.57	345.86	5.42	33.20	13.82	7.51
05774	219.17	261.37	6.12	29.64	13.06	9.35
05911	0.29	4.50	0.22	21.42	14.15	18.37
05913	3.06	26.54	0.47	34.43	22.69	29.46
05914	2.66	2.95	0.63	11.10	7.39	11.10
05915	35.28	57.58	1.12	10.54	7.21	8.95
05916	1.75	1.06	0.05	9.15	6.03	9.67
05954	19.87	29.98	3.49	19.52	12.90	12.78
05958	129.81	133.58	16.94	21.00	12.98	8.54
05962	60.04	55.67	8.23	24.44	18.16	21.59
05966	32.38	16.03	5.94	14.76	6.34	3.34
05970	26.60	5.83	7.63	24.14	12.56	10.35
05974	202.48	390.81	5.75	31.70	13.30	9.40
05978	72.87	117.30	2.18	23.26	15.92	15.35
06411	0.19	5.90	16.92	9.39	6.04	6.28
06412	0.71	44.70	25.53	43.03	28.16	33.94
06413	0.00	0.00	0.00	7.27	4.76	5.03
06414	1.75	61.62	47.60	16.22	10.79	15.24

Continued on next page

Table A.7 – continued from previous page

NUTS 3 Region	Biogas Potential in GWh_{GCV} from Animal Manure	Energy Crops	Grass-land	Bio-Waste Container	Garden and Park Waste	Organic Share in Municipal Waste
06431	18.43	182.36	367.75	24.34	10.88	8.17
06432	16.12	313.15	216.12	34.22	11.99	6.34
06433	3.45	177.29	85.40	23.87	10.67	9.49
06434	4.43	79.31	160.16	13.71	11.23	8.77
06435	44.03	342.21	818.83	35.20	17.47	13.74
06436	1.68	75.20	0.00	16.35	9.18	9.93
06437	26.99	98.82	383.50	5.70	6.26	2.86
06438	3.26	37.51	80.06	20.40	13.82	12.11
06439	4.13	62.21	207.27	10.81	11.54	4.70
06440	29.17	644.42	471.06	20.21	12.99	7.42
06531	20.01	229.33	427.94	28.25	11.29	7.87
06532	15.72	67.11	601.79	22.23	11.26	11.73
06533	24.05	239.39	374.86	16.51	7.72	7.91
06534	42.59	376.81	691.23	29.10	11.02	7.61
06535	81.47	351.27	1188.82	6.30	7.10	4.13
06611	0.00	2.72	11.80	11.78	7.68	9.21
06631	97.29	347.26	1241.33	17.77	10.38	7.19
06632	36.43	96.73	517.24	7.99	6.07	3.29
06633	33.54	489.58	399.57	34.90	10.50	9.18
06634	66.88	785.08	555.89	10.59	14.03	8.72
06635	92.62	516.00	1011.02	21.52	8.11	5.75
06636	8.58	261.23	489.26	7.96	5.15	2.76
07111	0.68	0.00	0.00	6.61	4.49	4.86
07131	19.95	109.14	369.44	9.68	6.44	5.74
07132	31.88	15.42	444.16	16.98	6.00	3.13
07133	12.85	167.80	302.38	14.16	7.41	4.88
07134	22.35	62.53	403.13	4.73	9.94	2.23
07135	14.06	98.43	0.00	4.18	5.15	2.16
07137	16.70	330.22	212.49	12.45	9.46	10.13
07138	23.32	28.93	368.98	25.50	7.94	5.42
07140	27.52	225.65	397.60	10.50	10.83	2.32
07141	20.54	226.69	308.18	12.45	6.02	5.45
07143	39.25	117.02	760.25	21.96	9.35	8.34
07211	0.85	0.00	28.42	6.75	4.57	0.00
07231	42.69	305.45	554.36	6.57	15.97	4.38
07232	181.46	1082.75	1382.29	5.71	7.34	5.50
07233	60.30	15.79	799.27	3.57	5.02	3.24
07235	32.96	117.82	482.57	8.69	22.21	10.49
07311	0.00	0.00	3.11	2.84	3.99	2.25
07312	0.53	0.00	21.93	5.79	3.97	5.05
07313	0.00	0.00	3.46	3.51	2.79	1.34

Continued on next page

Table A.7 – continued from previous page

NUTS 3 Region	Biogas Potential in GWh_{GCV} from Animal Manure	Energy Crops	Grass-land	Bio-Waste Container	Garden and Park Waste	Organic Share in Municipal Waste
07314	0.00	0.00	0.00	9.67	6.46	7.54
07315	0.00	0.00	0.00	12.32	8.22	8.56
07316	0.00	0.00	15.60	3.11	2.20	2.42
07317	0.93	0.00	18.28	3.65	1.67	1.44
07318	0.00	0.00	3.92	3.60	2.00	1.90
07319	0.11	0.00	10.79	4.82	3.38	3.57
07320	3.08	0.00	38.03	2.01	1.44	1.16
07331	0.76	770.67	0.00	13.47	5.99	4.94
07332	1.12	155.66	41.98	12.04	5.84	5.03
07333	12.15	585.29	253.06	4.42	6.64	2.63
07334	2.51	197.22	0.00	8.99	5.50	3.33
07335	16.52	49.19	326.04	6.43	10.91	4.60
07336	21.56	169.08	405.36	4.17	5.89	2.91
07337	2.17	219.75	88.96	6.93	5.92	3.15
07338	0.63	159.65	0.00	8.90	6.89	4.43
07339	2.31	529.37	59.69	13.01	11.20	5.59
07340	25.92	166.02	322.39	6.72	7.53	1.61
08111	1.30	0.00	16.21	36.64	24.02	26.88
08115	18.73	77.51	209.15	27.03	15.86	10.92
08116	12.62	58.19	279.39	30.78	20.91	13.66
08117	51.18	118.06	463.33	14.85	21.16	9.56
08118	29.36	314.64	170.46	31.37	27.88	15.93
08119	33.01	103.86	363.43	26.99	17.17	10.35
08121	0.17	0.00	7.24	7.20	5.26	4.47
08125	26.71	454.30	214.18	19.95	14.58	10.89
08126	78.48	286.53	272.68	6.47	9.86	5.04
08127	220.44	422.44	756.58	11.25	10.65	5.15
08128	65.11	358.54	252.03	10.35	7.01	1.99
08135	42.41	157.72	272.24	7.67	5.73	2.68
08136	145.09	387.92	864.45	18.36	16.96	7.23
08211	0.34	0.00	23.28	5.82	6.68	1.73
08212	0.52	0.00	17.36	18.08	12.86	9.52
08215	8.93	107.66	230.90	25.60	40.90	12.05
08216	4.33	8.13	127.53	13.73	14.45	4.33
08221	0.85	0.00	7.00	9.18	6.06	4.69
08222	0.06	0.00	0.00	17.96	11.93	15.49
08225	43.96	240.02	325.03	8.40	12.65	4.10
08226	23.41	236.22	217.66	33.29	22.06	14.13
08231	0.28	0.00	0.00	7.18	4.79	4.15
08235	20.04	22.38	280.57	9.58	9.70	2.17
08236	16.53	81.85	225.84	11.52	18.46	5.95

Continued on next page

Table A.7 – continued from previous page

NUTS 3 Region	Biogas Potential in GWh_{GCV} from: Animal Manure	Energy Crops	Grass-land	Bio-Waste Container	Garden and Park Waste	Organic Share in Municipal Waste
08237	19.23	63.54	284.98	8.61	5.27	1.71
08311	0.69	0.00	29.28	13.30	8.82	5.11
08315	41.80	36.24	706.47	15.11	13.35	7.58
08316	20.93	7.88	280.77	9.52	9.37	6.19
08317	47.17	85.64	618.07	24.67	22.78	17.70
08325	34.69	115.28	398.30	8.08	6.34	3.04
08326	50.87	110.13	685.66	12.31	9.99	5.67
08327	25.60	65.55	458.68	9.79	6.66	3.66
08335	41.06	173.84	398.65	24.10	11.67	7.04
08336	21.49	0.00	430.31	13.32	16.80	8.97
08337	53.08	136.76	675.45	9.86	11.36	5.14
08415	49.11	122.44	675.63	16.57	12.99	8.23
08416	11.98	31.61	210.86	13.03	9.17	4.57
08417	23.00	62.63	647.65	11.08	8.32	3.87
08421	8.78	0.00	18.95	7.20	4.88	3.30
08425	150.64	519.22	574.29	11.28	12.48	4.43
08426	179.53	629.19	714.65	11.40	9.82	5.93
08435	36.56	108.89	343.48	13.91	8.98	5.11
08436	217.80	377.39	1676.29	16.40	13.98	7.06
08437	83.42	323.13	589.85	7.68	7.51	2.91
09161	2.08	22.27	22.14	10.56	5.24	3.95
09162	1.52	12.87	35.65	85.19	55.36	68.51
09163	3.73	5.83	0.00	3.63	3.41	3.50
09171	62.46	139.11	213.96	6.37	5.05	4.41
09172	41.77	29.89	381.82	6.10	4.41	3.81
09173	51.95	13.93	764.91	7.34	6.70	4.38
09174	48.36	179.63	151.90	8.77	7.63	4.68
09175	49.06	90.54	271.44	8.07	9.84	3.06
09176	38.96	216.20	192.87	7.57	11.05	5.00
09177	128.83	305.10	351.05	9.65	6.13	3.87
09178	44.20	130.01	226.58	10.17	7.40	5.65
09179	23.63	86.12	124.75	12.54	8.53	6.93
09180	20.32	0.84	0.00	5.13	3.74	1.78
09181	51.88	116.03	445.72	6.91	12.89	2.81
09182	43.68	12.68	655.16	8.42	4.20	3.24
09183	121.59	230.40	394.36	6.58	6.65	3.36
09184	8.50	43.04	101.45	21.20	13.74	11.61
09185	39.09	128.09	229.84	5.56	4.33	2.12
09186	36.43	103.18	187.60	7.29	10.40	3.67
09187	168.71	171.13	1254.93	15.04	21.54	9.76
09188	13.60	21.41	186.69	7.85	5.46	3.63

Continued on next page

Table A.7 – continued from previous page

NUTS 3 Region	Biogas Potential in GWh_{GCV} from Animal Manure	Energy Crops	Grass-land	Bio-Waste Container	Garden and Park Waste	Organic Share in Municipal Waste
09189	149.66	225.85	934.34	10.23	7.62	5.80
09190	92.18	39.25	1179.67	7.81	6.50	3.37
09261	3.02	4.92	0.00	4.07	4.03	2.55
09262	0.00	2.72	0.00	4.48	2.43	1.56
09263	0.28	20.00	7.91	3.23	2.92	1.43
09271	46.87	221.16	282.41	10.41	6.28	3.63
09272	46.49	37.74	589.10	6.98	4.52	2.43
09273	47.22	148.24	163.75	6.99	5.73	3.62
09274	211.57	331.49	272.07	9.08	7.24	5.31
09275	193.69	233.26	642.37	16.77	10.38	5.85
09276	46.53	29.35	489.72	6.84	4.29	2.38
09277	166.40	366.58	509.85	7.00	6.64	3.24
09278	67.74	343.79	401.48	6.86	7.25	3.04
09279	85.02	260.03	126.87	5.53	5.30	2.57
09361	2.42	8.25	0.00	2.46	3.10	1.45
09362	0.12	4.94	16.60	8.54	10.36	6.41
09363	4.20	9.32	0.00	2.47	3.13	1.54
09371	76.39	162.47	368.67	6.08	7.71	3.07
09372	132.45	207.02	866.96	7.96	9.11	2.53
09373	69.78	185.64	391.50	7.66	9.80	4.06
09374	82.02	148.54	462.92	5.58	8.49	3.37
09375	53.01	285.36	298.92	11.12	18.35	6.32
09376	94.89	199.03	426.12	8.51	7.18	5.37
09377	77.97	148.15	340.38	4.31	3.81	2.29
09461	0.00	0.17	2.89	5.59	2.88	4.87
09462	4.12	11.00	0.00	4.24	2.86	2.95
09463	0.35	1.09	8.60	2.42	1.65	2.23
09464	2.75	8.97	0.00	3.76	5.39	1.12
09471	37.81	151.29	278.60	10.79	7.58	3.97
09472	69.15	144.05	529.42	6.13	8.36	3.05
09473	45.94	90.91	195.27	5.09	11.32	3.56
09474	17.94	68.57	258.59	9.05	5.10	3.48
09475	61.83	101.85	370.46	8.15	12.53	2.44
09476	15.17	21.69	201.58	3.99	6.21	3.01
09477	34.04	65.28	263.44	4.26	9.58	2.87
09478	21.32	56.31	175.47	3.91	5.08	3.43
09479	27.22	49.59	212.22	4.30	6.44	1.21
09561	6.06	17.04	0.00	2.59	2.91	1.46
09562	2.24	9.21	21.78	9.41	4.28	3.51
09563	1.78	8.92	16.18	7.29	4.82	4.21
09564	1.10	4.71	19.46	29.95	19.67	26.93

Continued on next page

Table A.7 – continued from previous page

NUTS 3 Region	Biogas Potential in GWh_{GCV} from Animal Manure	Energy Crops	Grass-land	Bio-Waste Container	Garden and Park Waste	Organic Share in Municipal Waste
09565	1.27	3.47	0.00	2.42	2.77	0.99
09571	186.18	490.83	964.58	12.12	9.12	4.46
09572	13.90	56.85	135.00	7.88	5.76	3.14
09573	20.16	81.94	82.54	10.94	4.69	3.16
09574	23.37	42.62	282.11	9.85	7.30	5.48
09575	119.68	350.74	400.70	6.04	9.69	2.54
09576	45.51	111.77	257.71	7.35	8.72	3.90
09577	74.85	199.54	417.00	8.17	4.63	2.36
09661	0.51	0.72	0.00	6.31	2.71	2.23
09662	0.00	0.10	0.00	3.05	4.82	2.72
09663	0.00	3.06	5.62	7.33	4.90	6.24
09671	9.16	22.67	196.64	10.20	11.09	2.05
09672	27.71	67.94	359.88	7.09	10.73	3.03
09673	27.07	118.37	320.84	4.68	13.22	2.16
09674	32.10	131.97	210.37	6.26	4.61	1.87
09675	42.52	210.15	120.91	7.63	6.17	2.01
09676	16.54	32.37	196.73	7.54	9.00	4.46
09677	14.94	95.54	226.86	12.08	6.17	4.49
09678	26.47	200.48	118.54	6.74	7.57	2.41
09679	38.88	359.36	96.49	14.11	7.97	4.78
09761	0.00	10.89	8.90	17.32	11.06	11.07
09762	0.00	0.00	0.00	2.70	2.70	1.33
09763	5.70	0.00	93.21	3.93	4.00	2.30
09764	5.11	12.02	0.00	3.00	2.19	1.35
09771	88.76	228.84	211.28	9.74	5.82	3.69
09772	89.39	240.63	402.91	25.69	10.86	8.18
09773	85.00	291.38	220.96	9.39	4.52	2.87
09774	64.34	172.12	324.70	7.23	10.41	3.33
09775	32.28	105.82	167.53	10.00	9.99	6.21
09776	35.49	4.65	435.85	4.72	5.02	2.78
09777	167.19	88.87	1720.34	8.09	8.06	3.65
09778	180.81	254.58	1161.78	8.25	11.25	4.33
09779	108.78	418.99	406.60	13.07	6.45	3.99
09780	105.23	6.50	1569.68	8.97	9.89	5.28
10041	4.20	37.74	153.96	19.23	13.11	7.11
10042	19.00	152.77	455.41	6.11	4.68	0.00
10043	8.24	46.25	205.89	7.85	5.49	0.00
10044	13.40	141.06	283.26	11.57	8.13	0.00
10045	11.01	93.49	365.91	8.49	6.09	0.00
10046	17.66	106.40	423.07	5.22	4.27	0.00
11000	0.91	59.61	57.98	206.75	132.43	181.45

Continued on next page

Table A.7 – continued from previous page

NUTS 3 Region	Biogas Potential in GWh_{GCV} from Animal Manure	Energy Crops	Grass-land	Bio-Waste Container	Garden and Park Waste	Organic Share in Municipal Waste
12051	0.79	0.00	13.07	4.20	2.91	3.30
12052	5.46	4.04	28.58	5.86	4.00	4.91
12053	12.25	77.47	15.40	3.41	2.39	2.34
12054	4.13	0.00	43.43	9.85	6.58	9.02
12060	73.74	319.75	243.39	10.42	10.76	8.10
12061	113.32	408.87	544.36	9.66	8.16	7.35
12062	235.97	682.95	602.86	6.15	5.38	4.68
12063	104.61	632.05	755.58	9.29	7.47	6.47
12064	154.33	1352.55	233.12	11.20	8.84	7.17
12065	93.83	452.34	577.49	12.19	9.39	8.73
12066	125.08	276.52	187.59	6.60	5.28	5.03
12067	124.87	688.09	381.34	10.71	8.74	8.45
12068	158.12	1094.59	881.35	5.82	5.58	3.82
12069	207.07	787.68	731.25	12.39	10.86	7.40
12070	234.21	1357.13	899.21	4.56	4.56	3.31
12071	100.27	326.68	300.89	6.91	5.87	4.81
12072	180.11	841.54	480.06	9.61	7.82	7.31
12073	185.71	1637.69	747.01	7.11	9.02	6.09
13003	3.79	0.00	28.76	12.10	8.15	11.20
13004	0.50	0.00	2.84	5.75	3.86	4.59
13071	375.69	4018.57	1025.43	15.42	13.80	13.30
13072	433.43	3138.62	838.50	12.54	10.84	8.46
13073	210.27	2698.28	777.53	13.20	10.93	12.73
13074	222.25	1182.15	336.95	9.18	7.78	5.80
13075	442.48	3268.42	1213.65	14.00	12.11	12.56
13076	592.23	3616.93	1264.92	12.58	18.02	7.64
14511	13.62	28.16	35.77	14.60	9.89	7.12
14521	190.09	477.28	566.29	20.42	15.48	11.26
14522	341.60	1880.38	542.61	18.35	14.24	7.20
14523	161.18	510.86	393.89	13.65	10.57	8.52
14524	130.01	632.16	207.00	19.06	13.77	9.72
14612	3.03	46.94	34.08	31.94	21.34	16.72
14625	210.87	1238.65	439.62	17.99	14.30	9.82
14626	153.43	1253.62	430.58	19.58	12.29	6.44
14627	191.36	1327.58	257.40	14.40	11.03	8.51
14628	143.90	693.47	514.24	14.53	11.20	8.46
14713	7.53	90.56	31.80	32.92	22.01	19.26
14729	155.17	1623.42	208.87	15.18	11.79	6.86
14730	208.45	1998.84	261.03	11.61	11.90	6.38
15001	6.07	33.95	67.27	9.61	3.41	3.55
15002	0.00	10.08	18.85	13.92	9.24	11.60

Continued on next page

Table A.7 – continued from previous page

NUTS 3 Region	Biogas Potential in GWh_{GCV} from Animal Manure	Energy Crops	Grass-land	Bio-Waste Container	Garden and Park Waste	Organic Share in Municipal Waste
15003	0.00	37.38	16.07	13.85	9.30	11.67
15081	288.08	2015.79	968.85	5.06	5.16	3.32
15082	133.92	1242.92	316.41	14.59	7.56	8.41
15083	433.25	3184.49	507.30	10.19	8.75	4.91
15084	198.81	1575.85	228.22	19.05	8.54	5.58
15085	128.57	1651.11	395.26	13.00	10.28	10.33
15086	417.41	1023.67	519.74	7.23	12.74	4.76
15087	145.42	1152.87	270.88	8.31	6.95	6.34
15088	245.78	1846.07	148.26	10.95	9.86	6.39
15089	220.07	1723.22	127.34	22.81	8.95	10.32
15090	347.45	1940.60	1176.82	14.44	6.32	2.67
15091	308.74	952.65	598.47	7.54	8.13	3.63
16051	4.75	184.82	25.33	12.34	9.52	9.05
16052	2.83	84.74	26.21	5.64	5.42	3.77
16053	0.12	0.00	0.00	9.19	4.32	3.45
16054	0.00	0.00	9.14	2.16	1.56	1.89
16055	0.00	0.00	0.00	3.77	2.57	2.69
16056	3.78	38.01	45.13	2.49	1.79	1.40
16061	60.19	603.35	309.26	5.95	5.01	3.74
16062	66.73	522.18	164.12	5.01	4.04	3.37
16063	75.31	484.62	816.36	7.38	6.12	4.15
16064	65.14	933.63	181.10	6.18	5.02	3.89
16065	54.98	929.10	186.82	6.92	4.01	2.90
16066	90.84	317.54	716.25	7.32	7.20	4.80
16067	50.17	700.01	317.62	8.04	6.13	2.94
16068	50.65	1001.43	70.19	4.15	3.46	2.81
16069	59.44	353.99	434.50	3.79	4.20	2.56
16070	46.26	302.60	268.07	6.44	5.11	5.13
16071	85.18	897.77	146.50	4.82	4.10	4.15
16072	12.86	80.70	106.93	3.34	3.73	2.40
16073	62.95	262.77	491.30	6.42	8.59	4.50
16074	104.43	595.80	312.80	5.06	4.03	2.64
16075	106.40	636.09	355.10	4.87	6.89	3.42
16076	100.73	736.54	317.68	5.94	6.22	3.97
16077	44.98	783.64	97.99	5.42	4.57	3.03

A.3 Optimal System Configurations

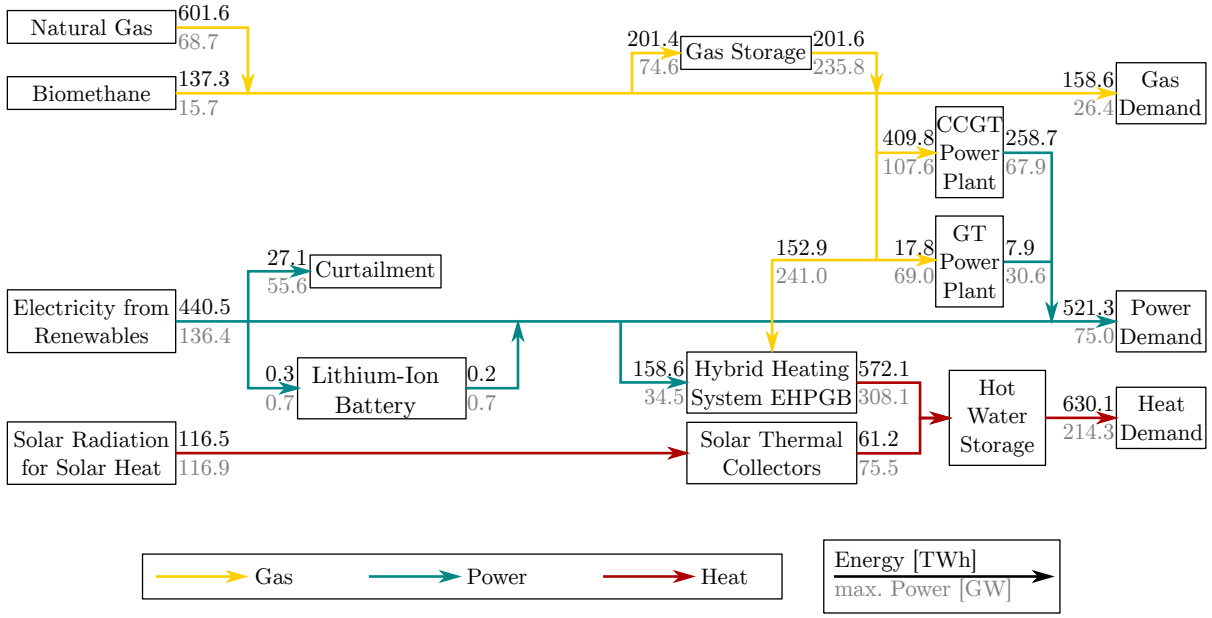

Figure A.1: Flow scheme of the IES for 60 % RE SNG.

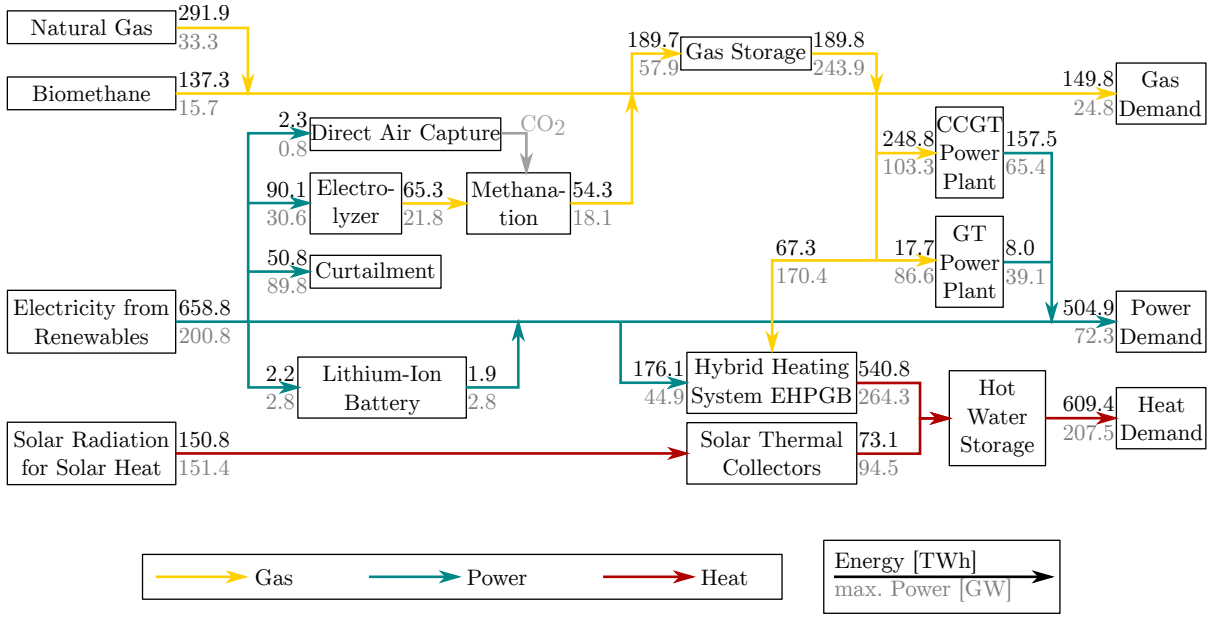

Figure A.2: Flow scheme of the IES for 80 % RE SNG.

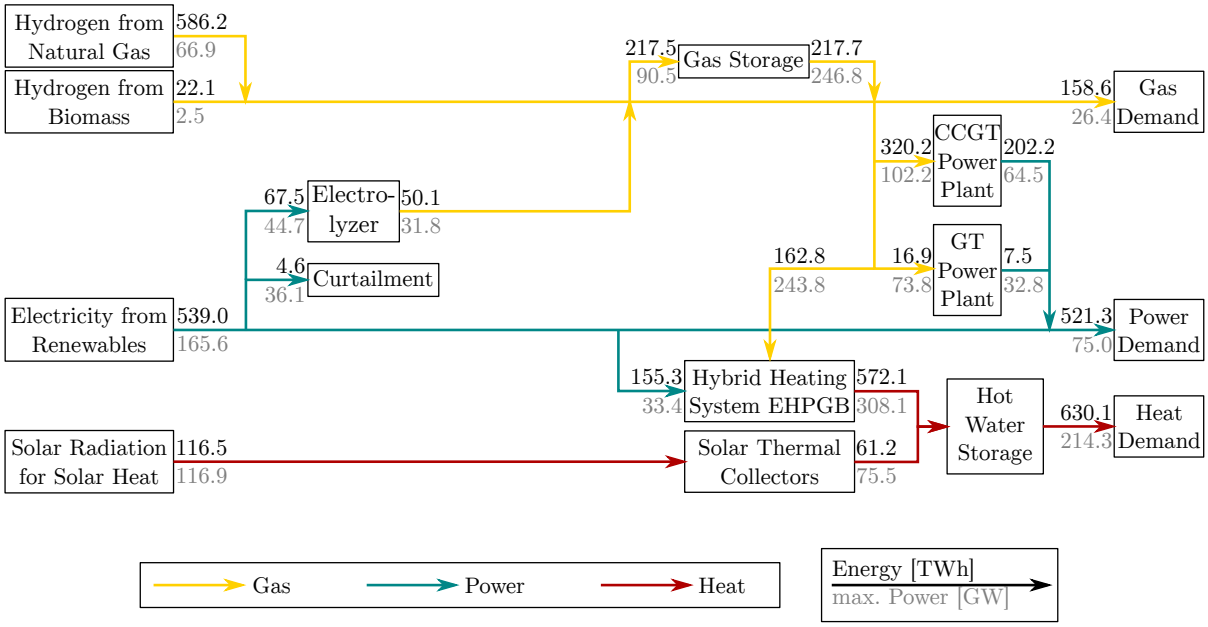

Figure A.3: Flow scheme of the IES for 60 % RE H2.

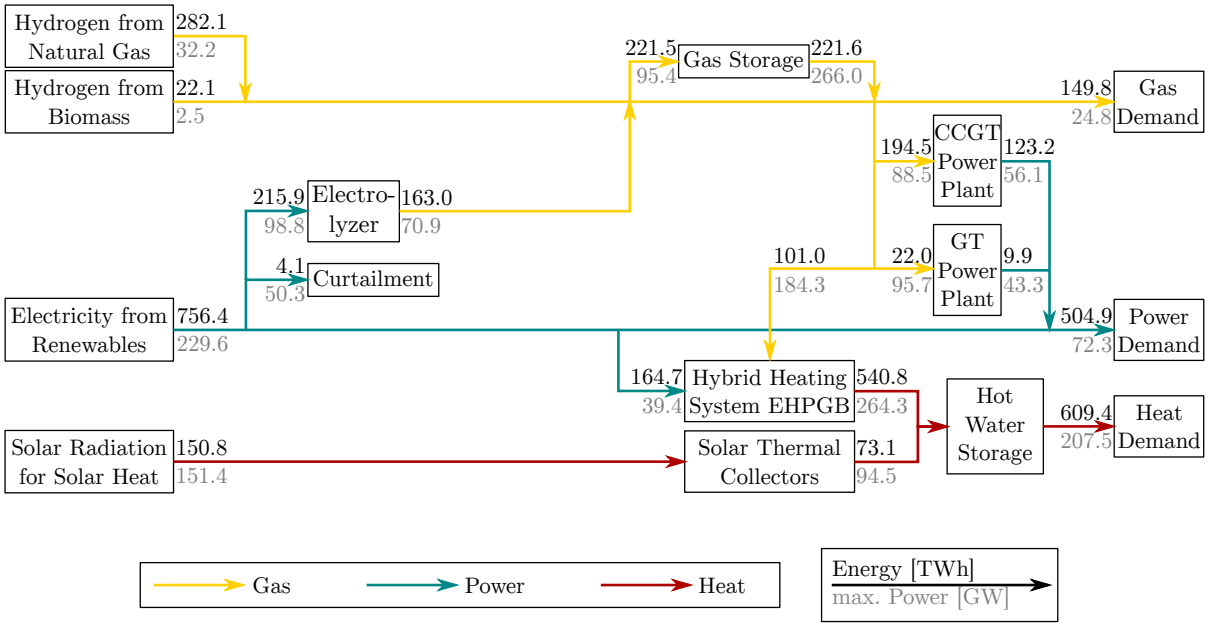

Figure A.4: Flow scheme of the IES for 80 % RE H2.

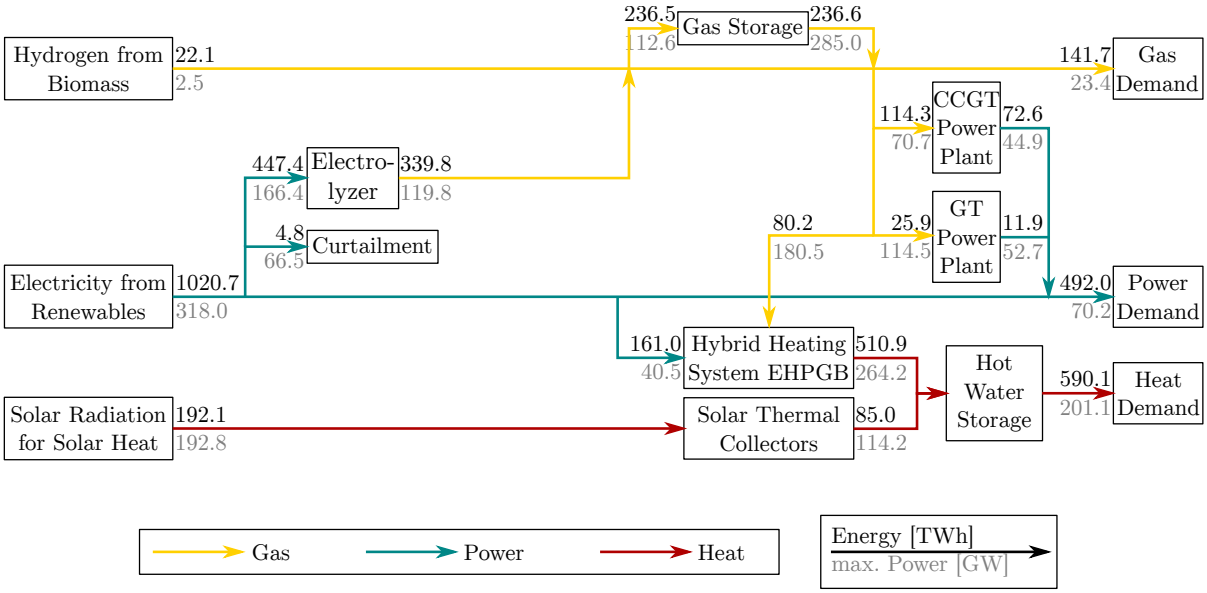

Figure A.5: Flow scheme of the IES for 100 % RE H2.

Table A.8: Results of the heating technology variations for 60 % RE SNG.

Variable	Unit	100_0_0	50_50_0	0_100_0	0_50_50	0_0_100
Nominal renewable power	GW_{el}	200.9	200.1	204.6	248.2	322.6
Planned year for renewable power	-	2033	2033	2034	2041	2052
Li-ion battery maximum power	GW_{el}	0.0	0.0	0.7	0.0	3.5
Li-ion battery capacity	GWh	0.0	0.0	1.5	0.2	16.5
Nominal PtG plant power	GW_{el}	0.0	0.0	0.0	13.7	59.8
Nominal CCGT power	GW_{el}	83.9	73.2	67.9	56.8	39.5
Nominal GT power	GW_{el}	229.7	136.6	44.3	41.0	31.0
Full load hours Li-ion battery (charging)	h	-	-	365	666	921
Full load hours PtG	h	-	-	-	2885	3531
Full load hours CCGT	h	3777	3891	3808	2845	1778
Full load hours GT	h	91	97	178	155	134
Gas storage capacity	TWh_{NCV}	100.0	114.3	116.7	132.2	174.3
Gas storage maximum injection capacity	GW_{NCV}	71.1	75.4	74.6	82.0	106.8
Gas storage maximum withdrawal capacity	GW_{NCV}	309.3	273.1	235.8	236.8	251.1
Imported natural gas	TWh_{NCV}	618.2	608.2	601.6	597.7	603.8
Used biomethane potential	TWh_{NCV}	89.3	137.3	137.3	137.3	137.3
Balance point temperature EHPGB	°C	-	12.7	11.2	8.5	-
Balance point temperature EHPEHR	°C	5.6	5.7	-	-	-
Relative CO_2 reduction	%	86.3	86.5	86.7	86.8	86.7
Cost annuity	bil. EUR	121.9	114.3	108.1	113.8	125.8

Table A.9: Results of the heating technology variations for 80 % RE SNG.

Variable	Unit	100_0_0	50_50_0	0_100_0	0_50_50	0_0_100
Nominal renewable power	GW_{el}	292.8	299.4	301.1	369.3	491.7
Planned year for renewable power	-	2047	2048	2049	2059	2087
Li-ion battery maximum power	GW_{el}	4.4	3.0	2.8	7.2	2.7
Li-ion battery capacity	GWh	18.1	12.6	11.0	33.6	14.4
Nominal PtG plant power	GW_{el}	21.9	27.6	31.3	75.8	136.3
Nominal CCGT power	GW_{el}	73.4	67.8	65.4	47.8	30.2
Nominal GT power	GW_{el}	224.0	140.0	54.8	48.9	36.1
Full load hours Li-ion battery (charging)	h	812	826	776	878	799
Full load hours PtG	h	2872	2949	2948	3386	3881
Full load hours CCGT	h	2475	2449	2408	1640	1116
Full load hours GT	h	67	80	146	130	123
Gas storage capacity	TWh_{NCV}	80.3	83.9	84.6	118.5	166.2
Gas storage maximum injection capacity	GW_{NCV}	52.8	55.9	57.9	83.1	119.9
Gas storage maximum withdrawal capacity	GW_{NCV}	297.8	271.8	243.9	257.6	270.1
Imported natural gas	TWh_{NCV}	295.7	293.7	291.9	295.2	313.0
Used biomethane potential	TWh_{NCV}	137.3	137.3	137.3	137.3	137.3
Balance point temperature EHPGB	°C	-	8.9	8.1	6.7	-
Balance point temperature EHPEHR	°C	4.4	4.6	-	-	-
Relative CO_2 reduction	%	93.8	93.8	93.9	93.8	93.4
Cost annuity	bil. EUR	118.8	113.2	109.2	120.6	137.0

Table A.10: Results of the heating technology variations for 100 % RE SNG.

Variable	Unit	100_0_0	50_50_0	0_100_0	0_50_50	0_0_100
Nominal renewable power	GW_{el}	436.7	437.9	440.0	553.0	667.6
Planned year for renewable power	-	2073	2074	2074	2106	2150
Li-ion battery maximum power	GW_{el}	11.4	13.5	12.9	5.3	0.0
Li-ion battery capacity	GWh	51.1	63.9	61.8	25.1	0.0
Nominal PtG plant power	GW_{el}	87.8	92.5	95.0	159.5	239.9
Nominal CCGT power	GW_{el}	61.0	59.7	57.1	38.1	22.0
Nominal GT power	GW_{el}	224.9	144.7	64.1	55.6	40.2
Full load hours Li-ion battery (charging)	h	866	869	863	713	-
Full load hours PtG	h	3408	3344	3367	3725	3889
Full load hours CCGT	h	1521	1463	1442	1062	739
Full load hours GT	h	57	69	123	109	112
Gas storage capacity	TWh_{NCV}	67.7	70.1	70.8	103.8	145.2
Gas storage maximum injection capacity	GW_{NCV}	57.1	59.8	61.2	98.6	145.3
Gas storage maximum withdrawal capacity	GW_{NCV}	299.0	283.1	261.5	276.0	288.8
Imported natural gas	TWh_{NCV}	0.0	0.0	0.0	0.0	0.0
Used biomethane potential	TWh_{NCV}	137.3	137.3	137.3	137.3	137.3
Balance point temperature EHPGB	°C	-	6.6	6.4	5.5	-
Balance point temperature EHPEHR	°C	3.7	4.2	-	-	-
Relative CO_2 reduction	%	100.6	100.6	100.6	100.6	100.6
Cost annuity	bil. EUR	119.6	115.8	112.5	128.1	147.4

Table A.11: Results of the heating technology variations for 60 % RE H2.

Variable	Unit	100_0_0	50_50_0	0_100_0	0_50_50	0_0_100
Nominal renewable power	GW_{el}	230.6	241.2	247.7	291.6	358.9
Planned year for renewable power	-	2038	2039	2040	2047	2057
Li-ion battery maximum power	GW_{el}	0.0	0.0	0.0	0.0	0.0
Li-ion battery capacity	GWh	0.0	0.0	0.0	0.0	0.0
Nominal PtG plant power	GW_{el}	31.7	40.0	44.7	77.8	126.0
Nominal CCGT power	GW_{el}	81.8	69.9	64.5	51.4	36.6
Nominal GT power	GW_{el}	232.0	139.7	46.2	42.9	33.6
Full load hours Li-ion battery (charging)	h	-	-	-	-	-
Full load hours PtG	h	1246	1395	1509	2025	2629
Full load hours CCGT	h	3328	3243	3132	2417	1667
Full load hours GT	h	85	90	162	160	148
Gas storage capacity	TWh_{NCV}	97.7	107.9	112.4	128.6	160.9
Gas storage maximum injection capacity	GW_{NCV}	80.9	88.0	90.5	111.8	146.3
Gas storage maximum withdrawal capacity	GW_{NCV}	317.7	285.1	246.8	256.2	267.9
Imported hydrogen from natural gas	TWh_{NCV}	605.2	593.1	586.2	578.1	581.5
Used potential of hydrogen from biomass	TWh_{NCV}	0.0	22.1	22.1	22.1	22.1
Balance point temperature EHPGB	°C	-	12.9	11.5	9.8	-
Balance point temperature EHPEHR	°C	5.7	5.8	-	-	-
Relative CO_2 reduction	%	100.0	100.0	100.0	100.0	100.0
Cost annuity	bil. EUR	138.9	131.3	125.5	129.4	137.0

Table A.12: Results of the heating technology variations for 80 % RE H2.

Variable	Unit	100_0_0	50_50_0	0_100_0	0_50_50	0_0_100
Nominal renewable power	GW_{el}	329.3	338.6	344.4	415.9	506.5
Planned year for renewable power	-	2053	2054	2055	2068	2091
Li-ion battery maximum power	GW_{el}	0.0	0.0	0.0	0.0	0.0
Li-ion battery capacity	GWh	0.0	0.0	0.0	0.0	0.0
Nominal PtG plant power	GW_{el}	87.4	94.7	98.8	143.0	201.2
Nominal CCGT power	GW_{el}	65.7	60.6	56.1	40.6	25.6
Nominal GT power	GW_{el}	236.1	147.6	57.7	51.1	40.5
Full load hours Li-ion battery (charging)	h	-	-	-	-	-
Full load hours PtG	h	2012	2090	2186	2653	2987
Full load hours CCGT	h	2383	2285	2197	1670	1225
Full load hours GT	h	84	95	172	166	172
Gas storage capacity	TWh_{NCV}	86.8	90.6	91.8	116.7	151.9
Gas storage maximum injection capacity	GW_{NCV}	87.7	92.7	95.4	126.8	168.9
Gas storage maximum withdrawal capacity	GW_{NCV}	323.8	293.6	266.0	277.3	288.1
Imported hydrogen from natural gas	TWh_{NCV}	286.3	283.9	282.1	284.3	291.4
Used potential of hydrogen from biomass	TWh_{NCV}	22.1	22.1	22.1	22.1	22.1
Balance point temperature EHPGB	°C	-	9.9	9.5	8.8	-
Balance point temperature EHPEHR	°C	5.2	5.7	-	-	-
Relative CO_2 reduction	%	100.0	100.0	100.0	100.0	100.0
Cost annuity	bil. EUR	122.9	117.0	112.8	119.2	127.5

Table A.13: Results of the heating technology variations for 100 % RE H2.

Variable	Unit	100_0_0	50_50_0	0_100_0	0_50_50	0_0_100
Nominal renewable power	GW_{el}	468.2	475.9	480.9	558.1	635.1
Planned year for renewable power	-	2081	2083	2084	2108	2137
Li-ion battery maximum power	GW_{el}	0.0	0.0	0.0	0.0	0.0
Li-ion battery capacity	GWh	0.0	0.0	0.0	0.0	0.0
Nominal PtG plant power	GW_{el}	156.4	162.9	166.4	221.6	288.6
Nominal CCGT power	GW_{el}	59.2	47.4	44.9	28.5	13.6
Nominal GT power	GW_{el}	243.9	155.6	67.0	59.8	49.1
Full load hours Li-ion battery (charging)	h	-	-	-	-	-
Full load hours PtG	h	2593	2625	2688	2956	3127
Full load hours CCGT	h	1803	1698	1617	1274	960
Full load hours GT	h	91	103	178	184	205
Gas storage capacity	TWh_{NCV}	80.1	82.6	83.5	101.1	130.7
Gas storage maximum injection capacity	GW_{NCV}	105.4	110.0	112.6	152.3	195.5
Gas storage maximum withdrawal capacity	GW_{NCV}	336.5	313.7	285.0	297.2	308.7
Imported hydrogen from natural gas	TWh_{NCV}	0.0	0.0	0.0	0.0	0.0
Used potential of hydrogen from biomass	TWh_{NCV}	22.1	22.1	22.1	22.1	22.1
Balance point temperature EHPGB	°C	-	8.9	8.6	8.1	-
Balance point temperature EHPEHR	°C	5.2	5.6	-	-	-
Relative CO_2 reduction	%	100.0	100.0	100.0	100.0	100.0
Cost annuity	bil. EUR	111.9	107.9	104.2	111.2	119.3

A.4 Quasi-Stationary Gas Grid Computation

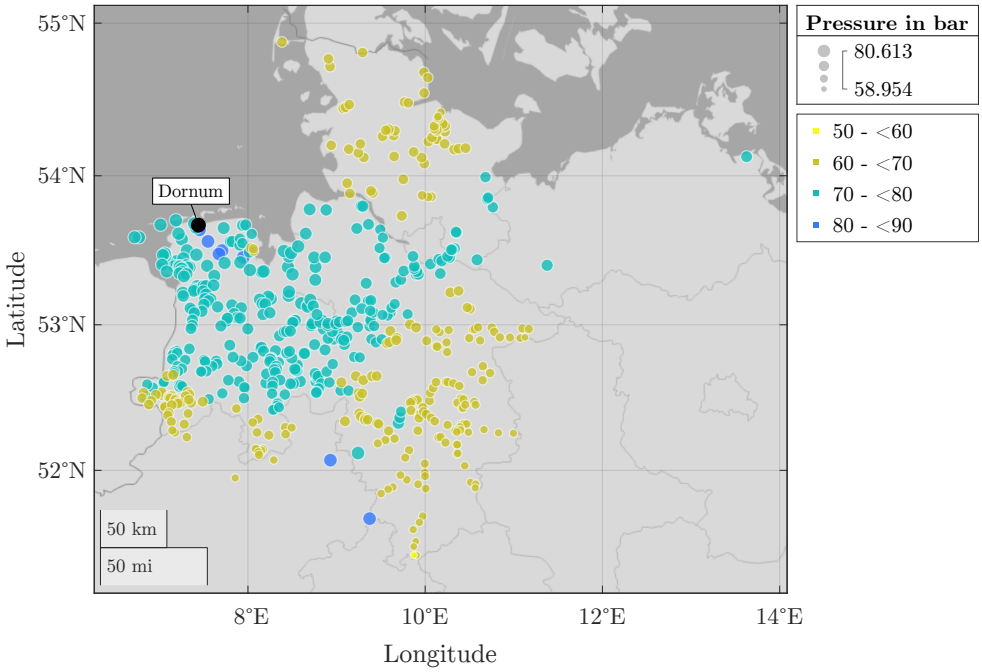

Figure A.6: Pressure values at every third node of the highest gas grid level at the 463rd hour for 100 % RE SNG 0_100_0 (low-pressure situation).

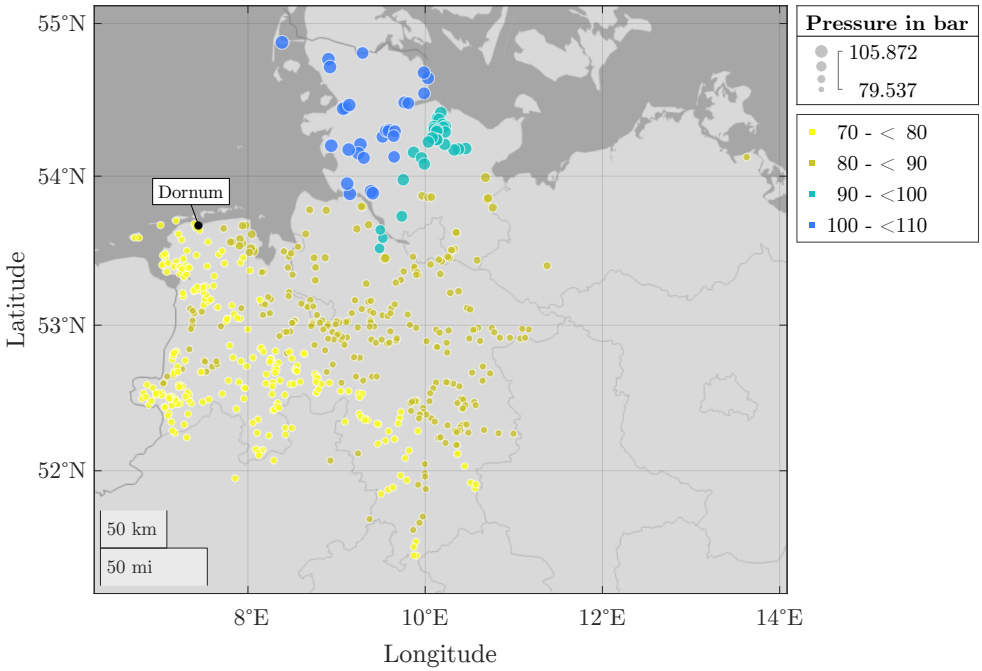

Figure A.7: Pressure values at every third node of the highest gas grid level at the 5628th hour for 100 % RE SNG 0_100_0 (high-pressure situation).